INTEGRATED LADLE METALLURGY CONTROL

INTEGRATED LADLE METALLURGY CONTROL

By

KEVIN JAMES GRAHAM, B.Eng.

A Thesis

Submitted to the School of Graduate Studies

In Partial Fulfilment of the Requirements

for the Degree

Doctor of Philosophy

McMaster University

DOCTOR OF PHILOSOPHY (2008)
(Materials Science and Engineering)

McMaster University
Hamilton, Ontario, Canada

TITLE: Integrated Ladle Metallurgy Control

AUTHOR: Kevin James Graham, B.Eng. (McGill University, Canada)

SUPERVISOR: Dr. Gordon A. Irons

NUMBER OF PAGES: xxviii, 390

ABSTRACT

The ladle metallurgical furnace (LMF) is a very flexible and common unit operation found in most steelmaking melt shops, and enables the adjustment and fine-tuning of molten steel's composition and temperature prior to casting. Despite the importance of ladle metallurgy to the overall steel making process very little has been achieved in the way of advanced ladle control. Limited sensors are available to monitor heat progress during refining and current control methods involve manual procedures. This thesis represents part of an ongoing study on the modelling of a full-scale LMF in real-time with the forward goal of improved control and optimization.

The first part of this thesis details a vision-based sensor for analyzing ladle eye dynamics online using a multivariate image analysis (MIA) technique based on principal component analysis (PCA). Predictive capabilities of the developed model are demonstrated using previously published cold model data over a wide range of operating variables. Further, preliminary work has confirmed the ability of the sensor for potential use in an industrial setting. The second part of this study concerns the development of metallurgical models for assessing the state of a ladle metallurgical furnace. Specifically, a multi-component kinetic model in combination with developed slag and steel thermodynamic solution models were used to quantitatively describe the kinetics of slag-metal reactions within 41 industrially sampled heats at ArcelorMittal Dofasco's LMF#2. Metal phase mass transfer coefficients for all elements in steel were assumed to follow the empirical relation derived from measured sulphur contents, while slag phase mass transfer coefficients were calculated by fitting the ratio of k_m^M / $k_{sl}^{M_xO_y}$ to the experimental results. On the basis of the fitted results, slag phase mass transfer coefficient correlations were evaluated using linear regression. Computed results from the model using these slag phase mass transfer coefficient correlations were found to be consistent with the experimental data. In regard to the developed thermodynamic solution models, original contributions to the modified interaction parameter formalism and cell model are presented. As process model predictions are invariably uncertain, the final part of this work involves the use of a stochastic model (extended Kalman filter) to account for process disturbances, model-mismatch and other sources of uncertainty that may result in significant error propagation causing poor process control and plant economics. Several case studies were performed to illustrate the effectiveness of the extended Kalman filter and its application to optimal sensor selection was introduced.

ACKNOWLEDGEMENTS

For certain, the cumulative results of this thesis have, from my view, conclusively confirmed one undeniable truth:

'Prediction is very difficult, especially about the future.' – Niels Bohr

In reaching this conclusion, this thesis benefited greatly from significant industrial and academic support. Foremost thanks are owed to ArcelorMittal Dofasco and in particular S. Waterfall, M. Ricci, S. Sun, G. Filipov, M. McGrath, and J. Popovich for their encouragement and efforts in facilitating plant trials, data collection, and laboratory work. Any apparent success resulting from this thesis is a testament to the willingness and efficacy of the aforesaid in seeking improved plant performance. Thanks are also owed to P. Van der Zalm and R. Minion of Heraeus Electro-Nite for providing sensors and instrumentation to the project. G.S. Casuccio and M. Potter of RJ Lee Group are credited for the inclusion analysis work and for providing in-kind assistance. The financial support of McMaster Steel Research Centre members (specifically ArcelorMittal Dofasco and Hatch) and the Natural Sciences and Engineering Research Council of Canada are also gratefully acknowledged.

My supervisor Dr. G.A Irons is thanked for his patience and for the freedoms granted during the course of this project. Dr. Irons is also thanked, along with supervisory committee members Dr. K. Coley and Dr. J.F. MacGregor for helpful discussions and feedback rendered. J. Thomson, K. Krishnapisharody, O.

Kelly, Dr. Malakhov, and Dr. Subramanian are acknowledged for their friendship and project involvement.

Special thanks are owed to E.M.J. Jahnsen for having initially nurtured my interest in graduate studies and for his valuable and unrestricted discussions throughout the project. T. Gustafson is acknowledged for his advice and readiness in answering questions.

Alison Cox is deserving of much thanks for her optimism, for helping me maintain some notion of work-life balance, and for most unfairly having to tolerate my state of petulance these past three years. This thesis is better for her contributions.

TABLE OF CONTENTS

LIST OF FIGURES

Chapter 1

Chapter 2

Chapter 3

Chapter 4

Chapter 5

Chapter 6

Chapter 7

LIST OF TABLES

Chapter 2

Chapter 3

Chapter 4

Chapter 5

Chapter 6

Chapter 1

INTRODUCTION

1.1. Modern Iron & Steelmaking

Two technologies dominate the production of steel: (i) integrated steelmaking, and (ii) electric furnace steelmaking. Integrated steelmaking involves smelting iron ore in a blast furnace to produce high carbon liquid iron, after which a basic oxygen furnace (BOF) is then used to lower the carbon content. Electric furnace steelmaking is essentially a scrap melting operation producing molten metal. A summary flowsheet illustrating the manufacturing process of both methods is presented as Figure 1-1. As seen, a great number of unit processing operations ranging from coke making, sinter and pellet plants, to reheat furnaces are needed in the production of high quality steel.

While not shown in Figure 1-1, a refining step most commonly termed Ladle Metallurgy or Secondary Metallurgy is needed in advance of casting. A key step in either the BOF or EAF steelmaking processes, ladle metallurgy allows for the removal of impurities (S, P, O, N, C, and H) and inclusions that are deleterious to the physical properties of steel. Ladles, which in yesteryear of steelmaking served primarily as transfer vessels, serve in present day as metallurgical reactors enabling a wide range of refining processes, namely: desulphurization, deoxidation, heating, alloying, degassing, and inclusion modification. As illustrated in Figure 1-1, upon satisfying target composition and temperature specifications during ladle metallurgy, refined molten steel is cast by a continuous caster into solid shapes suitable for further thermal and mechanical processing steps.

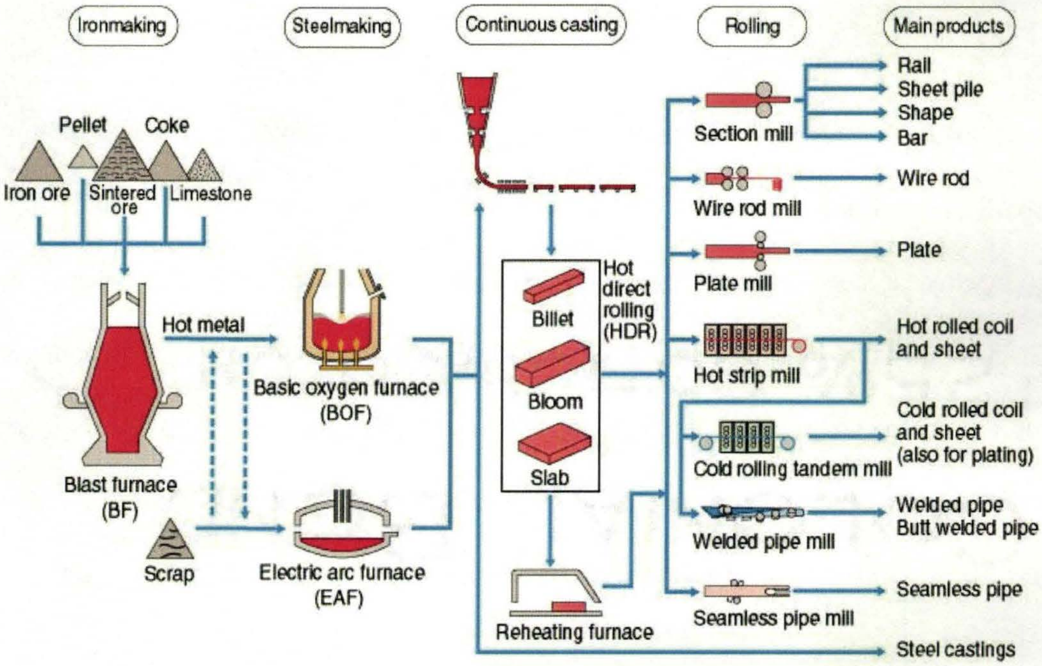

Figure 1-1: Schematic flowsheet of steelmaking operations in a modern steel plant. (JFE 21st Century Foundation, website: http://jfe-21st-cf.or.jp)

1.2. Ladle Metallurgical Furnace

While a variety of ladle metallurgy processing units are available to steelmakers, the ladle metallurgical furnace (LMF) is a very flexible and common piece of equipment found in most steelmaking meltshops. A schematic of the ladle metallurgical furnace is presented as Figure 1-2.

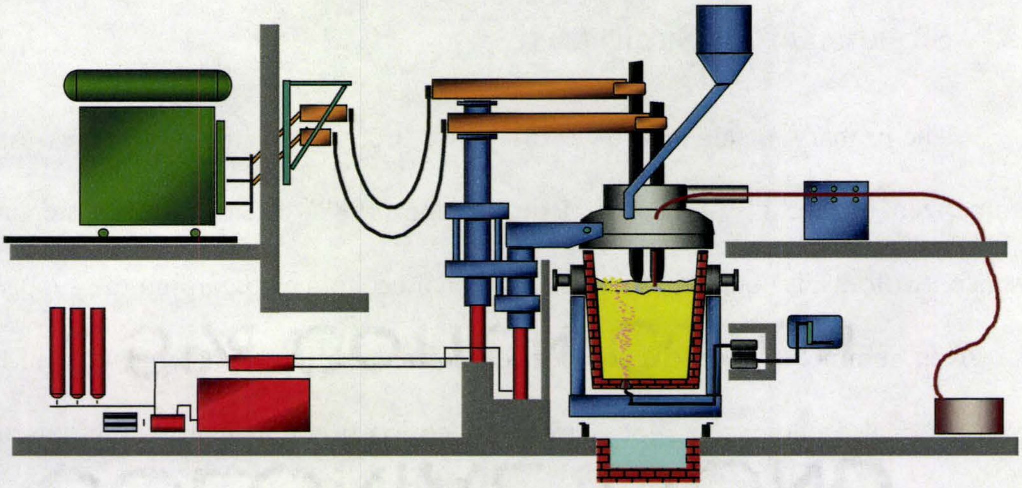

Figure 1-2: Schematic of Ladle Metallurgical Furnace (LMF). (Reproduced from Jahnsen, 2006)

As shown, a refractory lined cylindrical vessel called a ladle contains the steel and is used as a metallurgical reactor during refining, enabling both alloying and refining steps to be undertaken in a controlled manner. Heating within the ladle is provided by electric power that is delivered to the melt by graphite electrodes in the form of electric arcs. The electric arc is a plasma (charged gases and vapors) having a temperature in excess of 2,500°C. Further shown in Figure 1-2, is a top slag layer that serves to both protect the refractory lining from excessive wear due to arc radiation and to act as a sink for unwanted dissolved and solid constituents from the metal bath. Stirring is provided by bottom porous plug(s) fitted at the base of the ladle and has several benefits to the melt, namely: (i) removal of chemical and thermal stratifications, (ii) agglomeration and removal of inclusions, (iii) ease of alloy adjustments, and (iv) acceleration of chemical reactions. Reagent additions to the ladle can be made in lump form *via* a hopper and shoot arrangement or in wire form *via* a wire feeder.

1.3. Situation of the Subject

The primary metals industry is driven by strong competitive pressures. As summarized by Szekely, Evans, & Brimacombe (1988) these pressures are, in essence, twofold: (i) competition among national economies regarding the supply of a given commodity, and (ii) competition between different materials within a given national economy. In either case, competition becomes increasingly based on market differentiation resulting from the improved quality and / or development of new products and processes. As significant research and development efforts are typically needed to spark the development of a new product or process, it follows that in the intermediate term great emphasis is placed on optimizing existing operations.

Process optimization is generally regarded as meaning the best course of action from the available alternatives, where the 'best course of action' is typically defined in terms of economic value and / or process stability. In regard to engineering practice, engineers are usually dependent on mathematical models when making optimal day-to-day decisions. Such models, no matter whether they are theoretical or empirical in nature, serve to predict how a response (or set of responses) changes when other variables are manipulated. As highlighted by Ray & Szekely (1973), successful implementation of optimization procedures depend critically on the accuracy of direct measurements and / or the predictive ability of developed process models.

Although a significant amount of small-scale laboratory experimentation and mathematical modelling work has been carried out on various aspects of ladle refining, relatively little work has been undertaken on full-scale industrial operations. Reasons for the failure in extending the laboratory work to industrial systems are largely attributed to the significant control challenges within commercial steel plant operations, including: (i) elevated temperatures, (ii) dusty environments, (iii) electrical arcing, (iv) complex multi-component steel / slag systems, (v) uncertainty associated with plant measurements, and (vi) the significant variation in refining practices on a heat-to-heat and plant-to-plant basis. Recent summaries by Brooks and Subagyo (2002), and Carlsson et al. (1986) detail the current state of control practices and technological advances within ladle metallurgy. Their reviews highlight that while significant gains have been made in the comprehension of the physico-chemical and kinetic aspects of ladle processing, the maturation of sophisticated process control systems have lagged. Limited sensors are available to monitor heat progress and existing control methods involve empirical evidence and manual procedures that are too slow for application into feedback control schemes. As a result of these inherent limitations, ladle metallurgy operations have focused research efforts on obtaining process stability as opposed to process optimization.

At present, despite the clear importance of ladle metallurgy to the overall steelmaking process, no generally accepted, industrially validated process model exists to quantitatively predict heat status both continuously and reliably during the refining sequence (Jönsson & Jonsson, 2001). Recognizing this apparent knowledge gap in the literature and the resulting potential economic benefits to the steel industry in having a fully-functioning control system, the key work of this thesis is to develop a reliable process model for the ladle metallurgical furnace that is capable of real-time state estimation of unmeasured or infrequently measured properties during refining. The overall objective is to develop the framework for a first generation ladle control system that can be used by steelmakers for process optimization and quality assurance purposes. Extensive sampling on full-scale heats and the development of comprehensive mathematical models have been undertaken in order to achieve these research objectives.

1.4. Objectives of the Research

The general goals of the work have been previously mentioned. Specific objectives in the thesis include:

1. To develop a vision-based sensor for analyzing ladle eye dynamics in real-time using a multivariate image analysis (MIA) technique based on principal component analysis (PCA).

2. To acquire a detailed understanding of the activities of multi-component solutions. In this part, mathematical models will be developed for estimating the activities in steel and slag phases.
3. To study the topic of slag carryover mass from the electric arc furnace (EAF) and to develop a model capable of online prediction of integral processing parameters.
4. To develop a comprehensive multi-component kinetic model capable of quantitatively describing the experimentally sampled industrial heats from ArcelorMittal Dofasco. This work will make use of the developed steel and slag activity models, and also the slag carryover model.
5. To explore the topic of non-metallic inclusions during secondary metallurgy. In this part, the main intention is to gain some insight into inclusion behaviour as a function of operation conditions within the ladle metallurgy furnace.
6. To investigate use of the Kalman filter, a state estimation algorithm, in correcting for modelling errors due to natural fluctuations or limitations of measurement devices. Work will introduce the Kalman filter as a tool for optimally selecting which process parameters to update via measurements and consequently which existing or theoretical sensor set combinations to use.

1.5. Organization of the Thesis

The contents of this thesis are organized in 7 chapters and 6 appendices. Chapter 1 describes the situation of the subject as well as the motivation and objectives for the research. In Chapter 2, the results of work to develop a vision-based sensor for analyzing ladle eye dynamics are presented. Specifically, sensor proof-of-concept is first demonstrated in a laboratory setting before industrial findings are discussed. Chapter 3 details the development of the unified interaction parameter formalism and cell model, thermodynamic solution models used within this thesis for estimating the activities of slag and metal components. The developed models are shown validated against selected experimentally determined systems. In regard to the cell model, previously unpublished equations and numerical procedures have been presented enabling its extension to poly-anionic slags. The key work of this thesis is presented as Chapter 4, where a multi-component kinetic model has been developed for quantitatively predicting the status of 41 industrially sampled heats from ArcelorMittal Dofasco. Slag carryover characterization work is also reviewed here. Chapter 5 describes results obtained from a detailed investigation of inclusions using a computer-controlled scanning electron microscope (CCSEM) known as the Automated Steel Cleanliness Analysis Tool (ASCAT) from RJ Lee Group. Chapter 6 focuses on introducing the extended Kalman filter as a tool for improving both process control and economics within the LMF. Used extensively within the chemical engineering field, the Kalman Filter is commonly used for sensor selection and for assessing the importance of parameter errors, input errors or stochastic disturbances on model predictions. A summary of the findings and conclusions with respect to scientific and industrial applications from this work is presented as Chapter 7. Proposals for future research are also discussed. It should be noted that each chapter will contain a brief literature review to provide the reader with the necessary technical background and to summarize the previous state of the subject.

Chapter 2

MONITORING LADLE EYE DYNAMICS USING MULTIVARIATE IMAGE ANALYSIS[1]

2.1. Introduction

The ladle eye is well established as an important control feature in secondary metallurgy. Tight control over the ladle eye is, however, difficult in most operating plants due to lack of available feed-back data and the manual control of inert-gas flowrate. Improved control methods are therefore needed to satisfy the demand for products of higher purity and better controlled composition.

Since being introduced by Esbensen and Geladi (1989), multivariate image analysis (MIA) techniques (Geladi & Grahn, 1996) have steadily grown in application. Recent uses include the online monitoring of industrial processes such as lumber grading, boiler / rotary kiln flames, and snack food inspection (Bharati & MacGregor, 1998; Bharati & MacGregor, 2002; Lu & MacGregor, 2003; Szatvanyi et al., 2006). Of importance to the current study, Brooks and

---

[1] Most of the contents of this chapter were published as: K.J. Graham, K. Krishnapisharody, G.A. Irons, and J.F. MacGregor, "Ladle Eye Area Measurements using Multivariate Image Analysis", *Canadian Metallurgical Quarterly*, (2007), Vol. 46, No. 4, pp. 397-405.

Subagyo (2003a, 2003b) proposed using multivariate image analysis techniques to monitor ladle eye dynamics.

This chapter describes a vision-based sensor for analyzing ladle eye dynamics in real-time using a multivariate image analysis (MIA) technique based on principal component analysis (PCA) (Wold et al., 1987). Sensor proof-of-concept is first demonstrated using published cold model laboratory work (Krishnapisharody & Irons, 2006), and later demonstrated in an industrial ladle metallurgical furnace at ArcelorMittal Dofasco.

2.2. Literature Review

2.2.1. Gas Stirring in Ladles

Mixing is a common practice in most metallurgical vessels. Typically promoted by some variant of gas injection, electromagnetic forces, or vacuum driven circulation, mixing has several benefits to the melt, namely: (i) removal of chemical and thermal stratifications, (ii) agglomeration and removal of inclusions, (iii) ease of alloy adjustments, and (iv) acceleration of chemical reactions. The reader is referred to the article by El-Kaddah and Szekely (1983) for a more detailed overview of the attractions and drawbacks of the various mixing mechanisms.

Figure 2-1 summarizes the various methods of melt stirring currently in use within the industry. In regard to the ladle metallurgical furnace (LMF), stirring is typically accomplished by gas injection via porous plug(s) fitted at the base of the ladle.

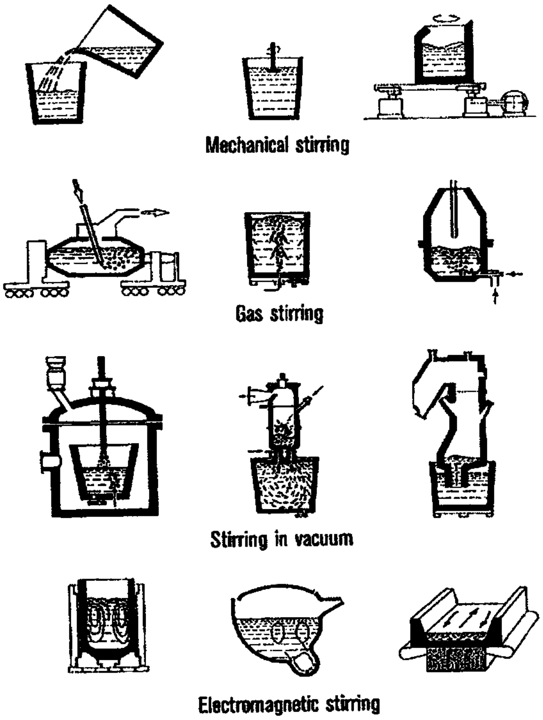

Figure 2-1: Different methods of melt stirring. (Oeters et al., 1988)

2.2.2. Ladle Eye Formation During Inert-Gas Purging

A consequence of inert-gas stirring involves the potential displacement of slag cover to the periphery of a ladle's upper surface due to the upwelling plume of gas breaking the slag-metal interface. Under such conditions the raised region where gas is discharged from the melt is termed the "spout", while the region where liquid metal is exposed to the atmosphere is called the "eye". Although ladle eyes are occasionally sought for alloy addition purposes, they are generally undesired as nitrogen absorption and melt reoxidation may occur across the gas-metal interface. It is further believed that slag emulsification beneath the eye may result in slag entrainment. On this basis, considerable research work has been undertaken in recent years to characterize the phenomena affecting eye and spout formation.

Yonezawa & Schwerdtfeger (1999) were among the earliest to conduct experimental work on eye formation in a gas-stirred ladle. In their work, laboratory scale experiments were performed using mercury and silicone oils to simulate liquid steel and slag. Experimental results demonstrated that ladle eye size increased with increasing gas flowrate and decreased with increasing top slag layer thickness. Two slightly different empirical expressions valid for different nozzle dimensions were proposed by Yonezawa & Schwerdtfeger (1999) by correlating the time averaged ladle eye area size to selected process variables using a polynomial regression technique:

for $0.01 < Q^2 / gh^5 < 10000$ and $d = 0.5$ mm

$$\log\left(\frac{A}{hH}\right) = -0.69897 + 0.9003\log\left(\frac{Q^2}{gh^5}\right) - 0.14578\left[\log\left(\frac{Q^2}{gh^5}\right)\right]^2 + 0.0156\left[\log\left(\frac{Q^2}{gh^5}\right)\right]^3 \tag{2-1}$$

for $0.01 < Q^2 / gh^5 < 2000$ and $d = 1.0$ and 1.5 mm

$$\log\left(\frac{A}{hH}\right) = -0.45593 + 0.83275\log\left(\frac{Q^2}{gh^5}\right) - 0.14732\left[\log\left(\frac{Q^2}{gh^5}\right)\right]^2 + 0.0179\left[\log\left(\frac{Q^2}{gh^5}\right)\right]^3 \tag{2-2}$$

where A is the eye area, H is the bath height, Q is the gas flow rate, h is the height of the top layer, and d is the diameter of the gas injection nozzle. On the basis of preliminary industrial trials, Yonezawa & Schwerdtfeger (1999) concluded that equation 2-2 is capable of estimating eye area in full-scale steel ladles.

Subagyo et al. (2003), believing that equation 2-2 failed to effectively unify both plant measurements and cold model experiments, used the experimental data of Yonezawa & Schwerdtfeger (1999) and attempted to derive a modified ladle eye area correlation. Their correlation was based on the assumption that eye area was always smaller than the base area of the spout. On introducing a new dimensionless number representing the ratio of eye and spout areas, Subagyo et al. (2003) proposed the following empirical equation:

$$\frac{A_e}{(h+H)^2} = 0.02\left[Q^2/(gh^5)\right]^{0.375} \tag{2-3}$$

The reasonable agreement between measured and calculated values in Figure 2-2 was used by Subagyo and coworkers (2003) to justify application of their correlation within ladles subject to similar process conditions.

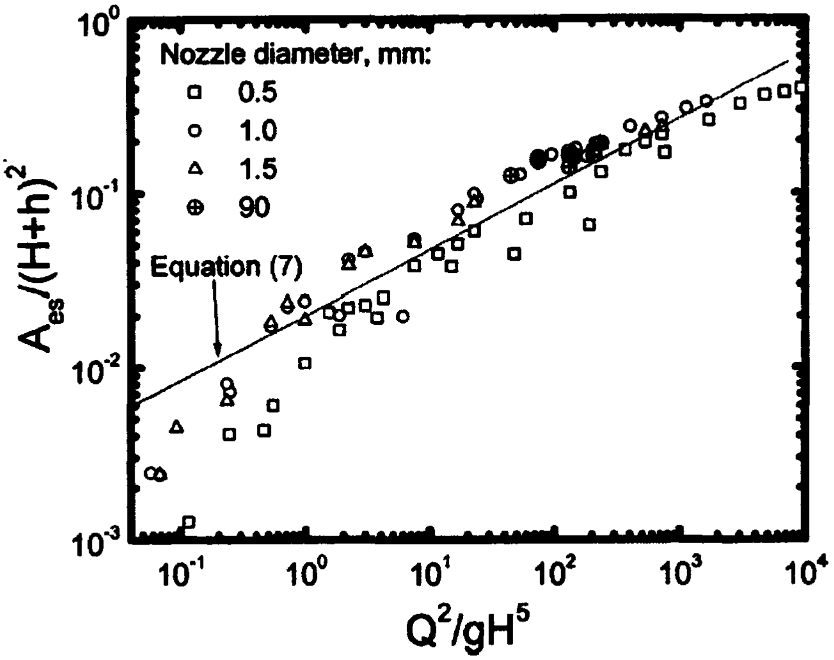

Figure 2-2: Eye size predictions using the correlation of Subagyo et al. (2003).

In an effort to investigate the ladle eye size from a more theoretical standpoint, Mazumdar & Evans (2004) developed a macroscopic model of ladle eye formation. Mazumdar & Evans (2004) assumed, as Subagyo et al. (2003) had done previously, that eye size was smaller than spout size. Based on the conical assumption of the plume and the idealized representation of the spout surface, Mazumdar & Evans (2004) used geometric arguments to obtain the following equation for eye size in its limiting form as:

$$\frac{A_e}{H^2} = K_1 - K_2\left(\frac{H}{Q^{2/3}}\right) \tag{2-4}$$

where Q is the flowrate of injected gas, K_1 and K_2 are constants dependent on the characteristics of the gas-liquid-metal system and / or the vessel dimensions. To assess the adequacy of their relation, Mazumdar & Evans (2004) compared the predicted results using equation 2-4 with the cold model and industrial data of Yonezawa & Schwerdtfeger (1999), shown as Figure 2-3.

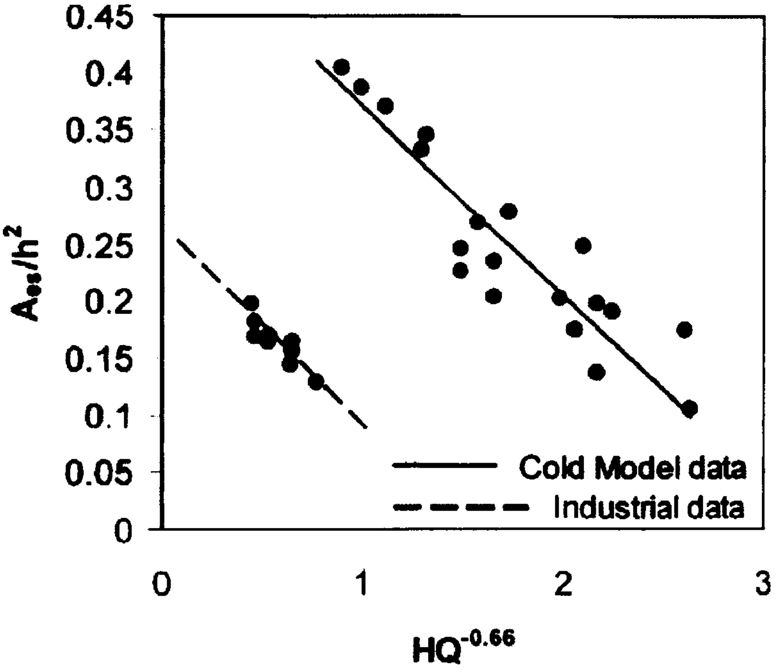

Figure 2-3: Variation of the dimensionless eye area with the parameter $HQ^{-0.66}$. (Mazumdar & Evans, 2004)

Iguchi et al. (2004) proposed another correlation for the eye area based on the estimation of the volume and height of molten metal carried by bubbles above the horizontal slag-metal interface. Assuming the molten metal column carried into the slag layer to be parabolic in shape, Iguchi et al. (2004) derived the following non-dimensional equation for eye area:

$$\frac{A_e}{H^2} = a_1 - a_2 \left[\frac{2g(\rho_m - \rho_s)h}{\rho_m U_p^2} \right] \tag{2-5}$$

where H is the depth of steel, h is the slag thickness, U_p is the plume velocity, ρ_m and ρ_s are the densities of the metal and slag, respectively, and a_1 and a_2 are constants.

As equation 2-5 was found valid over only a small range of the experimental data of Yonezawa & Schwerdtfeger (1999), Iguchi et al. (2004) developed an alternative empirical expression in semi-logarithmic scale as:

$$\log\left(\frac{A_e}{H^2}\right) = -0.222 - 0.741\left[\frac{2g(\rho_m - \rho_s)h}{\rho_m U_p^2}\right] \tag{2-6}$$

This equation was found to yield eye area approximations within a 60% scatter of the experimental results of Yonezawa & Schwerdtfeger (1999). Further, a similar range of scatter (100%) was reported for eye area approximations on their own experimental work for a metal-slag density ratio of unity. Iguchi et al. (2004) claim that the superior predictive ability of their correlation in comparison to the others within the literature is due to the inclusion of the many physical property parameters within its derivation.

The most recent work on the topic of ladle eye formation was completed by Krishnapisharody & Irons (2006). Aimed at obtaining an improved fundamental understanding of ladle eye formation, these researchers undertook extensive experimental work measuring eye sizes at room-temperature over a wide range of conditions, including different combinations of fluids to simulate liquid steel and slag. Further, a mechanistic mathematical model for the eye size was developed from fundamental fluid flow considerations. The major aspects are discussed below.

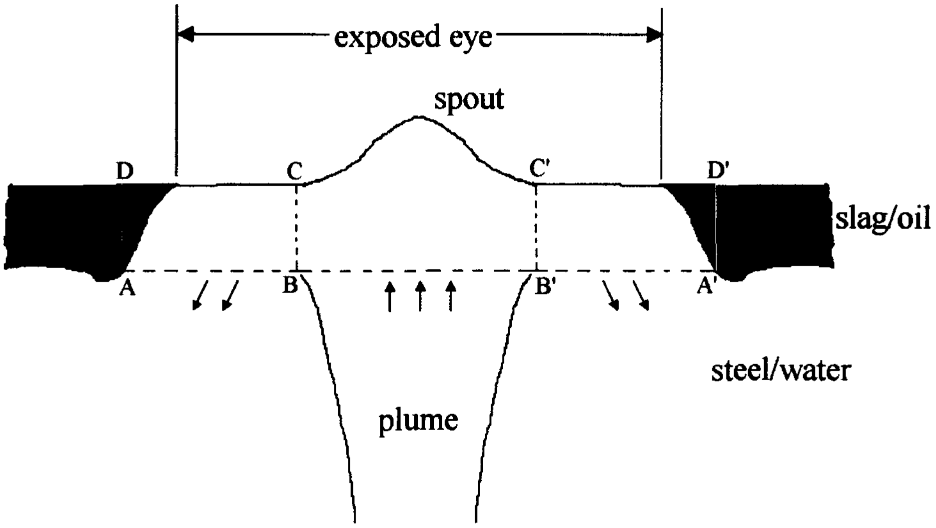

Figure 2-4. Schematic representation of slag eye formation in systems with thin top layer. (Krishnapisharody & Irons, 2006)

From their experimental work on different systems, Krishnapisharody & Irons (2006) noticed that eye size is usually larger than that of the spout zone, in the case of relatively thin slag layers relevant to ladle metallurgy applications. This observation was in contrast with the assumptions of Subagyo et al. (2003) and Mazumdar & Evans (2004), and forms the basis of their mechanistic model. The eye formation process for thin top layers was schematically depicted by Figure 2-4.

Applying conservation laws for mass and momentum over the labeled control volume (ABCD) in Figure 2-4, Krishnapisharody & Irons (2006) derived their mechanistic eye size model as a relationship between the non-dimensional eye area and the densimetric Froude number. The general form of the model was given as:

$$\frac{A_e}{A_p} = a + b\left(\frac{\rho_l}{\Delta\rho}\frac{U_p^2}{gh}\right)^{1/2} \tag{2-7}$$

where A_e and A_p are the areas of the eye and the plume respectively, U_p the plume velocity, h the slag thickness, and a and b numerical constants. Considering a conical plume shape, the above equation was further simplified to the form:

$$A^* = \frac{A_e}{H^2} = \gamma + \delta\left(\frac{\rho_l}{\Delta\rho}\right)^{1/2}\left(\frac{U_p{}^2}{gh}\right)^{1/2} \tag{2-8}$$

where H is the bath height and γ and δ are numerical constants. The non-dimensional eye area, A^*, was obtained as a function of non-dimensional density difference and the Froude number, Fr (= U_p^2 / gh). In order to validate their model, Krishnapisharody & Irons (2006) plotted the variation of the non-dimensional eye area (equation 2-8), using the available data on eye size from different liquid-liquid systems. These plots are given in Figure 2-5 and 2-6.

The effect of density difference between the liquids is clear from Figure 2-5, where the data from different systems are seen to fall on distinct lines. These different sets of data have been combined in Figure 2-6 by plotting the non-dimensional eye area against the densimetric Froude number. It was clear from these figures that equations 2-7 and 2-8 capture the eye formation behavior in different systems with vastly different density ratios within reasonable limits. On the basis of these observations, Krishnapisharody & Irons (2006) concluded that their model represents a reasonable macroscopic model for slag eye formation. The scatter in Figures 2-5 and 2-6 was attributed to the simplistic conical plume assumption used in deriving equation 2-8. It was subsequently shown that the scatter could be eliminated by using the actual plume area in equation 2-7 (Krishnapisharody & Irons, 2007).

In the same work, Krishnapisharody & Irons (2006) reviewed the ladle eye size correlations within the literature against available experimental data. Their findings demonstrate that equations 2-7 and 2-8 offer improved estimates over the previously available correlations within the literature.

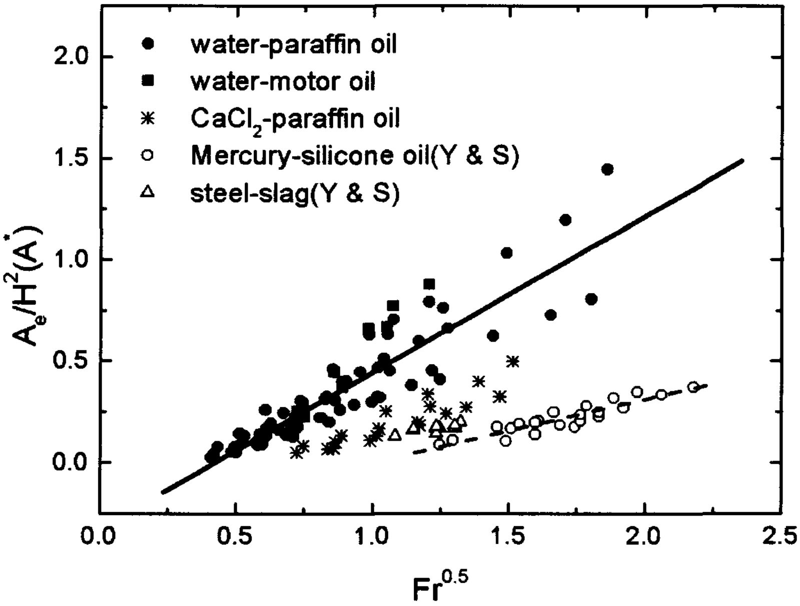

Figure 2-5: Variation of non-dimensional eye area: comparison with literature. (Krishnapisharody & Irons, 2006)

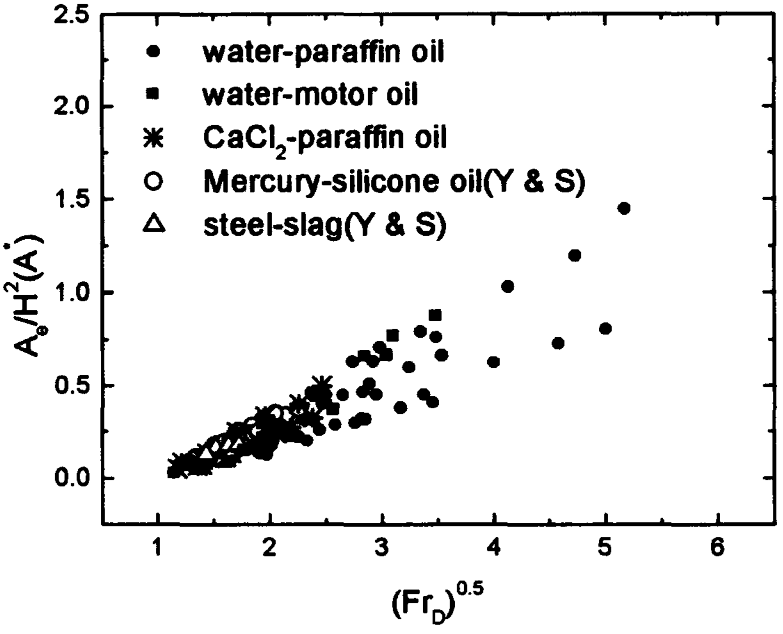

Figure 2-6: Non-dimensional eye area *vs.* densimetric Froude number. (Krishnapisharody & Irons, 2006)

2.2.3. Application to Industrial Operations

Although the mechanistic model of Krishnapisharody & Irons (2006) has been shown to accurately describe eye size for a wide range of flow rates, density ratios and heights, it has yet to be used for describing industrial systems. While Krishnapisharody & Irons (2006) suggest that their correlations may be applied to eccentric injections common to industrial operations, several factors limit direct application of these equations. The major drawback to using a mechanistic approach in estimating industrial ladle eye size is the uncertainty in the model parameters and how to update these parameters in real-time. A further challenge concerns the interaction of eccentric injection plumes with either the ladle sidewall or with each other due to the occurrence of plume wandering (Krishnapisharody & Irons, 2006).

Owing to these problems, and recognizing the success of online process monitoring techniques within the chemical engineering field, Subagyo & Brooks (2003) proposed using multivariate image analysis (MIA) in combination with a simple Kodak DC4800 digital RGB camera to monitor ladle eye dynamics. Initial tests of the MIA technique were carried out using discrete images captured by positioning the digital camera above the melt. Figures 2-7 to 2-9 summarize the results of MIA (using the model developed for this thesis) on previously unpublished images by Pan & Brooks (2004).

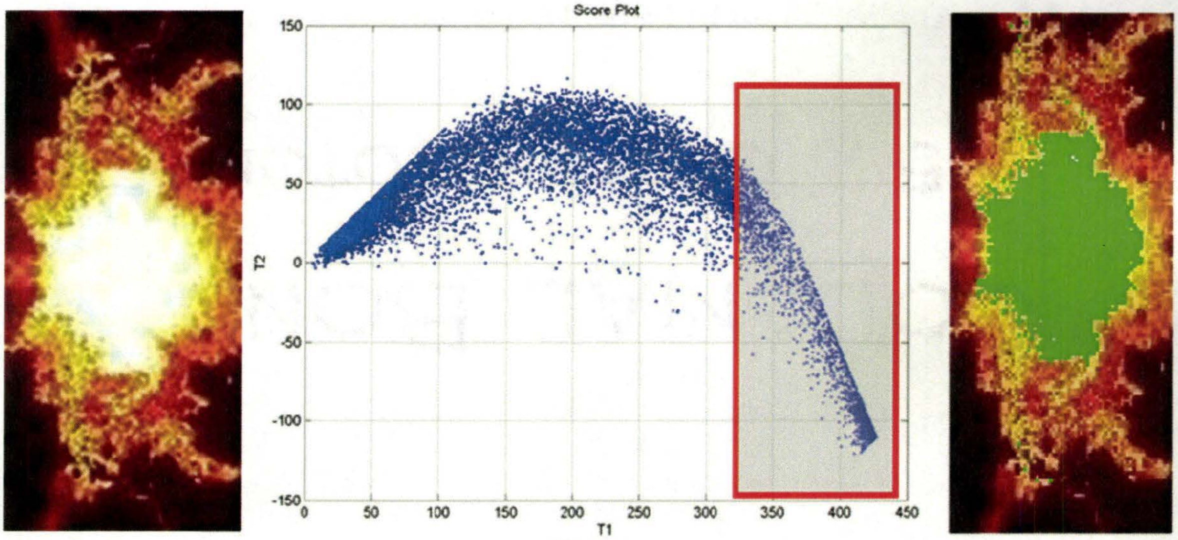

(A) (B) (C)

Figure 2-7: MIA ladle eye area identification results on an image taken with the ladle cover off. (A) Original image, (B) Score plot, and (C) Projection of applied mask on the image space.

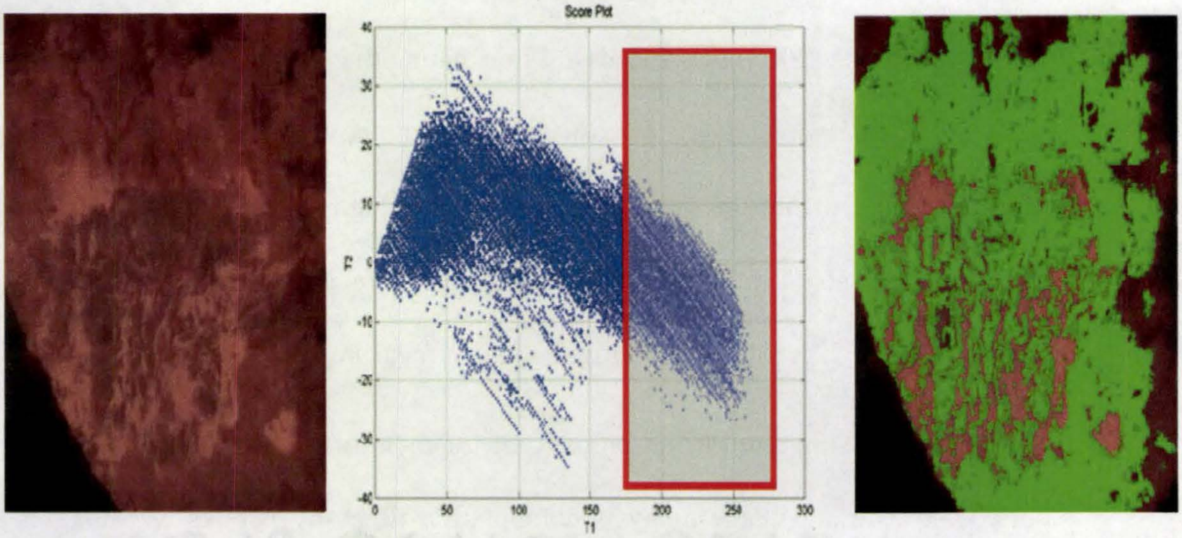

(A) (B) (C)

Figure 2-8: MIA ladle eye area identification results on an image taken with the ladle cover on. (A) Original image, (B) Score plot, and (C) Projection of applied mask on the image space.

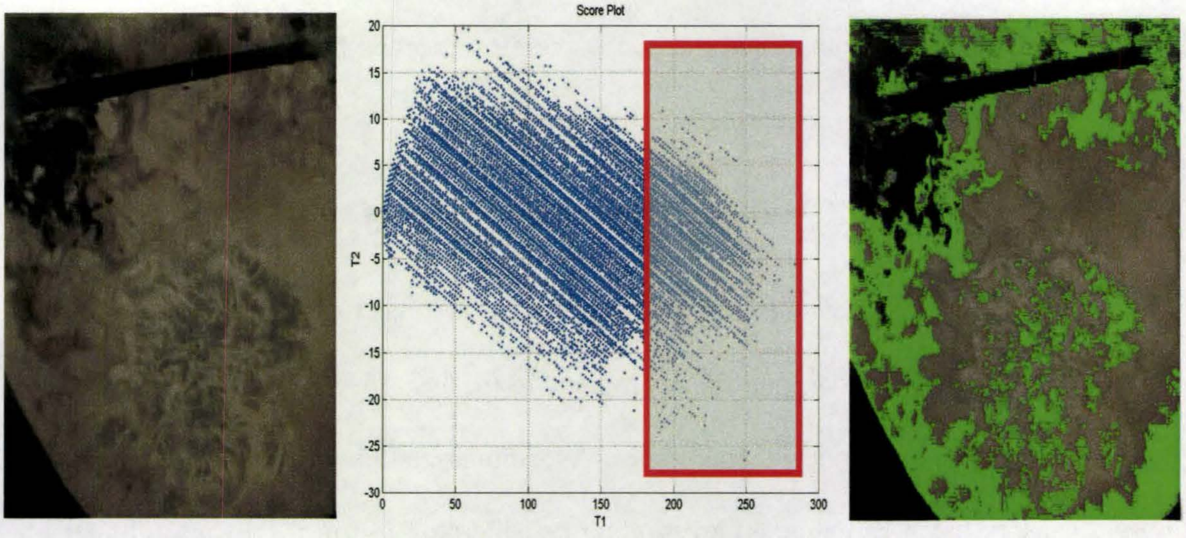

(A) (B) (C)

Figure 2-9: MIA ladle eye area identification results on an image taken with the ladle cover on and electrical arcing on. (A) Original image, (B) Score plot, and (C) Projection of applied mask on the image space.

As seen from the above figures, while the MIA method proposed by Subagyo & Brooks (2003) was successful in isolating the ladle eye when the ladle cover was off, the poor image contrast with the ladle cover on resulted in pixels being convoluted within the score space and consequently yielded poor masking results. On the basis of the good agreement from Figure 2-7 a patent was secured by Subagyo & Brooks (2002) covering the online measurement of molten phases.

Although suggested as an online tool for monitoring ladle eye dynamics, reported multivariate image analysis computation times by Brooks & Subagyo (2002) ranged between 0.5 to 14 minutes. Clearly, improved algorithms are needed for real-time control. In addition, the analyses by Subagyo & Brooks (2002) were all performed post-mortem using off-line images. The development of a suitable computational method is therefore needed for segmenting the score space in real-time processing.

2.2.4. Review of Multivariate Image Analysis

The field of machine vision has been a subject of study for the past 40 years, and has undergone rapid progress in the last 15 years due to advances in imaging and computer technologies. As summarized by Bharati (2002), imaging sensors (such as cameras) are finding considerable use in a growing number of industrial processes, where their primary function is to allow a computer to understand aspects of its surroundings (Marshall & Martin, 1992 ; Liu, 2004). Application of vision-based sensors are replacing human vision-based tasks and serve as inexpensive solutions to the increased demand for improved economics and quality control.

As digital images contain large amounts of data, it follows that a major restriction regarding the application of vision-based sensors is the ability to extract and relate relevant information in real-time to product quality and process performance (Bharati, 2002). This section provides background information of imaging sensors and reviews the multivariate image analysis (MIA) techniques used in this work for segmenting image features.

2.2.4.1. Multivariate Images

A digital image is the discretized rendering of a real object or scene in terms of both spatial coordinates and brightness, whereby the process of rendering is called imaging (Geladi & Grahn, 1996). Data contained within a digital image is characterized as pixels arranged most commonly in a two-dimensional matrix, where each pixel is represented by a set of numbers corresponding to its 'X' and 'Y' coordinates and brightness intensity on the image. The exact number of pixels and the range in brightness levels in an image is defined as its image resolution. Four main classifications of digital images exist, namely: (i) grayscale, (ii) binary, (iii) indexed, and (iv) RGB. The reader is referred to Baxes (1994) and Rosenfeld (2001) for a more comprehensive review on image properties.

A multivariate image is any image that can be represented by a stack of congruent images, where each congruent image is measured for a different wavelength, frequency or energy (Geladi & Grahn, 1996). Congruency was defined by Geladi & Grahn (1996) as two or more stacked images such that a pixel in one image has a pixel with equivalent spatial coordinates in other images. As summarized by Bharati (1997), RGB (red-green blue) colour digital images are a standard mode of presenting high resolution colour data. Pixel data within a RGB image is stored in separate red, green, and blue intensity matrices, and provide information about an image's colour level at the time it was recorded. Numeric colour intensity values range between 0 and 255, permitting a possible 16×10^6 unique colour combinations within a single RGB image. Figure 2-10 illustrates these principles as applied to the lumber grading industry.

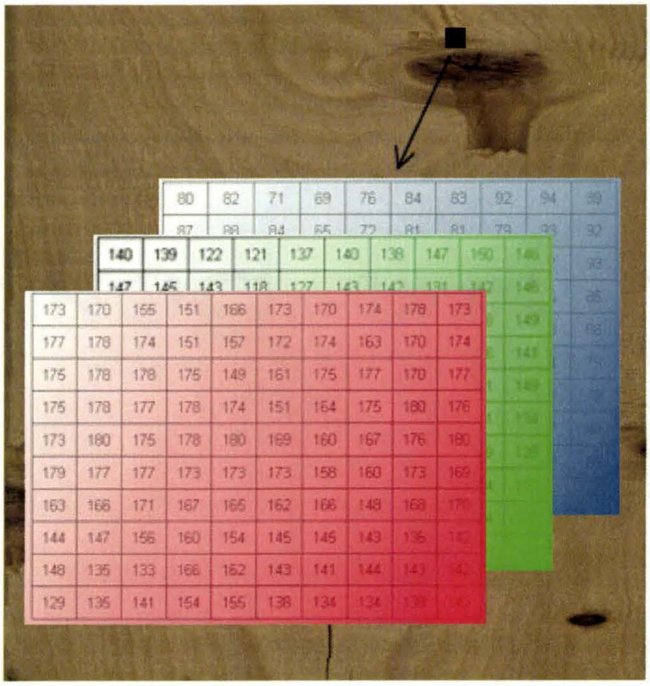

80	82	71	69	76	84	83	92	94	89

140	139	122	121	137	140	138	147	150	[illegible]

173	170	155	151	166	173	170	174	178	173
177	178	174	151	157	172	174	163	170	174
175	178	178	175	149	161	175	177	170	177
175	178	177	178	174	151	164	175	180	176
173	180	175	178	180	169	160	167	176	180
179	177	177	173	173	173	158	160	173	169
163	166	171	167	165	162	166	148	168	170
144	147	156	160	154	145	145	143	136	142
148	135	133	166	162	143	141	144	143	[illegible]
129	135	141	154	155	138	134	134	139	[illegible]

Figure 2-10: A magnified part of the lumber image, showing the numbers that represent the RGB layers (Prosensus, "Software for Colour Image Segmentation", March 19, 2008, from http://www.prosensus.ca/software/proportion/ProPortion_manual.pdf)

2.2.4.2. Image Analysis Techniques

Traditional image processing techniques involve manipulating pictorial information to improve, correct, analyze, or in some way alter an image (Baxes, 1994). As shown in Figure 2-11 (Baxes, 1994), these techniques are broadly grouped into five classes, where it should be noted that a combination of several processing techniques listed below may be required for achieving final objectives.

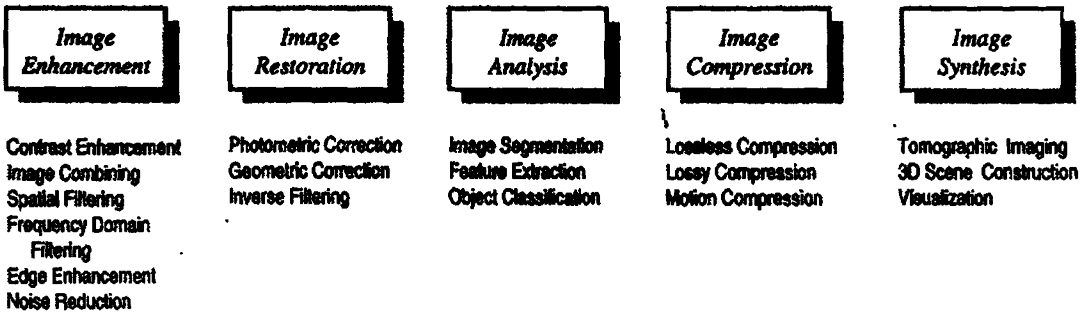

Figure 2-11: Summary of the five fundamental classes of digital image processing. (Baxes, 1994)

Unlike traditional image analysis techniques, multivariate statistics extract feature information from a digital image while working in the projected latent variable space of the original image. The most important feature of multivariate image analysis (MIA) is its ability to show image data as low-dimensional score plots. These score plots may then be used to reveal groupings, trends, and outliers within the original image. In their work, Bharati & MacGregor (2003) used a segmentation technique called 'masking' within the score plot to reveal characteristic features within the image space. The masking procedure takes advantage of the fact that pixels having similar colour intensities have similar score values and will therefore group in similar locations on the score plot.

The use of MIA methods for real-time monitoring of time-varying processes was first demonstrated by Bharati & MacGregor (1998) by monitoring a sequence of multi-spectral images of a satellite as it passed over a certain geographical region of the Earth's surface. Recent applications of the technique have included the online monitoring of industrial processes such as lumber grading, boiler / rotary kiln flames, and snack food inspection (Bharati & MacGregor, 1998; Bharati & MacGregor, 2003; Yu & MacGregor, 2003; Szatvanyi et al., 2006).

2.2.4.3. Multivariate Image Analysis (MIA)

The starting point for MIA involves principal component analysis (Wold et al., 1987 ; Jolliffe, 2002; Jackson, 1991) of the image to be analyzed. Principal component analysis (PCA) is a statistical projection method that approximates the correlation structure of a data matrix X by the matrix product of lower dimensions called principal components. Geladi & Grahn (1996) explained PCA algebraically as the decomposition of a matrix into simpler matrices:

$$X = \sum_{a=1}^{A} M_a \qquad (2\text{-}9)$$

where M_a is the simplified data matrix and A is the number of matrices. The minimum value of A is related to the rank of data matrix X. As explained in their text, all sub-matrices M_a have a rank of one and can be represented as a product of vectors:

$$X = TP^T + E = \sum_{a=1}^{A} t_a p_a^T + E \tag{2-10}$$

where T is the score matrix, P the loading matrix, A the number of principal components, and t_a and p_a the a-th column score and loading vectors of T and P for the a-th principal component. The residual matrix E is included in the model to account for unexplained data.

The loading matrix P is orthonormal and is computed as the eigenvectors of the covariance matrix X^TX. The score matrix T is determined by multiplying matrices X and P. Each score vector t_a is therefore a linear combination of the original dataset variables and the combination weights p_a. The principal component is defined as the orthogonal regression of a line through the data in the space spanned by X. The number of principal components may either be numerically determined by cross-validation (Wold, 1978), or based on the visual examination of residual images showing the percentage of the image explained (Geladi & Grahn, 1996). The stopping point for adding principal components is commonly regarded as being the point when the sub-space plane is no longer of lower dimension than the original dataset (Jackson, 1991).

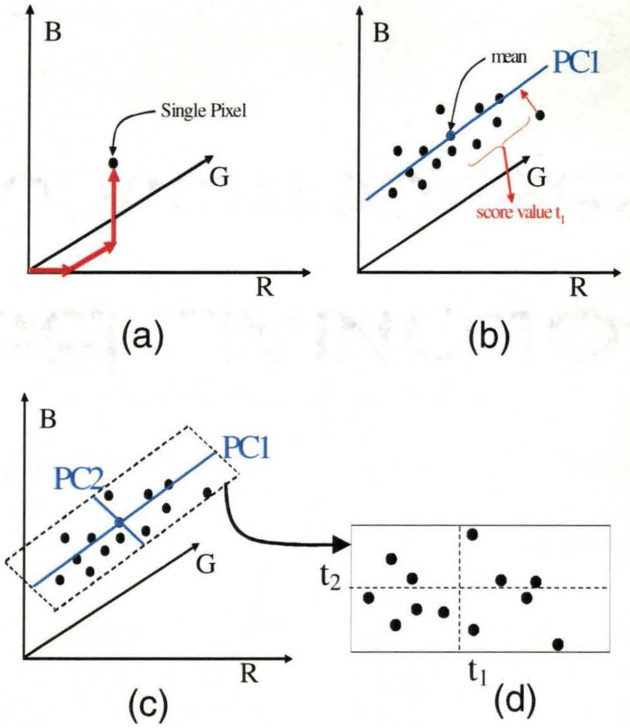

Figure 2-12: Geometric interpretation of PCA. (Reproduced from Eriksson et al., 2001)

To facilitate comprehension, Figure 2-12 presents a geometric interpretation of PCA adapted to RGB images. As shown in Figure 2-12 (a), a single pixel is plotted with respect to its numeric RGB intensity values as a single point within the three-dimensional space. After all pixels have been plotted, the first principal component (PC1) is then defined as a line in X-space going through the mean point and best approximating the data, Figure 2-12 (b). As a single principal component is generally unable to effectively model the variation in a given dataset, a second principal component (PC2) is typically required. As seen in Figure 2-12 (c), PC2 approximates as much new data as possible by being drawn orthogonally to PC1 and intersecting the average pixel point. It should be noted that principal components are ordered in that PC1 explains a greater variance in the image space than PC2. Having defined two principal components accounting for the greatest variation within the image, the three dimensional RGB image may now be represented as a two dimensional plane. As illustrated in Figure 2-12 (d), the spatial locations of pixels projected onto the plane are given by t_1-t_2 score values. While a third variable could also be chosen to describe the remaining variation, the advantage of PCA is in its ability to reduce dimensionality without losing significant information.

A key step required in advance to the determination of principal components via PCA is the unfolding of the three-dimensional multivariate image into an extended two-dimensional matrix. The unfolding step may be represented algebraically as follows:

$$\underset{n_x \cdot n_y \cdot n_z}{X} \xrightarrow{unfold} \underset{(n_x \cdot n_y) \cdot n_z}{X} \qquad (2\text{-}10)$$

As reviewed by Bharati (2002), unfolding of the image matrix breaks the spatial dependence of neighboring pixels in the (n_x x n_y) image plane and results in each pixel within the multivariate image being treated as a single row in the PCA analysis. Figure 2-13 illustrates the unfolding procedure of a 512 x 512 x 4 pixel multivariate image.

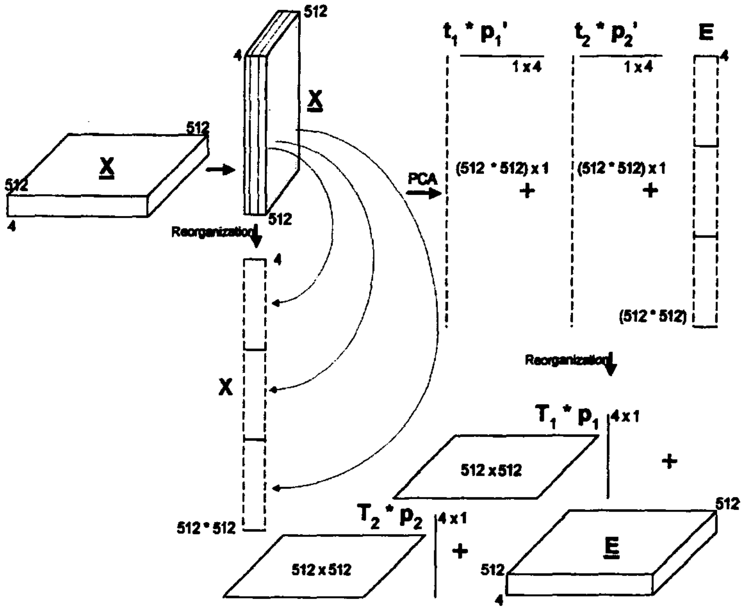

Figure 2-13: PCA decomposition of a 512 x 512 x 4 pixel multivariate image into a linear combination of reduced dimensional latent variable subspace. (Bharati, 2002)

Performing PCA on matrices is effectively accomplished using the nonlinear iterative partial least squares (NIPALS) algorithm (Wold, 1966), or the singular value decomposition (SVD) routine (Golub et al., 1996; Bharati, 2002). Huskoldsson (1996) recommends using the NIPALS algorithm on matrices having more than 50 rows or columns, and the SVD routine on small matrices where all singular values require determination. As seen in Figure 2-13, the row dimension of the unfolded image matrix is very large in comparison with the column dimension, thereby rendering the NIPALS algorithm as the optimal method for image matrix decomposition. The NIPALS algorithm performs the dimension of a matrix in a stage-wise manner, one principal component at a time. The calculation at each stage may be described by implementation of the algorithm (Wold, 1966; Wold, Geladi, Esbensen, & Ohman, 1987) summarized in Table 2-1.

Table 2-1: PCA NIPALS Algorithm

Procedure	Comments
1: Set 't' equal to a column of X	- Initialize the score vector
2: $p^T = t^T X / t^T t$	- Regress all columns of X onto t to get loadings
3: $p = p \big/ \left(p^T p\right)^{\frac{1}{2}}$	- Normalize loadings to unit length
4: $t = Xp / p^T p$	- Regress rows of X on p to get scores
5: $\lVert e_k \rVert = \left(\sum_{i=1}^{n} \lvert e_{ik} \rvert^2 \right)^{1/2}$	- Check the convergence of t (if not converged go to step 2)
6: $E = X - tp^T$	- Convergence: compute residual matrix and use it for determination of next principal component

2.2.4.4. Analysis of Score Plots

The two dimensional plane defined by the principal components is known as a score plot. MIA score plots allow for the compressed representation of pictorial information within an image in terms of the score values of the principal components. The score space and image space are complimentary (Esbensen & Geladi, 1989); pixels having similar spectral features have similar score combinations and will (regardless of their spatial location in the image space) appear in a similar region on the score plot. The number of pixels having equivalent score values and therefore appearing in an identical location on the score plot is called the pixel density. Colour-coded distributions are typically used to identify regions of high and low pixel concentration within the score space

(Esbensen & Geladi, 1989). An example of a score plot as applied to the lumber grading industry is presented as Figure 2-14.

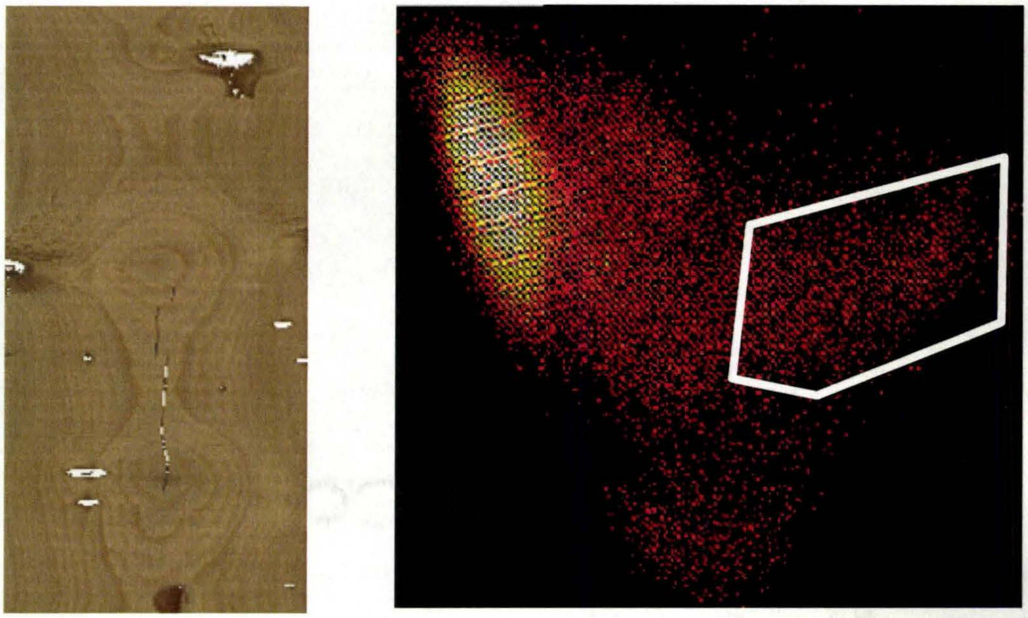

Figure 2-14: t_1-t_2 score plot (right) of a sample lumber image (left) where different image features can be segmented by 'masking'. (Bharati & MacGregor, 2003)

As seen in Figure 2-14, colour-coded score plots provide a good overview of pixel densities and location. As summarized by Geladi & Grahn (1996), the size, distance, and density of pixel clusters are notable characteristics within a score plot that may aid in the classification or discrimination of an image. The technique of delineating regions of interest with a score plot is called segmentation or masking (Esbensen & Geladi, 1989; Bharati, 1998) and is the backbone of MIA. Optimum selection of the mask size, location and shape is normally determined by trial-and-error and is therefore user dependent. Recently, Liu (2004) has proposed an automatic masking technique based on support vector machines (SVMs) for replacing the conventional masking method used in MIA. The concept of segmentation is illustrated in Figure 2-14, where a polygon mask has been defined in the score plot and the pixels contained within the mask have been mapped back to the image space, revealing characteristic defects within the lumber sample.

2.3. Experimental Procedure

2.3.1. Part I: Room Temperature Experiments

In advance to undertaking full-scale industrial trials, proof-of-concept of a numerical procedure for monitoring ladle eye dynamics was established in a controlled setting using the cold model laboratory work of Krishnapisharody & Irons (2006). As previously discussed, this work was considered necessary as the initiatives by Subagyo & Brooks (2002, 2003) were undertaken using an off-line image analysis procedure that proved incapable of real-time process monitoring of ladle eye dynamics.

Measurement of ladle eye size has been the focus of recent work by Krishnapisharody & Irons (2006). As shown in Figure 2-15, the cold model work was carried out using a 42cm diameter by 50cm high acrylic ladle, representing a 1/10th scale steel ladle. In the study, air at varying flowrates was injected into the bath through a centrally placed nozzle. Ladle eye movements were monitored for selected experimental conditions using a digital video camera positioned above the ladle. Tap water having a density ratio of 1.15 and calcium chloride ($CaCl_2$)

having a density ratio of 1.61 were used to simulate liquid steel, while liquid paraffin with yellow coloring was used to simulate the slag layer. A more detailed description of the experimental apparatus and procedure is available elsewhere (Krishnapisharody & Irons, 2006).

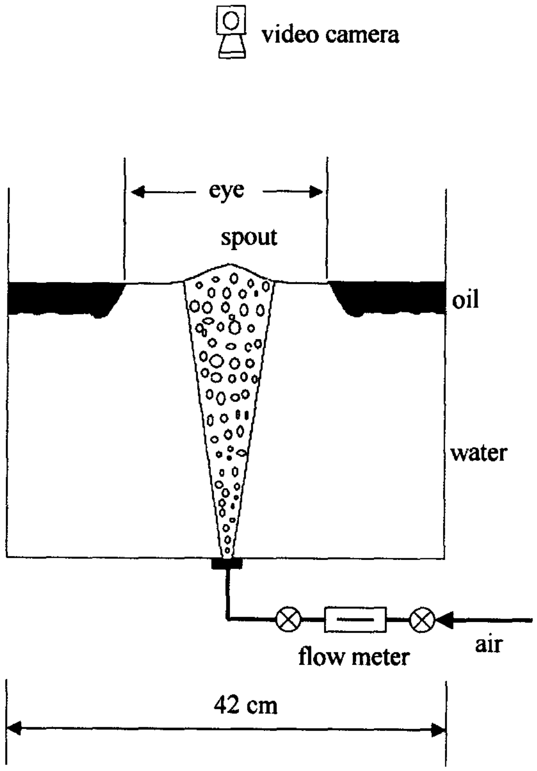

Figure 2-15: Schematic diagram of laboratory scale experimental set-up. (Krishnapisharody, 2007)

In their determination of ladle eye area, Krishnapisharody & Irons (2006) employed a manual detailed visual examination procedure for identifying ladle eye area pixels. Although such methods are labour intensive and not practical for real-time monitoring of ladle eye area, the laboratory results provide an excellent means for comparing the accuracy of the proposed MIA and vision-based sensor.

2.3.2. Part II: Industrial Trials at ArcelorMittal Dofasco

Full-scale industrial trials were undertaken at the number two ladle metallurgical furnace (LMF) station at ArcelorMittal Dofasco. Figure 2-16 presents a summary of the experimental setup and equipment used for the trials. As shown in Figure 2-16 (left), the Panasonic WV-CP470 colour digital camera was secured on a tripod and positioned on the LMF walkway, where it was aimed through the automatic slag door on the ladle roof. The camera has 480 lines of horizontal resolution in colour mode and acquires an RGB image using an interline transfer photon-sensitive charge coupled device (CCD).

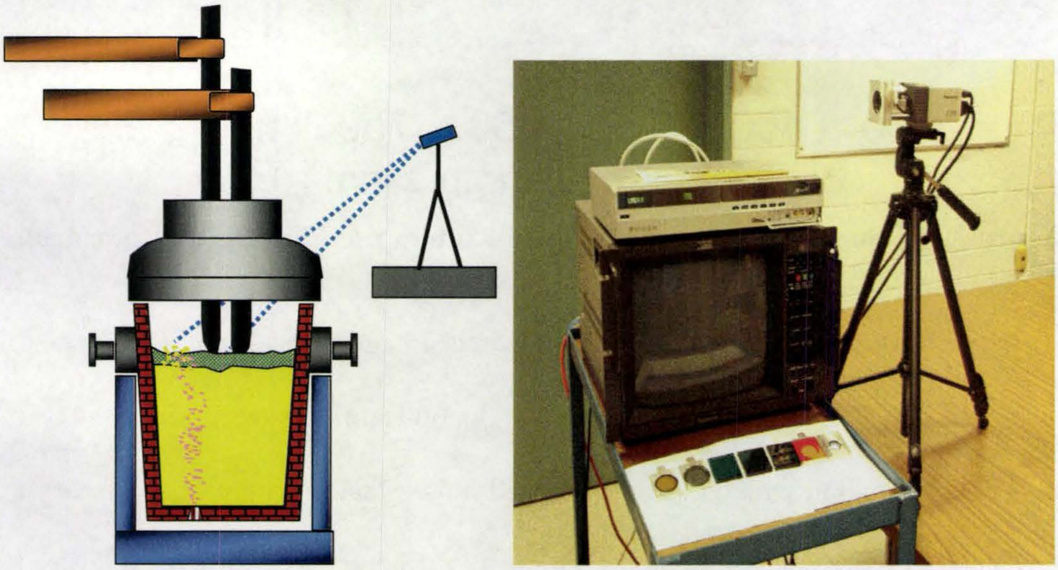

Figure 2-16: (left) Schematic diagram of full-scale experimental set-up at ArcelorMittal Dofasco, and (right) photograph of the imaging equipment used in the trials.

The described experimental design allowed for ladle eye dynamics to be monitored under all process conditions except electrical heating, which due to standard operating procedures required the slag door to be closed. Video footage from the ladle was displayed on a monitor and recorded using a digital versatile disc (DVD) player, Figure 2-16 (right).

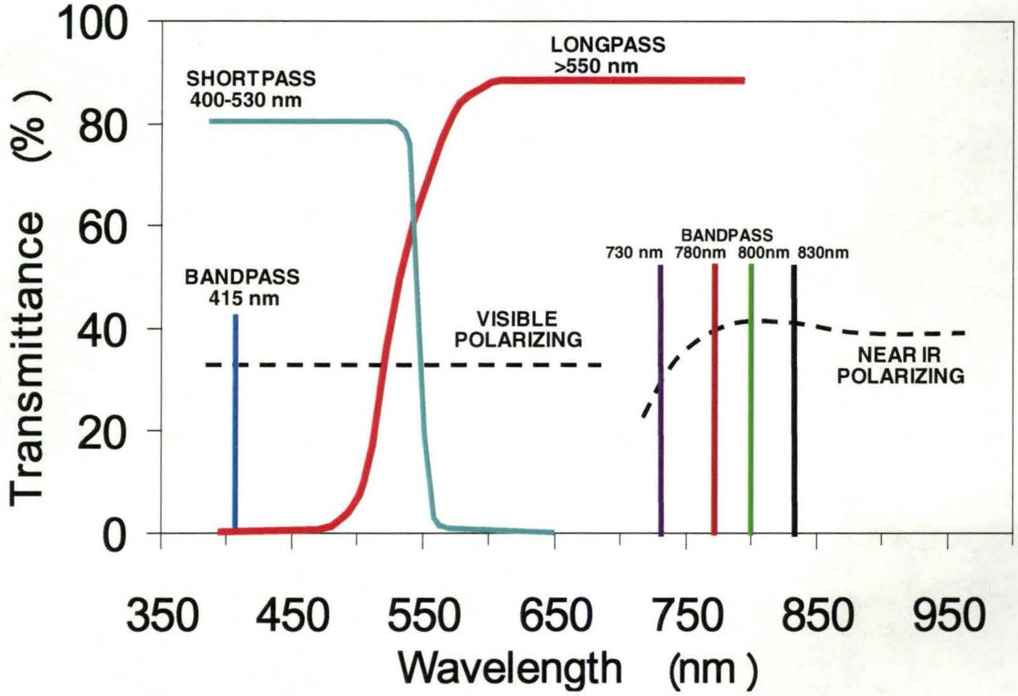

Figure 2-17: Summary plot of the optical filters used during the industrial trials.

In an effort to improve upon the previous imaging results of Brooks and coworkers (2003, 2004) with the ladle cover on, optical filters were purchased and used in combination with a custom designed holder that mounted on the front of the camera. Figure 2-17 summarizes the range of filters used during the industrial trials. A brief description of each class of filter is given as follows:

- Shortpass filters serve to attenuate longer wavelengths and transmit shorter wavelengths over the active range of the target spectrum.
- Longpass filters serve to attenuate shorter wavelengths and transmit longer wavelengths over the active range of the target spectrum.

- A bandpass filter is a combined shortpass and longpass filter that serves to usually lower the transmittance value and block all wavelengths outside a selected interval.
- Polarizers are optical filters that serve to block or transmit light according to its polarization.

2.4. Mathematical Formulation

Figure 2-18 presents the overall flowchart for the developed multivariate image analysis ladle eye area prediction model. The computer code developed for the study was written in MATLAB$^{\text{TM}}$ and calculations were performed on a 1.6GHz, 2GB RAM Acer Laptop equipped with an Intel Centrino Duo CPU. The average computation time for a typical image was less than half a second.

As shown in Figure 2-18, the computer algorithm allows for either a single or series of images to be continuously analyzed online or offline. The iterative loop was developed such that a masked region defined within a training image score plot area could be successively applied to all images within that experimental run. While a new training image was defined for each experimental run during the room temperature experiments, the difference between masked regions was in most cases negligible.

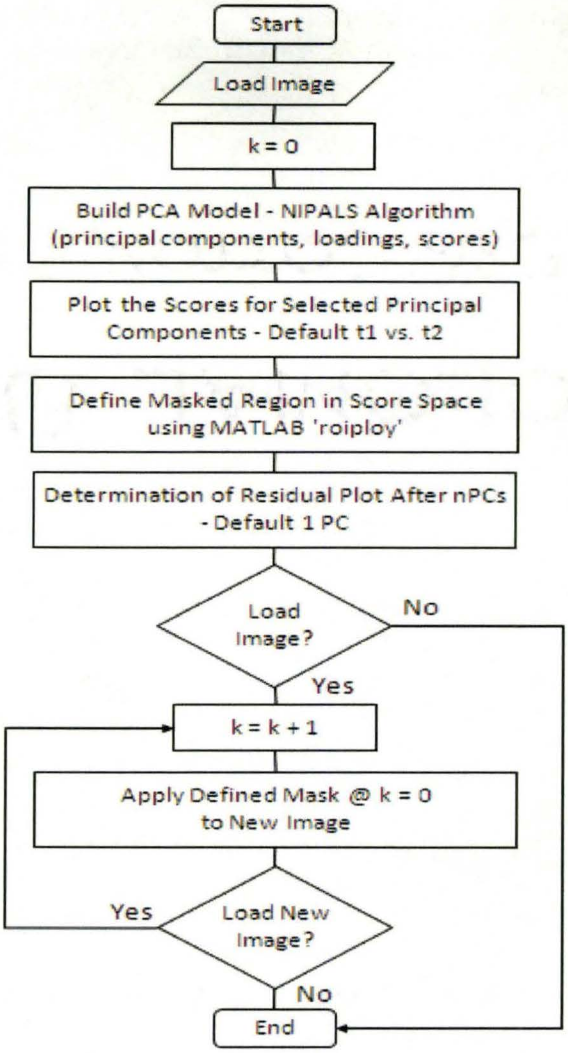

Figure 2-18: Flowchart for calculating ladle eye area using MIA

2.5. Results and Discussion

2.5.1. Part I: Room Temperature Experiments

Ladle eye areas were predicted using MIA for a variety of experimental conditions in the water-paraffin oil system. The range of experimental variables and conditions are summarized in Table 2-2.

Table 2-2: Values of experimental conditions used in the analysis

Process Variable	Value
Gas Flowrate (l / min)	1, 2, 4, 7, and 10
Bath Height (cm)	21, 31.5, and 42
Oil Height (cm)	1, 2, and 3

Prior to the analysis of each experimental run, an initial image was analyzed using the McMaster Advanced Control Consortium Multivariate Image Analysis (MACCMIA) (Kourti, MacGregor & Dunn, 2006) software package. MACCMIA was useful in that it allowed for the dynamic identification of image features by masking pixel areas within the score plot. Advanced identification of the ladle eye within the score plot at the start of each experiment was needed due to the changing lighting conditions in the experiments and their resulting influence on score plot geometry.

All experimental video streams were analyzed by a MIA based ladle eye area prediction model developed for the study. Using the “roipoly” (region of interest selection by polygon) command within the Image Processing Toolbox of MATLAB^{TM}, a mask was defined on the score plot highlighting the ladle eye area at time t = 0 for each experiment. The defined mask was then subsequently applied to all succeeding experimental images within the given video stream. Images were processed at 0.5 second frame rate intervals. Ladle eye size was subsequently determined by relating masked ladle eye pixel count to the cross-sectional area of the acrylic ladle using the following relationship:

$$A_{eye} = \frac{P_{eye}}{P_{total}} x A_{total} \tag{2-11}$$

where A_{eye} is the area of the eye, P_{eye} is the pixel count of the eye, P_{total} is the total pixel count of the ladle surface, and A_{total} is the total area of the ladle surface. It should be stated that for some experimental runs the acrylic ladle used for the experiments reflected light, resulting in pixels outside of the ladle having similar colour intensities as those within the ladle eye. As a result, all images were cropped before analysis in an effort to increase model accuracy.

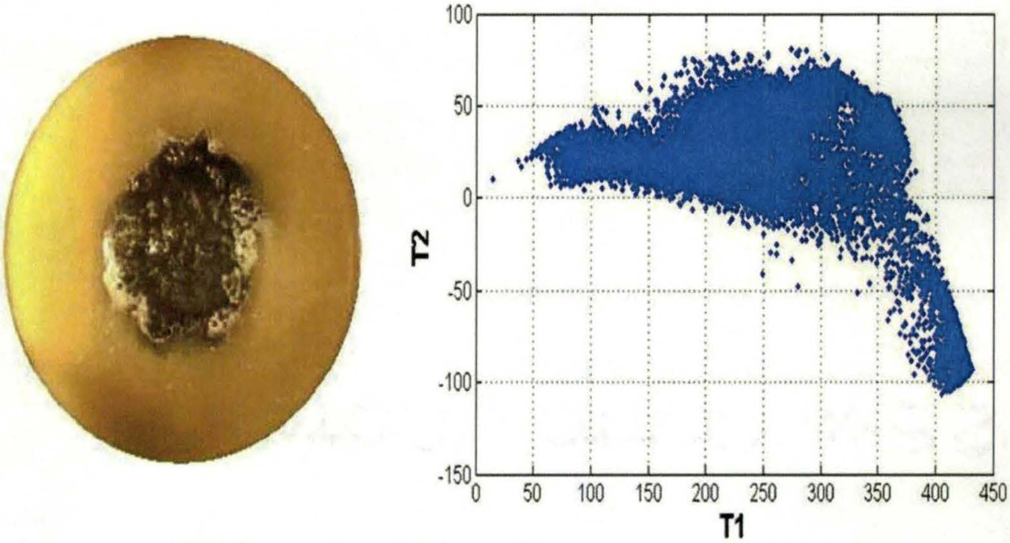

(a) **(b)**

Figure 2-19: (a) RGB image of a ladle surface depicting open eye area; (b) t_1 / t_2 score plot of the multivariate image upon performing PCA decomposition.

A representative RGB ladle surface image and its corresponding score plot (t_1 vs. t_2 score vectors) are presented as Figure 2-19. Process conditions for the experiment were: water height (*H*) = 42 cm, oil height (*h*) = 2 cm and gas flowrate (*Q*) = 4 liters per minute (lpm). Each point on the plot represents a unique image pixel, where pixels having equivalent colour intensities had identical positions on the score plot.

The cumulative percent sum of squares in the multivariate image explained by the first two PCs was 99.9%, where the first component explained 96.2% and the second component explained 3.7% of the variation. Loading vectors for the two principal components are listed in Table 2-3. As shown, PC1 represents something similar to an average of the RGB image layers, whereas PC2 accounts for the colour difference between red and blue layers.

Table 2-3: Principal component loadings

Layer	Loadings of Principal Components	
	PC 1	PC 2
1- Red	-0.6936	0.4822
2 - Green	-0.5993	0.0264
3 - Blue	-0.3998	-0.8757

Residual intensity images for the selected experiment are shown in Figure 2-20. Residual plots are informative as they allow model exactness to be illustrated pictorially. Well modeled areas in Figure 2-20 are depicted with dark colours, while areas of high residuals have light colours. From Figure 2-20 (a), it is observed that PC1 effectively models the ladle eye region. Addition of the second principal component resulted in a much more distributed residual plot, Figure 2-

20 (b). The high residual area remaining in Figure 2-20 (b) after the addition of two PCs is a result of light reflecting off the ladle surface being poorly modeled.

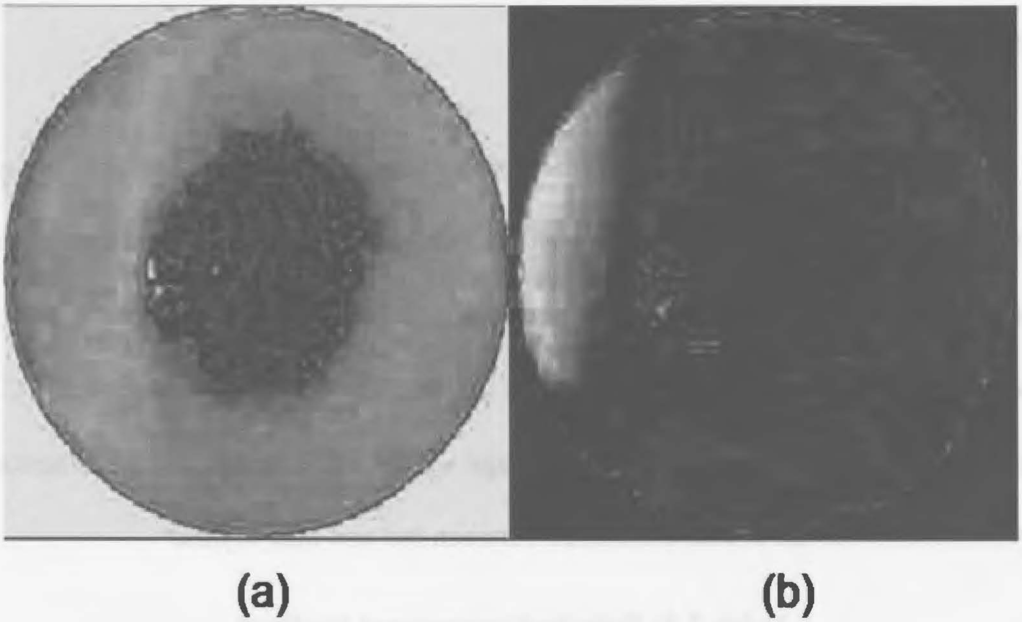

Figure 2-20: Residual plots after (a) one PC, and (b) two PCs.

Figure 2-21 demonstrates how selective masking of a score plot may be used to segment features within the experiment. Pixels contained within the defined mask were isolated and projected back to the image space having a solid white colour. As seen, the identified pixels were characteristic of the ladle eye region.

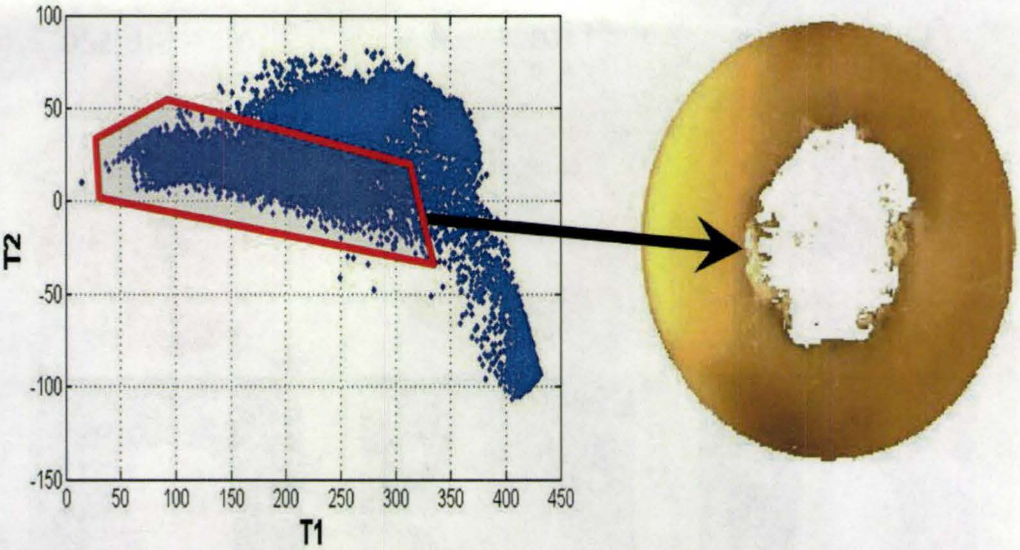

Figure 2-21: t_1 / t_2 score plot of the ladle top surface with a polygon mask over the identified ladle eye pixel cluster.

Having successfully located the ladle eye at time t = 0, the masked polygon region in Figure 2-21 was applied to all succeeding images in the given experimental run. Figure 2-22 summarizes the results. In an effort to improve interpretability, pixels inside the mask were designated white, while pixels outside the mask were colored black. As seen in Figure 2-22, ladle eye areas were properly identified in all analyzed images. The ability of a static mask to accommodate changing ladle eye geometry is due to score plot stability.

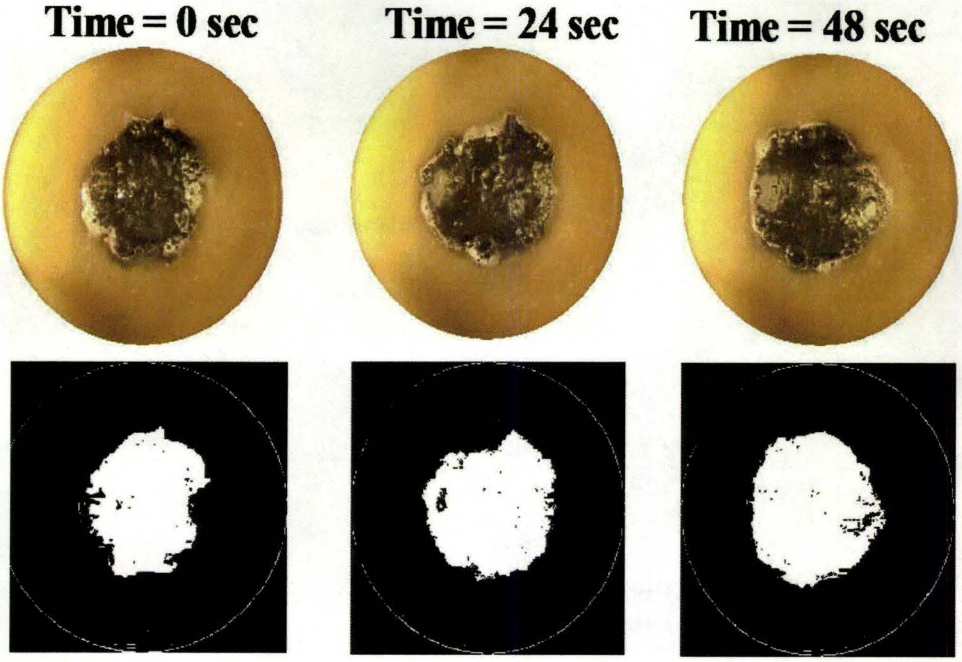

Figure 2-22: Results of time t=0 model applied to succeeding pictures

Instantaneous and cumulative average predicted ladle eye areas for the entire experimental run (water height = 42 cm, oil height = 2 cm and gas flowrate = 4 lpm) are summarized in Figure 2-23. Similar to the observations of Krishnapisharody & Irons (2006), instantaneous eye area was found to be highly dynamic. Over the duration of the experiment, ladle eye area changed from a low of 230 cm^2 to a high of 345 cm^2. Such behaviour may be attributed to the stochastic nature of bubbles in the up-welling gas plume (Yonezawa & Schwerdtfeger, 1999; Krishnapisharody & Irons, 2006). Representative of most experiments, in agreement with the observations of Krishnapisharody & Irons (2006), Figure 2-23 shows a leveling-off of the cumulative ladle eye area average at approximately 100 readings, or 50 seconds. Eye area measurements were therefore based on a minimum average of 120 readings.

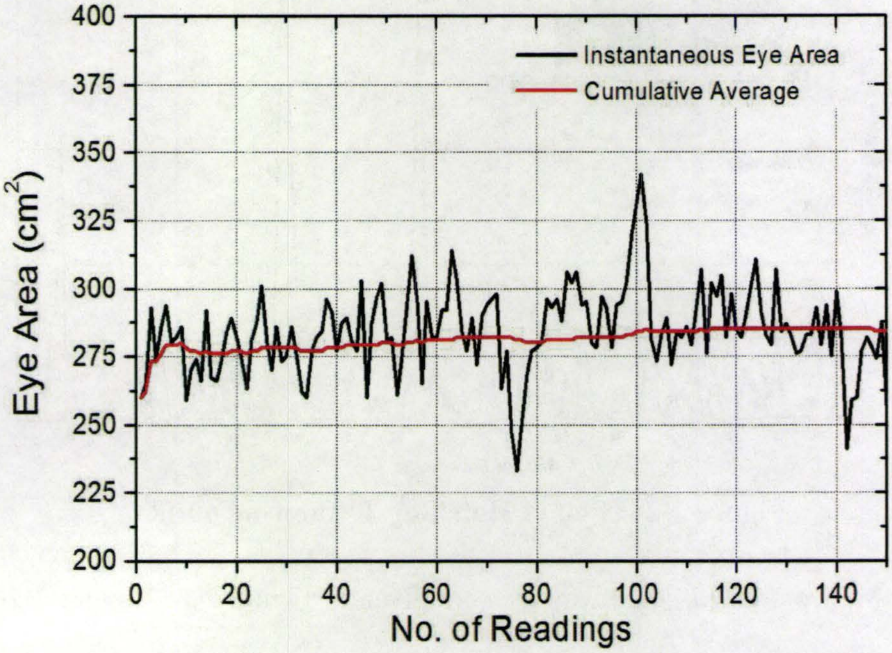

Figure 2-23: Instantaneous and average MIA predicted ladle eye areas

In order to track the validity of the predicted ladle eye area and to test for outliers / bad predictions, the Hotelling T^2 statistic (the multivariate equivalent of a student's-t test), was plotted at each time interval and is presented as Figure 2-24. As seen, several of the determined ladle eye pixel counts were noticeably outside the 99% upper confidence limit. Examination of these outliers revealed poor image pre-processing as the cause of high pixel count in two of the instances. More specifically, failure to crop the outer limits of the ladle surface resulted in reflected light outside of the ladle having a similar intensity as the ladle eye. All occurrences of poor image preprocessing were removed from subsequent analyses.

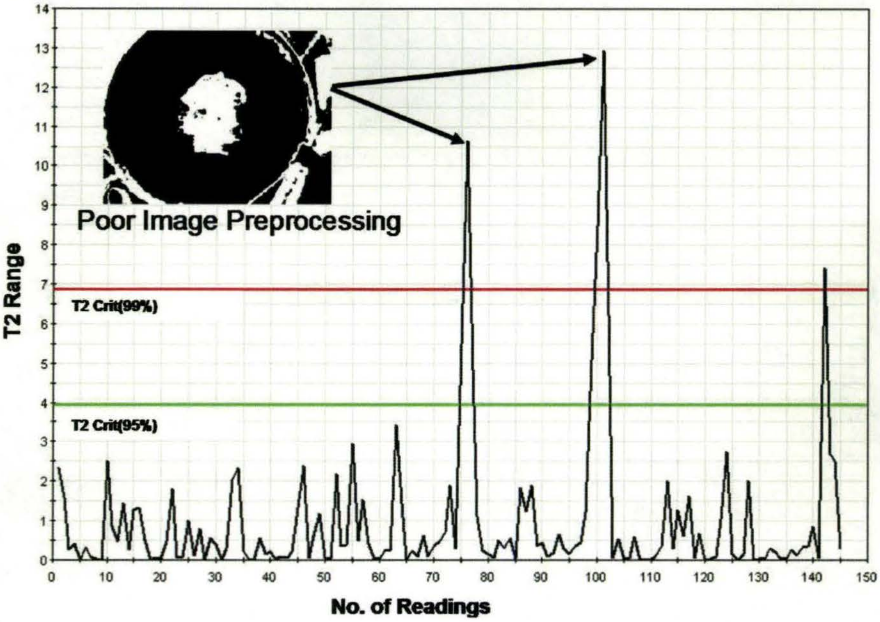

Figure 2-24: Plot of Hotelling T^2 showing outliers

MIA predicted ladle eye areas are given in Figure 2-25, Figure 2-26, and Figure 2-27 for all analyzed experimental conditions. As observed, ladle eye size increased with increasing gas flow rate and metal height, and decreased with increasing slag height. The non-linear expansion of the ladle eye area is due to the non-linear broadening of the bubble plume with bath height (Ebneth & Pluschkell, 1985). A detailed explanation of this phenomenon is given by Krishnapisharody & Irons (2006). The ladle eye area variation curve for process conditions H = 31cm and h = 1cm is missing from Figure 2-26 due to a transparent slag layer. In this case, MIA was unable to differentiate between ladle eye and slag image pixels.

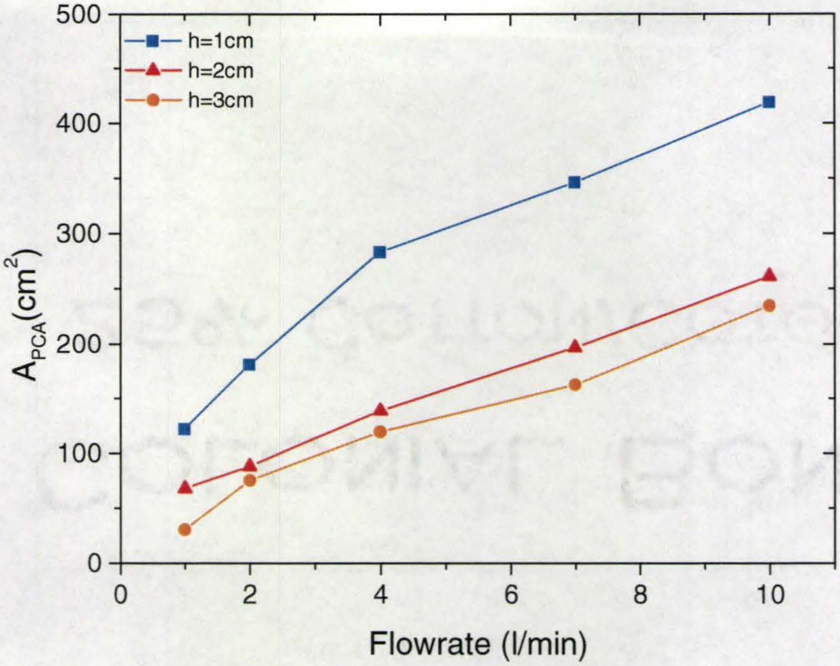

Figure 2-25: Variation of Ladle Eye Size with Gas Flowrate; H=21cm

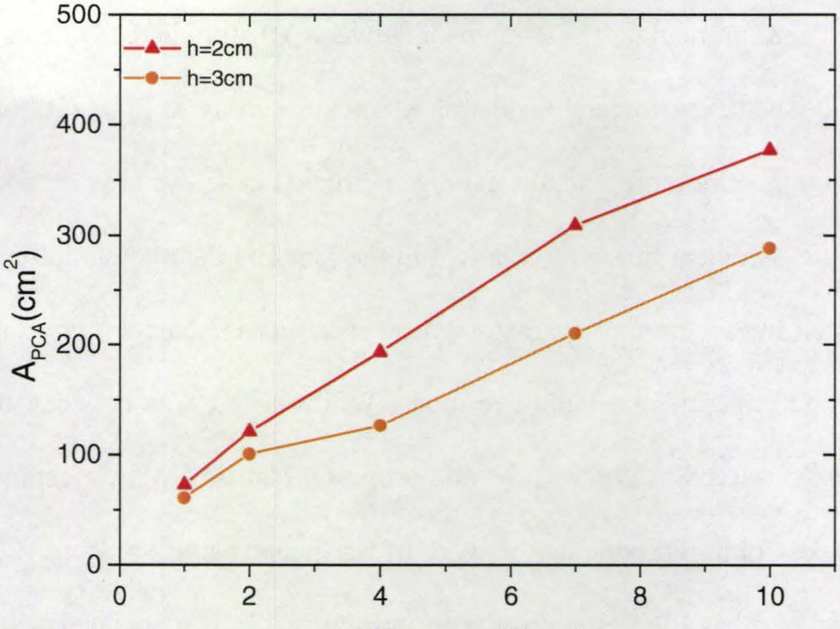

Figure 2-26: Variation of Ladle Eye Size with Gas Flowrate; H=31cm

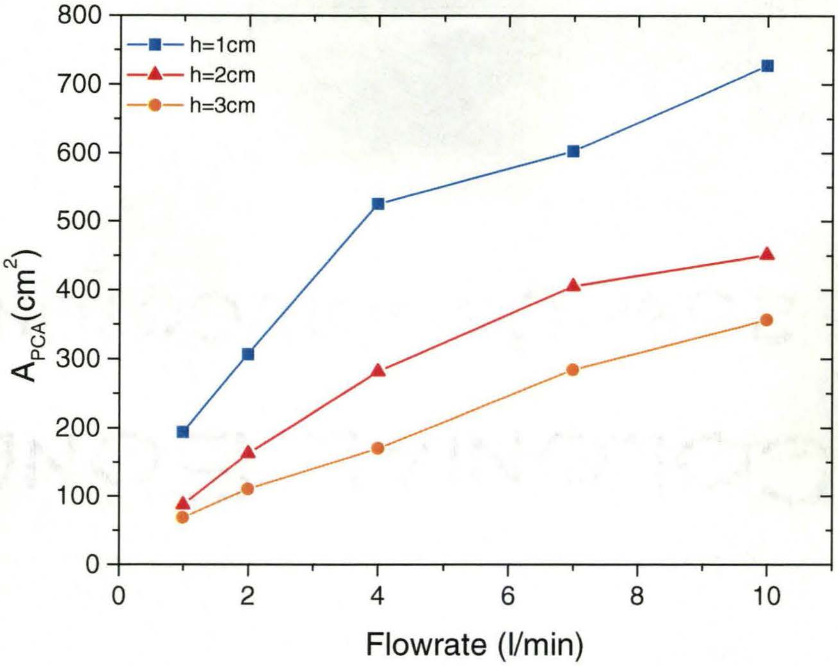

Figure 2-27: Variation of Ladle Eye Size with Gas Flowrate; H=42cm

Figure 2-28 summarizes the agreement between MIA predicted ladle eye areas and the published experimental results of Krishnapisharody & Irons (2006). Each data point on the plot represents the average predicted ladle eye area for a specific gas flow rate. An ideal linear fit is drawn in the plot and data points falling on or near to this line represent perfect or near perfect agreement between MIA predicted and experimental ladle eye areas. While differences between the two methods are observed in Figure 2-28, the proposed real-time MIA technique was clearly successful in reproducing the work of Krishnapisharody & Irons (2006). It should be noted that not all the error seen in Figure 2-28 is associated with MIA. The manual visual ladle eye area identification technique employed by Krishnapisharody & Irons (2006) is highly subjective and also contributes to the observed differences in ladle eye size.

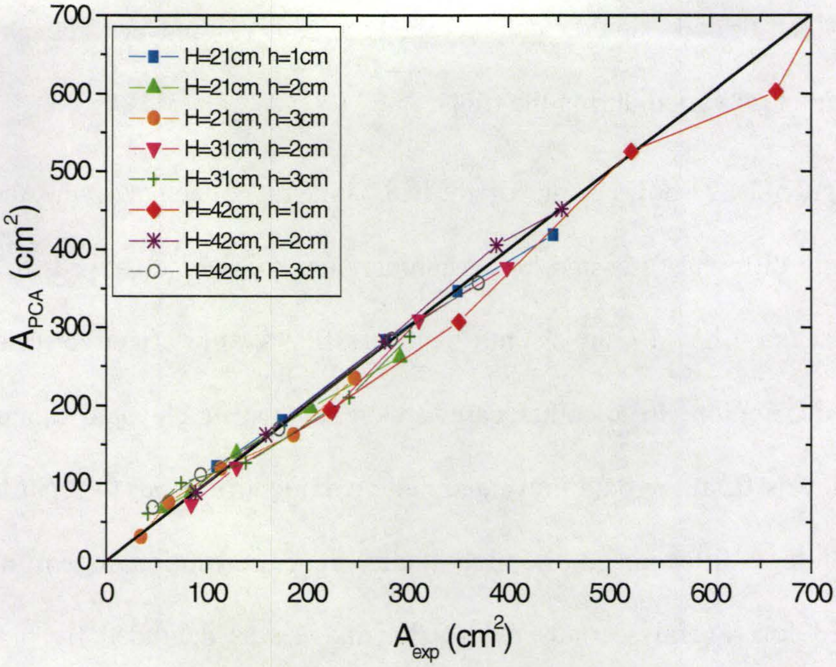

Figure 2-28: Comparison of predicted eye sizes for different slag (h) and metal (H) heights.

2.5.2. Part II: Industrial Trials at ArcelorMittal Dofasco

As previously described, the primary objective of this chapter is to demonstrate the capability of a vision-based sensor using MIA in monitoring real-time ladle eye dynamics within an industrial ladle metallurgical furnace. The following section discusses preliminary results and observations from applying multivariate image analysis on images taken at ArcelorMittal Dofasco's No. 2 LMF station. A schematic of the experimental setup and imaging equipment used for the trials is presented as Figure 2-16. As shown, argon gas was injected through bottom porous plugs at different flowrates to generate the ladle eye region. Images were taken from a fixed position using a standard Panasonic WV-

CP470 colour digital camera and recorded on a DVD player. The choice of sampling interval varied during the trials.

Figure 2-29 shows some of the first images collected of the ladle eye region using different filter and lens combinations. It can be observed from these images that only the 730 and 780nm bandpass filters were effective in isolating the ladle eye region. In all other cases, poor contrast or elevated radiant light intensity levels from the bath prevented ladle eye identification. In regards to the 730nm bandpass filter image, the high-quality image resolution shown in Figure 2-29 lasted for several seconds before the image was degraded by high light intensity. On the basis of these results, further trials were undertaken using the 780nm bandpass filter. In addition, 800 and 830nm bandpass filters were purchased and tested at the LMF but were found to yield sub-optimal images relative to the 780nm bandpass filter.

Figure 2-30 summarizes the results of performing MIA on a representative image taken of the ladle eye region using the 780nm bandpass filter. While image segmentation was successful in isolating the ladle eye, several regions where molten metal was entrained on crusty slag particles or splashed on ladle side walls were also identified. Figure 2-31 demonstrates how the addition of a forth user defined spatial dimension improved ladle eye area detection. Pixels contained within the defined rectangle in Figure 2-33 (top) were given one pixel intensity value while pixels outside the designated region were assigned another. The effect of adding a user defined spatial dimension was that the score space became biased with respect to pixels contained within the defined rectangle, thereby facilitating image segmentation and resulting in the ladle eye region being clearly separate from the other parts of the image.

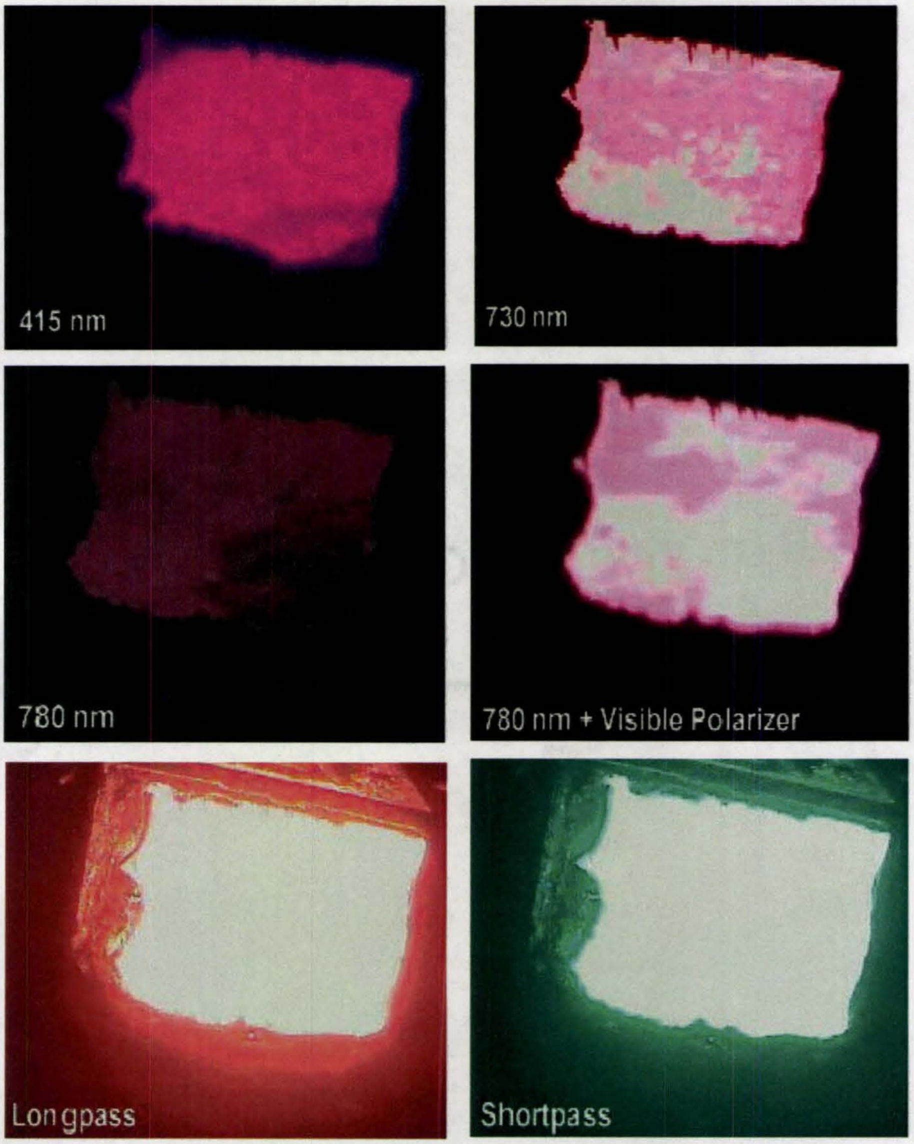

Figure 2-29: Sample images taken of ladle eye region at ArcelorMittal Dofasco LMF #2 using different filter and lens combinations (top left) 415nm, (top right) 730nm, (mid left) 780nm, (mid right) 780nm + Visible Polarizer, (bottom left) Longpass, (bottom right) Shortpass.

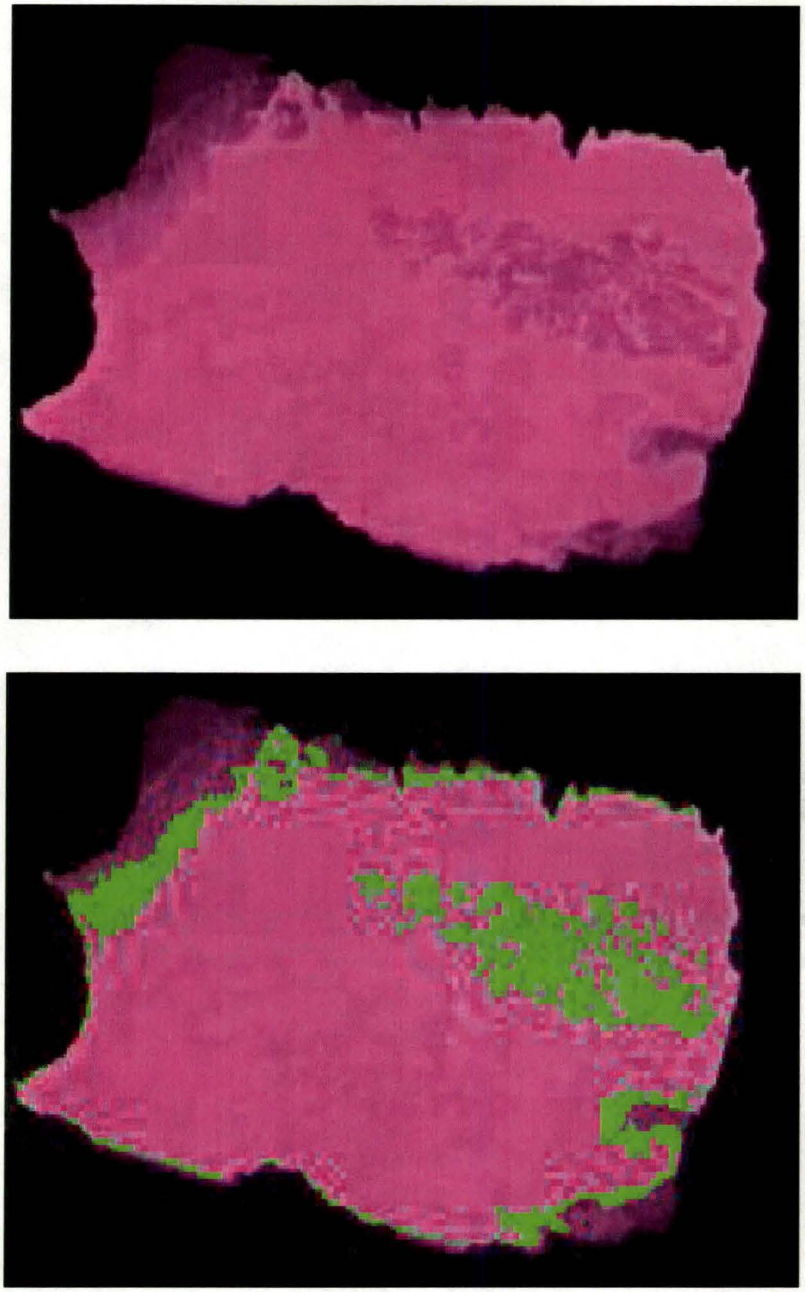

Figure 2-30: Results of multivariate image analysis model applied to a representative image taken using a 780nm bandpass filter. (top) Raw unprocessed image, and (bottom) Projection of applied mask on the image space.

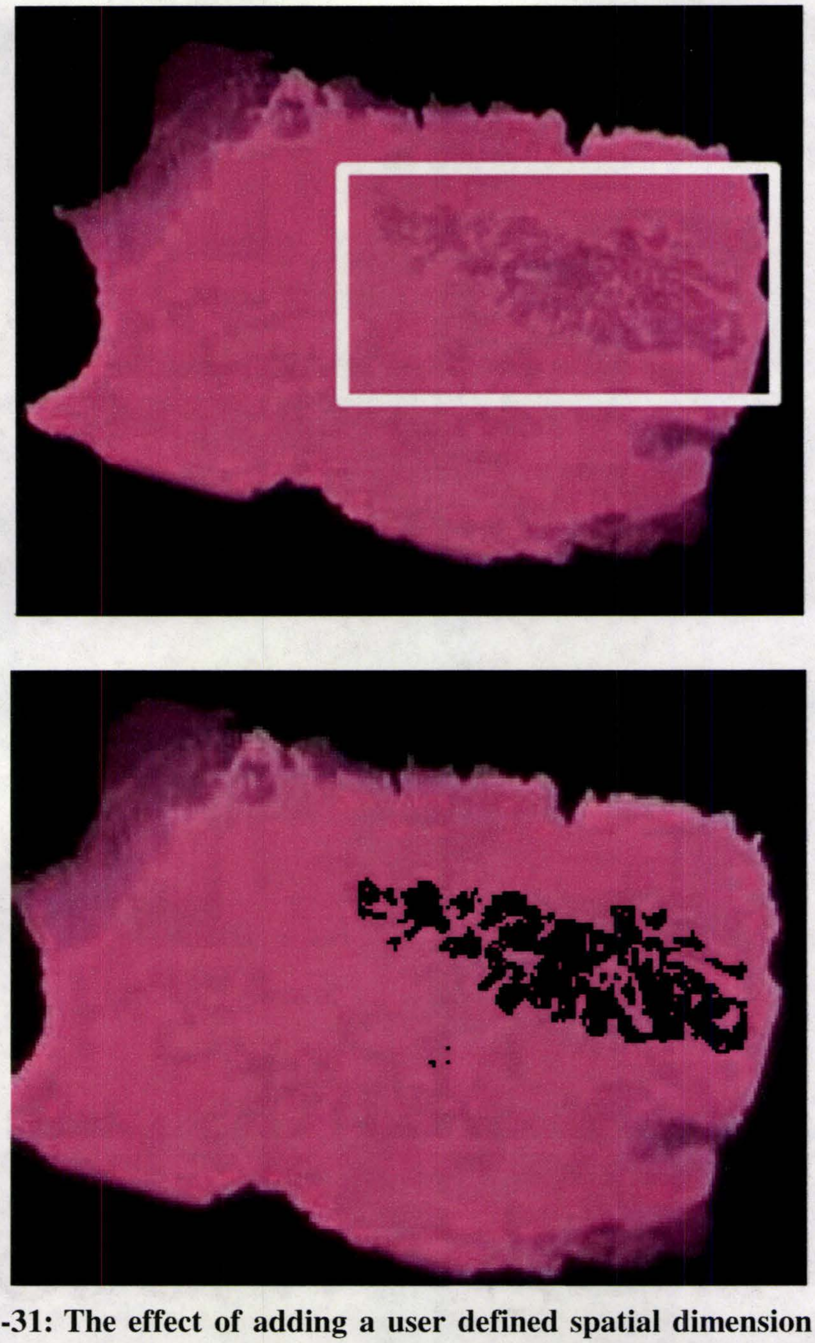

Figure 2-31: The effect of adding a user defined spatial dimension on ladle eye area identification results. (top) User defined spatial map, and (bottom) Corresponding image space after multivariate image analysis.

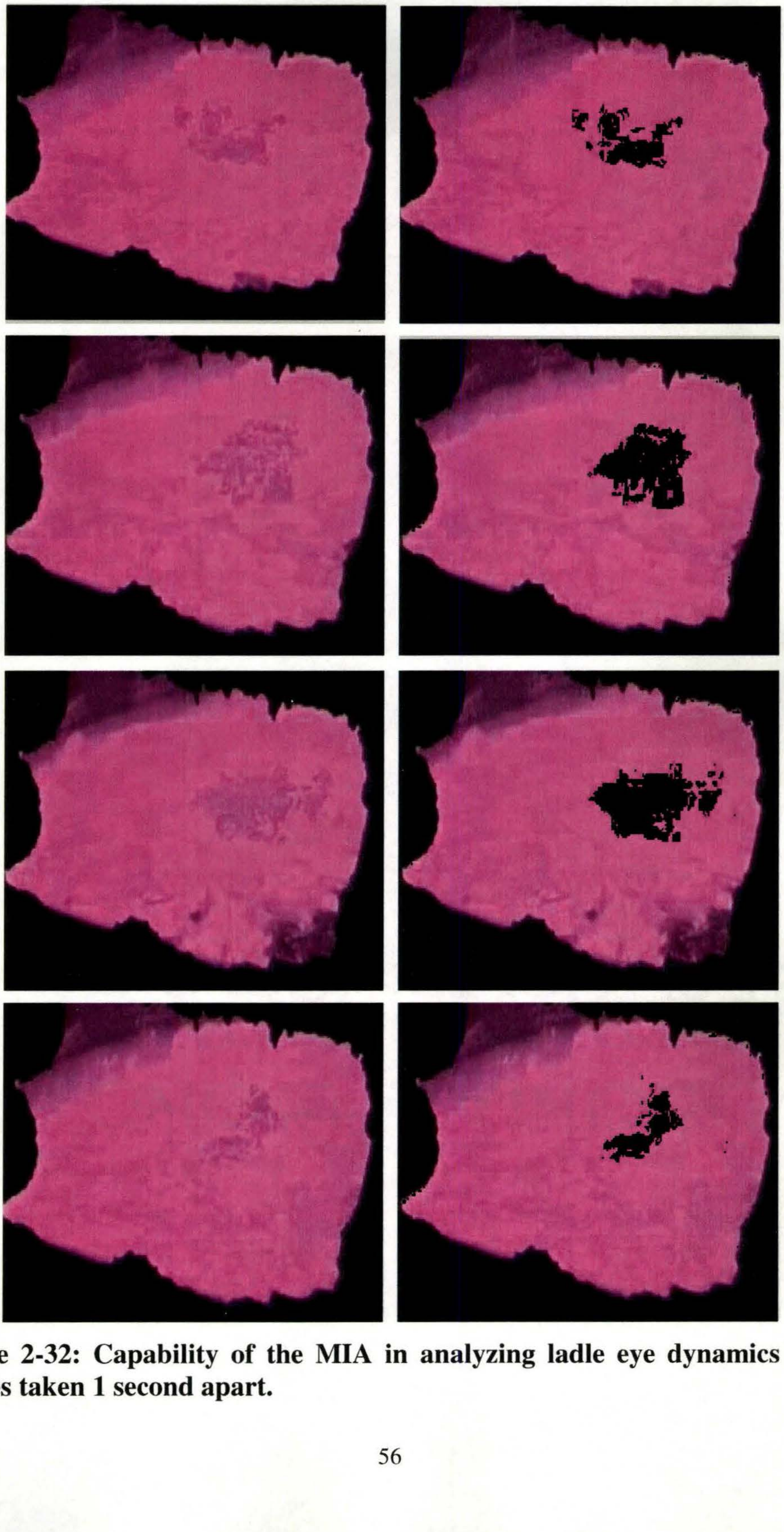

Figure 2-32: Capability of the MIA in analyzing ladle eye dynamics from images taken 1 second apart.

Figure 2-32 summarizes the application of MIA to consecutive 1 second interval images. Despite significant frame-to-frame changes, it is observed that MIA was effective in isolating ladle eye geometry. The added user defined spatial dimension remained unchanged during the analysis and the mask was obtained by a trial and error process.

2.5.3. Industrial Implications

The present work has several implications for the industrial operation of the ladle metallurgical furnace, namely:

1) A numerical procedure in combination with a vision-based sensor has been detailed to provide a direct measure of ladle eye size, an important control parameter during ladle processing that has previously gone unmeasured within an industrial LMF.

2) The current work represents a significant improvement over the previous work of Subagyo & Brooks (2003) in terms of model structure and computation speed. As a result, the developed computer algorithms permit for the potential automatic control of inert-gas stirring.

3) Additional benefits of a ladle eye control system include: i) online monitoring of porous plug performance, ii) improved alloy recovery by direct addition into ladle eye (minimal slag-alloy interaction), iii) facilitate heat management for ladle operators, iv) reduce wasted argon gas caused by over-

stirring, v) offers the ability to minimize steel exposure to reoxidation and nitrogen pickup from the ladle freeboard,

4) Serves as a platform on which future developments can be based.

Chapter 3

ACTIVITIES IN MULTI-COMPONENT SYSTEMS[2]

3.1. Introduction

A multi-component solution is any solution containing a mixture of elements or molecules existing over a range of composition, for which molten steel and slag are examples. Significant experimental work has been undertaken in an effort to characterize the thermodynamic properties of multi-component solutions. Examples of experimental techniques used include (Kubaschewski & Alcock, 1979): (i) vapour pressure measurements, (ii) gas-metal equilibria, (iii) electromotive-force measurements, and (iv) component distribution between immiscible liquids. As summarized by Gaye (1971), these methods typically involve measuring the partial molar property of one of the compounds in solution for various compositions, and then using computational methods such as the Gibbs-Duhem equation for determining the partial molar value(s) of unmeasured components. While these investigative results have been fundamental in our understanding of steelmaking reactions, their application for process control purposes was limited until the advent of thermodynamic modelling.

---

[2] Some of the contents in this chapter were published as: K.J. Graham and G.A. Irons, "Elaboration of the Cell Model for Application to Ladle Metallurgy Slags", *AIST Proceedings*, May 5-8 (2008), Pittsburgh, PA.

Thermodynamic solution models are in effect generalized analytical representations of multi-component solutions allowing for the assessment of thermodynamic properties using only a small number of coefficients determined from experimentally measured data. Numerous thermodynamic models of varying degrees of complexity have been developed for slag and metal systems. As summarized by Gaye & Lehman (1997) the convenient nature of these models has greatly contributed to the optimization of steelmaking practices.

This chapter presents a detailed investigation of the thermodynamic models used in this thesis. The literature is briefly reviewed, and original contributions to the modified interaction parameter formalism[3] and cell model are discussed. While the general theory behind the cell model has been well developed, very little has been published in regard to its development. As such, the major contributions from this chapter include presenting numerical procedures enabling cell model development. Further, previously unpublished equations are presented enabling cell model extension to poly-anionic slags.

3.2. Literature Review

3.2.1. Activities in Liquid Steel

Analytical representations to describe the thermodynamic properties of a multi-component solution are subject to the following preconditions (Darken, 1967a): (i) thermodynamic consistency, and (ii) agreement with limiting laws for

---

[3] Unified interaction parameter formalism work was completed in collaboration with Professor D.V. Malakhov and D. Purnomo as part of the course ‘Computational Thermodynamics’. Results have not yet been published.

the solute and solvent components. Additional prerequisites include that the model should be as simple as possible and capable of describing the experimental data over the entire range of concentration.

One of the earliest models proposed to describe the thermodynamic behaviour of metallic solutions was the interaction coefficient formalism (Wagner, 1952). Using a mathematical treatment based on the Taylor series expansion of the excess partial molar free energy in solution, Wagner proposed describing the manifold interactions of solute components on the activity coefficient of solute in steel as:

$$\ln\gamma_2\left(X_2,X_3,X_4,\ldots\right)=\ln\gamma_2^o+X_2\frac{\partial\ln\gamma_2}{\partial X_2}+X_3\frac{\partial\ln\gamma_2}{\partial X_3}+X_4\frac{\partial\ln\gamma_2}{\partial X_4}+\ldots$$

(3-1)

where the derivatives were taken for the limiting case of zero concentrations of all solutes, and higher order Taylor series terms were neglected. The term $\ln\left(\gamma_i^o\right)$ in equation 3-1 refers to the self-interaction coefficient of zeroth order and is zero when taking γ_i equal to unity at infinite dilution. Derivatives were assumed to be represented by interaction coefficient terms that serve as a measure of how an increase in the concentration of ‘j’ affects the activity coefficient of ‘i’:

$$\varepsilon_2^{(2)}=\left[\frac{\partial\ln\gamma_2}{\partial X_2}\right]_{X_1\to1}\qquad\varepsilon_2^{(3)}=\left[\frac{\partial\ln\gamma_2}{\partial X_3}\right]_{X_1\to1}\qquad\varepsilon_2^{(4)}=\left[\frac{\partial\ln\gamma_2}{\partial X_4}\right]_{X_1\to1}$$

(3-2)

Wagner (1952) also showed the existence of a reciprocal relation between the effect of component 'i' on γ_j and the effect of component 'j' on γ_i as:

$$\varepsilon_2^{(3)} = \varepsilon_3^{(2)} \tag{3-3}$$

For convenience, equation 3-1 is commonly expressed in terms of weight percentages as:

$$\log f_i = \sum_{j=1}^{n} e_i^j [\%j] \tag{3-4}$$

where the activity coefficient is f_i and the zeroeth-order term disappears in the transformation. Conversion between first-order interaction coefficients from one composition co-ordinate to the other is accomplished by the following equations (Lupis & Elliott, 1966):

$$\varepsilon_i^{(j)} = 230\left(M_j / M_{Fe}\right) e_i^{(j)} + \left(M_{Fe} + M_j\right) / M_{Fe} \tag{3-5}$$

$$\begin{aligned} \rho_i^{(j)} = {} & 230 / \left(M_{Fe}{}^2\right)\left[100 M_j{}^2 r_i^{(j)} + M_j\left(M_{Fe} - M_j\right) e_i^{(j)}\right] \\ & + (1/2)\left(\left\{M_{Fe} + M_j\right\} / M_{Fe}\right)^2 \end{aligned} \tag{3-6}$$

where M_i and M_j are the atomic weights of two elements in the solvent metal (iron), and $\rho_i^{(j)}$ and $r_i^{(j)}$ are the second order interaction terms in the different composition co-ordinate systems.

As discussed by Lupis & Elliott (1966), it is often necessary to treat multi-component systems at relatively high concentrations of solute components, where the relevant partial molar properties are no longer linear functions of composition. Under such conditions, the first order interaction formalism proposed by Wagner (1951) may be improved upon by incorporating the second order terms in the Taylor series expansion. Following this approach, Lupis & Elliott (1966) derived the following expression for the activity coefficient of a solute in liquid steel:

$$\ln\left(\frac{\gamma_i}{\gamma_i^o}\right)=\sum_{j=2}^{m}\varepsilon_i^{(j)}X_j+\sum_{j=2}^{m}\rho_i^{(j)}X_j^2+\sum_{j=1}^{m}\sum_{k>j}^{m}\rho_i^{(j,k)}X_jX_k \tag{3-7}$$

where the second term on the right contains the second order coefficients and the third sum contains the cross-product second order coefficients. Sigworth & Elliott (1974) provide the following reasons in favour of using second-order interaction coefficients: (i) first-order interaction coefficients are often inadequate for describing the thermodynamic behaviour of solute elements, (ii) intermediate and high-alloy steels require knowledge of activity coefficients at compositions well away from the infinitely dilute reference state, and (iii) increased mathematical difficulty is largely offset by the availability of computers.

Darken (1967a, 1967b), in his work on the thermodynamics of ternary solutions, applied Wagner's first-order interaction coefficient formalism to a ternary system and demonstrated it to be thermodynamically inconsistent at finite concentrations. Results of this study revealed the Gibbs-Duhem equation to be satisfied only in the very special case where all the interaction coefficients were equal. A quadratic formalism was thereby proposed to improve upon the representation of thermodynamic properties at finite (and even higher) concentrations (Darken, 1967a; Darken, 1967b). For a binary system, Darken (1967b) divided the entire composition range into three regions, two terminal regions connected by a central region. Thermodynamic behaviour within the terminal regions was regarded as being relatively simple, with the activity coefficient of the solvent being represented by the expression:

$$\log \gamma_1 = \alpha_{12} N_2{}^2 \tag{3-8}$$

Application of the Gibbs-Duhem equation yielded the corresponding expression for the activity coefficient of a solute component as:

$$\log \frac{\gamma_2}{\gamma_2^o} = \alpha_{12}\left(-2N_2 + N_2{}^2\right) \tag{3-9}$$

where N_2 is the mole fraction of the solute, γ_2^o the value of the activity coefficient of component 2 at infinite dilution in component 1, and α_{12} a constant (at constant temperature and pressure) characteristic of the binary system in the region of validity of the equations. The succeeding quadratic expressions were obtained by Darken (1967a) to describe the activity coefficients of a ternary system:

$$\log \gamma_1 = \alpha_{12} N_2^2 + \alpha_{13} N_3^2 + \left(\alpha_{12} + \alpha_{13} - \alpha_{23}\right) N_2 N_3 \tag{3-10}$$

$$\begin{aligned} \log \frac{\gamma_2}{\gamma_2^o} = {} & -2\alpha_{12} N_2 + \left(\alpha_{23} - \alpha_{12} - \alpha_{13}\right) N_3 + \alpha_{12} N_2^2 + \alpha_{13} N_3^2 \\ & + \left(\alpha_{12} + \alpha_{13} - \alpha_{23}\right) N_2 N_3 \end{aligned} \tag{3-11}$$

$$\log\frac{\gamma_3}{\gamma_3^o} = -2\alpha_{13}N_3 + (\alpha_{23} - \alpha_{12} - \alpha_{13})N_2 + \alpha_{12}N_2^2 + \alpha_{13}N_3^2 + (\alpha_{12} + \alpha_{13} - \alpha_{23})N_2N_3 \tag{3-12}$$

It is seen by inspection that equations 3-10 to 3-12 reduce to the desired relation for the binary system when N_2 or N_3 is set equal to zero. Further, the quadratic formalism was found to be thermodynamically consistent up to a solute concentration of about 20 to 30 atomic percent (Darken, 1967b).

In more recent studies, Pelton & Bale (1986, 1990) suggested a simple modification to Wagner's interaction parameter formalism, rendering it thermodynamically consistent, and thereby permitting for its application to non-dilute compositional regions. Pelton & Bale (1990) demonstrated that their newly proposed unified interaction parameter formalism (UIPF) reduced to Wagner's formalism at infinite dilution and to Darken's formalism in dilute solutions. Including second order interaction coefficients, the unified interaction parameter formalism was derived as follows (Pelton & Bale, 1986):

$$\ln\left(\frac{\gamma_i}{\gamma_i^o}\right) = \ln(\gamma_{solvent}) + \sum_{j=1}^{N}\varepsilon_{ij}X_j + \sum_{j,k=1}^{N}\varepsilon_{ijk}X_jX_k \tag{3-13}$$

$$\ln(\gamma_{solvent}) = -\frac{1}{2}\sum_{j=1}^{N}\sum_{k=1}^{N}\varepsilon_{jk}X_jX_k \tag{3-14}$$

The key notable difference between the modified and unmodified interaction parameter formalisms is the inclusion of a term within the UIPF to describe the activity coefficient of the solvent. A further advantage of the UIPF is that existing compilations of interaction parameters may be applied directly when computing activity coefficients.

3.2.2. **Activities in Liquid Slag**

Two classes of theories have been proposed to describe the structure of liquid slags: (i) molecular, and (ii) ionic. The molecular approach was motivated by the ability to predict the thermodynamic properties of a slag of one composition from the knowledge of the thermodynamic properties of a slag of a different composition (Gaskell, 1967). Its advantage comes at the cost of its principal disadvantage, namely that no knowledge of the structure of the reacting components is required. Slag is considered composed of a mixture of individual simple oxides, sulphides, fluorides, chlorides, or carbides that can either associate to form complex oxides or remain uncombined. As highlighted by Winkler & Chipman (1946), the immediate usefulness rather than the ultimate truth of the molecular models accounts for their popularity. The validity of the molecular theory of slags was disproved in the work of Korber & Oelsen (1933), who demonstrated that in contrast to the results of Schenck's molecular model (1945), that the chemical reactivity of FeO in equilibrium with CaF_2-rich and FeO-rich phases at 1450°C was different in both phases.

Herasymenko (1938a, 1938b) is credited as the first researcher to propose the ionic nature of slags, suggesting that liquid slags were comprised of a random disordered mixture of cations (Ca^{2+}, Fe^{2+}, etc.), anions (O^{2-}, F^{2-}, S^{2-}, etc.), and anion complexes (SiO^{4-}, PO_4^{3-}, AlO_3^{3-}, etc.). Direct evidence regarding the ionic structure of slags is, however, difficult, as no single measurable parameter has yet been determined to provide complete information on its structure (Gaskell, 1967). Structural interpretations remain based on inferential methods relying on indirect evidence from acidic silicate slag systems, where the low entropy of fusion and viscosity of silicate rich slags allow liquid structure to be inferred from analyzing the solid phase (Moore, 1990). The primary conclusion drawn from indirect studies on silica-rich slags is that each silicon ion shares an electron charge with four oxygen ions, forming the SiO_4^{4-} tetrahedron (Moore, 1990). The four negative charges on the tetrahedron is a result of each oxygen ion having one remaining residual negative charge. Electro-neutrality is thereby obtained when each oxygen ion is shared by two tetrahedral and the cation / oxygen ratio is that for pure silica. The tetrahedral structure of solid and liquid silica is presented as Figure 3-1. As seen, the main difference between pure liquid and solid silica slag structures is a more highly distorted lattice within the liquid phase (Richardson, 1974).

Slags are categorized as being composed of either acidic or basic oxides. An acidic oxide is defined as an oxide that accepts oxygen ions when dissolved in a basic melt, while a basic oxide is defined as an oxide that donates oxygen ions when dissolved in an acidic melt. As shown in Figure 3-2, adding basic oxides (cations such as Ca^{2+}, Na^{2+}, Mg^{2+}, Fe^{2+}) to liquid silica results in each added oxygen ion entering the network and separating the corners of two silica tetrahedra until silica exists as discrete SiO_4^{4-} groupings. At this point, no further structural changes result from the addition of basic oxides, and subsequent oxide additions act to increase metal and free oxygen ion concentration within the melt (Richardson, 1974). It should be noted that cations such as Ti^{4+}, P^{5+}, Al^{3+}, and Fe^{3+} form similar tetrahedra as Si^{4+} and may polymerize the slag by being incorporated into the structure as network-formers.

Benefits of a controlled slag phase include: (i) acceleration of chemical reactions, (ii) improved quality of the end steel, and (iii) favourable process economics. Effective slag control, however, requires accurate characterization of thermodynamic properties. Yokokawa & Niwa (1969), for instance, regarded the determination of silicate melt component activities as the most important factor governing the efficacy of steelmaking processes (e.g. oxidation, desulphurization, dephosphorization, non-metallic inclusions, etc.). Early attempts to predict the thermodynamic properties of slags comprised mostly of empirical correlations (Schneck, 1945) that were derived from costly and time-consuming experimental efforts. As a consequence of the significant improvement in plant performance resulting from the use of these equations, research efforts were undertaken to develop improved thermodynamic models capable of correctly characterizing the properties of multi-component slags in terms of ionic theory.

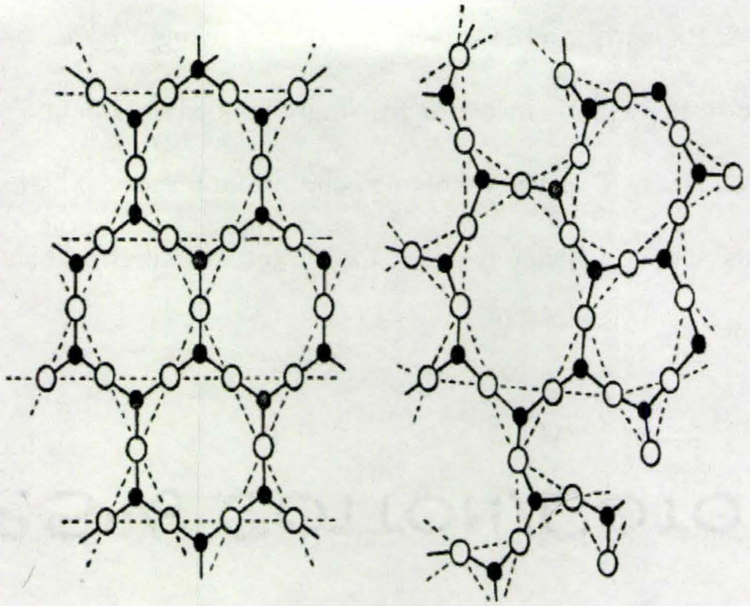

Figure 3-1: Schematic representation of the structure of pure silica, (left) in solid state, (right) in liquid state. (Richardson, 1974)

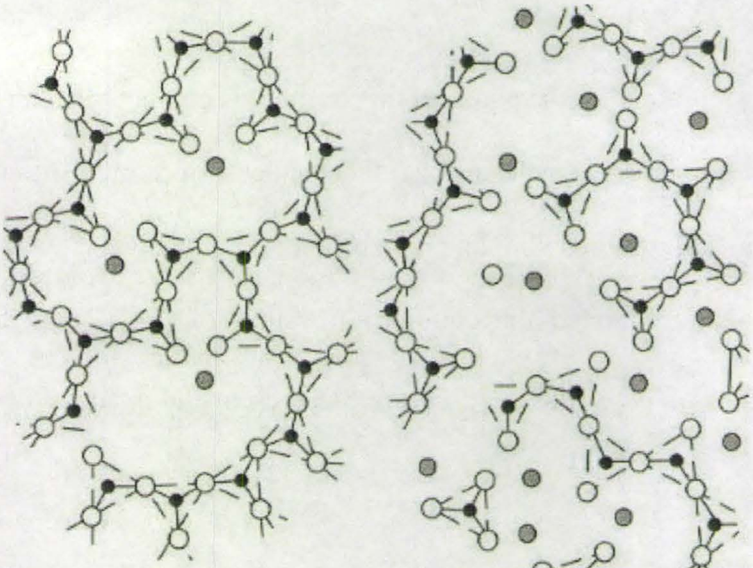

Figure 3-2: Schematic representation of the silicate structure after deploymerization with basic oxides. (Richardson, 1974)

Fincham & Richardson (1954) were the first to recognize that oxygen exists in only three forms within silicate melts, singly bonded O^-, doubly bonded O^o, and free oxygen anions O^{2-}. The following equilibrium reaction was suggested on the basis of the charge balance required for the tetrahedral co-ordination of oxygen with silicon:

$$2O^- \rightleftarrows O^o + O^{2-} \tag{3-15}$$

Adopting this model, Toop & Samis (1962a, 1962b) proposed that under equilibrium conditions equation 3-15 may be written as:

$$k_{3-15} = (O^o)(O^{2-})/(O^-)^2 \tag{3-16}$$

where $k_{3\text{-}15}$, representing the equilibrium constant, is characteristic of the cation in any binary or ternary melt and is independent of composition at a fixed temperature. On solving simple mass balance and charge equations, Toop & Samis (1962a) calculated the equilibrium values of (O^o), (O^-), and (O^{2-}) for various values of N_{SiO_2} and $k_{3\text{-}15}$; Figure 3-3 presents an example of one of these calculations.

The most significant contribution from the work of Toop & Samis (1962a) was in their having demonstrated that the activity of a basic oxide was proportional to the free oxygen concentration (O^{2-}) in the melt, Figure 3-4. Free oxygen concentration was evaluated using Temkin's method (1945) and for an appropriate selection of the equilibrium constant in reaction 3-15. Values of the equilibrium constant for different binary silicate systems were determined by fitting calculated free energy curves against experimentally determined ones.

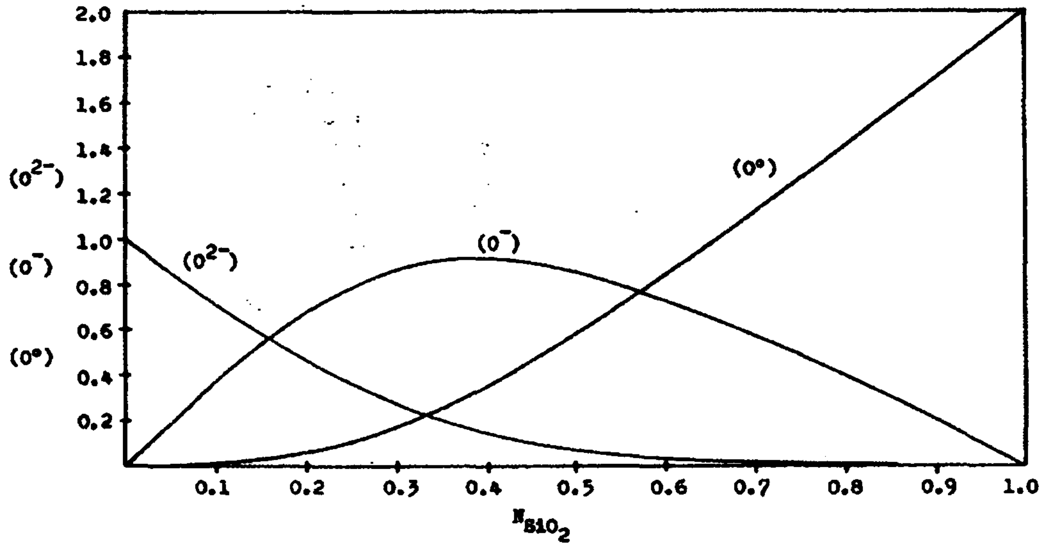

Figure 3-3: Equilibrium values of (O^0), (O^-), and (O^{2-}) versus N_{SiO2} for K_{3-15} = 0.06. (Toop & Samis, 1962a)

In their work on acid-base equilibria in the system $PbO-SiO_2$, Flood & Knapp (1963) took a more specific approach to the problem of polymerization in silicate melts. They considered liquid lead silicates to be ideal solutions of ions and selected anions that forced agreement between the calculated ideal activity of PbO and the experimentally determined activity. Three different types of liquid silicate structures were considered, which Flood & Knapp (1963) suggested probably depend on the polarizing strength of the cation present, namely: i) 0 – 20 mole per cent SiO_2, ii) 20 – 40 mole per cent SiO_2, and iii) 40 – 60 mole per cent SiO_2.

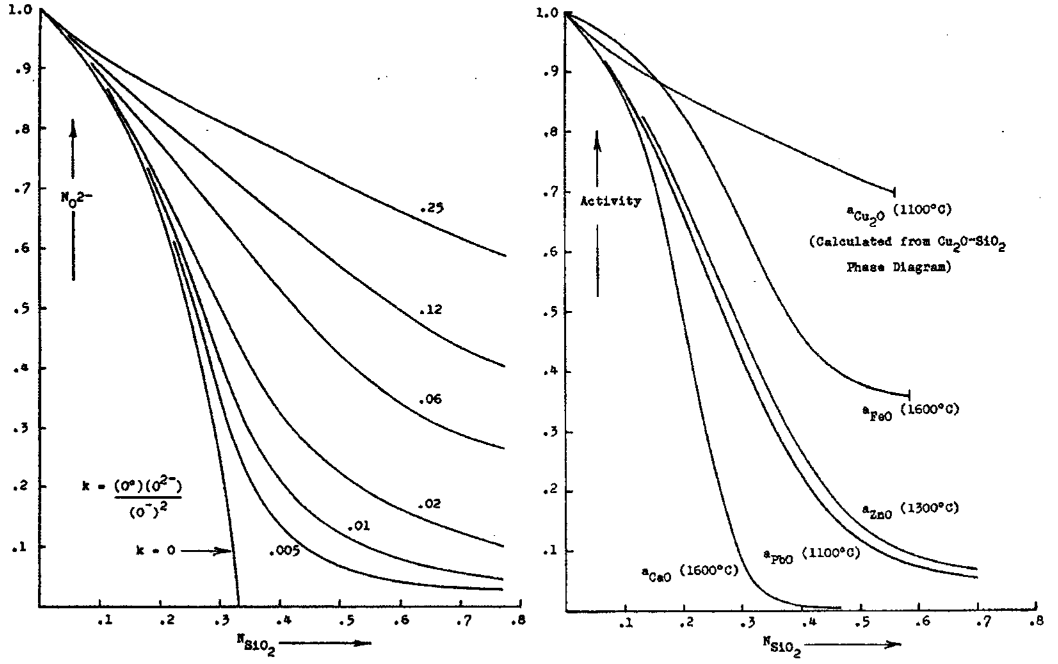

Figure 3-4: Comparison of Temkin's ionic fraction of oxygen ions versus N_{SiO2} for various values of $k_{3\text{-}15}$ against experimental activities of various metal oxides in binary silicates with respect to the pure liquid oxides. (Toop & Samis, 1962a)

As summarized by Gaskell (1967), the fundamental difference between the conclusions of Toop & Samis (1962a, 1962b) and Flood & Knapp (1963) is that the former authors suggested that the equilibrium constant was a function of temperature only, while the latter authors suggest that it was also dependent on composition. Figure 3-5 summarizes how liquid composition is changed by the addition of silica to lead oxide at 1100°C. Flood & Knapp (1963) admitted, however, that the assumption of ideal anionic mixtures within their model may conceal the true equilibrium involved. Consequently the calculations were not intended as decisive proof of the existence of SiO_4^{4-}, $Si_3O_9^{6-}$, and $Si_6O_{15}^{6-}$ silicate ions, but rather only as a logical indication.

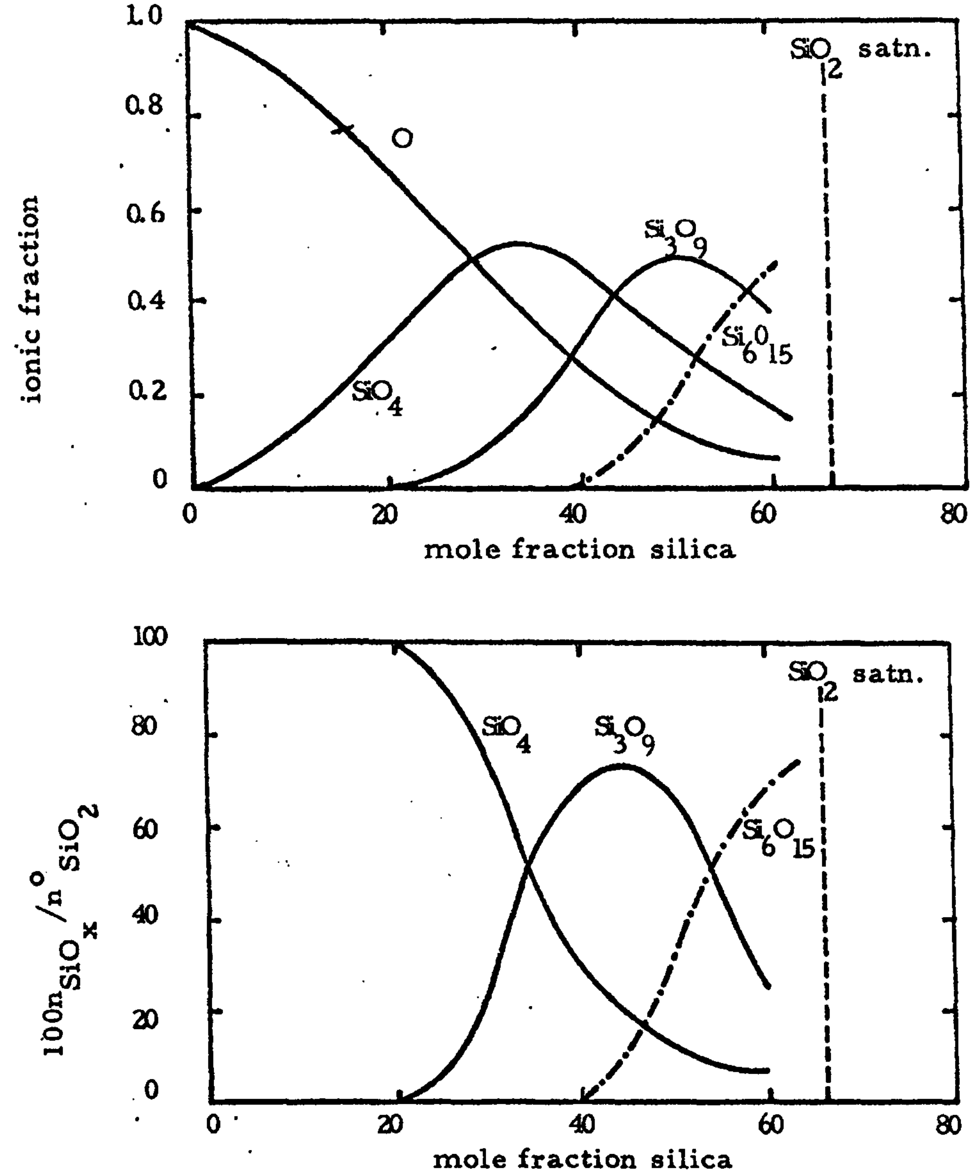

Figure 3-5: Constituent ions versus composition. (top) Anionic fractions N, (bottom) Distribution of Si atoms present in the different species versus SiO_2 fraction in the melt. (Flood & Knapp, 1963)

Masson (1965) detailed a more formal treatment of the Toop & Samis (1962a, 1962b) approach, expressing ion distribution in terms of fractions rather than concentrations of reactive groupings. In his work, Masson (1965) considered binary melts (MO-SiO_2) where the ratio of metallic oxide MO to silica was sufficiently high such that depolymerization was regarded as complete. Masson (1965) reasoned that as the silica content of depolymerized melts increased, a series of polycondensation reactions occurred whereby SiO_4^{4-} ions first dimerized and then reacted further with higher members of the series to form linear and branched polyanionic chains, resulting in the elimination of oxygen ions at each step. In a later publication, Masson (1972) stated the following generalized polycondensation reaction:

$$SiO_4^{4-} + Si_nO_{3n+1}^{2(n+1)-} \rightleftharpoons Si_{n+1}O_{3n+4}^{2(n+2)-} + O^{2-} \tag{3-17}$$

Analogous to the assumption of Toop & Samis (1962a, 1962b), although admittedly more limited, Masson (1965) assumed that all polycondensation reactions had the same equilibrium ratios and applied his model to the systems FeO-SiO_2, MnO-SiO_2, PbO-SiO_2, and CaO-SiO_2 by curve fitting experimentally determined activity plots for different equilibrium ratio values. A theoretical plot of curves of N_{SiO4} against N_O^{2-} for various values of k is presented as Figure 3-6.

Masson (1965) considered his model preliminary and listed the following limitations:

- Only binary systems were described. The Temkin equation was no longer applicable when a second cation was introduced.
- No provision was made for the possible formation of ring structures.

- Theory predictions were not expected to be of high accuracy for the lowest members of the series nor in regions close to the silica saturation.

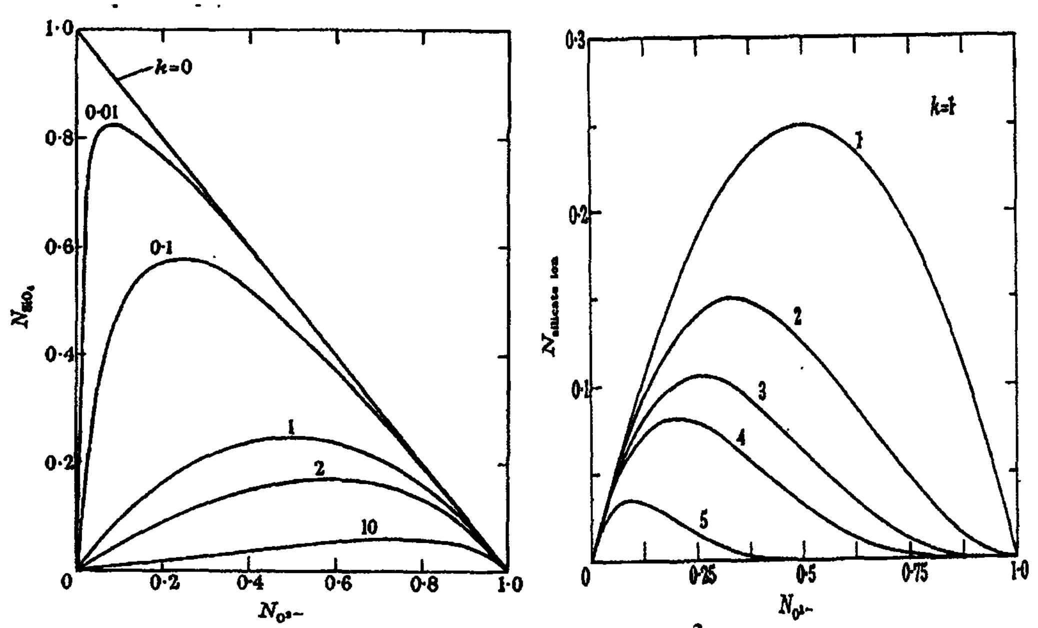

Figure 3-6: Theoretical curves of N_{SiO4} against N_O^{2-} for various values of k. (Masson, 1965)

Following the approach of Toop & Samis (1962a), Yokokawa & Niwa (1969a, 1969b) presented a method based on the quasi-lattice treatment of the random network model on the silicate structure. Their model assumed that the enthalpy change of reaction 3-15 was constant and independent of composition. By calculating the change in configurational entropy they derived an expression for the partition function of the solution. Calculated free energy of solution and activity plots for binary and ternary silicate melts were shown in good agreement with experimental systems. It should be noted that unlike the Toop & Samis (1962a) model, the Yokokawa & Niwa (1969a, 1969b) model was not based on Temkin mixing.

Kapoor & Frohberg (1973) derived equations for the free energy of mixing and activities of binary and ternary melts based on a statistical thermodynamic treatment. Slag comprised of pure oxides, silica, and their mixtures were assumed divided into cells in such a manner that each cell contained a single oxygen ion surrounded by cations. Cells were described as being symmetric (M_iOM_i and SiOSi) and asymmetric (M_IOM_{II}, M_IOSi, and $M_{II}OSi$) types where binary cell formation and interaction energies were iteratively adjusted to provide good agreement with the experimentally determined values. In order to predict the equilibrium state of the system, Kapoor & Frohberg (1973) evaluated the configurational integral of the state as follows:

$$\Omega = \sum_i g_i \exp\left(\frac{-\varepsilon_i}{k_b T}\right) \tag{3-18}$$

where Ω is the partition function, k_b is the Boltzmann constant, T is the temperature, and g_i is the degeneracy having energy ε_i.

A key advantage of describing the slag in terms of cells is that basic oxide and silica activities may be approximated in the absence of knowing the exact anionic complexes within the melt. Gaye and coworkers (1984, 1992a, 1992b, 1997) extended the cell model to multi-component solutions, including: SiO_2-TiO_2-Ti_2O_3-Cr_2O_3-Al_2O_3-Fe_2O_3-CrO-FeO-MnO-MgO-CaO-CaF_2-S. Results from their work have been included in the multiphase equilibrium package named Chemical EQuilibrium Calculation for the Steel Industry (CEQCSI). Gaye & Lehman (1997) improved the cell model by introducing a generalization of the central atoms model to describe the anion neighborhood within their oxisulphide model. More recently, Australia's Commonwealth Scientific and Industrial Research Organisation (CSIRO) has further extended the cell model to include additional non-ferrous oxides and have incorporated their findings within a multiphase equilibrium (MPE) package (2002, 2007).

3.3. Part I: Mathematical Model for the Determination of Steel Activities

Thermodynamic properties of solute elements in steel were determined using the unified interaction parameter formalism proposed by Pelton and Bale (1986, 1990). A computer subroutine was developed from equations 3-13 and 3-14 using first and second order interaction parameters as summarized in Table 3-1 and 3-2. Interaction parameters were largely taken from the compilations of Sigworth & Elliott (1974) and the Steelmaking Data Sourcebook (1988). As seen, the orders of magnitude of the interaction coefficients vary depending on the system under study; generally, the stronger the atomic interactions between the two components the larger the interaction coefficient values. As mentioned by Lupis (1981) higher order coefficients are typically not warranted by simple systems, but are required to reduce the prediction errors of multi-component systems. Pelton & Bale (1986) proposed the following equations for determining the second-order parameter ε_{ijk} from the $\rho_i^{(j)}$ and $\rho_i^{(jk)}$ interaction parameters already available within the literature:

$$2\varepsilon_{ijj} = 2\rho_i^j + \varepsilon_{jj} = \rho_j^{ij} + \varepsilon_{ij} \qquad (3\text{-}19)$$

$$2\varepsilon_{ijk} = \rho_i^{jk} + \varepsilon_{jk} = \rho_j^{ik} + \varepsilon_{ik} = \rho_k^{ij} + \varepsilon_{ij} \tag{3-20}$$

Recently, the present author was part (see footnote 2) of an in-depth review on the Pelton & Bale (1986) model undertaken in fulfillment of the course 'Computational Thermodynamics' offered at McMaster University. An interesting outcome from the study was finding that the solvent activity coefficient equation originally derived by Pelton & Bale (1986) was not a unique solution. The starting point in the investigation considered the relation first proposed by Darken (1967a) to demonstrate thermodynamic consistency between the activity coefficients of the solutes:

$$(1-X_3)\frac{\partial \ln \gamma_2}{\partial X_3} + X_3\frac{\partial \ln \gamma_3}{\partial X_3} = X_2\frac{\partial \ln \gamma_2}{\partial X_2} + (1-X_2)\frac{\partial \ln \gamma_3}{\partial X_2} \tag{3-21}$$

Activity coefficient expressions for γ_2 and γ_3 may be stated from the unified interaction parameter model as:

$$\ln \gamma_2 = \ln \gamma_2^o + \varepsilon_{22}X_2 + \varepsilon_{23}X_3 + \varphi(X_2, X_3) \tag{3-22}$$

$$\ln \gamma_3 = \ln \gamma_3^o + \varepsilon_{32}X_2 + \varepsilon_{33}X_3 + \varphi(X_2, X_3) \tag{3-23}$$

where $\varphi(X_2, X_3)$ represents an as yet to be determined function for representing the modified solvent activity term and satisfies Darken's equation. Substitution of equations 3-22 and 3-23 into equation 3-21 yields:

$$(1-X_3)\left(\varepsilon_{23} + \frac{\partial \varphi}{\partial X_3}\right) + X_3\left(\varepsilon_{33} + \frac{\partial \varphi}{\partial X_3}\right) = X_2\left(\varepsilon_{22} + \frac{\partial \varphi}{\partial X_2}\right) + (1-X_2)\left(\varepsilon_{32} + \frac{\partial \varphi}{\partial X_2}\right)$$

(3-24)

If $\varphi(X_2, X_3)$ is now assumed to have the following form:

$$\varphi(X_2, X_3) = \alpha_{22}X_2^2 + \alpha_{23}X_2X_3 + \alpha_{33}X_3^2 \qquad (3\text{-}25)$$

its partial derivatives may be easily determined as:

$$\partial\varphi/\partial X_2 = 2\alpha_{22}X_2 + \alpha_{23}X_3 \qquad (3\text{-}26)$$

$$\partial\varphi/\partial X_3 = \alpha_{23}X_2 + 2\alpha_{33}X_3 \qquad (3\text{-}27)$$

Substituting the partial derivatives into equation 3-24 gives:

$$(\varepsilon_{23} - \varepsilon_{32}) + X_2(\alpha_{23} - \varepsilon_{22} + \varepsilon_{32} - 2\alpha_{22}) + X_3(-\varepsilon_{23} + \varepsilon_{33} + 2\alpha_{33} - \alpha_{23}) = 0$$

(3-28)

From inspection, it is seen that a possible solution of equation 3-28 is obtained by setting coefficients α_{22}, α_{23}, and α_{33} as:

$$\alpha_{22} = -\frac{\varepsilon_{22}}{2} \qquad \alpha_{23} = -\varepsilon_{23} \qquad \alpha_{33} = -\frac{\varepsilon_{33}}{2} \qquad (3\text{-}29)$$

from which it follows that:

$$\varphi(X_2, X_3) = -\frac{1}{2}\sum_{i=2}^{3}\sum_{j=2}^{3}\varepsilon_{ij}X_iX_j \qquad (3\text{-}30)$$

Equation 3-30 is identical to the solvent activity coefficient expression first proposed by Pelton & Bale (1986), and clearly satisfies Darken's equation of thermodynamic consistency. It is, however, noted that the derived solvent activity coefficient expression is not unique, but is rather just one of an infinite number of possible algebraic expressions.

Table 3-1: First order interaction coefficients $e_i^{(j)}$ in liquid iron (1873K)

i \ j	Al	C	Ca	Mn	N	Nb	O	S	Si	Ti
Al	0.043	0.091	-0.047	0.035	0.015	-	-1.98	0.035	0.056	0.004
C	0.043	0.243	-0.097	-0.0084	0.11	-0.059	-0.32	0.048	-0.08	-
Ca	-0.054	-0.34	-0.002	-0.0067	-	-	-580	-140	-0.095	-
Mn	-	-0.041	-	0	-0.091	0.0035	-0.083	-0.048	-0.017	-0.05
N	0.01	0.13	-	-0.02	0	-0.068	-0.12	0.007	0.048	-0.6
Nb	-	-0.486	-	0.0093	-0.475	0	-0.72	-0.046	-0.01	-
O	-1.17	-0.421	-515	-0.021	-0.14	-0.12	-0.17	-0.133	-0.066	-1.12
S	0.041	0.111	-110	-0.026	0.01	-6.01	-0.27	-0.046	0.075	-0.18
Si	0.058	0.18	-0.066	-0.0146	0.092	0	-0.119	0.066	0.103	1.23
Ti	0.0037	-	-	-0.043	-0.14	-0.12	-3.4	-0.27	0.644	0.042

Table 3-2: Second order interaction coefficients $r_i^{(j)}$ in liquid iron (1873K)

i \ j	Al	C	Ca	Mn	N	Nb	O	S	Si	Ti
Al	-0.001	-0.004	-	-	-	-	39.82	-	-0.0006	-
C	-0.0007	-	-	-	-	-0.00024	-	-	0.0007	-
Ca	-	0.012	-	-	-	-	-	-	-	-
Mn	-	-	-	0	-	-	-	-	-	-
N	-	-	-	-	-	-	-	-	-	-
Nb	-	-	-	-	-	-	-	-	-	-
O	-0.01	-	-	-	-	-	-	-	-	-
S	-	-	-	0	-	-	-	-	-	-
Si	-	-	-	-	-	-	-	-	-	-
Ti	0.00184	-	-	-	-	-	-	-	-0.00184	-

3.4. Part II: Mathematical Model for the Determination of Slag Activities

Out of all the available slag thermodynamic solution models, the cell model has arguably been the most extensively and successfully applied model within the steel industry. The model describes slag properties as a mixture of components having molecular formulae $(M_i)_{ui}(O)_{vi}$ and $(M_i)_{ui}(S)_{vi}$ using a two sub-lattice thermodynamic approach. Fluorides may also be considered in the model. Anions (either O^{2-} or S^{2-}) are assumed contained within one sub-lattice, while cations are assumed filled by increasing order of their basicity (e.g.: Si^{4+}, Ti^{4+}, Ti^{3+}, Cr^{3+}, Al^{3+}, Fe^{3+}, Cr^{2+}, Fe^{2+}, Mn^{2+}, Mg^{2+}, Ca^{2+}) in the second sub-lattice. Conservation of charge is maintained using cationic and anionic mass balance equations:

Cations:
$$\sum_{k=1}^{p} R_{ii}^{k} + \sum_{k=1}^{p} \sum_{\substack{j=1 \\ j \neq i}}^{m} R_{ij}^{k} = \sum_{k=1}^{p} v_{i_k} x_{ik} \tag{3-31}$$

Anions:
$$\sum_{i=1}^{m} R_{ii}^{k} + \sum_{\substack{j=1 \\ j \neq i}}^{m} R_{ij}^{k} = \sum_{i=1}^{m} v_{i_k} x_{ik} \tag{3-32}$$

where R_{ii}^{k} and R_{ij}^{k} represent the number of symmetric (i-k-i) and asymmetric (i-k-j) cells, v_{ik} the anion stoichiometric index of the component, and x_{ik} the mol fraction of cation-i and anion-k. For a given system, Gaye et al. (1984, 1992a, 1992b, 1997) assumed that: (i) each cation appears in two cells, (ii) each symmetrical cell contains two i-cations, and (iii) that there are two asymmetrical cells. Energy parameters are used in the cell model to describe the behaviour of the formed cells within a solution, including:

- W_{ij}^{A} – formation energy of A-asymmetrical cells from A-symmetrical cells
- W_{ii}^{A} – stability energy of an A-symmetric cell relative to the oxygen symmetric cell
- E_{ij}^{A} – interaction energy between an A-symmetric and an A-asymmetric cell
- E_{ij}^{AB} – interaction energy between an A-symmetric and a B-symmetric cell

To ensure the satisfactory representation of some thermodynamic systems, selected formation and interaction energies were assumed to vary linearly with composition.

An important concept in thermodynamics is that of state, which can be considered on either a micro or macro scale. The concept of macrostate refers to classical thermodynamics, whereby the state is fixed when the values of the independent variables (pressure, volume, and temperature) are fixed (Gaskell, 2003). In contrast, a microstate is an atomistic concept referring to the specific energy arrangement of each molecule in a system at one instant in time. Statistical thermodynamics is the study of the microscopic behaviour of thermodynamic systems using probability theory, and provides a means for interpreting macroscopic predictions using microscopic state properties. As microstates are highly stochastic and un-measurable quantities, the Boltzmann distribution is used for predicting the fractional number of molecules occupying a set of states. It may be stated algebraically as:

$$p_i = \left(g_i\, e^{-\varepsilon_i/k_B T}\right)\Big/\Omega$$

(3-32)

where k_b is the Boltzmann constant, Ω is the normalization constant or partition function, p_i is the probability of particles occupying microstates-i and having energy ε_i, and g_i is the degeneracy. The partition function is a measure of the number of states accessible to the system at a given temperature and may be derived from the Boltzmann distribution by defining the probability that a system is in a microstate as unity (i.e. $\sum_i p_i = 1$):

$$\Omega = \sum_i g_i\, e^{-\varepsilon_i/k_B T} \tag{3-33}$$

As shown, the partition function is dependent on temperature and microstate energies, where g_i is the degeneracy factor and refers to the number of states having energy ε_i. Equation 3-33 is commonly simplified to consider only the 'most probable' energetic arrangement that maximizes the partition function:

$$\Omega = g\left(E\right)\exp^{\left(-E/RT\right)} \tag{3-34}$$

As summarized by Guggenheim (1952), the free energy of liquid slag may be approximated from the partition function as:

$$G^M \approx F^M = -RT\ln\Omega \tag{3-35}$$

where G^M is the free energy of mixing, F^M the Helmholtz free energy of mixing, R the ideal gas constant and T the temperature. Gaye and coworkers (1992a, 1992b), in developing the cell model, derived the configuration partition coefficient as:

$$\begin{aligned}\ln(\Omega) = &-\frac{1}{RT}\sum_{i,j,k} W_{ij}^k R_{ij}^k - 2\sum_{i,k} R_{ii}^k \ln Q_{ik} \\ &+\sum_{i=1}^{m-1} a_i\left(D_i \ln\left(\frac{D_i}{V_i}\right) - D_{i+1}\ln\left(\frac{D_{i+1}}{V_i}\right)\right) \\ &+2\sum_{i=1}^{m} Vi\ln\left(\frac{V_i}{D_1}\right) - \sum_{i,j,k} R_{ij}^k \ln\left(\frac{R_{ij}^k}{D_1}\right)\end{aligned} \tag{3-36}$$

Equation 3-36 has been shown to provide an accurate description of the thermodynamic properties of multi-component slags containing SiO_2-TiO_2-Ti_2O_3-Cr_2O_3-Al_2O_3-Fe_2O_3-CrO-FeO-MnO-MgO-CaO-S over a wide composition and temperature range. Where the stable state of a system corresponds to the number of distinct permutations of cells (R_{ii}^k and R_{ij}^k) that maximize the partition function and consequently minimize the free energy of solution. An explanation of the terms in equation 3-36 is given in Appendix A, along with a worked example for a slag composition of 55wt% CaO, 35wt% Al_2O_3, and 10wt% SiO_2 at 1873K. Interaction and formation energy parameter values used in the study were taken from the literature (1992a, 1992b). To the author's knowledge, energy terms for TiO_2 and Ti_2O_3 are not yet available in open literature.

3.4.1. Cell Fraction Determination

Cell fraction determination is arguably the most difficult calculation within the cell model. The objective here is to determine the equilibrium state of a melt by calculating the combination of cells (R_{ii}^k and R_{ij}^k) yielding the minimum value of free energy and satisfying the mass balance equations (equations 3-31 and 3-32). Partition function maximization is ensured by solving the following auxiliary independent constraints (Lehman & Gaye, 1992) determined on the basis of $\partial \ln \Omega / \partial R_{ij}^k = 0$:

$$R_{ii}^1 R_{jj}^1 = \left(R_{ij}^1 / P_{ij}^1\right)^2 \qquad i,j = 1\ldots m$$

$$R_{ii}^1\left(R_{11}^k / R_{11}^1\right) = \left(R_{ii}^k / P_{ii}^k\right) \qquad i = 1\ldots m, k = 2\ldots p \tag{3-37}$$

$$R_{ii}^1 R_{jj}^1 \left(R_{11}^k\right)^2 = \left(R_{11}^1\right)^2 \left(R_{ij}^k / P_{ij}^k\right)^2 \qquad i,j = 1\ldots m, k = 2\ldots p$$

$$\begin{aligned} \textit{with} \quad RT\ln\left(P_{ij}^k\right) &= W_{11}^k - \left(1-\delta_{ij}\right)\left(W_{ii}^k + W_{jj}^k\right) - W_{ij}^k \\ &+ RT\ln\left(Q_{i1}Q_{j1}\left(\frac{Q_{1k}}{Q_{11}}\right)^2\right) - 2\delta_{ij} RT\ln Q_{ik} \end{aligned} \tag{3-38}$$

As a means of simplifying the above system of constraints, Lehman & Gaye (1992) proposed a change of variables:

$$Y_i = \sqrt{R_{ii}^1} \quad ; \quad Y_j = \sqrt{R_{jj}^1} \quad ; \quad Y^k = R_{11}^k / R_{11}^1 \tag{3-39}$$

Substitution of which leads to the following modified constraints:

$$R_{ij}^{k} = P_{ij}^{k} Y_i Y_j Y^k$$

$$Y_i \sum_{j,k} P_{ij}^{k} Y_j Y^k = V_i \qquad i = 1 \ldots m \qquad (3\text{-}40)$$

$$Y^k = V^k \Big/ \sum_{ij} P_{ij}^{k} Y_i Y_j \qquad k = 2 \ldots p$$

In solving the modified system of constraints, two different numerical methods were attempted in this thesis. The first method involved an iterative convergence procedure to minimize the sum of squared residuals. While this method was found to work sufficiently well for the oxide system, it was unable to accurately converge on a solution for poly-anionic slags. The second method attempted involved extending the numerical technique originally suggested by Gaye & Welfringer (1984) for oxide slags to polyanionic slag systems. The extended procedure required the recursive solution of the constraints listed as equation 3-37 using second order Taylor series expansion, subject to the exponential perturbation of the P_{ij}^{k} matrix by the variable 'z' evaluated between 0 and 1. Following a similar approach outlined by Gaye & Welfringer (1984) for solving oxide slags, the transformed equations for the extended poly-anionic slags were determined as:

$$Y_i \sum_{j,k} \left(P_{ij}^{k}\right)^z Y_j Y^k = V_i \qquad i = 1 \ldots m \qquad (3\text{-}41)$$

$$Y^k = V^k \Big/ \left(\sum_{i,j} \left(P_{ij}^{k}\right)^z Y_i Y_j \right) \qquad k = 2 \ldots p \qquad (3\text{-}42)$$

where the second-order Taylor series expansion is of the form:

$$\left[Y_i\right]_{z+\Delta z} = \left[Y_i\right]_z + \Delta z\left[Y_i^{'}\right]_z + \frac{(\Delta z)^2}{2}\left[Y_i^{''}\right]_z \tag{3-43}$$

In the expression above, the first and second order derivates of Y_i are obtained by differentiating transformed equation 3-40 with respect to Y_i. The result of which yielded two systems of 'm' linear equations having the form:

$$\begin{aligned} \left(Y^{'}\right) &= (A)^{-1}\left(B^{'}\right) \\ \left(Y^{''}\right) &= (A)^{-1}\left(B^{''}\right) \end{aligned} \tag{3-44}$$

where previously unpublished equations for a poly-anionic slag were derived as:

$$a_{ij} = \begin{cases} Y_i \sum\limits_k Y^k \left(P_{ij}^k\right)^z & \textit{if } j \neq i \\ Y_i \sum\limits_k Y^k \left(P_{ij}^k\right)^z + \sum\limits_k \sum\limits_j Y_j Y^k \left(P_{ij}^k\right)^z & \textit{if } j = i \end{cases} \tag{3-45}$$

$$b_i^{'} = -Y_i \sum_k \sum_j Y_j Y^k \left(P_{ij}^k\right)^z \ln\left(P_{ij}^k\right) \tag{3-46}$$

$$b_i^{''} = -\sum_k \sum_j Y^k \left(P_{ij}^k\right)^z \left\{2Y_i^{'}Y_j^{'} + 2\left(Y_i^{'}Y_j + Y_j^{'}Y_i\right)\ln\left(P_{ij}^k\right) + Y_iY_j\left[\ln\left(P_{ij}^k\right)\right]^2\right\} \tag{3-47}$$

At the initial condition of z = 0, Y_i and Y^k are to be initialized as $Y_i = V_i/\sqrt{D_1}$ and $Y^k = V^k/D_1$, representing the probability of having a given cation or anion bond. On determining the values of $\left(Y^{'}\right)$ and $\left(Y^{''}\right)$, $\left[Y_i\right]_{z+\Delta z}$ is evaluated using equation 3-43 and then used for updating the Y^k vector before continuing with the next iteration. Table 3-3 outlines an algorithm that was developed for approximating the Y_i and Y^k vectors. While the presented algorithm is complete from a methodological perspective, it is incomplete from a computational perspective and the reader should use it as a guideline only.

Table 3-3: Algorithm 1 – Approximation of the Y_i and Y^k vectors

Procedure	Comments
Calculate Xi, Eijk, Wijk, Vi, Vk, D_i, Qik, Pijk	
z = 0	- Initialize 'z' variable
dz = 0.1	- Define incremental step
Y = Vi / sqrt(Di(1))	- Initialize Y_i vector
Yk(k) = Vk(k) / Di(1)	- Initialize Y_k vector
while (z < 1)	- Begin while-statement
PZ(i,j,k) = Pijk(i,j,k)^z	- Requires proper looping - Pijk is a symmetric matrix
if (i == j)	- Start if-statement
A(i,i) = Y(i)*Yk(k)*PZ(i,i,k) + PZ(i,j,k)*Y(j)*Yk(k)	- Requires proper looping (Eq. 3-45)
else	
A(i,j) = PZ(i,j,k)*Y(i)*Yk(k)	- Requires proper looping (Eq. 3-45)
end	- End if-statement
AI = A^-1	- Compute matrix inverse
B(i) = -PZ(i,j,k)*ln(Pijk(i,j,k))*Y(i)*Y(j)*Yk(k)	- Requires proper looping (Eq. 3-46)
dY(i) = AI(i,j)*B(j)	- Compute Y' (Eq. 3-45)
dB(i) = -Yk(k)*PZ(i,j,k)*(2*dY(i)*dY(j) + 2*ln(Pijk(i,j,k))*(Y(i)*dY(j) + Y(j)*dY(i)) + Y(i)*Y(j)*ln(Pijk(i,j,k))^2)	- Require proper looping (Eq. 3-45)
d2Y(i) = d2Y(i) + AI(i,j) * dB(j)	- Compute Y'' (Eq. 3-44)
Y(i) = Y(i) + dY(i)*dz + d2Y(i)*dz*dz / 2	- Update Y_i values (Eq. 3-43)
z = z + dz	- Move 'z' forward
end	- End while-statement
Yk(k) = Vk(k) / PZ(i,j,k)*Y(i)*Y(j)	- Update Yk values (Eq. 3-42)

Although the developed routine was found to be both robust and numerically efficient in converging to a solution for Y_i and Y^k vectors for all slags systems studied, these solutions were also found to violate the cation and anion mass balance constraints. As a result, a second iterative procedure was developed to refine the non-optimal solutions from Algorithm 1. While Gaye & Welfringer (1984) never mentioned the use of a refinement algorithm, it is believed that a similar procedure must have been used in their original work. This premise is supported by the excellent agreement between cell model predictions using the proposed refinement algorithm proposed within this thesis and the published results of Gaye & Coulomet (1984).

The recommended refinement procedure involves iteratively updating the Y_i and Y^k vectors using first-order Taylor series expansion until the predicted R_{ij}^k cell fractions satisfy the cation and anion mass balances, where:

$$Y_i^{new} = Y_i^{old} + \left(Y'\right) \tag{3-48}$$

$$Y_k^{new} = V_i \Big/ \left(Y_i^{new} \sum_{i,j} \left(P_{ij}^k\right) Y_j^{new} \right) \qquad k = 2 \ldots p \tag{3-49}$$

Y_i^{old} represents the approximated value using Algorithm 1, while Y_i^{new} and Y_k^{new} are the updated values determined from the recursive solution of:

$$\left(Y'\right) = \left(A\right)^{-1}\left(B'\right) \tag{3-50}$$

where:

$$a_{ij} = \begin{cases} Y_i \sum_k Y^k \left(P_{ij}^k\right) & if\ j \neq i \\ Y_i \sum_k Y^k \left(P_{ij}^k\right) + \sum_k \sum_j Y_j Y^k \left(P_{ij}^k\right) & if\ j = i \end{cases} \tag{3-51}$$

$$b_i' = V_i - Y_i \sum_k \sum_j Y_j Y^k \left(P_{ij}^k\right) \tag{3-52}$$

As seen, the refinement algorithm makes use of the cation mass balance (equation 3-31) for calculating b_i' and converging to the optimal solution. Table 3-4 details an algorithm that may be adopted for refining the Y_i and Y^k vectors. Again, while the presented algorithm is complete methodologically, it requires additional coding.

Table 3-4: Algorithm 2 - Refinement of the Y_i and Y^k vectors

Procedure	Comments
1: epsilon = 1	- Initialize error tolerance
2: **while (abs(epsilon) >1e-15)**	- Begin while-statement
3: **if (i == j)**	- Start if-statement
4: A(i,i) = Y(i)*Yk(k)*Pijk(i,i,k) + Pijk(i,j,k)*Y(j)*Yk(k)	- Requires proper looping (see Eq. 3-51)
5: **else**	
6: A(i,j) = Pijk(i,j,k)*Y(i)*Yk(k)	- Requires proper looping (see Eq. 3-51)
7: **end**	- End if-statement
8: AI = A^-1	- Compute matrix inverse
9: B(i) = Vi - Pijk(i,j,k)*Y(i)*Y(j)*Yk(k)	- Requires proper looping (see Eq. 3-52)
10: dY(i) = AI(i,j)*B(j)	- Compute Y' (see Eq. 3-50)
11: Y(i) = Y(i) + dY(i)	- Compute updated Y_i values (see Eq. 3-48)
12: Yk(k) = Vk(k) / Pijk(i,j,k)*Y(i)*Y(j)	- Compute updated Y^k values (see Eq. 3-49)
13: R(i,j,k) = Pijk(i,j,k)*Y(i)*Y(j)*Yk(k)	- Compute Rijk cell fractions (see Eq. 3-40)
14: epsilon = Vi(j) - sum(sum(R(:,j,:)))	- Check cation constraint - Requires proper for / if statements
15: epsilon = Vk(k) - sum(sum(R(:,:,k))	- Check anion constraint - Requires proper for / if statements
16: **end**	- End while-statement

3.4.2. Free Energy of Mixing Determination

Having solved for the cell fractions (R_{ii}^{k} and R_{ij}^{k}) that maximize the partition function, computing the free energy of mixing (liquid reference) is rather straightforward and may be computed as:

$$\begin{aligned} G^M &= -RT\ln(\Omega) \\ &= -RT\left(-\frac{\mathrm{E_{tot}}}{\mathrm{RT}}+\ln(g)\right) \\ &= \left(E_{form}+E_{\mathrm{int}}\right)-RT\left[\ln(P)+\ln(U)+\ln\left(U^*\right)\right] \end{aligned} \tag{3-53}$$

where E_{form} is the energy necessary for the formation of asymmetric cells from symmetric ones, E_{int} is the parameter introduced to describe the energy of interaction between different cells, P the total number of possible permutations of anions and cations, U the total number of randomly distinguishable permutations, and U^* the maximum number of randomly distinguishable permutations. Free energy solutions for the worked example are attached as Appendix B. The reader is referred to general thermodynamic texts (Lupis, 1983; Guggenheim, 1952) for a more detailed review of degeneracy and partition function terms.

3.4.3. Enthalpy and Entropy of Mixing Determination

Two different approaches for computing the enthalpy and entropy of mixing were attempted in this work. The first approach, as suggested by Gaye and Welfringer (1984) involved solving the Gibbs-Helmholtz equation using the central-difference method. While this procedure worked well, it required the determination of free energy (and consequently R_{ij}^{k}) at two different temperatures and was therefore found computationally expensive. The alternative procedure and recommended approach to solving the entropy and enthalpy of mixing involves restating the free energy of mixing as the state function:

$$G^M = H^M - TS^M \tag{3-54}$$

From which it follows that:

$$H^M = \sum_{i,j,k} W_{ij}^k R_{ij}^k + 2RT \sum_{i,k} R_{ii}^k \ln Q_{ik} \tag{3-55}$$

$$S^M = R \begin{pmatrix} \sum_{i=1}^{m-1} a_i \left(D_i \ln\left(\frac{D_i}{V_i}\right) - D_{i+1} \ln\left(\frac{D_{i+1}}{V_i}\right)\right) \\ +2\sum_{i=1}^{m} Vi \ln\left(\frac{V_i}{D_1}\right) - \sum_{i,j,k} R_{ij}^k \ln\left(\frac{R_{ij}^k}{D_1}\right) \end{pmatrix} \tag{3-56}$$

3.4.4. Component Activity Determination

Component activities referred to their pure liquid standard states can be determined by computing the partial molar free energy of mixing for each slag component as follows:

$$RT \ln(a_i) = G^M + \sum_{j=2}^{m} \left(\delta_{ij} - X_j\right) \left(\frac{\partial G^M}{\partial X_j}\right) \tag{3-57}$$

where δ_{ij} is Kronecker's symbol ($\delta_{ij} = 1$ for i = j and $\delta_{ij} = 0$ for i ≠ j). As seen, the free energy of mixing must be differentiated with respect to composition when solving for slag activity. As used by Gaye & Welfringer (1984), the central difference method was found to work well for calculating free energy derivatives:

$$\frac{\delta G^M}{\delta X_j} = \frac{\left[G^M\left(X, X_j + \Delta X_j\right) - G^M\left(X, X_j - \Delta X_j\right)\right]}{2\Delta X_j} \tag{3-58}$$

It is seen from equation 3-58 that the derivative of free energy with respect to a given slag component (excluding SiO_2), requires an incremental compositional change of that specific slag component in both the positive and negative directions (ie: $\pm\Delta X_j = X_j * 1e\text{-}5$ was used in this work). For each positive or negative incremental change of slag component-j an equal and opposite incremental composition change for SiO_2 was required (Jahnsen, 2006). Of particular note, cell fractions (R_{ij}^k) must be recalculated when solving for the partial derivatives because of the slight change in slag composition.

Calculated liquid reference activities may then be converted to the solid standard state using the relationship:

$$\frac{(a_i)_s}{(a_i)_l} = \exp\left(\frac{\Delta H_{ref} - T\Delta S_{ref}}{RT}\right) \tag{3-59}$$

where ΔH_{ref} and ΔS_{ref} are the enthalpy and entropy of melting for respective pure slag components. While the required conversion data for oxide species (SiO_2, Al_2O_3, Fe_2O_3, FeO, MnO, MgO, and CaO) is available from Gaye and Welfringer (1984), the conversion data for other oxide (TiO_2, Ti_2O_3, Cr_2O_3, CrO), and sulphide (S^{2-}) components remains currently unavailable in open literature.

3.4.5. Liquidus Temperature Determination

A numerical routine based on the 'bisection' method was developed for calculating the slag liquidus temperature by iteratively calculating the activities of a system at different temperatures until one of the stoichiometric components had precipitated as a solid phase. To facilitate the convergence speed of slag liquidus temperature, solid and liquid phase designation terms were introduced as 'S' and 'L'. If the activity of a component was calculated as being greater than unity then it was assumed to exist in solution as a solid phase, otherwise it was assumed to exist as a liquid phase. As shown in Figure 3-7 (left), the routine works by repeatedly dividing a set interval (T_{high} = 3,500K ; T_{low} = 1,000K) in half until the upper and lower bounds have converged to within 1K.

Of potential interest to steelmakers is that the developed routine may be further extended to calculate the percent solids and liquid fractions of a slag and its corresponding composition.

3.4.6. Saturation Point Determination

Slag saturation points were calculated by employing a similar routine as was used for determining slag liquidus temperature, Figure 3-7 (right). At initial upper and lower saturation points for a component (WT_{high} = 100wt% ; WT_{low} = 0wt%) the cell fractions (R_{ij}^{k}), free energy (G^{M}), and slag activities were recursively calculated until the upper and lower bounds have converged to within

0.01wt%. Slag saturation was assumed at a component activity (solid reference) of 0.9995 in order to ensure algorithm convergence at the true saturation point.

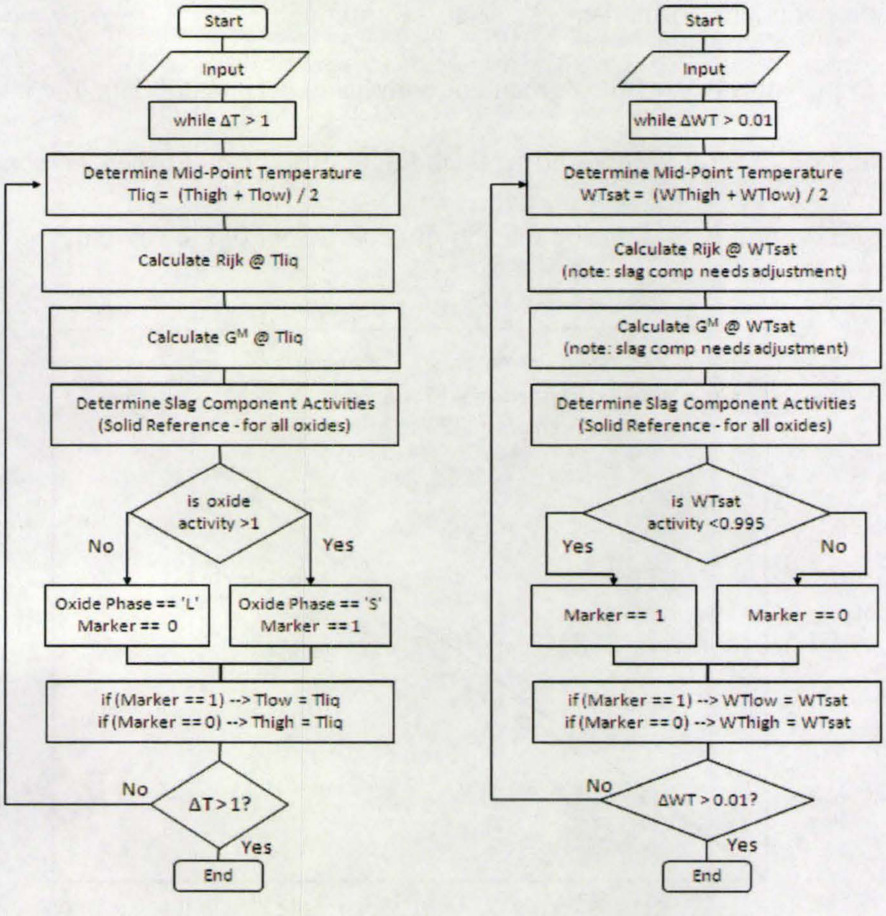

Figure 3-7: (left) Flowchart for calculating slag liquidus temperature, (right) flowchart for calculating slag saturation point.

3.5. Results

3.5.1. Part I: Unified Interaction Parameter Model Validation

Figures 3-8 and 3-9 present a comparison between unified interaction parameter model predicted and experimental determined activity coefficients for aluminum and iron in the Fe-Al system at 1600°C. Shown figures were reproduced using the data presented by Pelton & Bale (1986) and serve to illustrate the improved performance of the UIPM as compared to Wagner's interaction parameter formalism. As seen, even though a one parameter modified formalism provides reasonable agreement with the experimental data, the addition of a second-order term is required to fit the data exactly. A further advantage of the UIPM is its ability to describe the activity coefficient of the solvent.

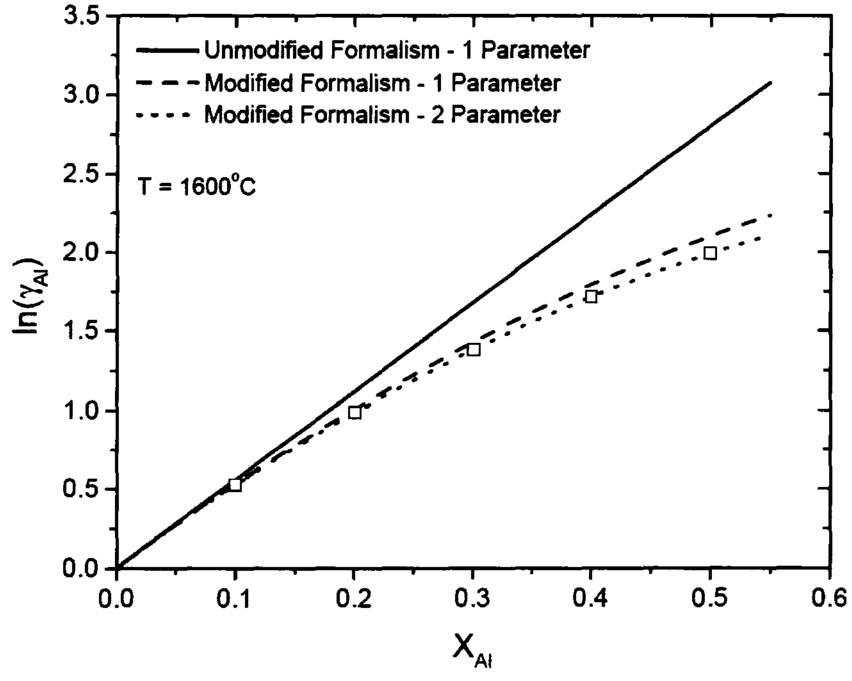

Figure 3-8: Comparison of experimental (□) (Hultgren et al., 1973) and predicted activity coefficient values of Al in Fe-Al alloys at 1600°C.

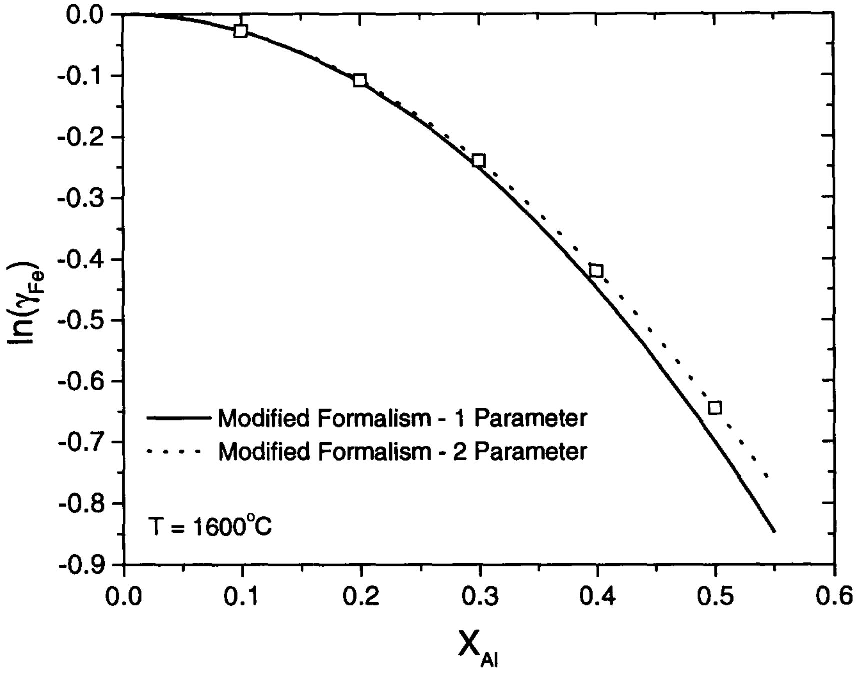

Figure 3-9: Comparison of experimental (□) (Hultgren et al., 1973) and predicted activity coefficient values of Fe in Fe-Al alloys at 1600°C.

3.5.2. Part II: Cell Model Validation

Selected phase and iso-activity diagrams evaluated using the cell model are presented as Figures 3-10 to 3-15. As seen in all cases, the cell model predicted binary, ternary, and quaternary systems are in good agreement with the experimentally determined values. A similar good agreement was observed in systems not presented in this thesis, with predicted systems being identical to the previously published results of Gaye & Welfringer (1984), and Gaye & Coulomet (1984).

3.5.2.1. Binary System

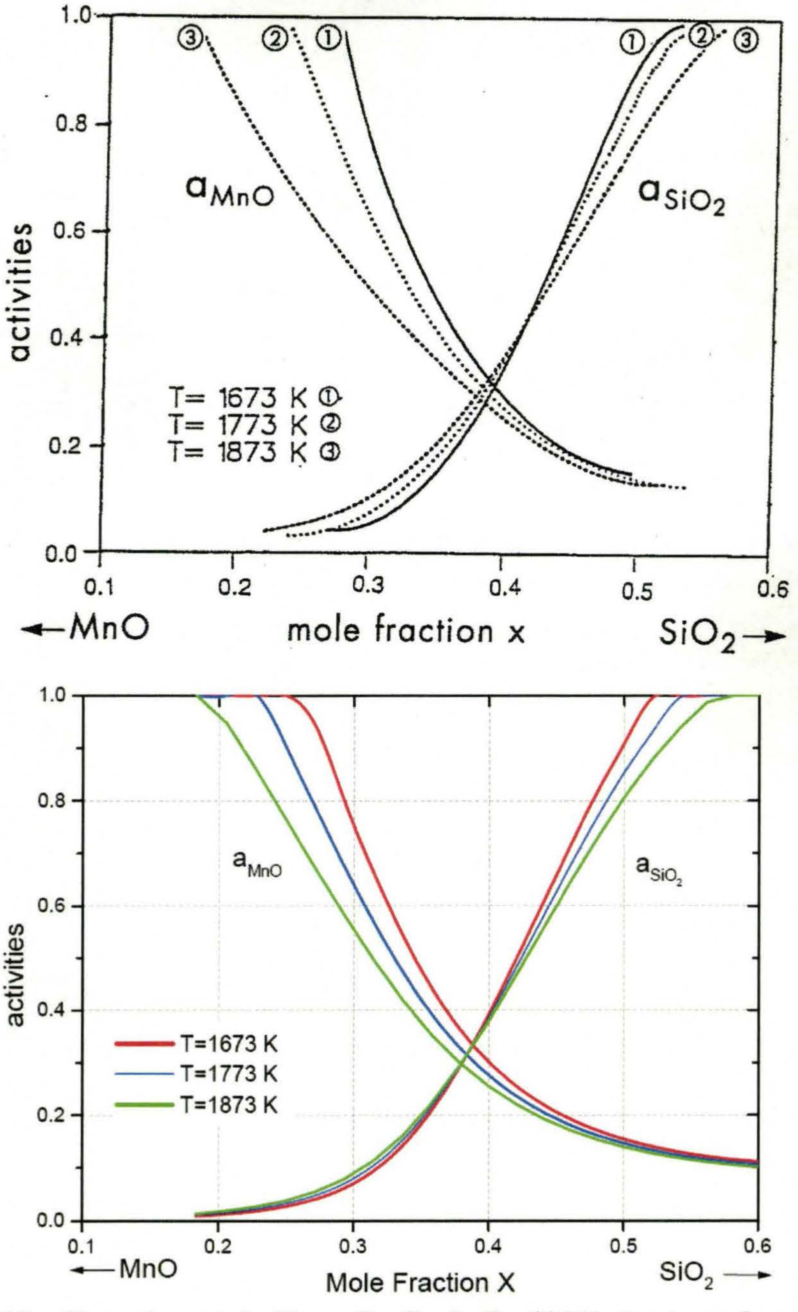

Figure 3-10: Experimental (Rao & Gaskell, 1981) (top) and cell model predicted (bottom) activity curves for MnO and SiO_2 at 1400, 1500, and 1600°C. Activities are referred to pure solids.

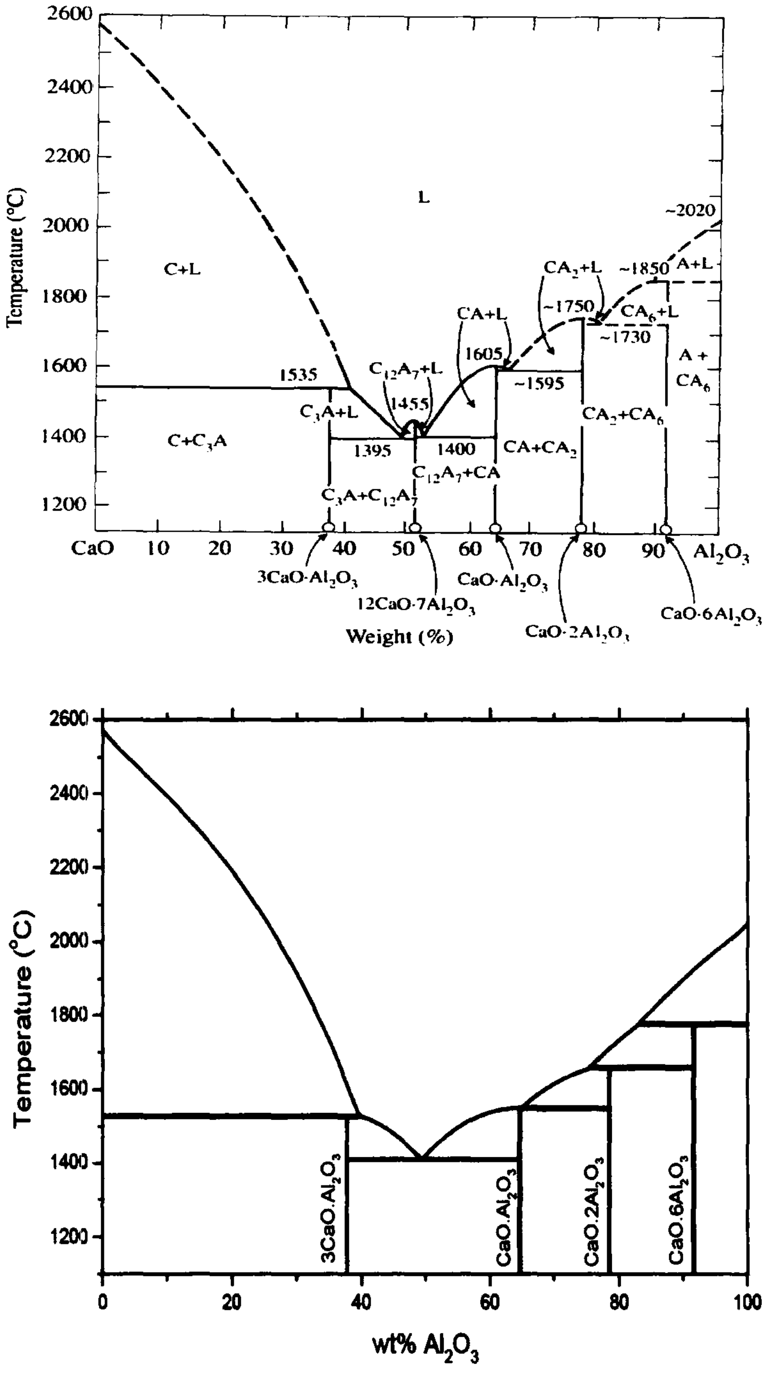

Figure 3-11: Experimental (Rankin & Wright, 1915) (top) and cell model predicted (bottom) CaO-Al_2O_3 phase diagram.

3.5.2.2. Ternary System

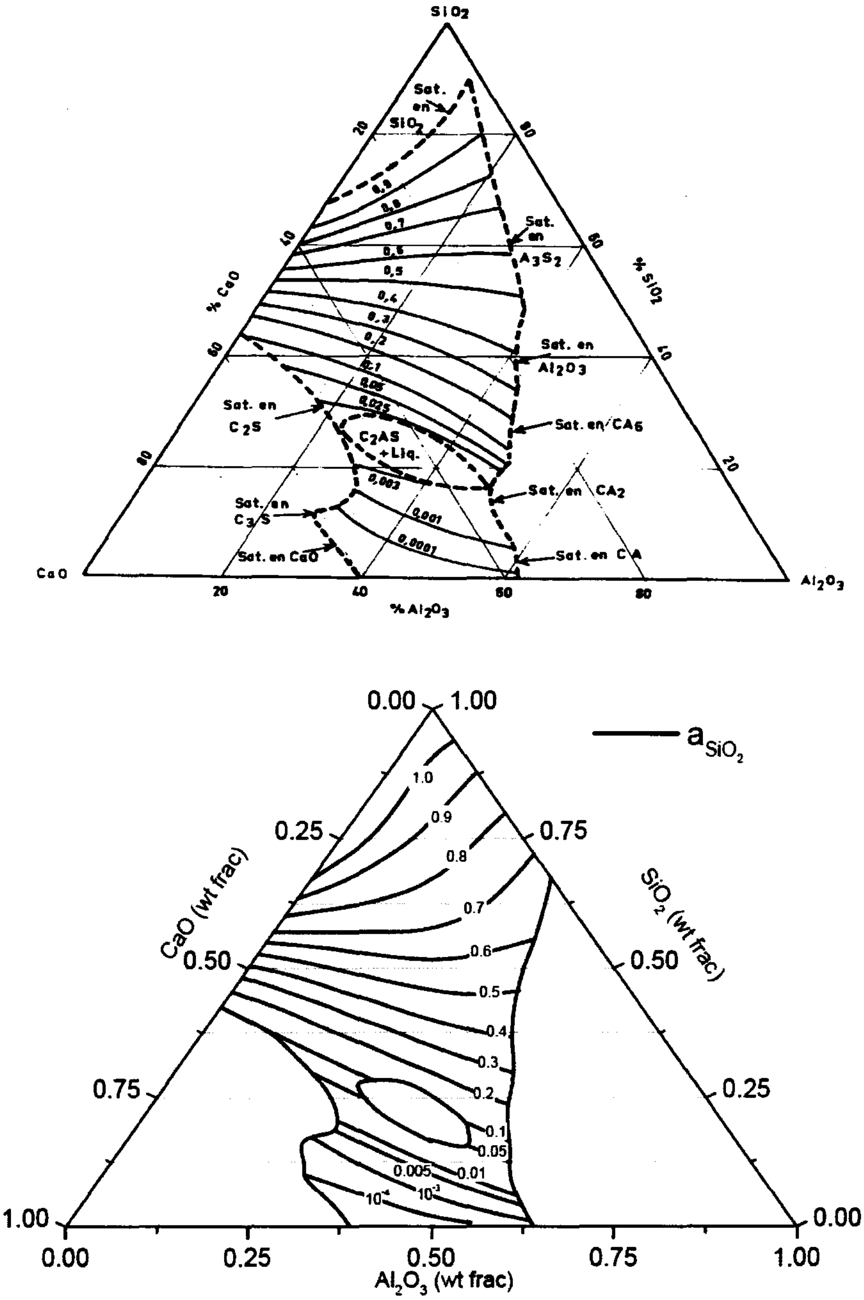

Figure 3-12: Experimental (Rein & Chipman, 1965) (top), and cell model computed (bottom) iso-activity lines for SiO_2 in Al_2O_3-CaO-SiO_2 slags at 1,550°C.

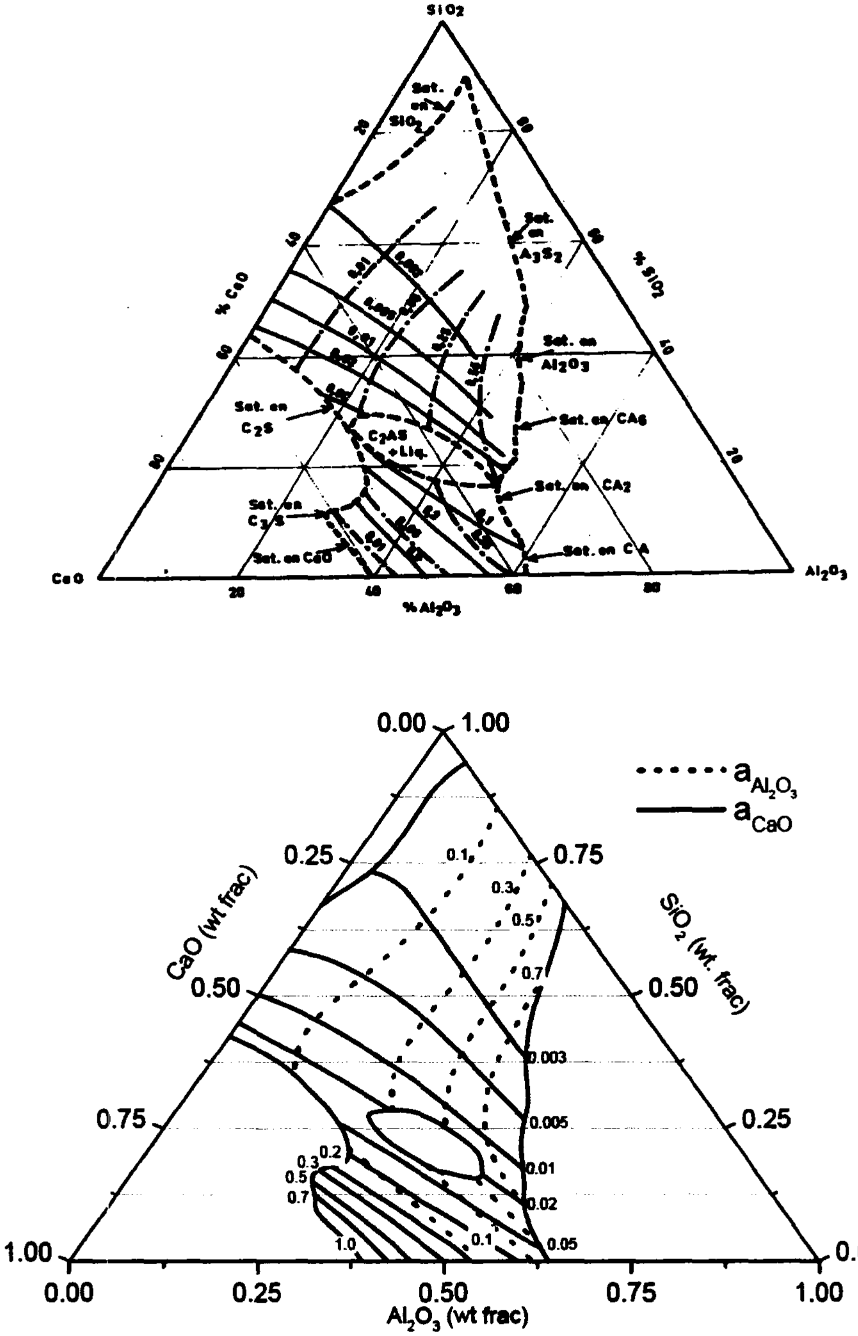

Figure 3-13: Experimental (Rein & Chipman, 1965) (top), and cell model computed (bottom) iso-activity lines for Al_2O_3 and CaO in Al_2O_3-CaO-SiO_2 slags at 1,550°C.

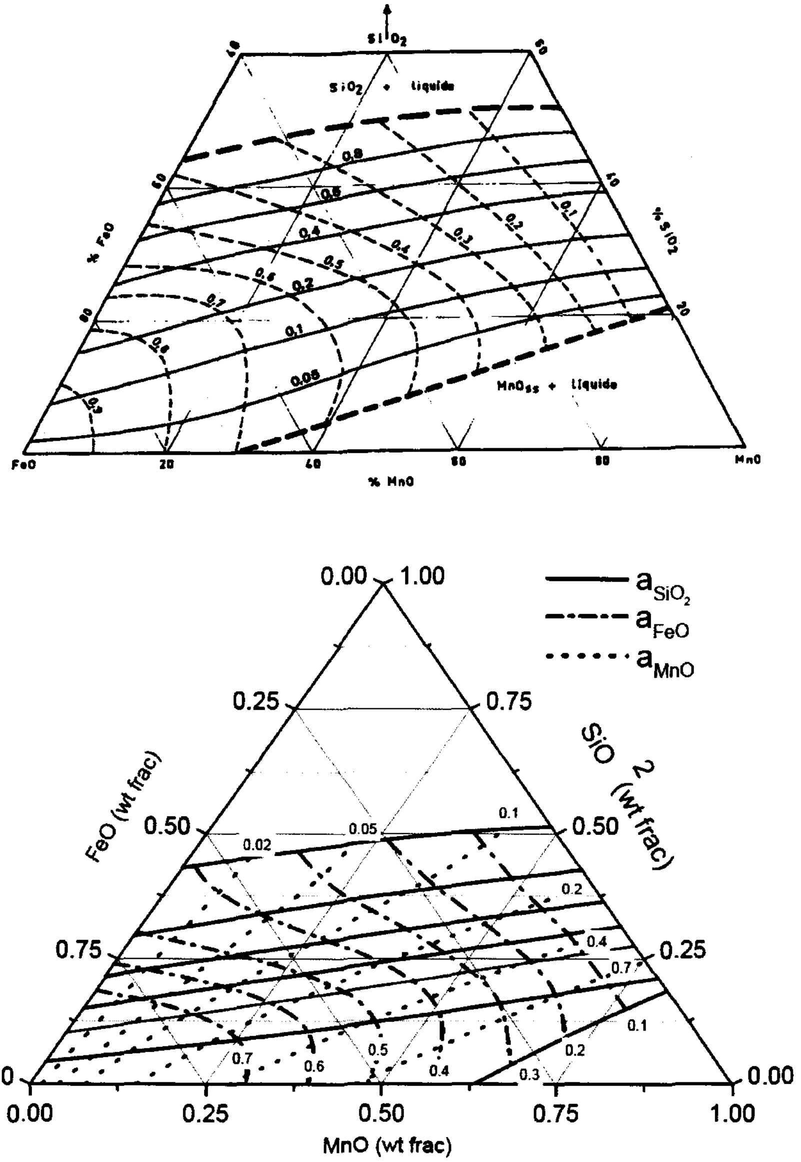

Figure 3-14: Experimental (Gaye & Riboud, 1981) (top), and cell model computed (bottom) iso-activity lines for SiO_2, MnO and FeO in SiO_2-MnO-FeO slags at 1,550°C.

3.5.2.3. Quaternary System

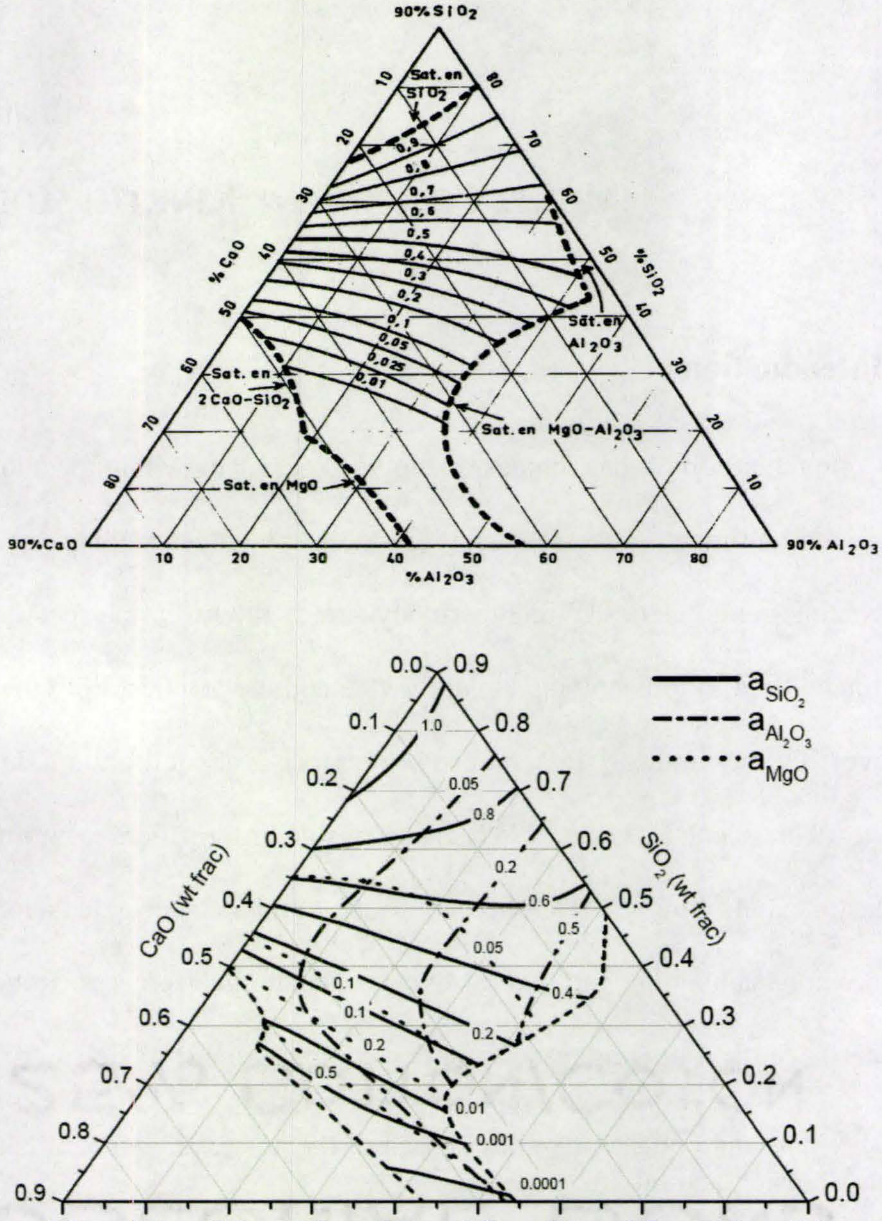

Figure 3-15: Experimental (Rein & Chipman, 1965) (top), and cell model computed (bottom) iso-activity lines for SiO_2, Al_2O_3 and MgO in SiO_2-Al_2O_3—CaO-MgO slags at 10%MgO and 1,600°C.

Chapter 4

MULTI-COMPONENT KINETIC MODEL[4]

4.1. Introduction

Comprehension of the complex phenomena occurring within metallurgical smelting and refining processes requires a good understanding of both thermodynamics and kinetics. While thermodynamics allows for the specification of an ultimate limit, it tells nothing about the rate and the practical limit that may be achieved. Further, industrial operations seldom occur at equilibrium (Hatch & Chipman, 1949; Faral & Gaye, 1984). As a result, information regarding the kinetic factors controlling the rate of reactions is of great technical and economic importance for maintaining full-control over a metallurgical process. Robertson (1995) has listed the following reasons for developing a kinetic model:

1. They represent a quantitative description of the process in terms of heat and mass transfer, and mixing.
2. They allow an accurate prediction of process performance under other conditions of temperature, feed composition, etc., for which experimental data may not be available.

---

[4] Most of the contents of this chapter were published as two separate manuscripts: (1) K.J. Graham, G.A. Irons, "Integrated Control in the Ladle Metallurgy Furnace", *SCANMET III, 3rd International Conference on Process Development in Iron and Steelmaking*, pp. 385-396.; and (2) K.J. Graham, M. Ricci, S. Waterfall, and G.A. Irons, "Slag Carryover Control at ArcelorMittal Dofasco", *AIST Proceedings*, May 5-8 (2008), Pittsburgh, PA..

3. They give a dynamic description of the evolution (over time) of phase composition and temperature, and so they can be used to advise operators when to take process actions, such as the addition of coolant and changes in gas blowing rate.
4. They may be used to describe the chemistry and operation of the process to regulators, and other parties interested in the operation of the plant.
5. A single process model may be combined with models of other unit processes, and incorporated in a description of the whole plant.
6. A model may be used to illustrate the best possible mode of operation.

This chapter details the development of a multi-component kinetic model for the state of an industrial ladle metallurgical furnace (LMF). Extensive industrial sampling results carried out at ArcelorMittal Dofasco will be discussed, and results comparing the experimental and predicted data presented. The forward goal of this work is to incorporate the information in this chapter for improving real-time control and optimization at the LMF.

4.2. Literature Review

4.2.1. Metallurgical Reactions

As claimed by Pomfret & Grieveson (1983), most metallurgical reactions are heterogeneous in nature, occurring between two different phases. The overall rates of heterogeneous reactions are dependent on three main process steps: (i) rate of transport of reactants to the interface, (ii) chemical reaction rate at the interface, (iii) rate of transport of products from the interface. Usually, the slowest process step will control the overall rate and is therefore termed the 'rate-limiting step'. As metallurgical reactions typically take place above the melting temperatures of reacting metals, chemical reaction is generally not regarded as being rate limiting. The concept of 'local equilibrium' at the interface was first introduced by Darken (1958) for the metallurgical literature. A notable exception to this generalization, however, is the absorption and desorption of nitrogen in liquid iron, where the rate of reaction is limited by mixed control (Battle & Pehlke, 1986). Provided chemical reaction control can be neglected, two important consequences follow, namely: (i) chemical equilibrium may be assumed at the interface, and (ii) the reaction may be considered transport controlled. Numerous researchers (Asai, Kawachi, & Muchi, 1983; Deng & Oeters, 1990; Deo & Grieveson, 1986; Kawai, Shinozaki, & Mori, 1982) have demonstrated the dependence of metallurgical reaction rates on the transport of reactants and products to and from the slag-metal interface.

4.2.2. Mass Transport Control

The movement of species across a flowing interface may be treated as the sum of a diffusional contribution and a bulk flow contribution (Geiger & Poirer, 1980):

$$N_{A,x} = -CD_A\left(\frac{\partial X_A}{\partial x}\right) + C_A v_x^* = C_A v_{A,x} \qquad (4\text{-}1)$$

where the first term on the right-hand side of equation 4-1 represents the diffusive contribution and the second term is the molar flux resulting from bulk motion. Here v_x^* is the local molar average velocity in the x-direction, and $v_{A,x}$ is the velocity of A in the x-direction with respect to stationary coordinates, D_A is the diffusivity of A, and C is the local total molar concentration in the solution. For the case of a binary (A/B) fluid, equation 4-1 becomes:

$$N_{A,x} = -CD_A\left(\frac{\partial X_A}{\partial x}\right) + X_A\left(N_{A,x} + N_{B,x}\right) \tag{4-2}$$

As stated by Wilkinson (2000), the solution of equation 4-2 is non-trivial since it requires knowledge of the relationship between the fluid velocity and the total flux. The situation may, however, be simplified by reverting to the condition of quiescent flow (i.e. $v = 0$) and neglecting internal reaction. Under such conditions mass transfer occurs by diffusion perpendicularly away from the interface, and the rate at which concentration changes with time is given by Fick's Second Law:

$$\frac{\partial X_A}{\partial t} = D_A\frac{\partial^2 X_A}{\partial x^2} \tag{4-3}$$

where the diffusion coefficient is assumed independent of concentration. If the interface between solid and fluid establishes a condition of local equilibrium (i.e. $X_A = X_A^o$ at x = 0), and the concentration far from the interface maintains the bulk concentration (i.e. $X_A = X_A^\infty$ as x → 0) then equation 4-3 reduces to:

$$\frac{X_A - X_A^\infty}{X_A^0 - X_A^\infty} = erf\left(\frac{x}{2\sqrt{D_A t}}\right) \tag{4-4}$$

The diffusion flux at the surface (i.e. x = 0) may therefore be stated as:

$$N_{A,x} = -CD_A\left.\frac{\partial X_A}{\partial x}\right|_{x=0} = C\left(X_A^o - X_A^\infty\right)\sqrt{\frac{D_A}{\pi t}} \tag{4-5}$$

where t is the characteristic time. Equation 4-5 specifies that the surface flux is proportional to the concentration difference times a diffusive contribution term. In general, however, an additional contribution to mass transfer is caused by bulk convection, which has the effect of increasing the concentration gradient and therefore the flux (Wilkinson, 2000). As the solution of this problem is often more complex, a simplified approach is to introduce the mass transfer coefficient as a new parameter:

$$N_{A,x} = k_D \left(C_A^o - C_A^\infty \right) \tag{4-6}$$

where k_D is the mass transfer coefficient and relates the flux to the overall driving force in the presence of convection. The mass transfer coefficient has units of distance per unit of time.

Mass transfer coefficients may be determined experimentally or via the simultaneous solution of the continuity and momentum equations for both the total material flux and each individual component. As noted by Wilkinson (2000), this subject is deeply connected with fluid flow, where dimensionless groups are typically used to correlate mass transfer to experimental conditions. For a more in depth review of mass transfer coefficient correlations, the reader is referred to basic texts which address rate phenomena (Themelis, 1995). It should be noted that several simple mass transfer models have been developed for conditions where mass transfer correlations do not directly apply, namely: (i) Film theory, and (ii) Higbie penetration model.

The Film model is commonly used to define reactions and proposes that mass transfer resistance is concentrated at the boundary layer. The boundary layer thickness is approximated as the distance over which 99% concentration change occurs. Within this layer, flow velocity is assumed negligible and flux is given by:

$$N_A = \frac{D_A}{\delta} C\left(X_A^o - X_A^\infty\right) \tag{4-8}$$

with the result that $k_D = D_A/\delta$ when compared with equation 4-6. As summarized by Geiger & Poirer (1980) this approach is often used in cases where the flux is measured and the overall concentration change is known.

The mass penetration theory states that if two fluids of different velocities are in contact with each other, then non-equilibrium conditions will exist for a specific period of time; interfacial packets of one fluid are subjected to unsteady state diffusion of the other phase by the diffusing species. The surface renewal theory was proposed by Higbie (1935), and results in the mass transfer coefficient having a relationship of the form:

$$k_{m,i} = 2\sqrt{\frac{D_A}{\pi t_e}} \tag{4-9}$$

where t_e is the exposure time of the fluid element at the interface. Equation 4-9 assumes that all elements have equivalent exposure times at the interface irrespective of hydrodynamic conditions. Dankwerts (1951), however, amended the theory using an average time of exposure calculated from an assumed distribution of residence times of particles at the surface.

4.2.3. Slag-Metal Mass Transfer

Slag-metal mass transfer kinetics have been the subject of many studies within the metallurgical field. As stated, the overall mass transfer rate for such reactions involve three elementary steps:

1. Transfer of reactants from the metal phase to the slag / metal interface

$$\frac{dn_i}{dt} = (k_m A) C_{Vm} \left(X_{i,m}^{b} - X_{i,m}^{*} \right) \tag{4-10}$$

2. Chemical reaction at the slag-metal interface

$$\frac{dn_i}{dt} = k_f A C_{Vm} X_{i,m}^{*} - k_b A C_{Vs} X_{i,sl}^{*} \tag{4-11}$$

3. Transfer of products away from the slag-metal interface

$$\frac{dn_i}{dt} = (k_{sl} A) C_{Vs} \left(X_{i,sl}^{*} - X_{i,sl}^{b} \right) \tag{4-12}$$

where X_i^* and X_i^b represent the mol fraction of any element 'i' at the interface or in the bulk in either the metal or slag phases, k_m and k_{sl} are the metal and slag mass transfer constants, k_f and k_b are the forward and backward rate constants, C_{Vs} and C_{Vm} the molar concentrations of metal and slag, and A the slag-metal interfacial area. Rearranging the above equations gives:

$$\left(\frac{1}{k_m A} \right) \frac{dn_i}{dt} = C_{Vm} \left(X_{i,m}^{b} - X_{i,m}^{*} \right) \tag{4-13}$$

$$\left(\frac{1}{k_f A}\right)\frac{dn_i}{dt} = C_{Vm}X^*_{i,m} - \left(\frac{k_b}{k_f}\right)C_{Vs}X^*_{i,sl} \tag{4-14}$$

$$\left(\frac{1}{k_{sl} A}\right)\frac{dn_i}{dt} = C_{Vs}\left(X^*_{i,sl} - X^b_{i,sl}\right) \tag{4-15}$$

where k_f/k_b is the equilibrium molar concentration partition ratio of element-i and may be expressed as the parameter $L'_i = k_f/k_b = C_{Vs}X^*_{i,sl}/C_{Vm}X^*_{i,m}$ when the interface is assumed to be at equilibrium. The equilibrium partition ratio is commonly used in terms of weight percent and mol fraction, whereby the following relation holds in converting between the different composition co-ordinates:

$$L'_i = L''_i\left(\frac{C_{Vs}}{C_{Vm}}\right) = L_i\left(\frac{W_{sl}}{W_m}\right) \tag{4-16}$$

where L''_i is the equilibrium partition ratio on a mol fraction basis and L_i is the equilibrium partition ratio on a weight percent basis. At steady state, the rate of change in equations 4-13, 4-14 and 4-15 are equivalent and taken together yield an expression for the overall rate of reaction as:

$$\frac{dn_i}{dt} = k_{ov}A\left(C_{Vm}X^b_{i,m} - C_{Vs}\frac{X^b_{i,sl}}{L'_i}\right) \tag{4-17}$$

The second term on the right hand side represents the driving force for mass transfer expressed in terms of mol fraction in the metal phase. The overall mass transfer rate constant (k_{ov}) represents the sum of the resistances in series and can be stated as:

$$\frac{1}{k_{ov}} = \frac{1}{k_m} + \frac{1}{k_{sl}L'_i} + \frac{1}{k_f} \tag{4-18}$$

While all three reaction steps may jointly influence the overall reaction rate, in many cases one particular step is rate controlling. Since, as previously stated, chemical reaction is not typically the rate limiting step in metallurgical reactions occurring at elevated temperatures, the overall reaction rate constant is often simplified to:

$$\frac{1}{k_{ov}} = \left(\frac{1}{k_m} + \frac{1}{L'_i k_{sl}}\right) \tag{4-19}$$

The following conclusions can be made based on equation 4-19:

- When $\frac{1}{L'_i k_{sl}} << \frac{1}{k_m}$ mass transfer is controlled in the metal
- When $\frac{1}{L'_i k_{sl}} >> \frac{1}{k_m}$ mass transfer is controlled in the slag

General practice within the literature has been to assume that mass transfer is metal phase controlled provided that the elemental partition ratio (L'_i) remains large.

4.2.4. Desulphurization of Steel

Sulphur, with few exceptions, is unwanted in steel. Problems associated with its presence are due primarily to the formation of low melting point inclusions at grain boundaries which act as crack initiators during downstream processing, increasing the corrosion rate of steel (Bristow et al., 2000). Sulphur, is introduced into the steelmaking process primarily from the coke used for reduction and smelting purposes, and its removal is most commonly achieved using calcium and / or lime additives. The overall effectiveness of either reagent additive is directly dependent on its intimacy of contact with residual sulphur. As summarized by Wilson & McLean (1980), the following process conditions favour the removal of sulphur from steel:

- Low oxygen potential within the melt
- Strong stirring at the slag / metal interface
- High temperature to ensure slag fluidity and lime dissolution
- Highly basic slag phase

4.2.5. Thermodynamics of Desulphurization

Of all the slag-metal reactions in the modern iron and steelmaking process, the thermodynamics and kinetics of sulphur transfer have arguably been the most rigorously studied, and may be represented by the following ionic exchange reaction:

$$[S]+(O^{2-})=[O]+(S^{2-}) \tag{4-20}$$

where sulphur is partitioned between the metal and slag phases. The thermodynamics of the above reaction states that sulphur is present in the slag as sulphide. In reality, at oxygen potentials in excess of 10^{-6} atm the sulphur may exist in slag as sulphate ions (Fincham & Richardson, 1954). As iron and steelmaking processes generally operate under reducing conditions, the former assumption remains valid. A simplified approach to desulphurization is to recognize that CaO in slag is the primary desulphurizer:

$$[S]+(CaO)=[O]+(CaS) \tag{4-21}$$

For the limiting case of unit activities of CaO and CaS, the equilibrium constant may therefore be expressed as:

$$K_{4-21}=\frac{h_O}{h_S} \tag{4-22}$$

where h_O and h_S are the Henrian activities of dissolved oxygen and sulphur in metal. Due to the low solubility of calcium and equilibrium sulphur in liquid iron, desulphurization equilibria data is difficult to determine experimentally (The Japan Society for the Promotion of Science: The 19th Committee on Steelmaking, 1988). A literature survey of the free energy data for lime slag desulphurization was undertaken and is summarized as Table 4-1.

Table 4-1: Thermodynamic data for lime slag desulphurization.

Reaction	ΔG^o (J)	Reference
$CaO_{(s)} + [S]_{Fe} = CaS_{(s)} + [O]_{Fe}$	104,700 - 25.8T	Elliott et al., 1960
	108,950 - 29.3T	Kubaschewski et al., 1979
	109,400 - 31.3T	Kay et al., 1986
	114,000 - 32.2T	Inoue et al., 1994
	114,300 - 32.5T	Suito et al., 1996

The free energy temperature dependence for the lime slag desulphurization reaction is illustrated in Figure 4-1. As seen, the values of Kay & Subramanian (1986) and Elliott & Gleiser (1960) are significantly different from those of Kubaschewski et al. (1967), Inoue et al. (1994), and Suito et al. (1996). The thermodynamic data of Kubaschewski et al. (1967) is used for the present research.

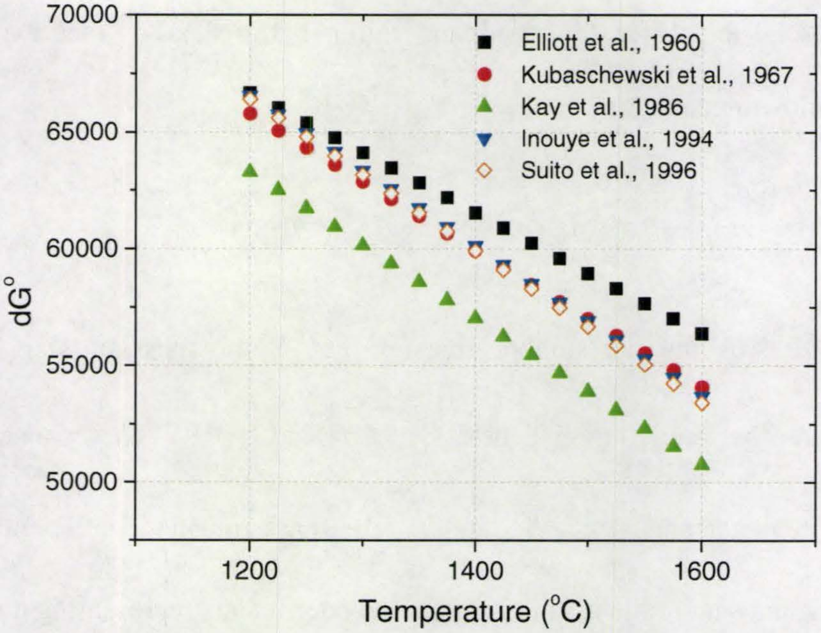

Figure 4-1: The free energy temperature dependence of $[S]+(CaO)=[O]+(CaS)$.

4.2.6. Kinetics of Desulphurization

Among the first studies on the rate of sulphur transfer were a series of papers by Chang & Goldman (1948), Derge et al. (1950), and Goldman et al. (1954). These kinetic studies focused on quantifying the effects of changing reaction conditions (i.e. slag composition, addition of deoxidants to the metal, and addition of reducible oxides to the slag) on sulphur transfer, and provided a good approach for understanding its reaction mechanism. Chang & Goldman (1948), investigating the transfer of sulphur from carbon saturated iron to $CaO\text{-}Al_2O_3\text{-}SiO_2$ slags, interpreted their data by assuming that the rate of transfer of sulphur from metal to slag is proportional to the concentration of sulphur in the metal phase and that from slag to metal is proportional to the concentration of sulphur in the slag phase. The net transfer of sulphur from metal to slag was then expressed using the following equation:

$$\frac{dW}{S\,dt}=\frac{d(wt\%S)}{dt}=AK_m[wt\%S]^m-AK_s(wt\%S)^n \tag{4-23}$$

where dW/dt was the net sulphur transfer rate, S the mass of slag, A the interfacial area between slag and metal, $[wt\%S]$ and $(wt\%S)$ the concentration of sulphur in metal and slag, K_m and K_S the mass transfer coefficients from metal to slag and slag to metal, and m and n the coefficients representing the order of the forward and reverse transfer reaction respectively. Assuming constant slag weight and metal sulphur concentration, experimental results were plotted as

$d(wt\%S)/dt$ versus $(wt\%S)$, and are presented here as Figure 4-2. The straight line fit obtained by Chang & Goldman (1946) confirms first order reaction kinetics with respect to sulphur in the metal. These findings were corroborated by subsequent investigators (Ramachandran et al., 1956; Ward & Salmon, 1960; Kim, 1978).

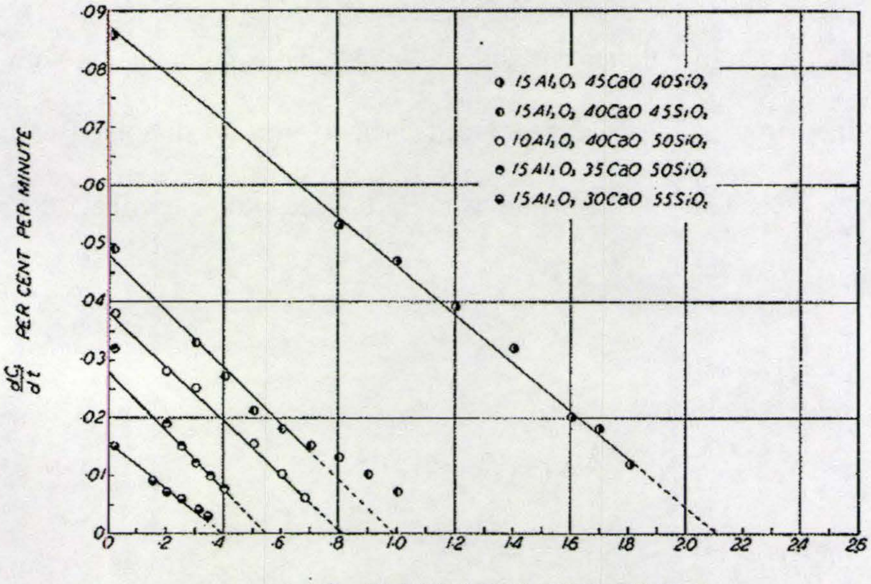

Figure 4-2: dC_S/dt versus $(wt\%S)$ plots for five slags at 1,540°C. (Chang & Goldman, 1948)

Chang & Goldman (1948), however, were careful to note that although sulphur transfer from metal to slag and slag to metal follows first order kinetics, it does not necessarily imply that it proceeds uni-molecularly. This statement resulted from their having observed an increase in the slag iron content during desulphurization in the early stages of their experiments.

Following the work of Chang & Goldman (1948), Derge et al. (1950) demonstrated that sulphur and iron transfer exceeded final equilibrium concentrations during the initial stages of reaction when sulphur transfer proceeded rapidly, and decreased in the later stages when sulphur transfer had slowed down. In view of these observations, Derge et al. (1950) reasoned that sulphur and iron enter the slag from metal together as some iron-sulphur compound, whereby sulphur is stabilized in slag by its combination with calcium and formed iron oxide is later reduced back to iron by dissolved carbon. The following reaction mechanism was proposed to describe the overall desulphurization process:

$$[FeS]=(FeS) \tag{4-24}$$

$$(FeS)+(CaO)=(CaS)+(FeO) \tag{4-25}$$

$$(FeO)+[C]=[Fe]+\{CO\} \tag{4-26}$$

To provide quantitative evidence of iron oxide reduction in slag, Derge et al. (1950) measured the rate of carbon monoxide evolution during sulphur transfer. While carbon monoxide evolution was observed to increase with temperature, discrepancies and unsatisfactory material balances for carbon monoxide evolution were reported. This problem was overcome by Ramachandran, King, & Grant (1956).

Goldman et al. (1954) evaluated the effectiveness of individual elements on the mechanism of sulphur transfer proposed by Derge et al. (1950). Figure 4-3 summarizes the results for all elements found showing a positive effect on the rate of sulphur transfer. Comparison was made based on the relative influence of rate constants with initial concentration of alloying element. As shown, carbon, silicon, manganese, and aluminum all increased the rate of sulphur transfer from iron to carbon-saturated slag with increasing effectiveness in the order provided. Copper, nickel, and phosphorous had no observable influence on the rate. These results were later confirmed by numerous investigators (Turkdogan et al., 1955; Ramachandran, King, & Grant, 1956; Deo & Grieveson, 1986).

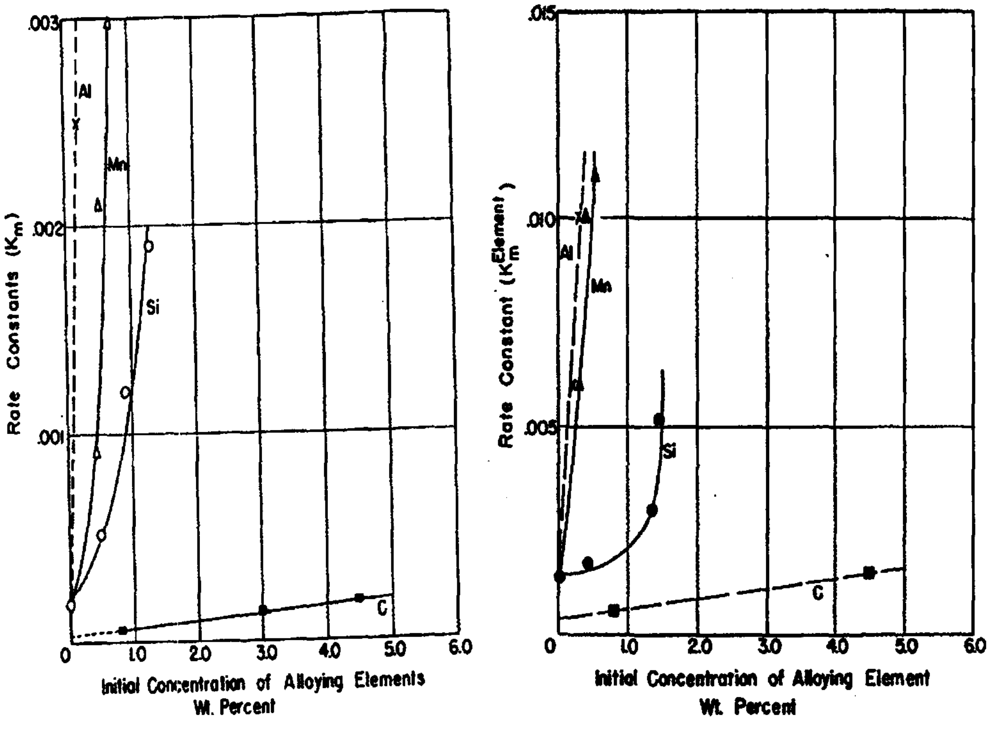

Figure 4-3: Comparison of the effect of alloying elements on rate constants for sulphur transfer with: (left) acid slags, and (right) basic slags. (Goldman et al., 1954)

On the basis of their findings, Goldman et al. (1954) suggested that not only does manganese replace iron as the principal carrier of sulphur across the slag-metal interface in an alloyed system, but that it expedites desulphurization. The observed increase in desulphurization by manganese occurred despite manganese having a negative effect on the activity coefficient of sulphur in the melt. In contrast to manganese, silicon and aluminum were suspected as supplanting carbon in deoxidizing the melt. The following modified three-stage mechanism was proposed:

$$[MS] = (MS) \tag{4-27}$$

$$(MS) + (CaO) = (CaS) + (MO) \tag{4-28}$$

$$(MO) + [R] = [M] + (RO) \tag{4-29}$$

where R = C, Si, Al, Mn and M = Fe, Mn, Si

Turkdogan et al. (1955) explained the ability of deoxidants to increase the rate of desulphurization in carbon-saturated iron using the concept of a sluggish carbon-oxygen reaction. The influence of aluminum, manganese and silicon on the rate of sulphur removal by a calcium-aluminate slag at 1,505°C is shown as Figure 4-4 (Turkdogan et al., 1955). As a result of their work, Turkdogan et al. (1955) proposed that the first stage of desulphurization involved the ionization of iron and sulphur according to:

$$[Fe] + [S] = (Fe) + (S) \tag{4-30}$$

Alloy additions were found to participate by replacing dissolved iron in the above reaction. Ionic charges were omitted in the analysis due to the stated uncertainty of the degree of ionization of solutes in slag (Turkdogan, Hancock, & Pearson, 1955). The following consecutive step involving iron or added deoxidants was assumed to occur in slags containing suspended carbon:

$$(Fe)+(O)+(C)=[Fe]+\{CO\} \qquad (4\text{-}31)$$

If carbon were absent from slag, then oxygen was assumed to dissolve in iron via:

$$(Fe)+(O)=[Fe]+[O] \qquad (4\text{-}32)$$

On the basis of the experimental evidence that deoxidizers increase the rate of desulphurization, Turkdogan et al. (1955) concluded that carbon monoxide evolution was the rate limiting step during metal-slag sulphur transfer. This conclusion was later supported by the classical electrochemical work of Ramachandran, King, & Grant (1956).

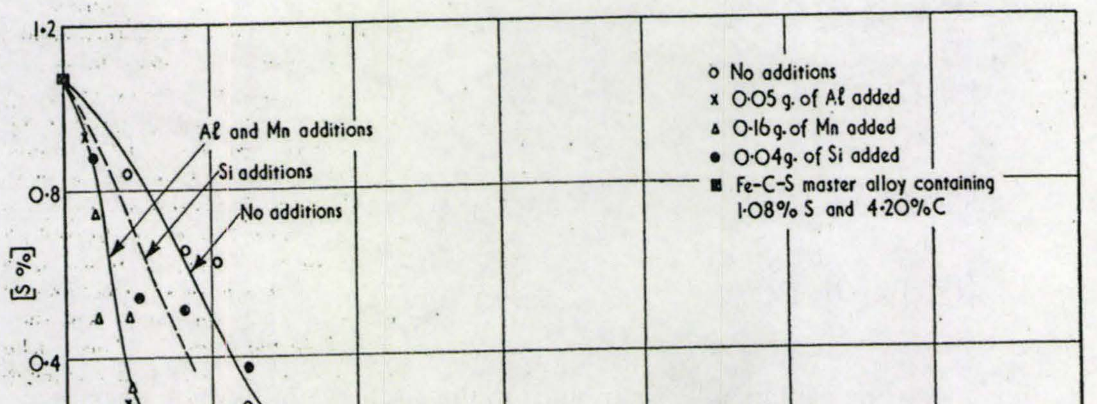

Figure 4-4: Rate of desulphurization of carbon-saturated iron by a calcium aluminate slag at 1,505°C. (Turkdogan et al., 1955)

The electrochemical reaction mechanism was established by Ramachandran, King, & Grant (1956) by performing experiments measuring both the simultaneous rate of transfer of elements and the evolution of carbon monoxide gas during desulphurization. Their work showed that sulphur transfer could be explained by the electrochemical theory, with slag-metal reactions being considered as redox reactions. Sulphur transfer from the metal phase to the slag phase was considered a cathodic reaction:

$$[S]+2e^{-}=\left(S^{2-}\right) \tag{4-33}$$

To preserve electroneutrality some or all of the following anodic reactions were assumed to occur simultaneously to sulphur transfer:

$$[Fe]=\left(Fe^{2+}\right)+2e^{-} \tag{4-34}$$

$$[Si]=\left(Si^{4+}\right)+4e^{-} \tag{4-35}$$

$$[Al]=\left(Al^{3+}\right)+3e^{-} \tag{4-36}$$

$$\left(O^{2-}\right)=[O]+2e^{-} \tag{4-37}$$

Carbon monoxide evolution was attributed to the discharge of oxygen ions at the slag-metal interface according to the reaction:

$$[C]+\left(O^{2-}\right)=\{CO\}+2e^{-} \tag{4-38}$$

Preservation of electroneutrality demands that the transfer rate of electronegative elements (sulphur) be equivalent to the sum of the transfer rate of electropositive elements (silicon, aluminum, iron, and / or carbon monoxide evolution). This was expressed by Ramachandran et al. (1956) as follows:

$$2\dot{n}_S = 2\dot{n}_{Fe} + 4\dot{n}_{Si} + 3\dot{n}_{Al} + 2\dot{n}_{CO} \qquad (4\text{-}39)$$

where n_S, n_{Si}, n_{Al}, n_{Fe}, n_{CO} are the rate of transfer of reacted species in mol per sec. Selected results from the work of Ramachandran et al. (1956) are presented as Figure 4-5.

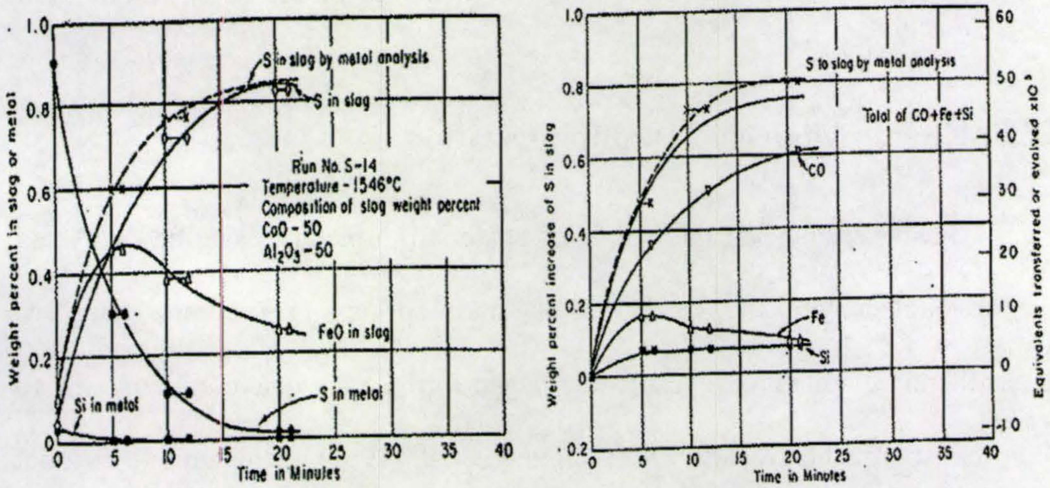

Figure 4-5: Increase in sulphur in slag, chemical equivalents of S, Fe, Si transferred to the slag or the number of equivalents of CO evolved. (Ramachandran et al., 1956)

From the observed results of sulphur transfer experiments under varying experimental conditions such as sulphur content, slag / melt composition, and melt geometry, Kim (1978) corroborated the work of Ramachandran et al. (1956) by finding that desulphurization was controlled by an electrochemical reaction. Kim (1978) listed the following reasons to explain why the molecular reaction mechanism suggested by Derge et al. (1950) lost ground to the more fundamental explanation based on electro-chemical theory:

1. It is inconsistent with the ionic theory of slags and such molecular reactions cannot explain the phenomena of the uphill sulphur transfer from a lower concentration of sulphur to a higher sulphur concentration by counter flow of oxygen, which was experimentally demonstrated to occur (Turkdogan & Grieveson, 1962)
2. The molecular reaction mechanism is also unable to explain the effect of applied current on the desulphurization kinetics (Ward & Salmon, 1963)
3. A mass balance for carbon monoxide evolution and other transferred elements in slag and metal cannot be achieved on the basis of molecular reactions.

4.2.7. Kinetic Models of Desulphurization

Having established that sulphur transfer from metal to slag or vice versa is: (i) coupled with the oxidation of other species in the melt, and (ii) electrochemical in nature, investigators began formulating quantitative models to interpret experimental results. De Hemptinne et al. (1961) attempted to develop a quantitative relationship to describe the work of Ramachandran et al. (1956). The theory was based on the measured rate of evolved carbon monoxide, which was assumed to occur as an interfacial reaction. Lu (1971), in his paper on the applications of irreversible thermodynamics to slag-metal reactions, discussed the simplifications and debatable assumptions by De Hemptinne et al. (1961) and derived an alternative formulation assuming that the rate of interfacial reactions is determined by electrical potential difference across the interface. The developed model has, however, been limited in application due to the complexity in determining the required phenomenological coefficients.

In contrast to chemical reaction control, numerous researchers (Asai, Kawachi, & Muchi, 1983; Deng & Oeters, 1990; Deo & Grieveson, 1986; Kawai, Shinozaki, & Mori, 1982; Ward & Salmon, 1963) have demonstrated that at elevated steelmaking temperatures metallurgical reaction rates are controlled by mass transfer. On this basis, and assuming chemical equilibrium at the interface, kinetic models taking coupled slag-metal reactions into account have been developed by Kawai and Mori (1982) and Robertson et al. (1984). While both of these kinetic models have reportedly been used in solving simultaneous dephosphorization and desulphurization reactions, the Robertson model has found greater industrial applications (Kitamura et al., 1991; Swamny, 1996; Monaghan et al., 1998). Further, the model was found successful (Robertson, Deo, & Ohguchi, 1984) in describing the experimental results of Ramachandran et al. (1956), and Kim (1978).

The mixed mass transfer control model of Robertson et al. (1984) may be understood by considering the following generalized coupled reactions occurring at the slag-metal interface:

$$[M]+\sigma[O]=M^{2\sigma+}+\sigma O^{2-}=MO_\sigma \tag{4-40}$$

and

$$[M]+\sigma[S]=M^{2\sigma+}+\sigma S^{2-}=MS_\sigma \tag{4-41}$$

where σ is a stoichiometric coefficient, and $[M]$ is any number of metallic components including Fe, Mn, Al, Si, and Ca. Bulk slag and metal are considered thoroughly mixed such that no concentration gradients exist except in the boundary layer. Sulphur is transferred from the bulk of the metal to the interface and then into the slag as sulphide ions. Oxide ions transfer counter to sulphide ions and positive $M^{2\sigma+}$ ions may transfer in either direction. The actual driving forces used are molar concentration differences for the oxides and sulphides between the interface and the bulk. As demonstrated by Robertson et al. (1984), this procedure implies the ionic nature of the slag and maintains electroneutrality by associating the $M^{2\sigma+}$ ions according to stoichiometry and to the chemical potentials of the various oxides and sulphides.

Recently, several researchers (Andersson et al., 2000; Subagyo et al, 2002; Peter et al., 2005) have attempted to develop kinetic-based models for assessing the state of a LMF. The kinetic model of Conejo et al. (2007) is identical to the original work of Robertson et al. (1984) and will not be reviewed here. Andersson and coworkers (2000) used a fundamental approach in developing a model where slag-metal reactions were coupled with heat and fluid-flow equations. While a short heuristic comparison by the authors revealed that plant results agreed in general terms with calculated results, the prohibitively long computation times of the model (approximately 140 hrs) deadens its potential for online control.

Peter et al. (2002) undertook extensive sampling trials at Nucor Yamato and Nucor Arkansas, and developed a process model in METSIM using what the authors describe as a multitude of modules and streams to simulate different heats. METSIM is a heat and mass balance software package capable of performing dynamic simulations for a variety of metallurgical processes. Figure 4-6 schematically illustrates the developed model. Peter et al. (2002) showed that METSIM model predictions were in close agreement with experimental data. It should be noted that these results were iteratively obtained by manual adjustment of process streams and on some occasions artificial reagent additions (i.e. Fe_2O_3). Despite the good agreement and its potential value as an off-line tool, it is clear that the model of Peter et al. (2005) is unsuitable for real-time control.

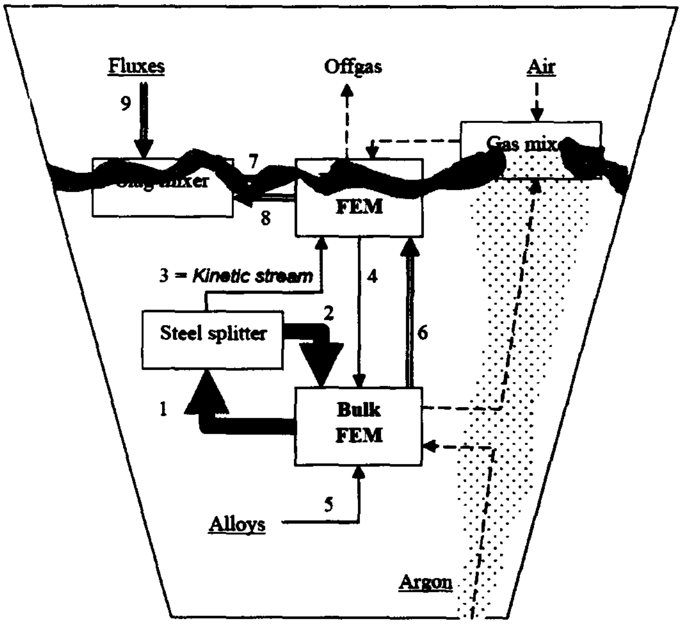

Figure 4-6: Schematic illustration of developed METSIM model used for simulating steel treatment in the ladle (Peter et al., 2002).

Subagyo & Brooks (2002) developed an inferential model to predict desulphurization for changing process conditions within a ladle. Their model was derived using first order rate equations for sulphur and oxygen in steel and based on the assumption that only the FeO content in slag was responsible for determining the equilibrium oxygen content. Perfect mixing was assumed in the slag phase, and empirical metal phase mass transfer coefficient correlations were taken from the literature (Asai et al., 1983; Ishida et al., 1981). In their paper, Subagyo & Brooks (2002) tested the validity of the model by comparing predicted results with plant data from ArcelorMittal Dofasco. Figures 4-7 and 4-8 summarize the results from their work.

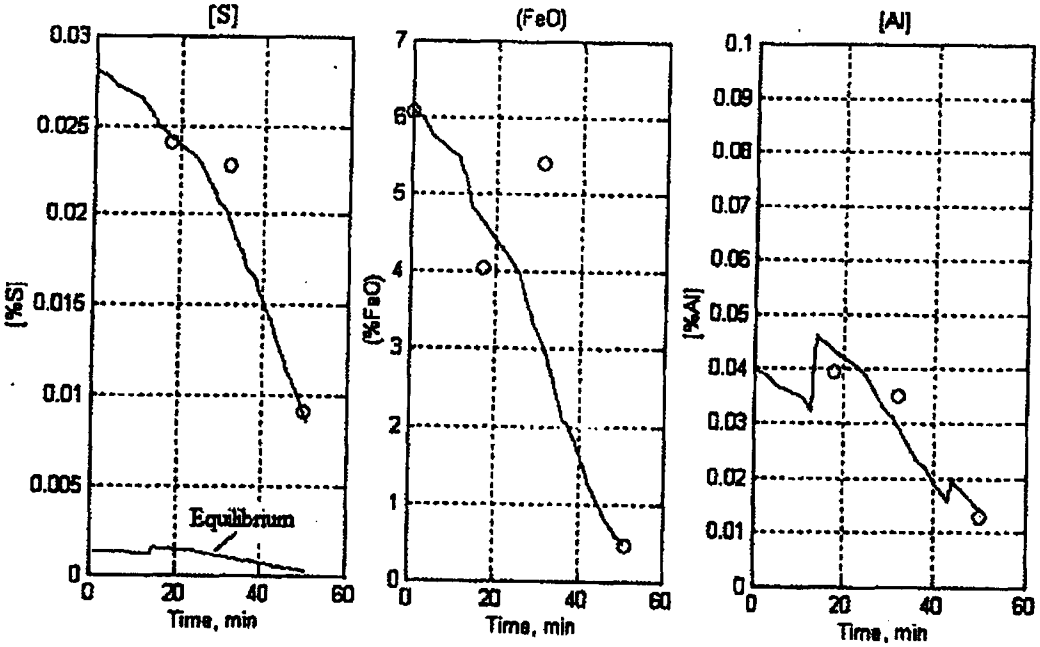

Figure 4-7: Comparison of Measured and Predicted Values of [S], (FeO), and [Al]. (Subagyo et al., 2002)

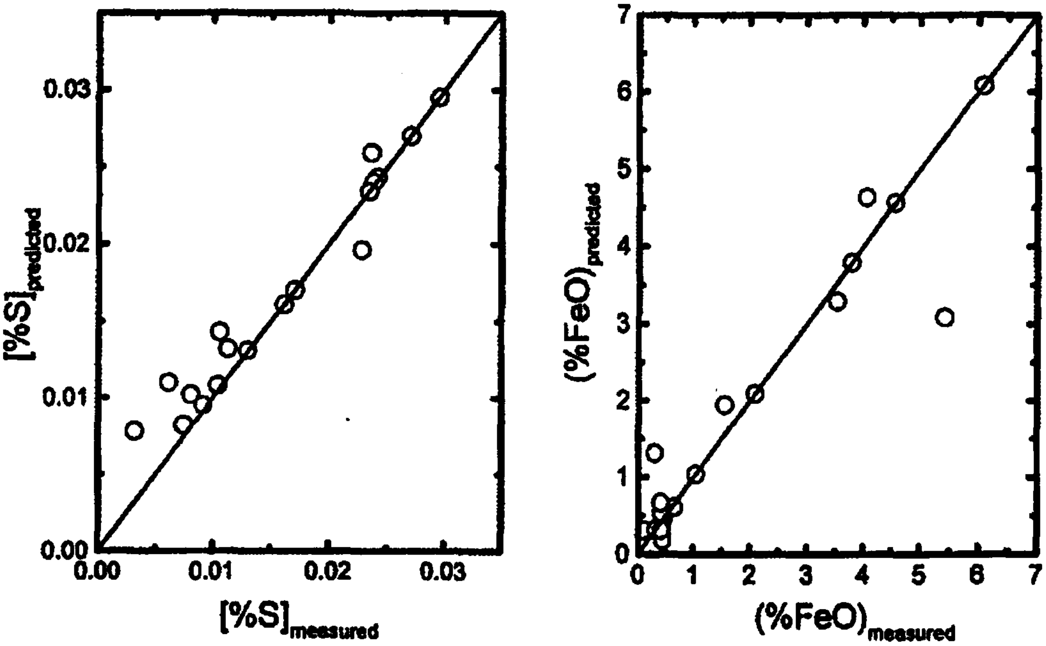

Figure 4-8: Comparison of Measured and Predicted Values of [S] and (FeO) (6 heats). (Subagyo et al., 2002)

Subagyo & Brooks (2002) concluded that the good agreement seen in Figure 4-8 justifies the use of their model as an online control tool. The reader should be made aware, however, that a detailed review of Figure 4-8 and its corresponding heat data by the present author has revealed that one-third of the data presented by Subagyo & Brooks (2002) were not predicted by the model at all but rather used as initialization inputs. As these initialization points appear on Figure 4-8 showing perfect agreement between measured and predicted values of [S] and (FeO), they misleadingly improve the accuracy of the developed model. Removal of these data points therefore leaves the validity of the Subagyo & Brooks (2002) model in question. These problems aside, the Subagyo & Brooks (2002) model is computationally efficient and if corrected would have considerable value as an online control tool.

4.3. Apparatus and Procedure

4.3.1. Process Description

ArcelorMittal Dofasco is the only integrated steel plant in Canada producing part of its steel by the electric arc furnace (EAF) process. Its twin shell EAF facility was commissioned in September 1996 and over the last 10 years has evolved into a world class facility, producing 1.3 MT of commercial and automotive grade steels annually. At the time the shop was built, the furnace and transformer combination were one of the largest and highest productivity installations in North America. Figure 4-9 and Table 4-2 summarize the melt shop layout and relevant furnace details. A unique design feature of the furnace included the future possibility of operating with up to 30% hot metal charge.

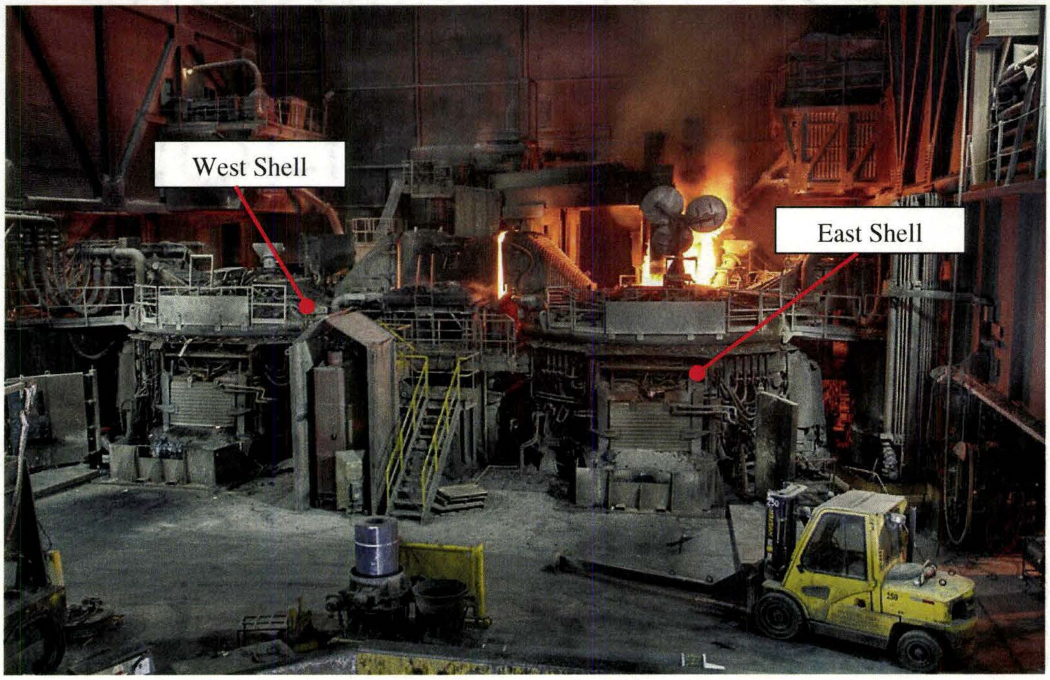

Figure 4-9: ArcelorMittal Dofasco EAF melt shop layout

Table 4-2: Relevant Process Design Variable for Fuchs Twin Shell EAF

Parameter	Description
Transformer	120 / 134 MVA AC
Electrode Diameter	610 mm
Burner Configuration	6 x 4 MW Phoenix Sidewall Burners 1 x 7 MW Phoenix Slag Door Burner
Oxygen Injection	2 x 2500 m^3 / h Phoenix OmniJet
Carbon Injection	2 for Slag Foaming with Pet Coke
Argon Bottom Stirring	3 x DPP Plugs (150 L/min/plug max flow)
Shell Diameter	7.3 m
Tapping Configuration	Round Bottom Tapping
Avg. Tap-to-Tap Time	60 min
Avg. Power-On Time	45 min
Avg. Electrical Power	88 MW
Avg. Electrical Energy Consumption	400 kWh / t

Steel is tapped from the EAF into ladles and refined using a twin station (two roofs), swiveling electrode gantry, Fuchs ladle metallurgy furnace. Selected fluxes, including lime, calcium aluminate, and deoxidants are added during the tap and combine with slag carryover to constitute the slag phase. At the LMF, alloying elements are added and the melt heated in order to satisfy end grade specifications. Argon stirring within the melt is accomplished via two eccentrically positioned porous plugs at the bottom of the ladle. Table 4-3 summarizes the relevant process details, while an illustration of the LMF station at ArcelorMittal Dofasco is presented as Figure 4-10.

Table 4-3: Relevant Process Design Variables for Fuchs Twin Station LMF

Parameter	Description
Transformer	20 / 24 MVA AC
Electrode Diameter	406 mm
Argon Bottom Porous Plugs	2 (backup soft-stir top lance)
Heat Size	165t
Ladle Dimensions	3.8 m OD / 3.2m ID x 3.5m Height
Avg. Tap-to-Tap Time	80 min
Avg. Refining Time	50 min
Avg. Power-On Time	20 min
Avg. Electrical Energy Consumption	500 kWh / heat

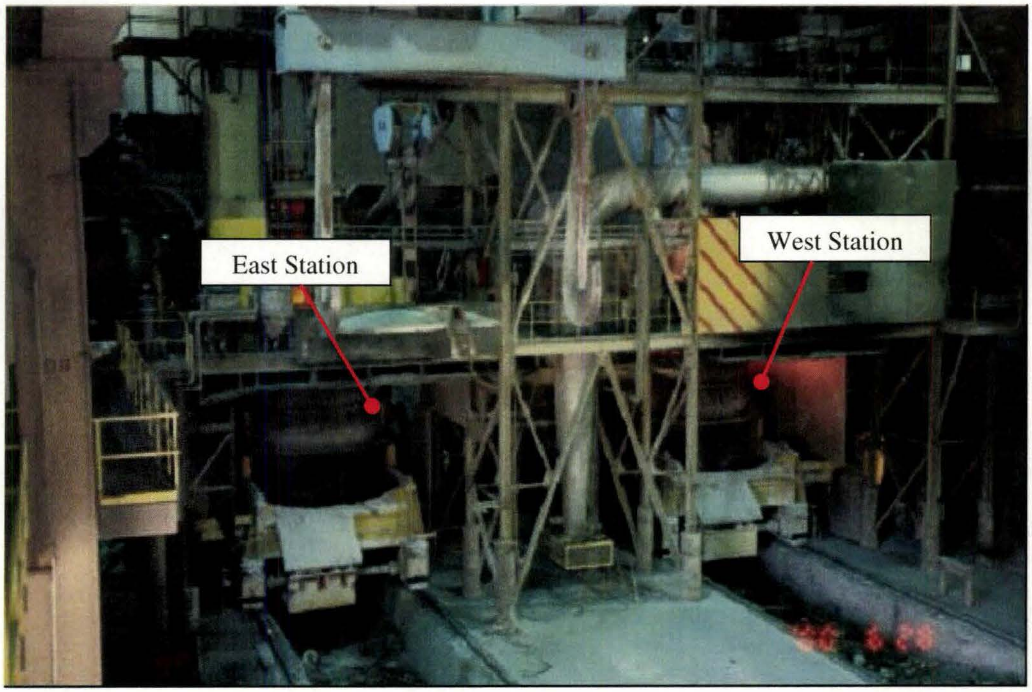

Figure 4-10: ArcelorMittal Dofasco LMF station layout

4.3.2. Slag Carryover Sampling / Estimation Procedure

Pressures to reduce LMF operational variability and to improve steel quality have resulted in slag carryover control during EAF tapping becoming an increasingly important process control parameter. Benefits of a controlled slag carryover process have been well documented and include (da Silva et al., 1993):

- Improved deoxidation efficiency
- Optimal conditions for desulphurization
- Reduced refractory wear
- Cleaner steels

The challenge in an industrial operation is that limited information on slag carryover variability is available on a heat-to-heat basis and thereby prevents the implementation of optimum slag conditioning practices. Although methods to minimize slag carryover have been developed and implemented (Fruehan 1998), the challenge in this research work was to develop a control method that would both maximize ArcelorMittal Dofasco's existing information systems and fit the obvious time constraints of this project. A further goal was to reduce the reliance on operator skill and manual procedures in estimating slag carryover by developing an online system that would increase process stability.

The experimental procedure for estimating slag and steel mass at the start of each heat involved using slag depth probes in combination with a developed slag density model. After tapping from the EAF, steel was transferred by ladle car to the ladle metallurgy furnace. Bath oxygen activity and temperature were measured by Celox probe (see section 4.3.4.3) and a visual examination of the slag surface was performed. If the melt temperature was found close to liquidus, and / or if large slag skulls were observed on the bath surface, then electrical heating was commenced. Once a suitably high bath temperature and fluid slag had been obtained, argon flowrate to the bottom porous plugs was reduced, and both a slag sample and slag thickness measurement was taken.

Two different methods were used for measuring slag depth. The first involved using the Delta Dist L sensor from Heraeus Electro-Nite (Philadelphia, PA), while the second was by manual dip-test using a 3.2cm OD steel bar. Dip-test measurements were performed at the ladle sanding station located at the north end of the LMF station. This location was selected for the following reasons: i) the steel bar was able to be kept vertical during measurement, and ii) it ensured that each measurement was taken from the identical sample location.

4.3.3. Experimental Sampling Procedure

Figure 4-11 summarizes the sampling methodology used for the industrial trials. As seen, after deoxidation, simultaneous metal and slag samples as well as temperature and dissolved oxygen measurements were systematically taken before and after any process change (i.e. argon stirring and heating). Metal samples were taken by an automatic sampler using consumable dual 2-in-1 temperature and sample probes from Heraeus Electro-Nite (Philadelphia, PA), while slag samples were taken manually using a slag stick. Bath oxygen activity was measured using automatic immersion probes (Celox, Heraeus Electro-Nite). In total, 41 heats of different grades and processing sequences were sampled for the study.

Also shown in Figure 4-11 is the precise location and combination of reagent additions during the refining cycle. Standard operating practice at ArcelorMittal Dofasco is to add alloys under conditions of high argon flow, thereby ensuring that slag cover has been displaced to the periphery of the ladle and that additions are made directly into the 'eye', where liquid metal is exposed to the atmosphere.

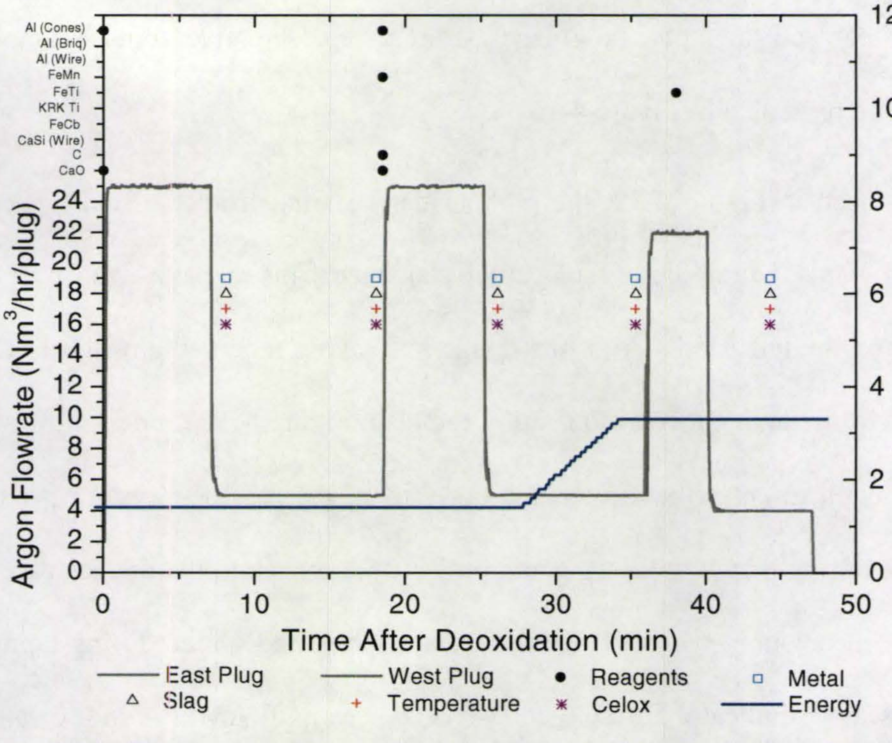

Figure 4-11: Representative study plot summarizing stirring, heating and sampling procedure (Heat 40). The points represent the timing of reagent additions and sampling. Cumulative electrical heating energy is plotted.

4.3.4. Measurement Devices

4.3.4.1. AMEPA Slag Detection System

The AMEPA TDS (AMEPA, Wuerselen-Aachen, Germany) slag detection system was installed on the EAF stream at ArcelorMittal Dofasco in November 2006. The system is comprised of an infrared vision-based sensor enclosed within an air-cooled, high-grade steel housing. It provides real-time identification and tracking during EAF tapping. Compressed air is used to protect and keep the lens dust free during tapping, while an automatic shutter protects the lens between taps. Recorded images are analyzed using image processing techniques contained within the AMEPA system as means for distinguishing between steel and slag phases. Images from a representative furnace tapping sequence are presented as Figure 4-12.

As seen in Figure 4-12, the molten metal stream from the EAF appears slag free towards the middle of the heat tap sequence. This is made clear from the bar graph on the left hand side of the image not having recorded any slag within the viewable stream area. Near the end of the heat, Figure 4-12 (upper), however, slag has begun to enter the tap stream. As shown, the AMEPA system isolates slag pixels during image processing and projects them back to the image space as a solid green colour. An AMEPA index value is reported online during tapping and serves as an indicator for slag carryover, where high AMEPA index values indicate high slag pixel counts and consequently high slag carryover volume. A

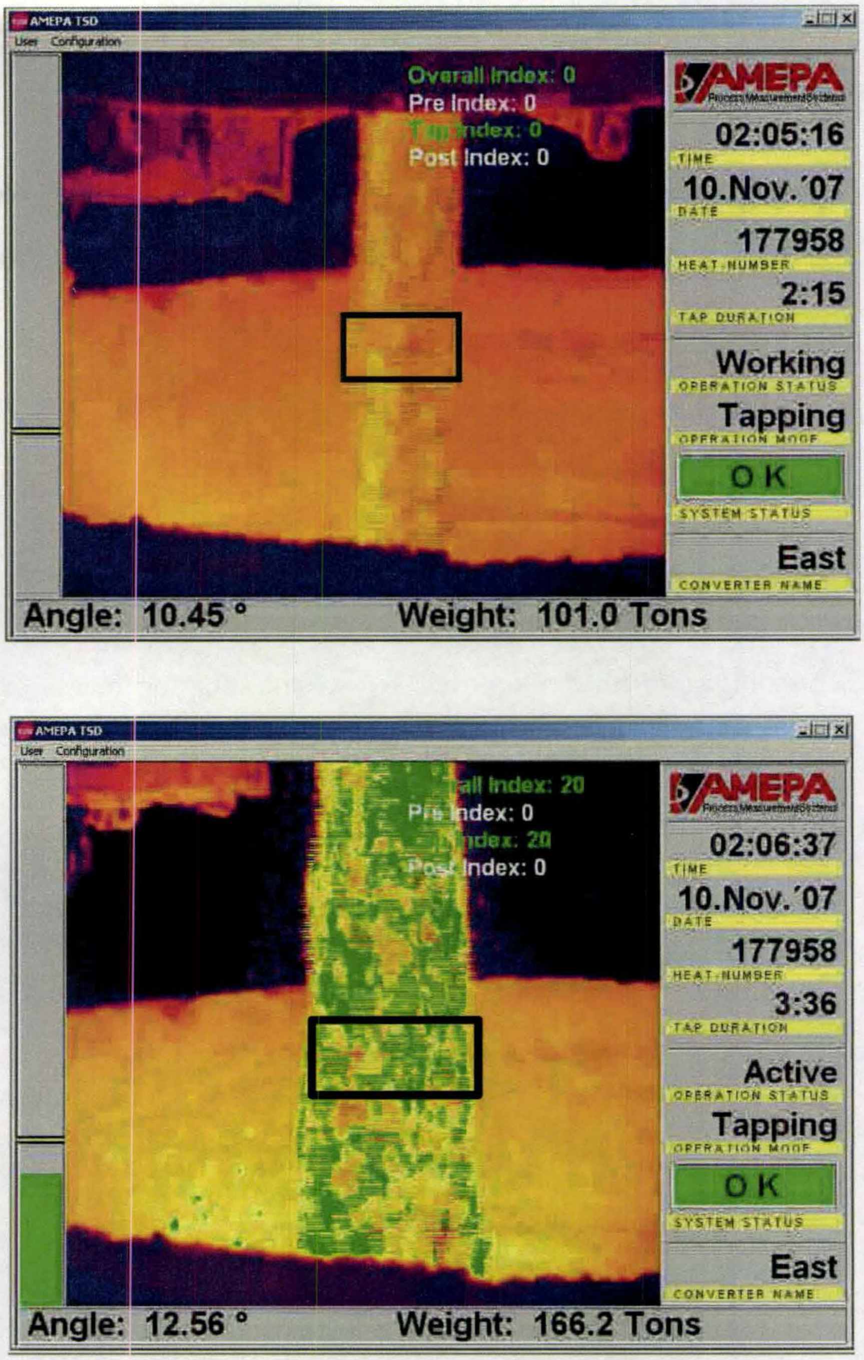

Overall Index: 0
Pre Index: 0
Tap Index: 0
Post Index: 0

02:05:16
TIME
10.Nov.'07
DATE
177958
HEAT NUMBER
2:15
TAP DURATION
Working
OPERATION STATUS
Tapping
OPERATION MODE
OK
SYSTEM STATUS
East
CONVERTER NAME
Angle: 10.45 ° Weight: 101.0 Tons

all Index: 20
Pre Index: 0
ndex: 20
Post Index: 0

02:06:37
TIME
10.Nov.'07
DATE
177958
HEAT NUMBER
3:36
TAP DURATION
Active
OPERATION STATUS
Tapping
OPERATION MODE
OK
SYSTEM STATUS
East
CONVERTER NAME
Angle: 12.56 ° Weight: 166.2 Tons

Figure 4-12: Sample AMEPA images captured during EAF tapping. (Upper) Middle of tap; (Lower) End of tap.

key feature of the AMEPA TDS (AMEPA, Wuerselen-Aachen, Germany) system includes an audible alarm that sounds once a user defined slag threshold limit has been exceeded. At the onset of the alarm, a signal is transmitted to a PLC, and the furnace is automatically returned to the upright position.

Good heel management practices at the EAF have shown that desired target ladle tap weight may be achieved in advance to any slag detection by the AMEPA system. A PLC is used to reset furnace position under such conditions.

4.3.4.2. Slag Depth Measurement

The traditional method employed by steelmakers for measuring slag thickness is by dip-test. The practice involves submerging a steel rod into the melt for a given residence time, thereby permitting the bar to burn-off at the slag-metal interface. Upon removing the bar from the melt, slag thickness is determined by measuring the length of adhered slag on the steel rod. As reported in the literature (Meszaros et al., 2000), dip-test accuracy is questionable for several reasons, namely:

- Operator variability (ie: immersion time, holding position)
- Interpretation of slag-steel burn-off position
- Slag splashing within the ladle
- Crusted top slag layer

Recognizing the need for accurate slag thickness measurement, Heraeus Electro-Nite (Philadelphia, PA) has recently developed a consumable slag thickness and freeboard measurement sensor. The Delta Dist L sensor comes attached to a tubular cardboard sleeve enabling its easy use on automatic immersion samplers. Figure 4-13 presents schematics illustrating the two-step slag measurement technique. In the first step, slag level is detected by a small steel contact strip fitted at the nose of the probe. Upon further immersion of the sensor, a small coil contained within the probe identifies the slag-steel interface by recording a second and characteristically different current. Slag depth thickness is then calculated by knowing the time interval between the two recorded current signals. A key assumption in the determination of slag depth is the constant immersion speed of the automatic lance. Heraeus Electro-Nite (Philadelphia, PA) reports the accuracy of the Delta Dist L sensor to be within 1.27 to 2.54cm (Heraeus Electro-Nite, 2008).

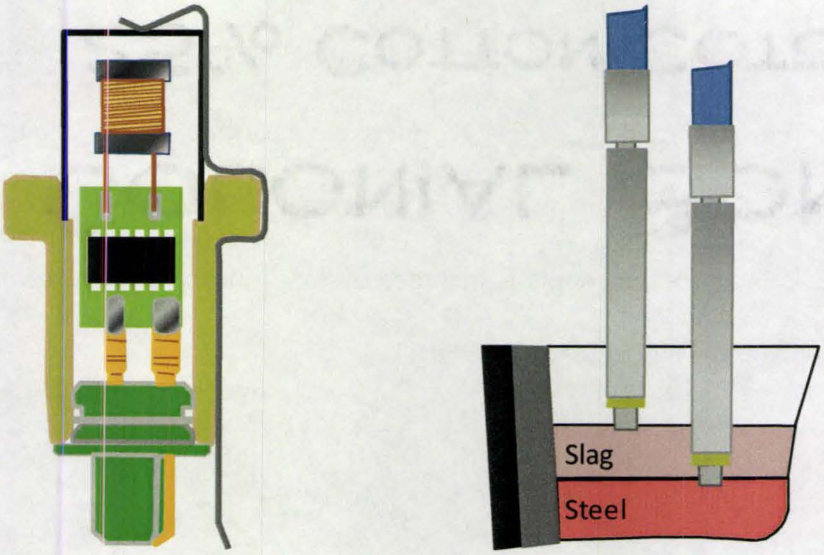

Figure 4-13: (Left) Schematic diagram of the Delta Dist L sensor; (Right) Illustration summarizing the two stages of sensor submersion. (Reproduced from Heraeus Electro-Nite, 2008)

4.3.4.3. Dissolved Oxygen Measurement

Oxygen potential is well established as an important control parameter in the refining of steel. Since the original study of solid state electrochemical cells by Kiukkola & Wagner (1957), who successfully applied a solid ZrO_2-CaO electrolyte for measuring the dissolved oxygen concentration of molten iron, a significant amount of research work has been undertaken to develop oxygen sensors capable of online measurement of oxygen activity in molten metal. Pratt (1990) provides a good review on dissolved oxygen sensors, listing over a hundred systems that have currently been developed.

Celox oxygen probes from Heraeus Electro-Nite (Philadelphia, PA) were used in this study to measure the dissolved oxygen content of steel. The single-use probes are comprised of an electrochemical oxygen cell consisting of a solid zirconia (ZrO_2) electrolyte partially stabilized with magnesia (MgO), and a chromium / chromic oxide (Cr / Cr_2O_3) reference electrode. A paperboard tube is also provided for insulation protection when the probe is immersed into the molten steel, and a thermocouple is included in the probe to measure temperature. The electrochemical cell is represented as:

$$Mo_{(S)}\left|\left(Cr + Cr_2O_3\right)_{(S)}\right|ZrO_2 + MgO\left|\left[O\right] - Fe_{(l)}\right|Mo_{(S)} \tag{4-42}$$

The electromotive force (EMF) of the cell is given by the Nernst equation:

$$E = \frac{RT}{4F} \ln \left(\frac{P_{O_2}^{''}}{P_{O_2}^{'}} \right) \tag{4-43}$$

where E is the cell voltage, R the ideal gas constant, T the absolute temperature, F the Faraday constant, $P_{O_2}^{''}$ and $P_{O_2}^{'}$ the respective oxygen partial pressures at the interface between the electrolyte and the electrode material. As the oxygen potential of the reference electrode is only a fraction of the measured temperature, it can in theory be used in combination with equation 4-43 to determine the oxygen potential in the melt. In practice, however, several factors limit this direct calculation, namely:

- Electronic conduction in the $ZrO_2(MgO)$ electrolyte
- Polarization of the reference electrode ($Cr + Cr_2O_3$)

As a result of these limitations, empirical formulations are used to relate the dissolved oxygen activity to EMF and temperature readings (Heraeus Electro-Nite, 2007):

$$\log(h_O) = 1.36 + 0.0059\left[E + 0.54(T - 1550) + 0.0002E(T - 1550)\right] \tag{4-44}$$

where T is the temperature in degrees Celsius. A Multi-Lab Celox is used to display and store the Celox measurements.

4.3.4.4. Combination Temperature and Metal Sample Probe

The Heraeus Electro-Nite (Philadelphia, PA) 2-in-1 combination sensor integrates a QuicK-Spec® immersion probe to sample liquid steel, and a Positherm® ML thermocouple to measure temperature. A schematic drawing of the device is presented as Figure 4-14. The sampling device consists of two identical halves held together by a spring clip. An inlet pipe allows for molten steel to fill the hollow space between the two halves. After the measurement lance is withdrawn from the molten metal, the solidified sample is removed by breaking open the sampling components.

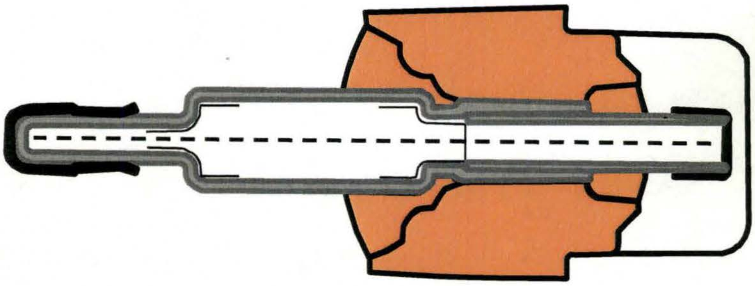

Figure 4-14: Schematic drawing of the molten metal sampling device. (Reproduced from Baerts, 1992)

4.3.4.5. Materials

All materials used in the study are commercially available and were provided by ArcelorMittal Dofasco. Bulk alloy additions to steel included aluminum, ferromanganese, ferrotitanium, ferrosilicon, ferroniobium, carbon, and calcium silicide. Aluminum was added either as cones, briquettes or cored wire. Calcium silicide was also added in the form of cored wire. Lime was the sole slag flux added subsequent to deoxidation, with its addition rate varying significantly from operator to operator.

Nominal compositions of reagents used within the study were taken from vendor supplied chemical specifications to ArcelorMittal Dofasco. Alloy recoveries were estimated from reviewing historical plant data at ArcelorMittal Dofasco.

4.3.5. Chemical Analysis

All chemical analyses were performed within the iron and steel laboratory at ArcelorMittal Dofasco. Analytical procedures and instrumentation units used were subject to the American Association for Laboratory Accreditation (A2LA) standards and were performed to international standard ISO/IEC 17025:2005.

4.3.5.1. Metal Analysis

Steel sample chemical composition was determined using an ARL 4460 Atomic Emission Spectrometer (AES). Dual thickness samples were prepared by grinding one side flat using either a Herzog dual belt system or milling machine before a sample manipulation system (SMS) automatically loaded it onto a high-voltage spark stand for analysis. Secondary checks were performed on carbon, sulphur and nitrogen samples using a Leco analyzer CS444 and CS44LS if AES analyses were believed high or if they exceeded end-point specifications.

The basic principle of AES is that a high energy spark is created across an argon-filled gap between an electrode and steel sample. The spark excites elements within the steel sample and creates an emission of radiation with wavelengths characteristic of the sample composition. The spectrum of emission lines is then separated into distinct elements where the measured intensity of each line is accurately converted to concentration. Reliability of the results is based on the accuracy of analyzer to reproduce the composition of available standards.

4.3.5.2. Slag Analysis

Slag samples were prepared for analysis by first manually crushing in a stainless steel mortar and pestle. A high strength magnet was then passed over the crushed sample to remove metallic iron, after which ten grams of the metallic-free slag and one gram of binder were weighed out in a crucible. The combined slag sample was then placed in a puck and ring pulverizer and milled for approximately four minutes. The ground sample was then pressed into a disc to form a clean, uniform and flat surface and analyzed using a Philips PW2400 Sequential X-Ray Spectrometer to determine its chemical composition.

X-ray fluorescence spectrometry is a commonly used instrumental means for detecting the elemental composition of steelmaking slags. The method relies on the sample material being irradiated with high-energy primary x-ray photons, which causes excited inner electrons to be ejected from the atom. Following the removal of an inner electron, an outer orbital electron falls to fill the vacant hole. The rearrangement of electrons is accompanied by a characteristic emission in energy which once sorted relates to the elemental composition of the sample.

Known standards are used to calibrate an X-ray spectrometer and to ensure its accuracy.

4.4. Mathematical Model

Accurate feedback data is beneficial to achieving control of a metallurgical process. In ladle metallurgy, knowledge of a heat's progress allows for advanced planning and the potential optimization of the operation. As real-time data is difficult to obtain in ladle metallurgy, metallurgical models may be used to provide estimates of sought variables. A well tuned model can provide information on important variables such as slag composition, metal composition, and temperature.

A coupled multi-component kinetic process model based on the Robertson model (1984) was developed for assessing the state of a ladle metallurgical furnace. While the Robertson model (1984) has previously been applied to simulate hot metal dephosphorization in a 350 metric tonne scale torpedo car at Yawata Works (Kitamura et al., 1991), the current research marks the first attempt at using the model for quantifying steel desulphurization in an industrial setting. As will be shown, the process model is capable of calculating the time dependent variation of key slag and metal components during ladle refining.

4.4.1. Model Formulation for Coupled Oxide Components

As previously stated, the mixed mass transfer control model of Robertson et al. (1984) may be understood by considering the following generalized interfacial slag-metal reaction:

$$M+\sigma O= MO_{\sigma} \tag{4-45}$$

For which the equilibrium constant is given as:

$$K_{MO_{\sigma}}=\frac{a_{MO_{\sigma}}}{h_M\left(h_O\right)^{\sigma}} \tag{4-46}$$

where $K_{MO_{\sigma}}$ is the equilibrium constant, σ the stoichiometric coefficient for oxygen, $a_{MO_{\sigma}}$ the activity of the oxide component, and h_O and h_M the respective Henrian activities for oxygen and selective metallic components in steel. While the original work of Robertson and co-workers (1984) treated sulphide species in a similar manner as equation 4-45, this study will use a simplified formulation. The primary reason for having to modify the Robertson model for sulphur transfer within this study is due to the Philips PW2400 sequential x-ray spectrometer within the ArcelorMittal Dofasco laboratory reporting sulphur in slag as a 'lumped' elemental amount instead of as a detailed spectrum of slag sulphide components.

The basic approach proposed by Robertson et al. (1984) involves first rearranging equation 4-46 for each slag-metal equilibrium reaction in terms of an expression for the interfacial oxide concentration as follows:

$$X^*_{MO_\sigma} = \frac{K_{MO_\sigma}\left(f_M X^*_M MM_M\right)\left(f_O X^*_O MM_O\right)^\sigma}{\gamma_{MO_\sigma}(0.5585)^{1+\sigma}} \tag{4-47}$$

where $X^*_{MO_\sigma}$ represents the interfacial oxide mole fraction in slag, X^*_M and X^*_O the interfacial metal and oxygen mole fractions in steel, f_M and f_O the Henrian activity coefficients of dilute components in metal, γ_{MO_σ} the Raoultian activity coefficient of oxide in slag, and MM_M and MM_O the molar mass of the metallic component and oxygen. Equation 4-47 may be simplified by combining the thermodynamic quantities as:

$$\Phi_{MO_\sigma} = \frac{K_{MO_\sigma} f_M MM_M\left(f_O MM_O\right)^\sigma}{\gamma_{MO_\sigma}(0.5585)^{1+\sigma}} \tag{4-48}$$

Figure 4-15 shows a schematic of the concentration profile at the slag-metal interface. This frame of reference was adopted for deriving the flux density equations and assumes mixed mass transport control.

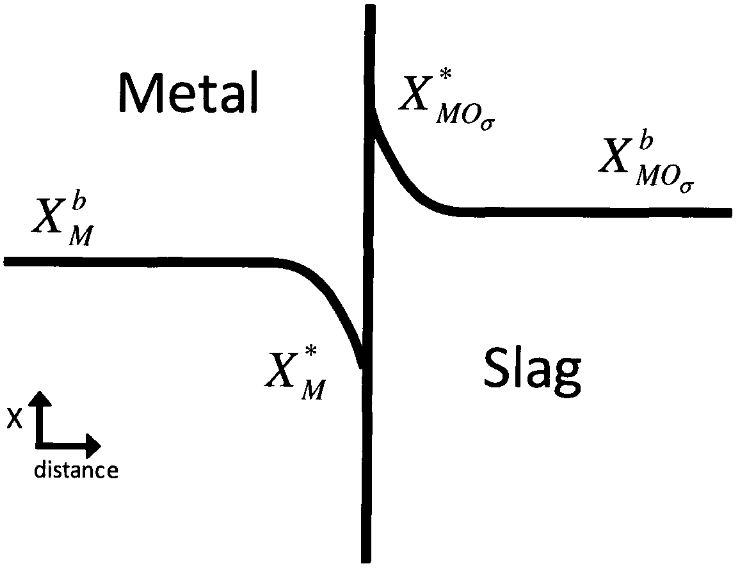

Figure 4-15: Schematic of concentration gradients at the interface for mixed transfer control.

Assuming conservation of mass, flux density equations for each interfacial slag-metal reaction may then be stated as:

$$k_m^M \, C_{Vm} \left(X_M^b - X_M^* \right) = k_{sl}^{MO_\sigma} \, C_{Vs} \left(X_{MO_\sigma}^* - X_{MO_\sigma}^b \right) \tag{4-49}$$

where k_m^M and k_{sl}^{MxOy} are the mass transfer coefficients in the metal and slag phases for the respective metal and oxide components, C_{Vm} and C_{Vs} represent the molar volumes of metal and slag, and X^b and X^* the bulk and interfacial mol fractions of metal and oxide components in either the slag and metal phases. Substitution of the interfacial oxide concentration into the respective flux density equation for each metallic component yields, upon rearrangement, an expression for the interfacial concentration of metallic components in terms of mass transfer coefficients and bulk metal and slag phase concentrations:

$$X_M^* = \left(\frac{X_M^b + k_M^* X_{MO\sigma}^b}{1 + k_M^* \Phi_{MO\sigma} X_O^*} \right) \tag{4-50}$$

where

$$k_M^* = \left(\frac{k_{sl}^{MO_\sigma} C_{Vs}}{k_m^M C_{Vm}} \right) \tag{4-51}$$

Exact solution of the interfacial slag and metal concentration at any instant in time requires coupling all slag-metal reactions using an overall oxygen mass balance equation:

$$k_m^O C_{Vm} \left(X_O^b - X_O^* \right) = \sum_{i=1}^{n} \sigma_i C_{Vs} k_{sl}^{MO_\sigma} \left(X_{MO_\sigma}^* - X_{MO_\sigma}^b \right) \tag{4-52}$$

Equation 4-52 expresses the fact that the total amount of oxygen change in the metal phase equals the total oxygen change in the slag phase. Substitution of the metallic and oxide interfacial concentration expressions into equation 4-52 yields a single non-linear equation containing only interfacial oxygen concentration as an unknown. A detailed derivation of the model is presented as Appendix C.

While the interfacial oxygen content is unable to be measured experimentally, Robertson et al. (1984) demonstrated that it may be determined numerically. For the purposes of this study, a numerical solver based on the Newton-Raphson method was developed for finding the root of the oxygen mass balance equation (i.e. the interfacial oxygen content). Once the oxygen concentration at the interface was determined, all other interfacial values were subsequently computed and composition trajectories were projected forward by numerical integration of first order differential equations having the form:

Metal Phase - $$-\frac{dX_M}{dt} = k_m^M\left(\frac{A}{V_m}\right)\left(X_M^b - X_M^*\right) \tag{4-53}$$

Slag Phase - $$\frac{dX_{MO_\sigma}}{dt} = k_{sl}^{M_xO_y}\left(\frac{A}{V_{sl}}\right)\left(X_{MO_\sigma}^* - X_{MO_\sigma}^b\right) \tag{4-54}$$

Table 4-4 summarizes the relevant thermodynamic data for the interfacial slag-metal reactions considered in the current study. On the basis of these reactions, the slag was assumed comprised of simple oxides FeO, MnO, CaO, MgO, TiO_2, SiO_2, and Al_2O_3.

Table 4-4: Thermodynamic data for slag-metal reactions

Reaction	ΔG^o (J)	log K	Reference
$Al_2O_3 = 2[Al] + 3[O]$	1,225,000 - 393.8T	$-63,980/T + 20.57$	*
$SiO_2 = [Si] + 2[O]$	576,440 - 218.2T	$-30,110/T + 11.40$	*
$TiO_2 = [Ti] + 2[O]$	681,350 - 228.5T	$-35,585/T + 11.93$	Taylor (1985)
$MnO = [Mn] + [O]$	284,900 - 127.6T	$-14,880/T + 6.67$	*
$FeO = [Fe] + [O]$	117,700 - 49.8T	$-6,150/T + 2.604$	*
$MgO = [Mg] + [O]$	90,000 - 81.9T	$-4,700/T - 4.28$	Itoh et al. (1997)
$CaO = [Ca] + [O]$	645,200 - 148.7T	$-33,700/T + 7.78$	Suito et al. (1996)

* The Japan Society for the Promotion of Science: The 19th Committee on Steelmaking (1988)

4.4.2. Model Formulation for Sulphur

When a reaction at the slag-metal interface is limited by diffusion, the rate equation can be algebraically stated by applying boundary layer theory. Adapting equations 4-10 and 4-12 to sulphur transfer from metal to slag yields:

$$\frac{dn_S}{dt} = k_m^S A C_{Vm} \left(X_{S,m}^b - X_{S,m}^* \right) \tag{4-55}$$

$$\frac{dn_S}{dt} = k_{sl}^S A C_{Vs} \left(X_{S,sl}^* - X_{S,sl}^b \right) \tag{4-56}$$

where $X_{S,m}^b$ and $X_{S,sl}^b$ represent the bulk concentrations of sulphur in metal and slag, and $X_{S,m}^*$ and $X_{S,sl}^b$ the equilibrium sulphur concentration in metal and slag. The assumption of equilibrium at the interface implies that sulphur in slag is related to sulphur in metal by

$$k_m^S C_{Vm} \left(X_{S,m}^b - X_{S,m}^* \right) = k_{sl}^S C_{Vs} \left(X_{S,sl}^* - X_{S,sl}^b \right) \tag{4-57}$$

Rearranging this equation yields an expression for the equilibrium sulphur concentration in metal as:

$$X_{S,m}^* = \frac{k_m^S C_{Vm} X_{S,m}^b + k_{sl}^S C_{Vs} X_{S,sl}^b}{k_m^S C_{Vm} + k_{sl}^S C_{Vs} L''_S} \tag{4-58}$$

The equilibrium sulphur concentration in the slag is consequently determined as:

$$X_{S,sl}^* = L''_S \, X_{S,m}^* \tag{4-59}$$

By coupling equations 4-55 and 4-58, sulphur transfer from metal to slag is seen dependent on bulk concentrations, slag and metal mass transfer coefficients, slag-metal interfacial area, and the sulphur partition ratio. Of these essential parameters, only the bulk compositions are readily measured. It should be noted that a common simplification made in the literature when deriving the equilibrium sulphur content is to assume negligible initial sulphur in slag (Pomfret & Griveson, 1983). Although this assumption holds true in a controlled laboratory setting where slag may be controlled to have a minimal initial sulphur concentration, it is invalid for industrial systems due to the significant sulphur content in carryover slag volume from previous operations (i.e. EAF or BOF).

4.4.2.1. Sulphide Capacity

Sulphide capacity (C_s) is defined as the potential capacity of a liquid slag to hold sulphur as a sulphide. The higher the sulphide capacity value, the higher the potential for a given slag to hold sulphur. Sulphide capacities are obtained by equilibrating slag and gas phases with respect to sulphur and oxygen partial pressures as follows:

$$\tfrac{1}{2}\{S_2\}+\left(O^{2-}\right)=\tfrac{1}{2}\{O_2\}+\left(S^{2-}\right) \qquad (4\text{-}60)$$

The reaction is valid at reducing conditions having oxygen pressures less than 10^{-6}atm, which is generally the case during iron and steelmaking conditions. The equilibrium constant for equation 4-60 is:

$$K_{4-60} = \left(\frac{a_{S^{2-}}}{a_{O^{2-}}} \right) \sqrt{\frac{P_{O_2}}{P_{S_2}}} = \frac{(\%S)\,\gamma_{S^{2-}}}{a_{O^{2-}}} \sqrt{\frac{P_{O_2}}{P_{S_2}}} \tag{4-61}$$

where P_{O_2} and P_{S_2} are the equilibrium partial pressures of oxygen and sulphur in gas with slag, and $a_{S^{2-}}$ and $a_{O^{2-}}$ are the interfacial activities of sulphur and oxygen in slag. The interfacial activity of sulphur in slag may alternatively be expressed as the product of its molar concentration and activity coefficient. As the activity of free oxygen ions is unable to be measured, Fincham & Richardson (1954) introduced the concept of sulphide capacity as:

$$C_S = \frac{K_{4-60}\, a_{O^{2-}}}{\gamma_{S^{2-}}} = (\%S) \sqrt{\frac{P_{O_2}}{P_{S_2}}} \tag{4-62}$$

From inspection of equation 4-62, it is seen that sulphide capacity increases with increasing basicity, where the basicity of a slag is a measure of its ability to donate oxygen ions when dissolved in a melt. The basicity or oxygen donating ability of slag increases with increasing percentages of basic oxides dissolved in it. In the present work, the sulphide capacity of slag was computed using the following empirical equations proposed by Young et al. (1992).

for $\Lambda < 0.8$:

$$\begin{aligned} \log(C_s) = & -13.913 + 42.84\Lambda - 23.82\Lambda^2 - \left(\frac{11,710}{T} \right) \\ & -0.02223(wt\%SiO_2) - 0.02275(wt\%Al_2O_3) \end{aligned} \tag{4-63}$$

for $\Lambda \geq 0.8$:

$$C_s = -0.6261 + 0.4808\Lambda + 0.7197\Lambda^2 + \left(\frac{1{,}697}{T}\right) - \left(\frac{2{,}587\Lambda}{T}\right) + 0.000514\left(wt\%FeO\right) \qquad (4\text{-}64)$$

As seen, the sulphide capacity equations by Young et al. (1992) are a function of optical basicity (Λ), which is a term originally proposed by Duffy & Ingram (1971) for representing the oxygen donating ability of a slag. Duffy & Ingram (1971) proposed the following equation for computing the optical basicity of slags:

$$\Lambda = \frac{\sum (x_i\, n_i\, \Lambda_i)}{\sum (x_i\, n_i)} \qquad (4\text{-}65)$$

where x_i is the mole fraction of component 'i', n_i is the number of oxygen atoms in oxide molecule 'i', and Λ_i is a spectroscopically measured quantity defined as the optical basicity of component 'i'. Table 4-5 lists the optical basicity values for selected slag components.

Table 4-5: Selected optical basicity values (Young et al., 1992)

Oxide	n_i	Λ_i
K_2O	1	1.4
P_2O_5	5	0.4
TiO_2	2	0.65
CaS	0	0
FeO	1	1.00
CaO	1	1.0
MnO	1	0.98
SiO_2	2	0.46
MgO	1	0.78
Al_2O_3	3	0.60

4.4.2.2. Sulphur Partition Ratio

Equilibrium sulphur concentrations may be determined by equilibrating slag and metal phases according to the ionic exchange reaction for sulphur given previously as equation 4-20. For which the equilibrium reaction is given by:

$$K_{4-20} = \frac{h_O a_{S^{2-}}}{a_{O^{2-}} h_S} \tag{4-66}$$

where h_O and h_S are the Henrian activities of dissolved oxygen and sulphur in liquid steel, and $a_{O^{2-}}$ and $a_{S^{2-}}$ the Raoultian activities of oxygen and sulphur in slag. Replacing $a_{S^{2-}}$ with weight percent sulphur in slag and rearranging yields:

$$L_S = \frac{(wt\%S)}{[wt\%S]} = \frac{C'_S f_S}{h_O} \tag{4-67}$$

where C'_S is the modified sulphide capacity and is related to C_S as:

$$\log C_S = \log C'_S - \log K_S = \log C'_S + \frac{935}{T} - 1.375 \tag{4-68}$$

The equilibrium constant K_S is for the sulphur exchange reaction between metal and gas phases with respect to sulphur and oxygen partial pressures. Stated in terms of sulphide capacity the sulphur partition ratio becomes:

$$L_S = \frac{(wt\%S)}{[wt\%S]} = \frac{C_S f_S K_S}{h_O} \tag{4-69}$$

As seen from equation 4-69, the sulphur partition ratio increases with increasing slag basicity and decreasing oxygen activity. Further, increasing temperature has a negative impact on the partition ratio due to the deoxidation reaction being exothermic.

4.4.3. Model Assumptions

The following simplifying assumptions were made in the model:

- The chemical kinetics of all reactions were assumed fast, with equilibrium being assumed established at the interface.
- Bulk slag and metal phases are assumed homogeneously mixed such that bulk phase concentration gradients were assumed negligible.
- Interaction between ladle refractory and slag-metal was neglected.
- Slag and metal phases were assumed to have identical temperatures. Temperature gradients within the metal-slag phases were assumed negligible.
- Slag was assumed to exist as liquid. No attempt made to describe the effect of slag solid fraction on reaction kinetics.

4.4.4. Overall Model Structure

Figure 4-16 presents a schematic flowsheet of the numerical routine developed and implemented as an overall multi-component kinetic control system.

As shown, the cell model and UIPM discussed in Chapter 3 were used to calculate phase activities.

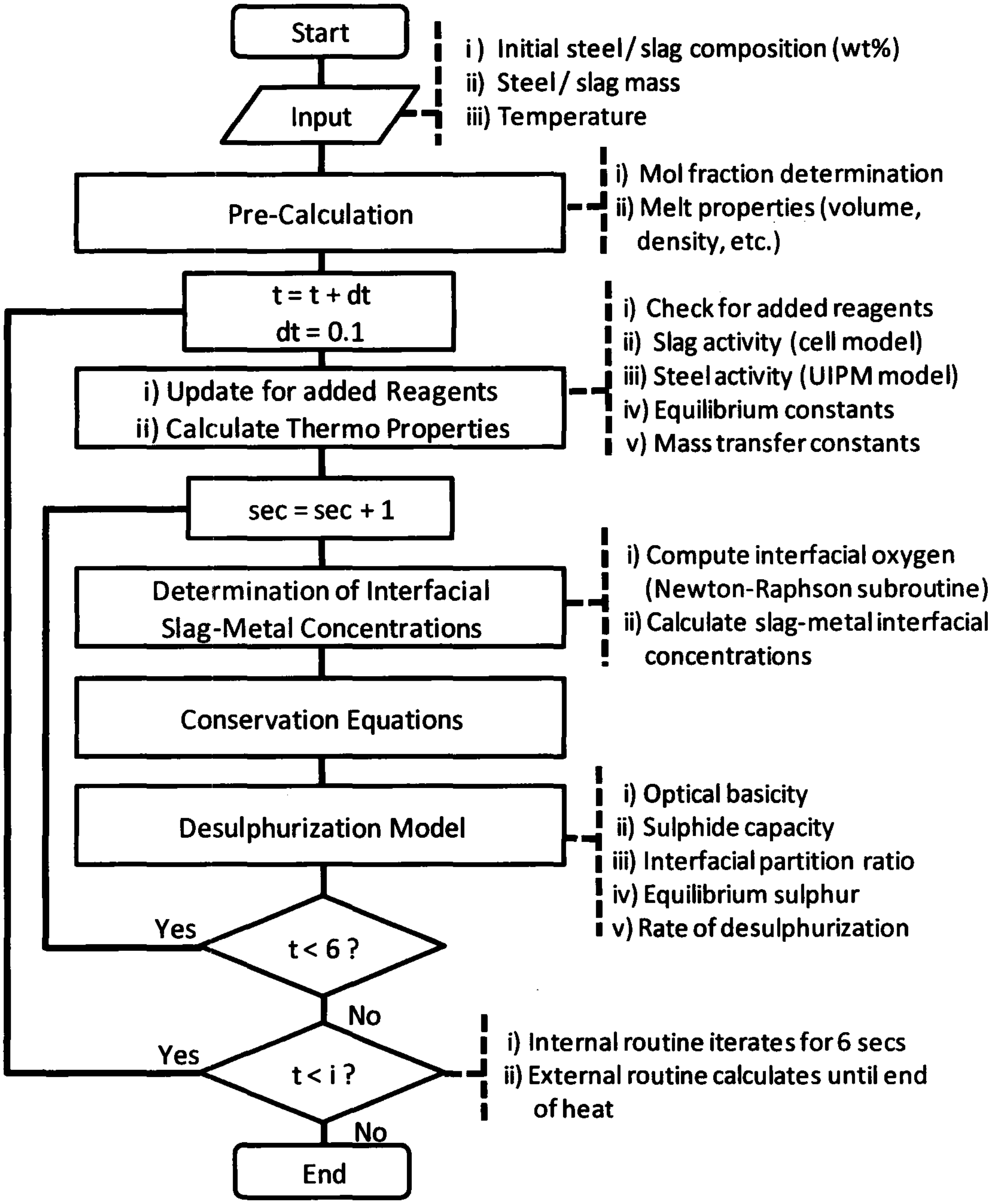

Figure 4-16: Flowchart schematic of overall multi-component kinetic model.

4.5. Experimental Results

4.5.1. Slag Carryover Characterization

Figure 4-17 summarizes the agreement between dip-test and Delta Dist L sensor measured slag depth for all 37 heats observed. An ideal linear fit is also drawn in the plot, where data points falling on or near to the linear fit represent perfect or near perfect agreement between the two slag measurement methods. The average measured slag depth for the Delta Dist L sensor was found to be 14.1 ± 2.57 cm (5.54 ± 1.01 inches), and 13.92 ± 2.36 cm (5.48 ± 0.93 inches) for the dip-test. All slag measurements ranged between 9.5 and 21.5 cm (3.75 and 8.5 inches). A hypothesis based test on the ratio of the different slag depth measurement results using an F-statistic indicates that the two variances are statistically equivalent.

It should be noted that the automatic immersion lance at ArcelorMittal Dofasco is positioned directly over top of one of two bottom porous plugs. On several occasions, despite low argon flow conditions within the melt, the Delta Dist L sensor entered directly in the “spout” region (where gas is discharged from the melt) yielding poor results. Under such circumstances, repeat slag depth measurements were taken at the LMF and these irregular events were omitted from Figure 4-17.

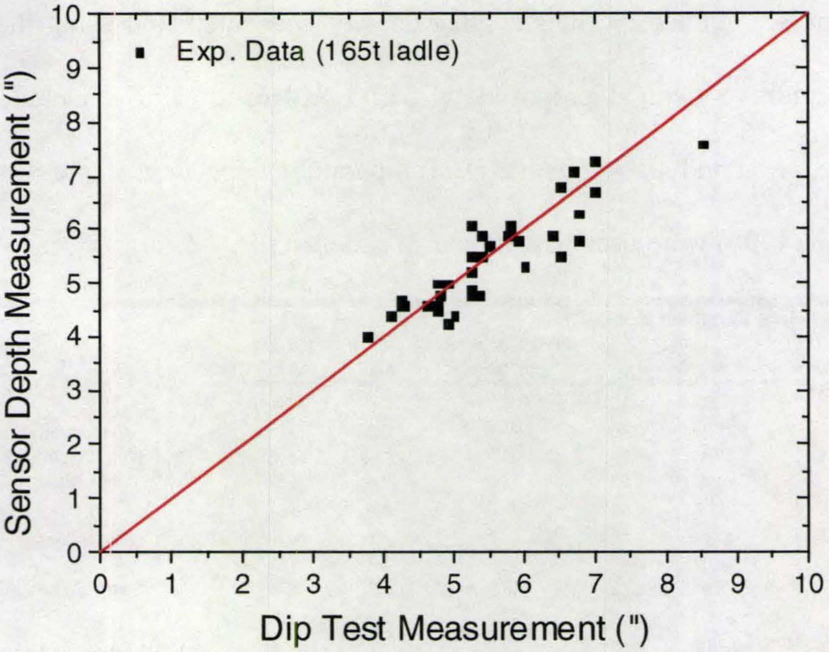

Figure 4-17: Comparison of dip-test and Delta Dist L sensor measured slag depth

The good agreement between dip-test and Delta Dist L measurements suggests that slag depth may be accurately determined within the ladle. On that basis, efforts were taken to convert the measured slag depth into an estimate of overall slag mass, a much more useful quantity from a process control perspective. Figure 4-18 summarizes a representative sample calculation of slag carryover and other melt properties.

Model inputs required for the calculation include slag composition, temperature and height, as well as ladle diameter. A simple erosion model was used (linear with heat time) in the study to account for the effect of refractory erosion on ladle diameter. As illustrated from Figure 4-18, calculation of slag mass and by default slag carryover mass allows for the subsequent determination of steel mass, volume, and height. Slag density was calculated using the widely accepted additive method proposed by Mills & Keene (1987). Details on the model are presented in Appendix D. Temperature dependent expressions from Turkdogan (1996) were used to estimate steel density.

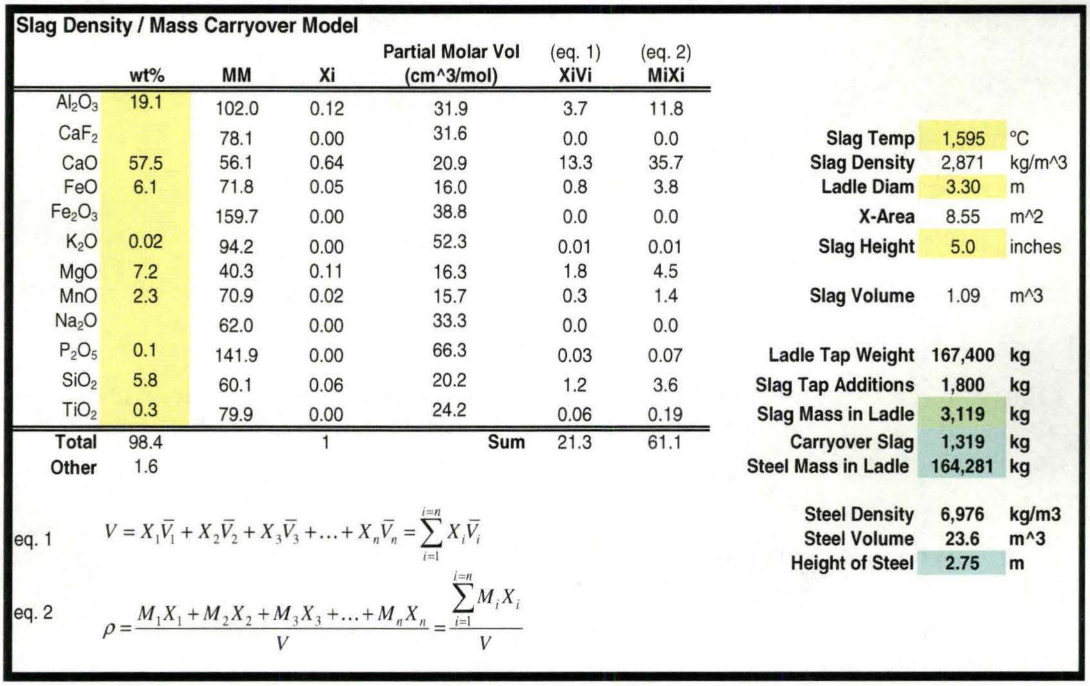

Slag Density / Mass Carryover Model

	wt%	MM	Xi	Partial Molar Vol (cm^3/mol)	(eq. 1) XiVi	(eq. 2) MiXi
Al_2O_3	19.1	102.0	0.12	31.9	3.7	11.8
CaF_2		78.1	0.00	31.6	0.0	0.0
CaO	57.5	56.1	0.64	20.9	13.3	35.7
FeO	6.1	71.8	0.05	16.0	0.8	3.8
Fe_2O_3		159.7	0.00	38.8	0.0	0.0
K_2O	0.02	94.2	0.00	52.3	0.01	0.01
MgO	7.2	40.3	0.11	16.3	1.8	4.5
MnO	2.3	70.9	0.02	15.7	0.3	1.4
Na_2O		62.0	0.00	33.3	0.0	0.0
P_2O_5	0.1	141.9	0.00	66.3	0.03	0.07
SiO_2	5.8	60.1	0.06	20.2	1.2	3.6
TiO_2	0.3	79.9	0.00	24.2	0.06	0.19
Total	98.4		1	**Sum**	21.3	61.1
Other	1.6					

eq. 1 $$V = X_1\bar{V}_1 + X_2\bar{V}_2 + X_3\bar{V}_3 + \ldots + X_n\bar{V}_n = \sum_{i=1}^{i=n} X_i\bar{V}_i$$

eq. 2 $$\rho = \frac{M_1X_1 + M_2X_2 + M_3X_3 + \ldots + M_nX_n}{V} = \frac{\sum_{i=1}^{i=n} M_iX_i}{V}$$

Slag Temp	1,595	°C
Slag Density	2,871	kg/m^3
Ladle Diam	3.30	m
X-Area	8.55	m^2
Slag Height	5.0	inches
Slag Volume	1.09	m^3
Ladle Tap Weight	**167,400**	**kg**
Slag Tap Additions	**1,800**	**kg**
Slag Mass in Ladle	**3,119**	**kg**
Carryover Slag	**1,319**	**kg**
Steel Mass in Ladle	**164,281**	**kg**
Steel Density	**6,976**	**kg/m3**
Steel Volume	**23.6**	**m^3**
Height of Steel	**2.75**	**m**

Figure 4-18: Sample calculation for estimating the selected melt properties

As off-line slag chemical analysis is quite time-consuming, the detailed slag carryover determination procedure is not practical for online control purposes. As such, a relationship was developed between estimated slag carryover mass and observed AMEPA index. Figure 4-19 shows that slag carryover mass was found to increase linearly for AMEPA index values below 220, and exponentially at values higher than 220. In both instances curve fitting was determined by minimizing the sum of squared residuals. An interesting observation from Figure 4-19 is the presence of significant slag carryover volumes at negligible AMEPA index values. The existence of slag carryover mass within the ladle at these low index values was confirmed by the presence of easily reducible oxides (6-16wt% FeO and 2-5wt% MnO) within the slag phase. These findings suggest either: (i) that tapped steel is in effect shielding slag (perhaps due to vortexing) from being recorded by the AMEPA slag detection system, and / or (ii) that the AMEPA system is unable to detect all slag carryover from the highly disturbed flows seen at the end of a tap cycle.

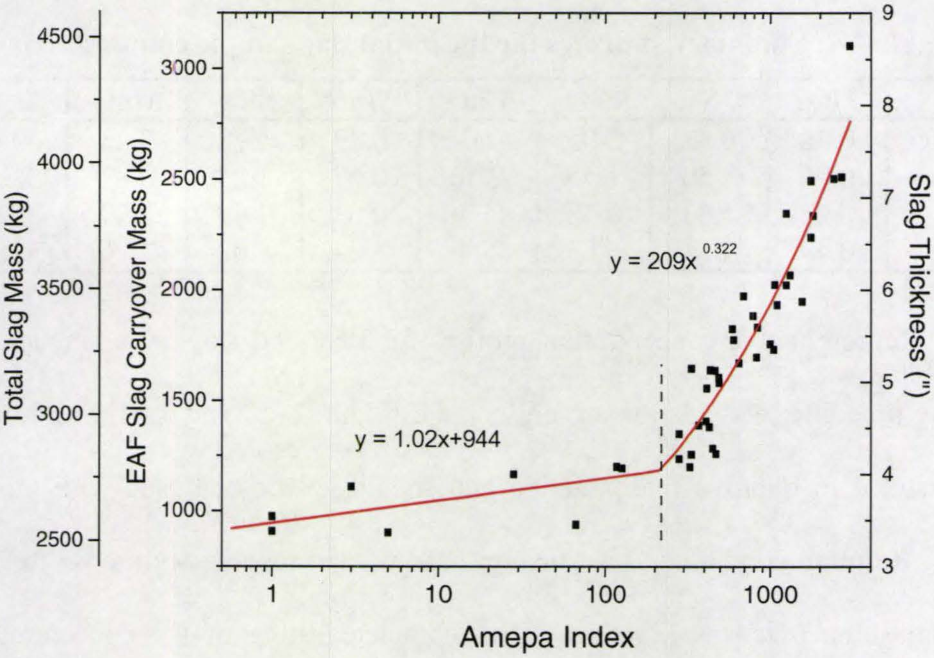

Figure 4-19: Relation between AMEPA index and slag carryover mass

4.5.2. Bulk Chemical Sampling Results

A summary of the initial average steel and slag compositions for all experimental heats is presented as Table 4-6 and 4-7. Variation within the data is largely attributed to the different grades observed.

Table 4-6: Summary statistics for the initial steel sample composition

	C	Mn	S	Si	Als	N	Ca	Ti
Average	0.0432	0.2510	0.0338	0.0169	0.0503	0.0057	0.0003	0.0008
Std Dev	0.0080	0.1603	0.0112	0.0301	0.0200	0.0007	0.0002	0.0002
Min	0.0258	0.0897	0.0116	0.0039	0.0148	0.0044	0.0001	0.0004
Max	0.0633	0.5658	0.0725	0.1521	0.0947	0.0071	0.0008	0.0014

Table 4-7: Summary statistics for the initial slag sample composition

	TiO2	S	FeO	CaO	MnO	SiO_2	MgO	Al_2O_3
Average	0.32	6.52	2.05	51.35	0.89	4.78	7.23	30.41
Std Dev	0.06	3.50	1.55	2.50	0.67	1.25	0.83	2.64
Min	0.22	1.63	0.48	45.70	0.03	2.49	5.89	21.99
Max	0.49	16.72	6.64	55.47	3.24	8.02	9.56	35.13

Representative concentration profiles for steel and slag as a function of refining time after deoxidation are presented as Figure 4-20 and 4-21. Solid lines are included to improve interpretation and should not be confused with model results. Refining conditions (i.e. stirring, heating, and reagent additions) for the heat are summarized as Figure 4-11. A complete listing of the concentration profiles and experimental conditions for all heats is given as Appendix F.

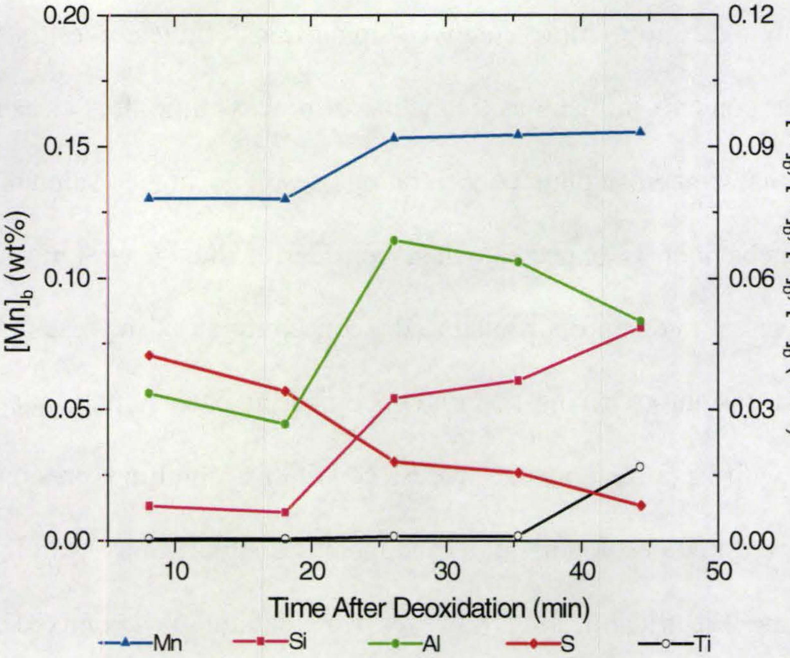

Figure 4-20: Concentration profile of Mn, Al, Si, S, and Ti in steel (Heat 40).

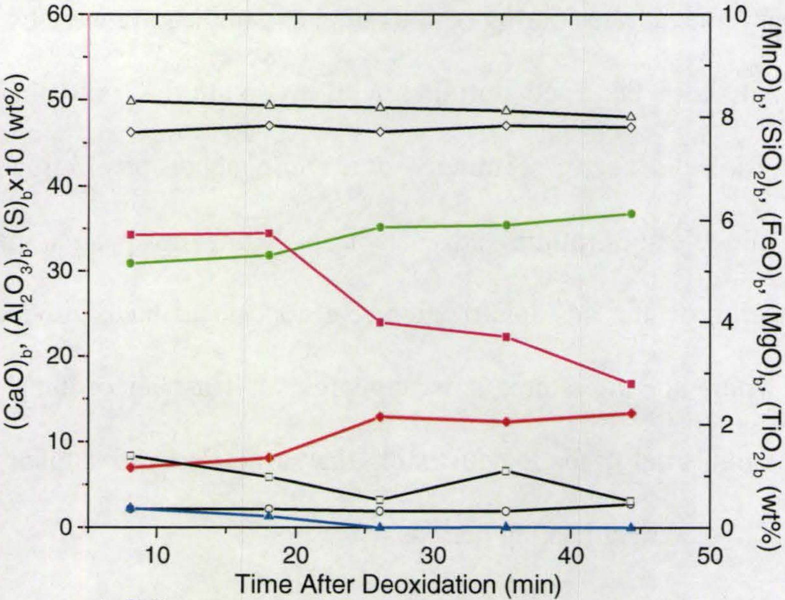

Figure 4-21: Concentration profile of MnO, CaO, Al_2O_3, S, SiO_2, FeO, MgO and TiO_2 in slag (Heat 40).

Figure 4-22 shows representative sulphur transfer rate curves for different initial sulphur contents in metal as a function of process time. It is clear from the rate curves that higher sulphur concentrations result in higher sulphur transfer rates. This behaviour is expected when considering the general reaction rate theory, as reaction rate is proportional to the concentration of the reacting species (i.e.: Rate = Constant x Driving Force). On comparing each sulphur rate curve in Figure 4-22 with its corresponding process conditions found in Appendix F, it is further observed that desulphurization rate increases significantly with increasing argon flow rate. Electrical heating, however, was found to have a mixed effect on the rate of desulphurization. Results from the industrial trials have shown that while sulphur removal rates during periods of electrical heating were by and large comparable to those observed during low flow conditions only, instances of sulphur reversion did occur, seemingly as a consequence of electrical heating, towards the mid to end of refining on select heats. While the apparent influence of electrical heating on the desulphurization rate appears to have previously gone unreported within the literature, it is supported at least anecdotally from the results of the industrial trials demonstrating that at no time did sulphur reversion occur outside of electrical heating periods.

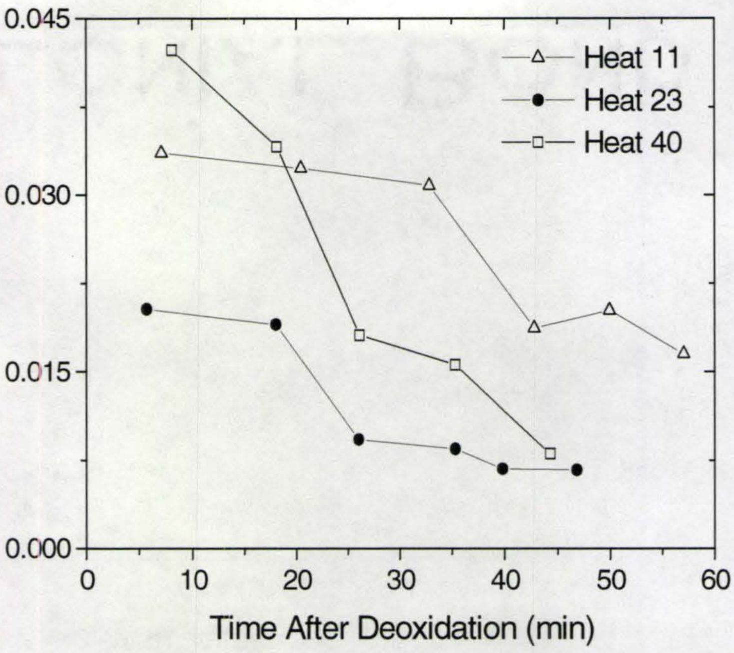

Figure 4-22: Comparison of sulphur transfer curves for different sulphur content in metal (Heat 11, 23, 40).

Figure 4-23 presents desulphurization rate curves, for the same heats as given in Figure 4-22, plotted as the change in sulphur content in slag as a function of time; the figure serves to illustrate some of the inherent difficulties faced in modelling an industrial process. While slag sulphur concentration was found to change in an approximate equal and opposite rate to sulphur concentration in steel, there were occasions (Heat 40 between 25 and 35 minutes) where both the sulphur concentration in slag and metal phases moved in the same direction. Such occurrences are an indication of sampling and / or analysis error(s), or that sulphur is possibly being lost to the atmosphere, refractory and / or inclusions.

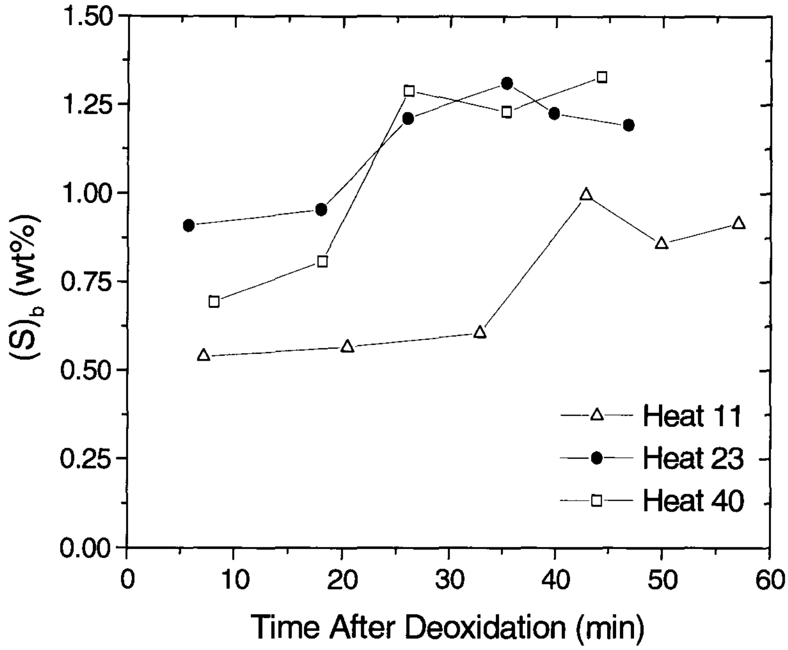

Figure 4-23: Comparison of the sulphur transfer rate curves plotted as the change in slag sulphur content, for the same heats (Heat 11, 23, 40) as shown in Figure 4-22.

4.5.3. Dissolved Oxygen Behaviour

Figure 4-24 compares the measured oxygen sensor readings against calculated equilibrium curves for pure alumina, calcium aluminate, and spinel inclusions at a temperature of 1873K. The cell model and unified interaction parameter formalism were used to calculate the steel and slag activities at the respective compositions. While it is difficult to draw firm conclusions from the plot, particularly given that the oxygen measurements were taken between within a temperature range of 1540 and 1640°C, Graham & Irons (2008) suggested on the basis of the shown pure alumina curve marked as (1) in Figure 4-24, that alumina inclusions in the melt were being fluxed by ladle slag. This observation was in accordance with the earlier reported results by Turkdogan (1996).

Inclusion analysis results on heat samples taken from these trials and analyzed by RJ Lee Group (Monroeville, PA), however, revealed that formed inclusions were in fact predominately pure alumina at the start of deoxidation and later transformed to spinels and less frequently to calcium aluminates.

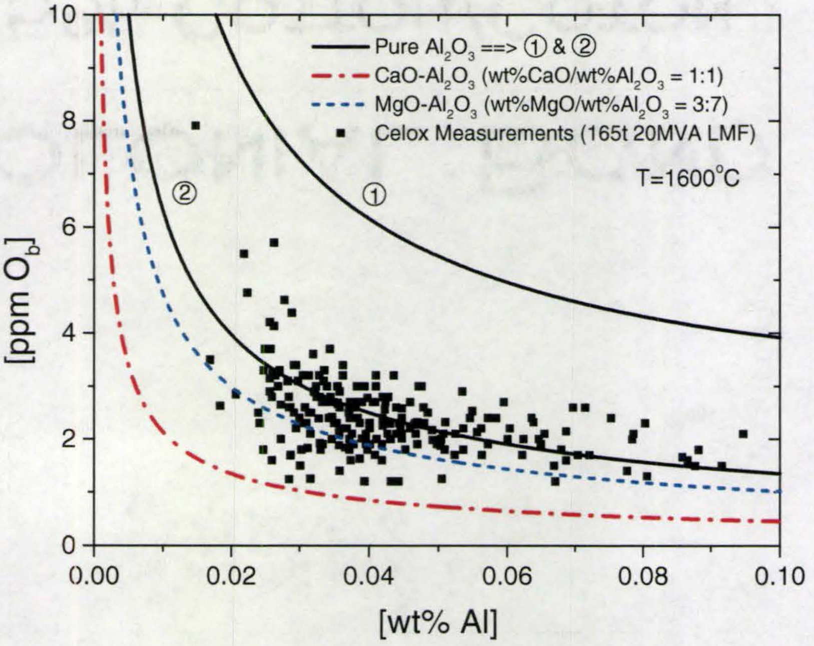

Figure 4-24: Comparison of Celox measured dissolved oxygen content with equilibrium calculated values at 1873K for pure Al_2O_3, calcium aluminate, and spinel inclusions after deoxidation.

After careful review, the poor agreement between the calculated equilibrium curve (1) and the Celox (and subsequent inclusion analysis results) was entirely due to the choice of equilibrium constant for the aluminum deoxidation reaction. Equilibrium curve (1) was plotted using the equilibrium constant relation proposed by Itoh et al. (1997), and is in direct contrast to the excellent agreement exhibited by the equilibrium curve (2), which was plotted using the equilibrium constant data presented in Table 4-4 and recommended by

The Japan Society for the Promotion of Science (1984). On the basis of the pure alumina equilibrium curve (2) it becomes clear that inclusions are in fact predominately pure alumina in nature. The significant difference between equilibrium curves (1) and (2) serves to highlight the difficulty in trying to develop mathematical models for interpreting metallurgical data.

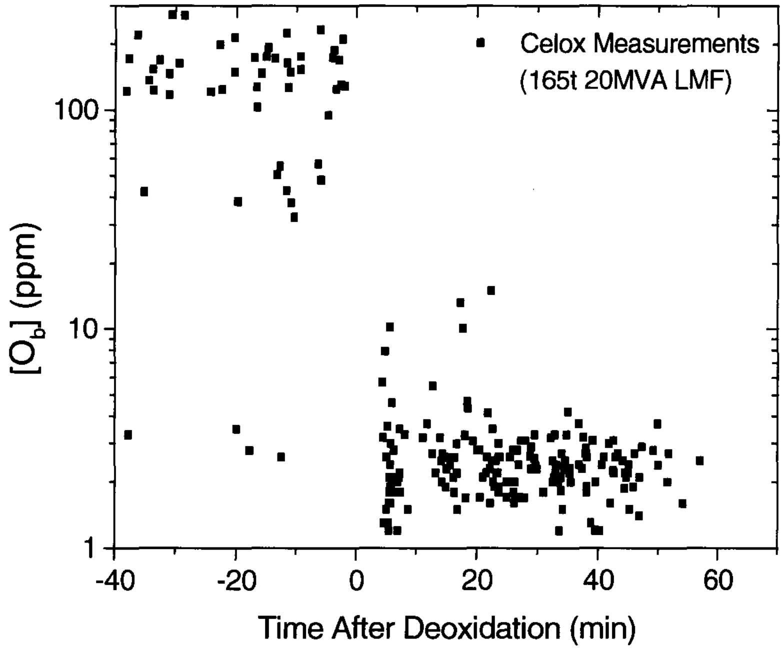

Figure 4-25: Time varying dissolved oxygen profile

Figure 4-25 summarizes the results of the Celox measurements taken during the trials as a function of time after deoxidation. As seen, the dissolved oxygen contents of incoming steel to the LMF ranged between 3 to 300ppm. The wide range in observed values is largely due to differences in the deoxidizer mix at furnace tapping. Further shown in Figure 4-25, is that deoxidation at the LMF results in an immediate and distinct step-wise lowering in dissolved oxygen content. The few post deoxidized dissolved oxygen contents in excess of 5ppm were observed on heats having abnormally long pre-processing retention times at the LMF due to complications at the caster.

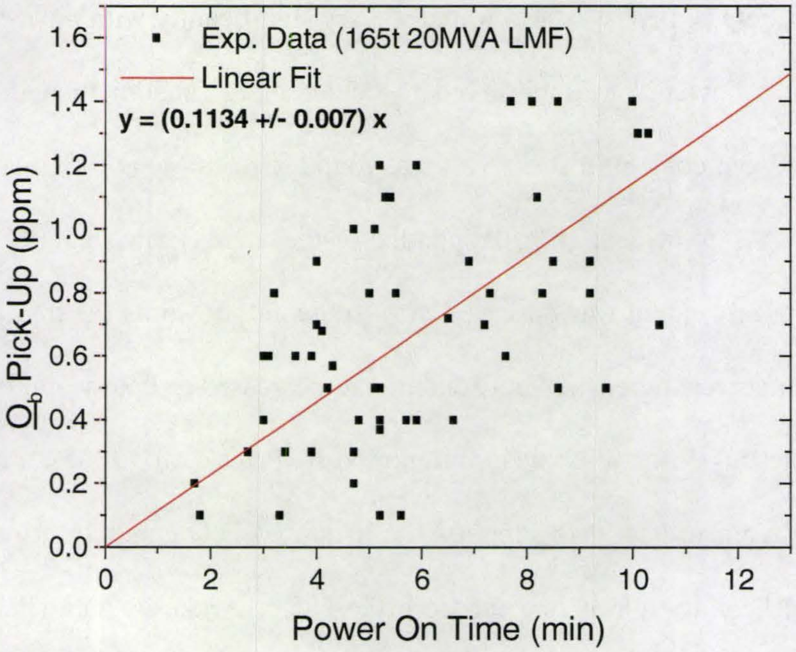

Figure 4-26: Effect of power on time on the (top) dissolved oxygen content in steel.

An interesting outcome of the trials was the observed increase in dissolved oxygen content during periods of electrical arcing, Figure 4-26. While the linear regression fit with power on-time shown in Figure 4-26 is admittedly poor, the fact remains that not once did the dissolved oxygen content after electrical heating fall below its initial value at the commencement of heating. This evidence suggests that electrical heating has a significant influence on the oxygen potential within the melt. To this end, the significant volume of oxygen pick-up seen during periods of power-on time may serve as one possible explanation for the occurrence of sulphur reversion during periods of electrical heating. The scatter in the data observed in Figure 4-26 is likely due to the measurement error of the Celox probe having a standard deviation of ± 1ppm (Heraeus Electro-Nite, 2007).

Slag FeO content was also found to vary significantly with power on time. Its behaviour, however, was observed to be far more random than that of the dissolved oxygen content in steel, as it was found to decrease approximately 20% of the time. As is evident from Appendix F, the increase in slag FeO content during electrical heating was observed most frequently towards the middle to end of the refining cycle, after the FeO content had decreased to below approximately 1wt%. While this observation went unreported by Peter et al. (2005), a review of their Nucor Yamato heat data supports the increased FeO content during periods of electrical heating. It was unclear from the Nucor Arkansas data (Peter et al., 2005) whether electrical heating occurred between slag samples.

4.5.4. Bath Temperature Estimation

A direct benefit of having undertaken an extensive sampling regimen whereby heats were divided into periods of low stir, high stir and electrical heating was that it enabled very simple relationships to be developed for describing the behaviour of temperature during refining. As shown in Figure 4-27, periods of electrical heating resulted in a bath temperature gain of 3.35°C / min. Figure 4-28 demonstrates that stirring in absence of electrical heating resulted in a temperature loss of 1.33°C / min. In contrast to expectations, increasing the gas stirring rate and the addition of alloys were found to have a negligible influence on the rate of temperature loss.

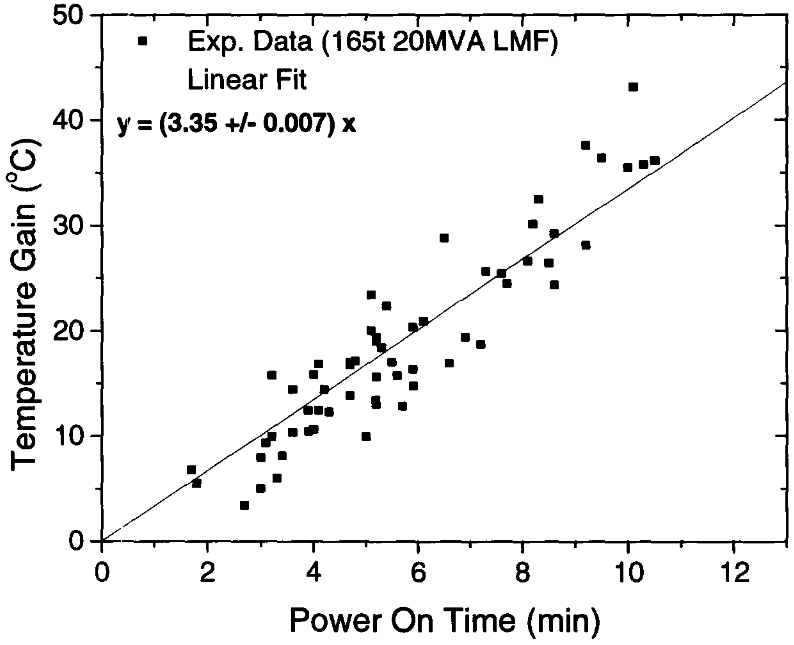

Figure 4-27: Temperature gain with power on time

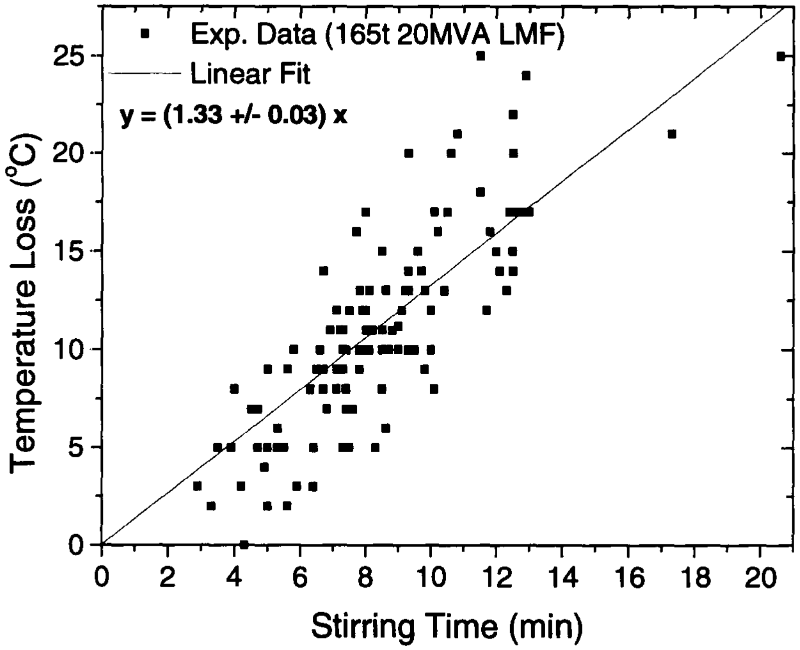

Figure 4-28: Temperature loss with stirring time

The good agreement found in most heats between predicted and measured temperature indicates that the simplicity of the temperature loss and gain relationships defined in Figure 4-27 and 4-28 does not detract from their ultimate usefulness. On the average, the presented temperature relationships were found to be within ± 4°C from the final end of heat temperature measured using a thermocouple, with the range between 0.4 and 16.4°C.

4.5.5. Mass Transfer Coefficient Determination

The assumption of local equilibrium at the slag-metal boundary implies that the reaction rate is governed by interfacial equilibria and by convection / diffusion transport to and from the interface. On this basis, mass transfer rates may be written as 4-48 to 4-51, where the difference between bulk and interfacial concentrations represent the driving force for equilibrium and k_m^M , $k_{sl}^{M_xO_y}$, k_m^S , and k_{sl}^S are the respective mass transfer coefficients. At steady state, equations 4-55 and 4-56 (or 4-53 and 4-54 for any metallic element) may be equated and rearranged to express the total mass transfer resistance as the sum of metal and slag phase resistances in series:

$$k_{tot} = \left(\frac{1}{k_m^i} + \frac{1}{L_S k_{sl}^i} \right) \qquad (4\text{-}70)$$

Richardson (1974) pointed out that over normal ranges of liquid properties, slag phase mass transfer coefficients will be lower than the metal phase mass transfer coefficients by no more than one order of magnitude. In their work, Ward &

Salmon (1960) obtained slag phase mass transfer coefficients for sulphur at a magnitude of 10^{-2} x k_m^S, but reported that these values were subject to a high degree of experimental uncertainty. Chang & Goldman (1948) reported similar values as Ward & Salmon (1960) for k_m^S and k_{sl}^S, observing a negligible change in k_{sl}^S for changes in slag composition. It is typically assumed within the literature that mass transfer control is rate limited by mass transfer within the metal phase, provided that the equilibrium partition ratio of metallic element-M remains large.

As shown in Figure 4-11 three distinct process events were found typical of the LMF practice at ArcelorMittal Dofasco, namely:

- Low argon flowrate with arcs off
- Low argon flowrate with arcs on
- High argon flowrate with arcs off.

A key requirement in developing a kinetic model capable of accurate real-time state prediction within the LMF was therefore the determination of empirical mass transfer coefficient correlations for these widely different process conditions.

4.5.5.1. Sulphur

Figure 4-29 summarizes the measured bulk sulphur partition ratio determined from the trials as a function of the FeO content in slag. As seen, highly oxidizing slags from the EAF result in low bulk sulphur partition ratios and it is only after deoxidation that the slags become more favourable for desulphurization. On the basis of these findings, and in agreement with the literature (Chang & Goldman, 1948; Ramachandran et al., 1956; Ward & Salmon, 1963), desulphurization for a reduced slag is expected to be metal phase controlled.

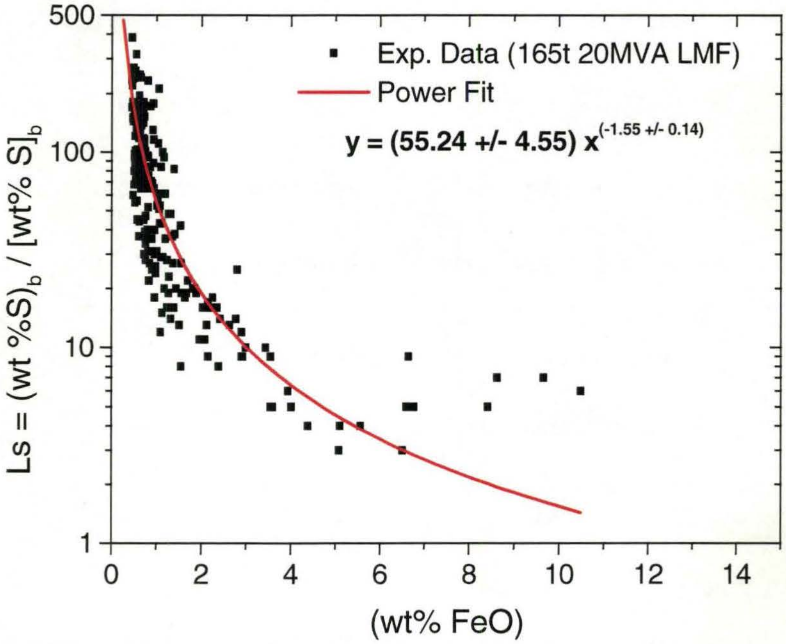

Figure 4-29: Plant data showing the relation between FeO content in slag and measured bulk sulphur partition ratio.

Sulphur mass transfer may be described using the integrated form of the rate equation assuming first order kinetics and diffusion control as:

$$-\ln\left(\frac{[wt\%S]_t-[wt\%S]_e}{[wt\%S]_o-[wt\%S]_e}\right)=k_m^S\left(\frac{A}{V_m}\right)\left(\frac{[wt\%S]_o}{[wt\%S]_o-[wt\%S]_e}\right)t \qquad (4\text{-}71)$$

where $[wt\%S]_t$ is the sulphur content at any given time, $[wt\%S]_o$ the initial sulphur content in steel, $[wt\%S]_e$ the equilibrium sulphur content in steel, V_m the volume of metal, and A the slag-metal interfacial area.

While the equilibrium sulphur concentration in equation 4-71 may be computed using equation 4-58, an apparent inconsistency within the metallurgical literature is that its solution differs widely amongst researchers. Ward & Salmon (1960) simplified the integrated rate equation for sulphur by assuming the equilibrium sulphur concentration to be negligibly small. Jonsson and coworkers (1998) evaluated the equilibrium sulphur content using a bulk oxygen activity assumed in equilibrium with dissolved aluminum in steel and alumina in top slag. Subagyo & Brooks (2002) suggested an alternative solution for the equilibrium sulphur concentration by using an interfacial oxygen value that was assumed in equilibrium with FeO in slag. Further still, numerous researchers have calculated equilibrium sulphur on the basis of the dissolved oxygen content in steel measured from a Celox probe. Clearly, much of the confusion surrounding the determination of equilibrium sulphur is due to the uncertainty in determining the sulphur partition ratio, and more specifically the equilibrium oxygen activity.

A comparative analysis was undertaken in order to rationalize the differences between the alternative methods proposed for computing the equilibrium sulphur partition ratio. Figure 4-30 summarizes the results, where the four analyzed methods included:

- Measured bulk slag and metal sulphur contents
- Celox probe measured bulk oxygen activity
- Calculated dissolved oxygen assuming equilibrium between dissolved aluminum and alumina in top slag (Jonsson et al, 1998)

- A calculated interfacial oxygen activity by coupling the equilibrium reactions for FeO, MnO, CaO, MgO, TiO_2, SiO_2, and Al_2O_3 and assuming a homogenized bulk composition within the slag phase (a more complex description than that supposed by Brooks & Subagyo (2002))

This final case considers conditions of metal phase control and that the interfacial oxygen activity may be determined by solving a simplified form of the overall oxygen mass balance previously introduced when describing the Robertson model (1984):

$$\frac{1}{M_O}\left(X_O^b - X_O^*\right) = \sum_i^m \left(\frac{y_i}{x_i}\right)\frac{1}{M_i}\left(X_i^b - X_i^*\right) \qquad (4\text{-}72)$$

where the equilibrium concentrations of non-oxygen elements may be calculated using equation 4-72. Slag component activities were calculated using the cell model, while the activities of metal components were calculated using the unified interaction parameter formalism. Table 4-4 lists the relevant equilibrium constant expressions.

$$X_i^* = \sqrt[x]{\left(K_{M_xO_y} a_{M_xO_y}\right) \Big/ \left(f_M^{\,x}\left\{f_O X_O^*\right\}^y\right)} \qquad (4\text{-}73)$$

As seen, the technique proposed by Jonsson et al. (1998) yields sulphur partition ratios 10 to 100 times higher at the start of processing than was determined from any other method. Further seen from this method is that calculated sulphur partition values appear invariant to FeO content in slag. In contrast to the high values calculated using the Jonsson et al. (1998) approach, results show that the measured bulk sulphur partition ratios converge towards the end of the heat to those calculated using Celox bulk oxygen activity. While this trend was found representative of all sampled heats, the closeness of the convergence was in most cases not as good as that presented here.

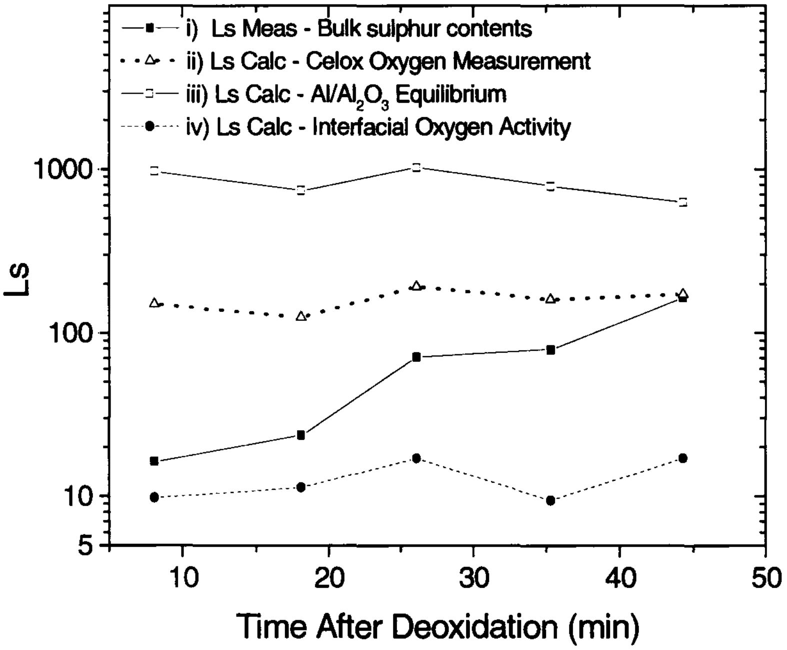

Figure 4-30: Comparison of the measured and calculated sulphur partition ratios (Heat 40).

Also shown in Figure 4-30 is the predicted equilibrium sulphur partition calculated by considering the extension of the method supposed by Subagyo & Brooks (2002) to include coupled interfacial reactions. Results using this method were found heavily dependent on the FeO content in slag, where determined interfacial oxygen concentrations were an order of magnitude higher than measured bulk values. It is interesting to note that these findings are in agreement with the early observations of Faral & Gaye (1984), who reported that iron content of the slag is a poor indicator of oxygen equilibrium potential at the slag-metal interface. On the basis of these results, however, it remains unclear how Subagyo & Brooks (2002) were able to report such low metal phase equilibrium sulphur contents (Figure 4-7) in their work. Moreover, these findings suggest that a homogenized bulk composition is not being achieved within the slag and that slag phase mass transfer coefficients may have an important impact on the rate of desulphurization that has seldom been reported.

As a first approximation and due largely to the uncertainty surrounding the optimal choice for calculating the equilibrium sulphur partition ratio, the equilibrium sulphur content in metal was assumed small compared to the measured sulphur contents (Ward & Salmon, 1960). Although preliminary analysis shows this assumption to be reasonable, its validity will be assessed at the end of this chapter.

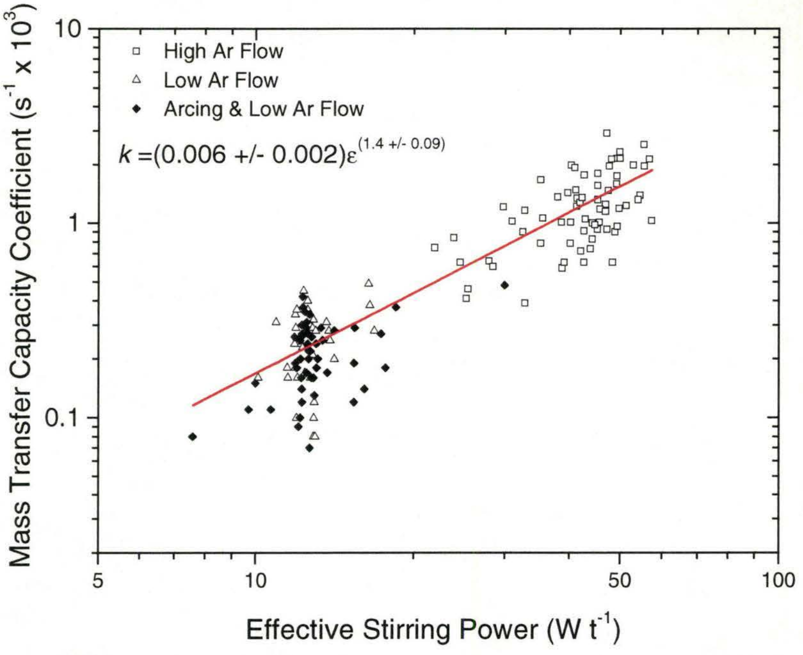

Figure 4-31: Relationship between mass transfer capacity coefficient and effective stirring power.

Figure 4-31 summarizes the relationship between the calculated desulphurization mass transfer capacity coefficient (a lumped parameter including the mass transfer coefficient, slag-metal interfacial area, and steel volume) and stirring conditions within the 165t industrial ladle at ArcelorMittal Dofasco. The effective stirring power relation derived by Pluschkell (1981) was used to describe the buoyant energy of injected gas. The determined correlation in Figure 4-31 was based on over 150 distinct ladle events and exhibits excellent agreement in light of the difficulties associated with industrial sampling. A possible explanation for the apparent differences in rate constants at low flow rates may be a result of the differences in steel alloy concentration and bath temperature. The only omissions from Figure 4-31 were during periods of electrical heating where sulphur reversion had occurred.

A summary plot comparing the mass transfer coefficients calculated within this study against those from other works is given as Figure 4-32. The most widely used mass transfer correlation within the literature is that of Asai et al. (1983), and is based on the 2.5t pilot scale experiments of Ishida and coworkers (1981) studying the effect of gas flow rate on the desulphurization kinetics of slag-metal reactions. In the absence of their own experimental data, Sugabyo & Brooks (2002) and Conejo et al. (2007) incorporated this correlation within their kinetic models.

A unique characteristic of the empirical correlation from Asai et al. (1983) is the presence of a break-point at a stirring power of approximately 60 W / t, where then higher stirring powers yield significantly higher values of the mass transfer capacity coefficient. Asai et al. (1983) reasoned that the abrupt increase in the mass transfer capacity coefficient was due to the onset of an emulsified slag-metal region with increased stirring power, resulting from the improved temperature uniformity within the slag phase. Asai et al. (1983) further commented that the break-point was only observed in high temperature experiments and not in low temperature experiments where slag and metal phases were at equivalent temperatures. This latter point has gone largely unnoted within the metallurgical literature and might serve as a possible explanation as to why a similar break-point was neither observed in the current industrial trials nor those of Peter et al. (2005).

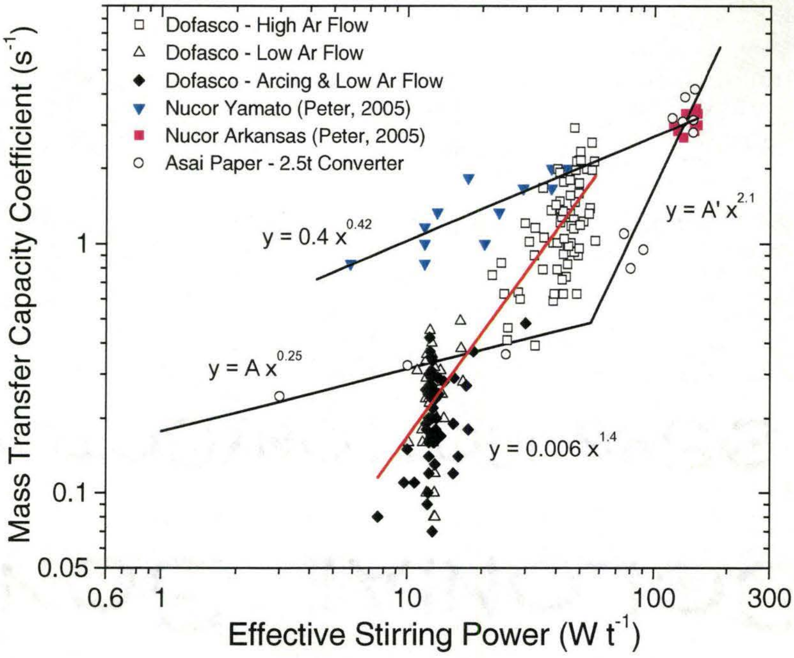

Figure 4-32: Comparison plot showing the effect of stirring power on the mass transfer capacity coefficient.

Peter et al. (2005), making a similar assumption as was made in this thesis, determined mass transfer capacity coefficients on the basis of a negligible equilibrium sulphur concentration. In contrast to this study, however, Peter et al. (2005) calculated a single overall mass transfer coefficient for each heat sampled instead of separate mass transfer coefficients for the process conditions during the refining sequence. While model predictions were reported in close agreement with experimental data, it would seem that such an approach might lead to significant computation errors for heats undergoing mixed flow conditions. A further point of interest from Figure 4-32 is the significant difference in stirring energy within the Nucor Arkansas, Nucor Yamato and ArcelorMittal Dofasco ladles, despite all ladles having similar geometries. On an argon gas flow rate basis, Nucor Arkansas ladles (2 bottom porous plugs) had stirring rates 5-10 times greater than ladles at Nucor Yamato (1 bottom porous plug) (Peter et al., 2005), and 2-5 times greater than those at ArcelorMittal Dofasco (2 bottom porous plugs). Flow conditions within Nucor Arkansas ladles seem abnormally high when considering the fact that ArcelorMittal Dofasco operates just below the maximum possible bottom porous plug gas flow rate threshold, reported at 30 to 35 Nm^3 / hr (Turkdogan, 1996). Attempts by the present author to reconcile the difference in flow conditions have been unsuccessful.

4.5.5.2. Oxygen

Figure 4-33 shows a schematic illustration of the hypothetical oxygen concentration gradient in steel assuming metal phase control. In theory, and as shown, the bulk oxygen content in steel is dependent on the oxygen potential at both the slag-metal and metal-inclusion interfaces.

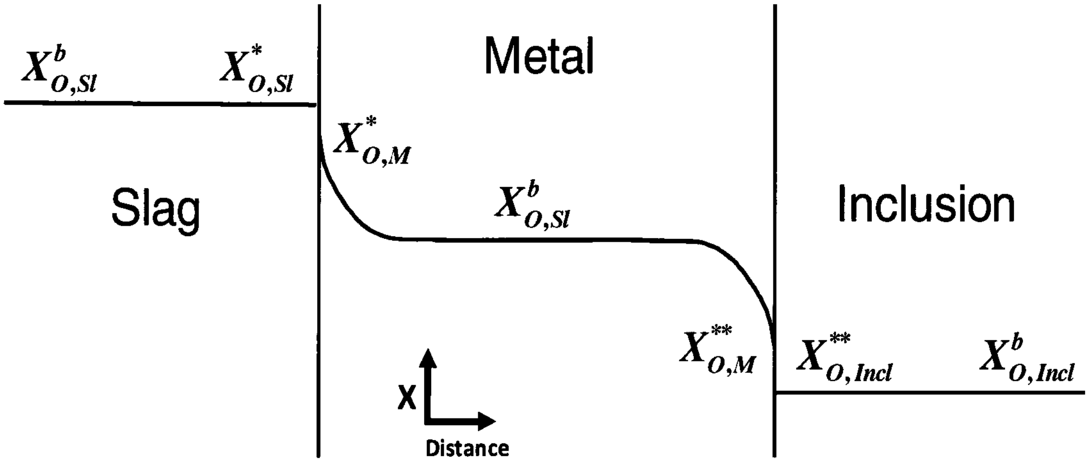

Figure 4-33: Schematic of the oxygen concentration gradients at the slag-metal and metal-inclusion interfaces for metal phase control.

The following first order rate equation expresses the change in bulk oxygen concentration with time:

$$\frac{dn_O}{dt}=k_O^* A^* C_{Vm}\left(X_{O,M}^* - X_{O,M}^b\right)-k_O^{**}A^{**}C_{Vm}\left(X_{O,M}^b - X_{O,M}^{**}\right)$$

(4-74)

where k_O^* and k_O^{**} are the mass transfer coefficients at the slag-metal and metal-inclusion interfaces, X_O^b, X_O^*, and X_O^{**} represent the mol fraction of oxygen at the interface or in the bulk in the metal, slag, or inclusion, A is the area at either the slag-metal or inclusion metal interface, and C_{Vm} is the molar concentration of metal. The first term on the right hand side of equation 4-74 represents the degree of reoxidation, while the second term represents the amount of oxygen removed by deoxidation.

Subagyo et al. (2002) proposed using separate integrated rate equations at the slag-metal and metal-inclusion interfaces for predicting dissolved oxygen content in steel:

$$\ln\left(\frac{\left[wt\%O_i\right]_j-\left[wt\%O_b\right]}{\left[wt\%O_i\right]_{j-1}-\left[wt\%O_b\right]}\right)=-k_O\Delta t \qquad (4\text{-}75)$$

$$\ln\left(\frac{\left[wt\%O_b\right]_j-\left[wt\%O_{be}\right]}{\left[wt\%O_b\right]_{j-1}-\left[wt\%O_{be}\right]}\right)=-k_O\Delta t \qquad (4\text{-}76)$$

where $\left[wt\%O_i\right]$, and $\left[wt\%O_b\right]$ represent the weight percent of oxygen at the interface and in the bulk, and $\left[wt\%O_{be}\right]$ the equilibrium oxygen concentration in the bulk metal. While the approach in equations 4-75 and 4-76 is correct, Subagyo & Brooks (2002) wrongly assumed that the same mass transfer coefficient (k_O) is valid at both interfaces. As is well documented within the literature, inclusion-metal surface area is far greater than slag-metal interfacial area. As a consequence, mass transfer rates are therefore significantly greater at the inclusion-metal interface than at the slag-metal interface.

Attempts to determine oxygen mass transfer coefficients from the industrial trials on the basis of equations 4-75 and 4-76 were unsuccessful. However, good agreement was found, Figure 4-34, when calculating dissolved oxygen concentration assuming equilibrium with dissolved aluminum in steel and pure alumina inclusions from the following expression.

$$[wt\%O]=10^{-4}\left(\left\{a_{Al_2O_3}K_{Al_2O_3}\right\}/[wt\%Al]^2\right)^{\frac{1}{3}} \qquad (4\text{-}77)$$

where $K_{Al_2O_3}$ is the equilibrium constant for the aluminum deoxidation reaction presented in Table 4-4, $[wt\%Al]$ the concentration of aluminum in the steel bulk, and $a_{Al_2O_3}$ the activity of alumina inclusions. Figure 4-34 makes clear that the dissolved oxygen content in aluminum killed steel is controlled by the inclusions in steel.

While the above procedure for estimating the dissolved oxygen content of steel proved accurate for all 41 aluminum killed heats (including several heats undergoing FeSi and CaSi treatment) sampled at ArcelorMittal Dofasco, its accuracy is ultimately limited to conditions where the activity of alumina is or close to unity. As such, a numerical procedure (Jahnsen, 2006; Gustafson, 2008) has been developed and included as Appendix E for estimating the dissolved oxygen activity in iron-silicon-manganese deoxidized steels. Future work will be undertaken to substantiate its application to non-aluminum killed heats.

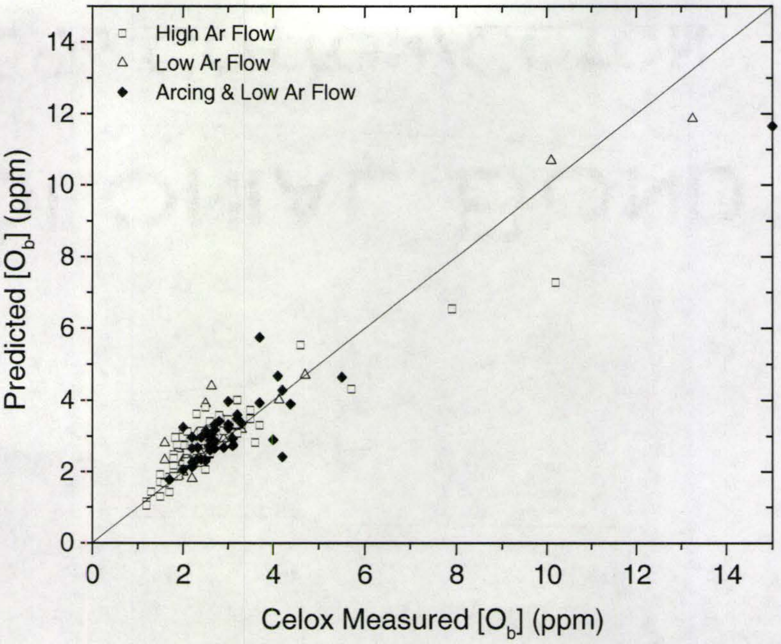

Figure 4-34: Comparison between Celox measured and predicted values of dissolved oxygen content in steel.

4.6. Model Validation

Representative results showing the agreement between experimental and model predictions are presented as Figures 4-35 to 4-37. Appendix F contains a complete listing of all simulated heats. Predicted results were simulated using the developed coupled multi-component kinetic model in combination with the unified interaction parameter formalism model and cell model summarized in Chapter 3. Steel and slag compositions were initialized using the chemical analysis measurement results taken after deoxidation. Metal phase mass transfer coefficients for all elements in steel were assumed to follow the empirical relation given in Figure 4-31, while slag phase mass transfer coefficients were calculated by fitting the ratio of $k_m^M \ / \ k_{sl}^{M_xO_y}$ to the experimental results.

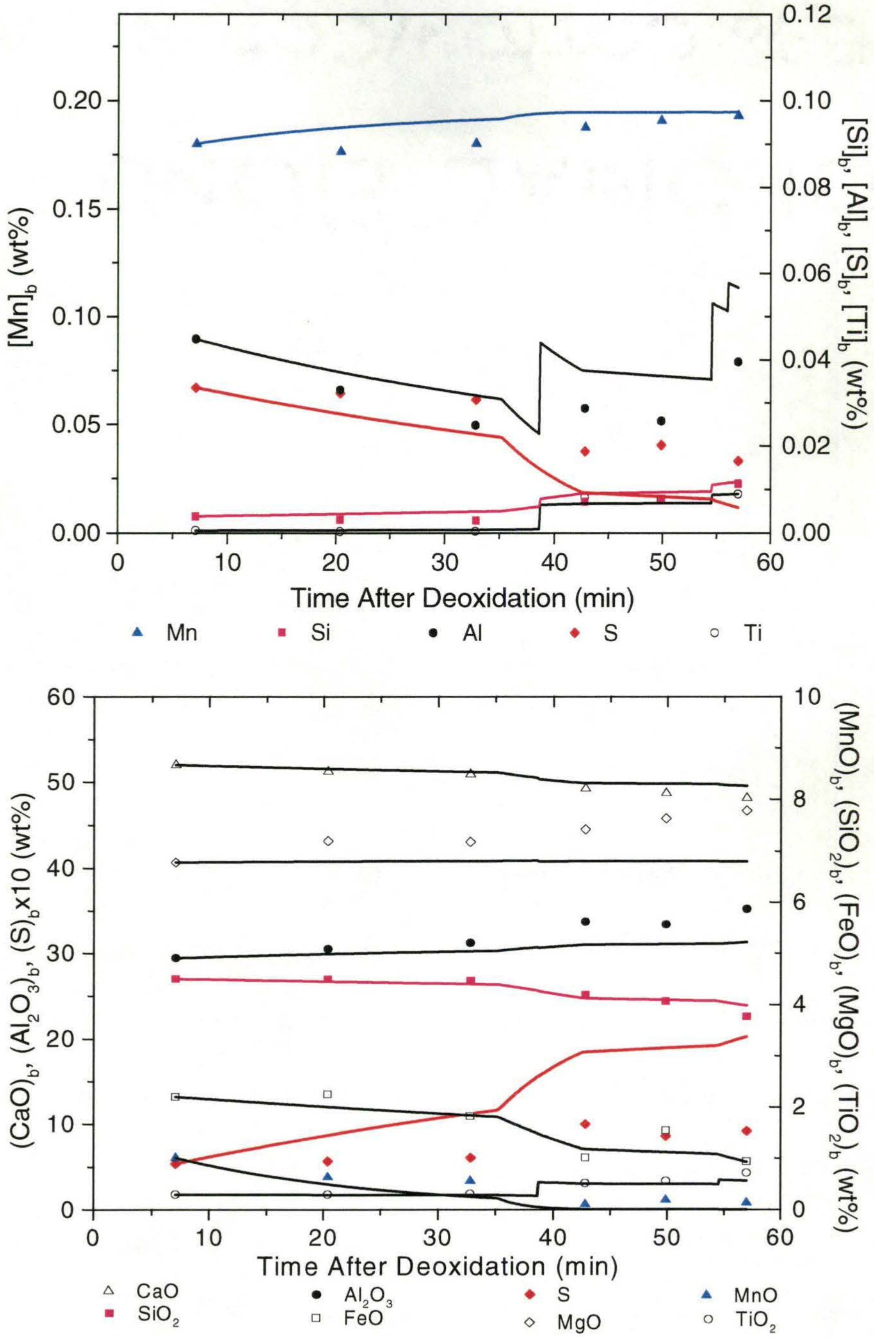

Figure 4-35: Comparison of experimental and model predicted results for Heat 11 using fitted slag phase mass transfer coefficients. (top) Steel concentration profile, (bottom) slag concentration profile.

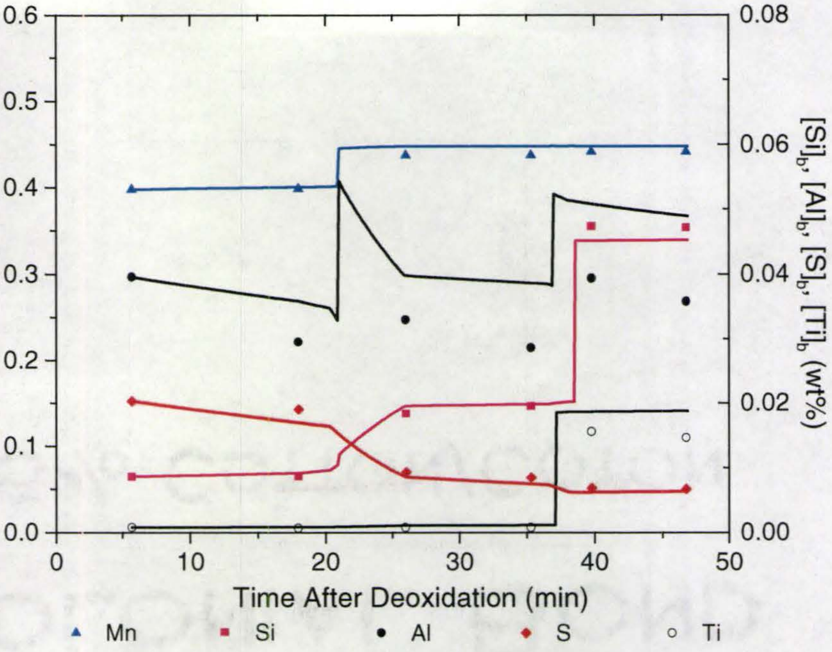

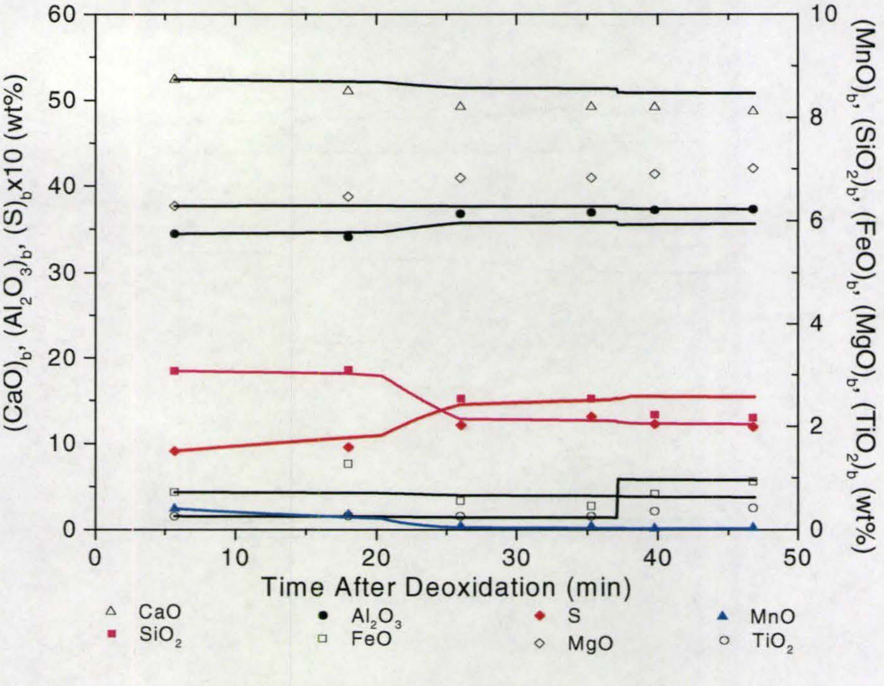

Figure 4-36: Comparison of experimental and model predicted results for Heat 23 using fitted slag phase mass transfer coefficients. (top) Steel concentration profile, (bottom) slag concentration profile.

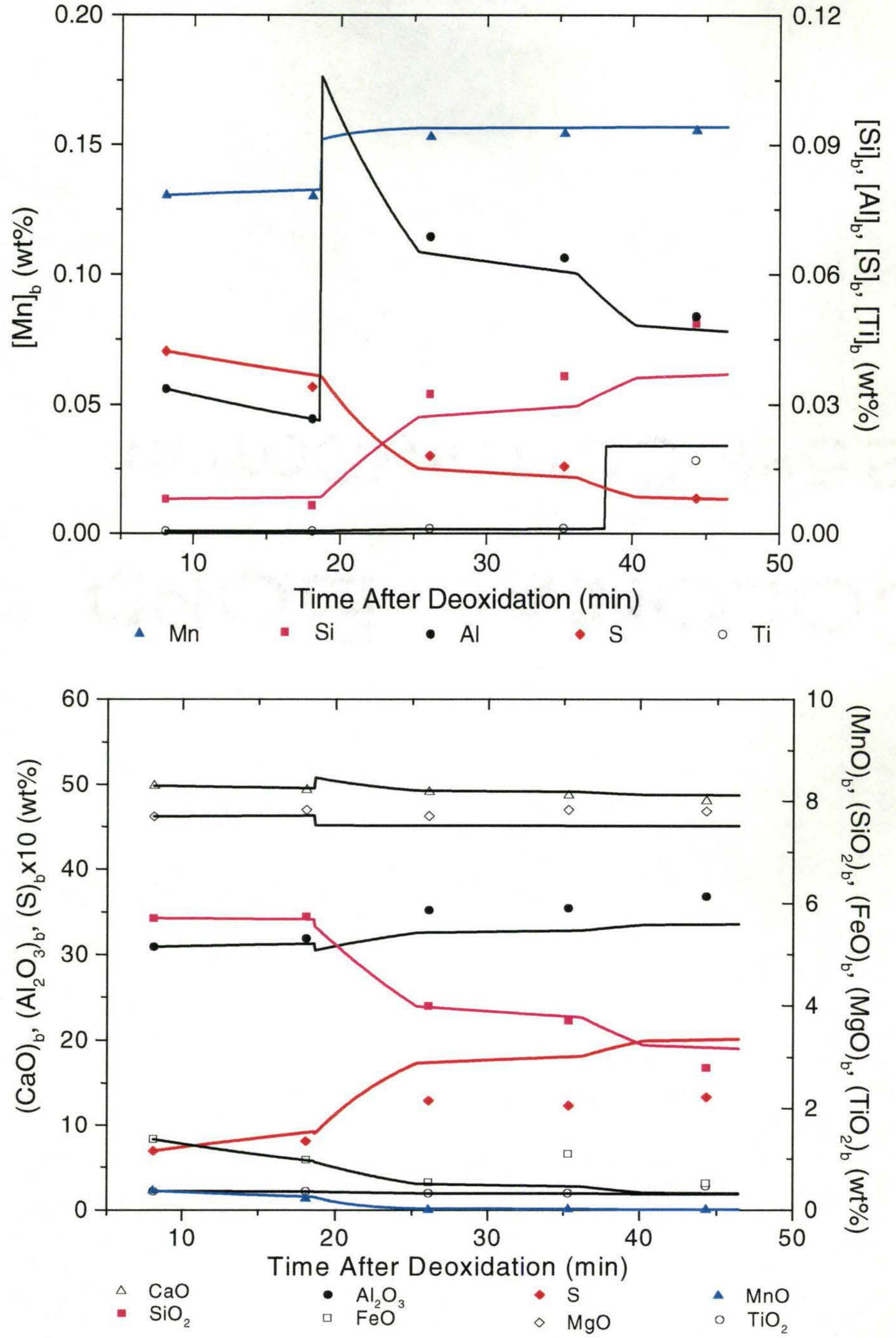

Figure 4-37: Comparison of experimental and model predicted results for Heat 40 using fitted slag phase mass transfer coefficients. (top) Steel concentration profile, (bottom) slag concentration profile.

Figure 4-38 to 4-42 summarize the cumulative modelling results. Key notable differences between model predictions and experimental results include the sulphur and alumina contents in slag. As previously discussed, deviations in slag sulphur content is likely due to loss of sulphur to the atmosphere, refractory and / or inclusions. Results from this study indicate that as much as 30% sulphur on average (5.9 kg of sulphur / tonne of slag) may be lost during refining. The loss of sulphur to the atmosphere is supported by the fact that at iron and steelmaking temperatures elemental sulphur is stable only as a gas (Bodsworth, 1972). The agreement between predicted and experimental alumina content in slag, however, was found dependent on the variability of the undetermined slag composition content (determined from chemical analysis). If the undetermined slag composition content remained near constant during refining then good agreement typically followed, otherwise significant deviations were observed.

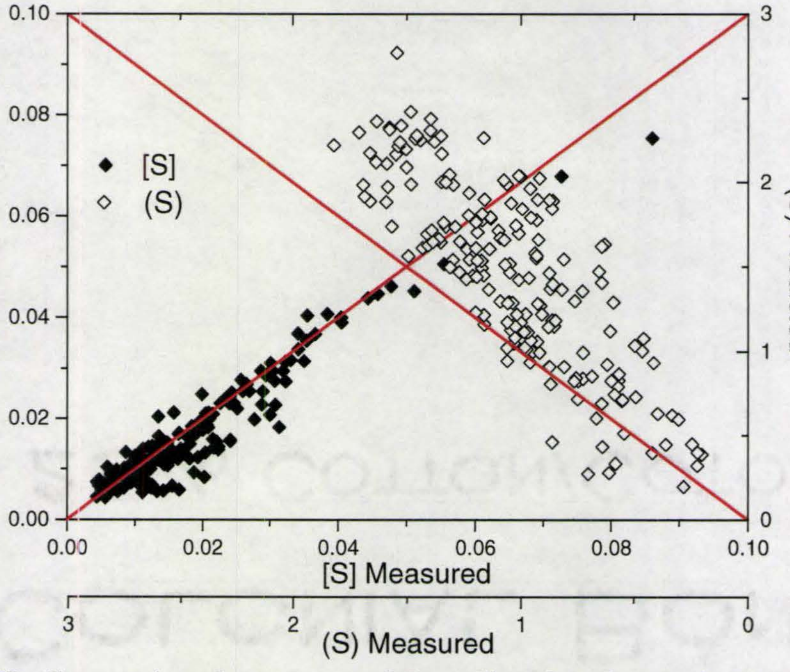

Figure 4-38: Comparison between model predicted and experimental sulphur content in steel and slag.

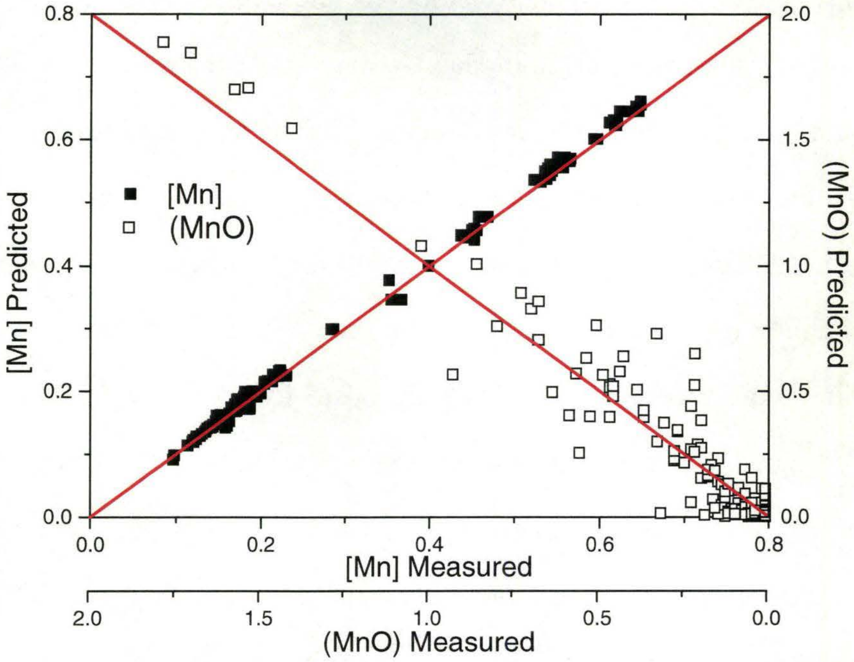

Figure 4-39: Comparison between model predicted and experimental Mn content in steel and MnO content in slag.

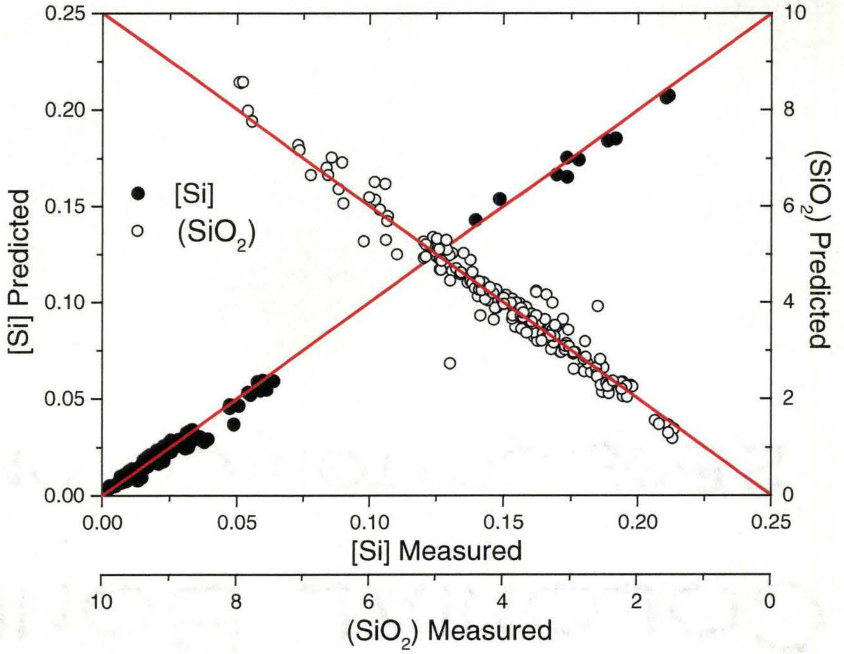

Figure 4-40: Comparison between model predicted and experimental Si content in steel and SiO_2 content in slag.

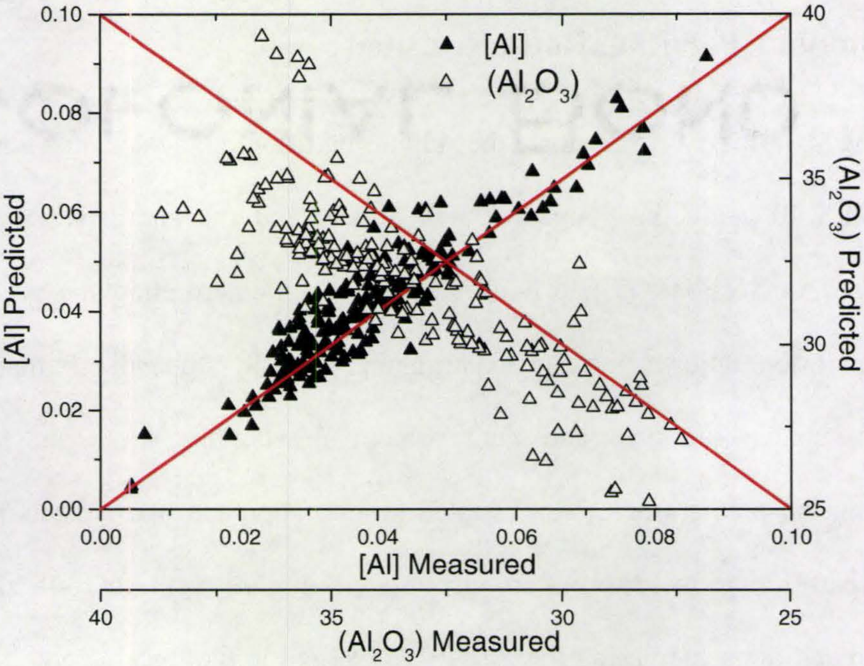

Figure 4-41: Comparison between model predicted and experimental Al content in steel and Al_2O_3 content in slag.

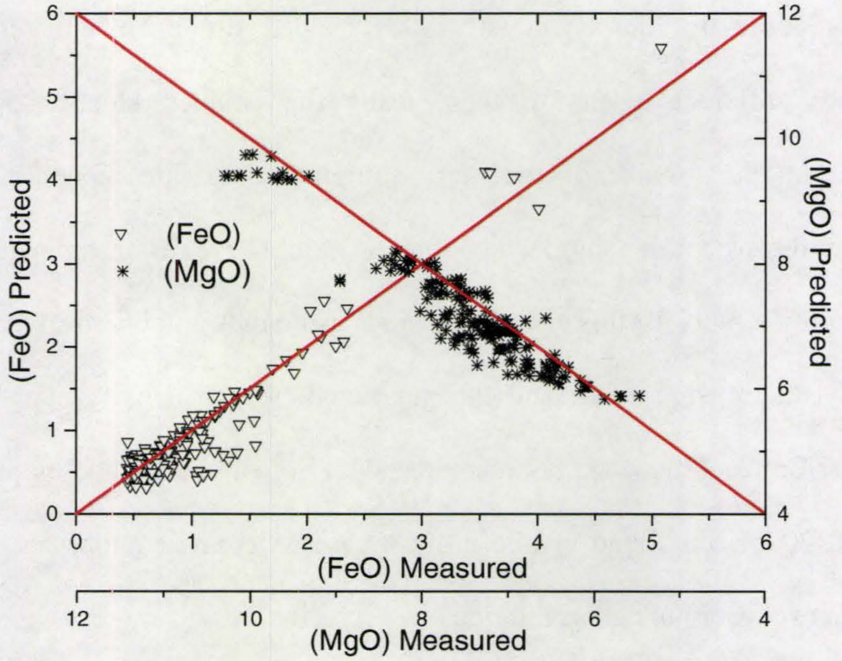

Figure 4-42: Comparison between model predicted and experimental FeO and MgO content in slag.

4.7. Discussion

4.7.1. Sulphur Partition Ratio Revisited

Figure 4-43 to 4-45 compare the sulphur partition ratio calculated for heats 11, 23, and 40 using the coupled kinetic model and the alternative methods summarized in Section 4.5.4.1. It is apparent when interpreting the predicted sulphur partition ratios using the experimental data in Appendix F that both aluminum content in steel and FeO content in slag are the main factors influencing the predictions of the coupled kinetic approach used in this thesis. Sulphur partition ratios show step increases in Figure 4-43 to 4-45 due to aluminum additions decreasing the activity of oxygen in the metal at equilibrium with the slag. Further seen is that predicted sulphur partition ratios using the method proposed by Jonsson et al. (1998) yielded similar, albeit sometimes significantly different results to those using the coupled kinetic approach. Therefore, in the absence of the more complicated kinetic model it seems reasonable to consider the approach of Jonsson et al. (1998) as an estimate of the sulphur partition ratio. To this end, the methods using bulk sulphur measurements, Celox oxygen measurements, and the interfacial oxygen activity approach of Subagyo & Brooks (2005) are not recommended. In fact, the method by Subagyo & Brooks (2005) was found invalid in most cases, yielding equilibrium sulphur contents in excess of bulk concentrations.

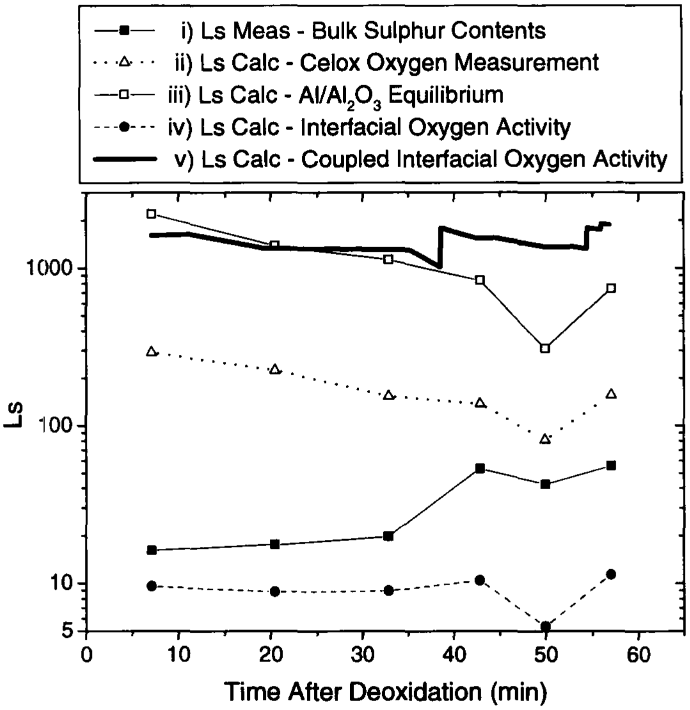

Figure 4-43: Comparison between the multi-component kinetic model predicted against measured / calculated sulphur partition ratios (Heat 11).

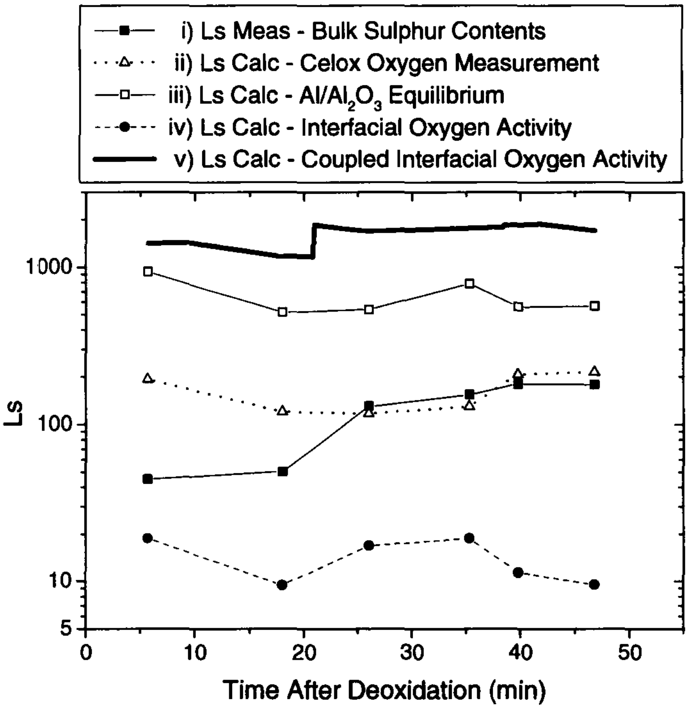

Figure 4-44: Comparison between the multi-component kinetic model predicted against measured / calculated sulphur partition ratios (Heat 23).

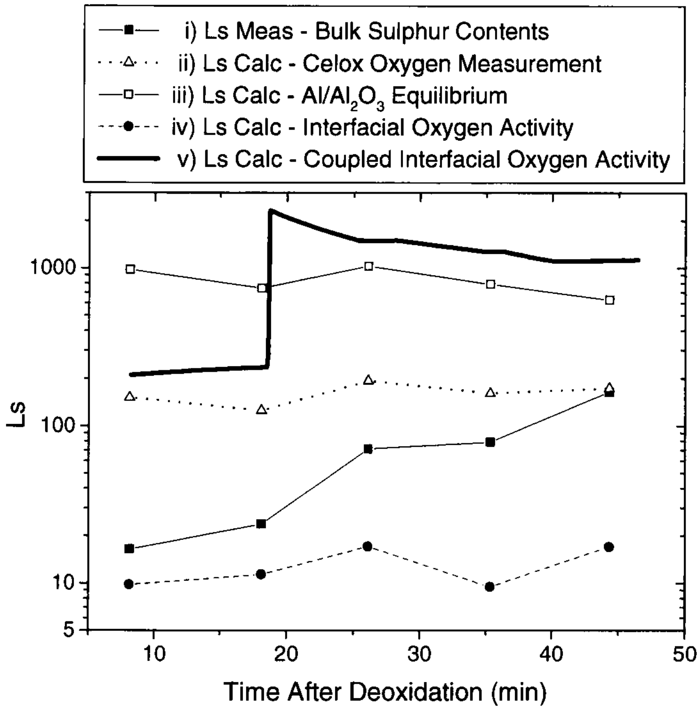

Figure 4-45: Comparison between the multi-component kinetic model predicted against measured / calculated sulphur partition ratios (Heat 40).

The high sulphur partition ratios calculated using the coupled kinetic model of Robertson et al. (1984) support the original assumption of negligible equilibrium sulphur content made when calculating the mass transfer correlation shown in Figure 4-31.

4.7.2. Slag Phase Mass Transfer Coefficients

A key assumption within this study was that slag phase mass transfer coefficients were taken as ratios of the metal phase mass transfer correlation in Figure 4-31, where the stated mass transfer correlation for sulphur in an argon-gas stirred ladle was assumed valid for all elements in steel. While the assumption that metal phase mass transfer coefficients in steel are identical is an approximation, its basis is well supported by the literature. Geiger & Poirer (1980) state that the remarkable characteristic of diffusion in liquid metals is that diffusion coefficient values are all approximately the same order of magnitude. The picture, however, is more uncertain in molten slags as relatively little diffusion data are available.

Peter et al. (2005) compared the results of two different Metsim models: (i) allowing for the determination of slag phase mass transfer coefficients, and (ii) assuming perfect mixing within the slag phase. Results from their analysis revealed no significant differences between model predictions for either case. The authors explained the similarity between the models on the basis of the following observations: (i) the slag phase was well-mixed, (ii) slag volumes were low, and (iii) slag was easily emulsified. The generalized explanation offered by Peter el al. (2005), however, fails to explain the results from the present study despite the similar process conditions at Nucor Arkansas, Nucor Yamato and ArcelorMittal Dofasco. Further, the conclusions of Peter et al. (2005) appear to conflict with the fundamental observations previously documented within the literature.

Figure 4-46, taken from the work of Riboud & Lucas (1981), summarizes the concentration profiles perpendicular to a slag-metal interface observed during their investigation into the influence of mass transfer on surface phenomena. Liquid metal (iron-aluminum system) and liquid slag (CaO-SiO_2-Al_2O_3) were heated at the same temperature and brought into contact. Quenched samples taken during intense slag-metal reaction were analyzed using an electron microprobe.

As seen in Figure 4-46, Riboud & Lucas (1981) observed enrichment in Al_2O_3 reaction product all along the slag-metal interface, and within a very short distance from the metal (5-15 μm).

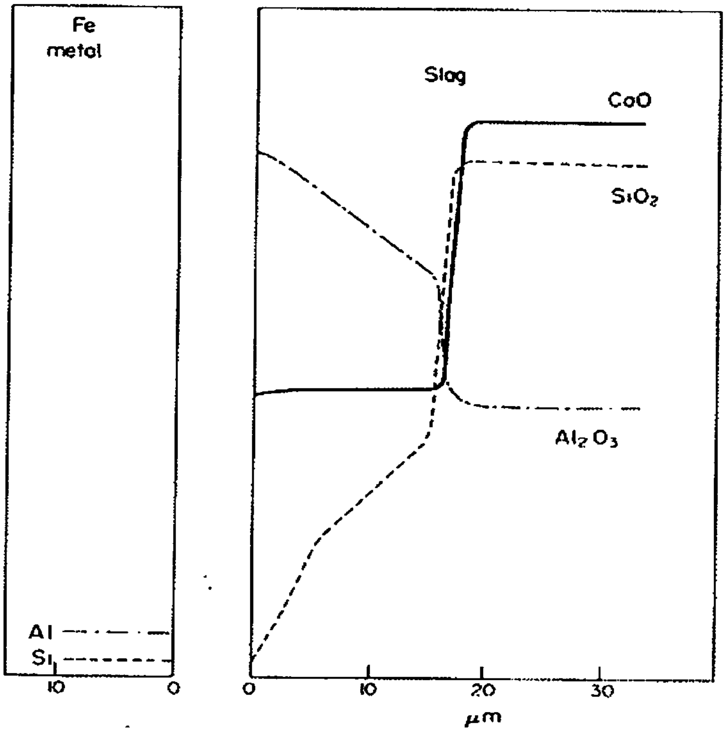

Figure 4-46: Concentration profiles, perpendicular to the interface, obtained with an electron microprobe: Fe-Al alloy reaction with slag (40wt% CaO; 40wt%SiO_2; 20wt%Al_2O_3)

Summarizing the results within the literature, Geiger & Poirer (1980) state that the curious result that has not yet been satisfactorily explained is why the self-diffusion coefficient for oxygen in basic slags is greater than the self-diffusion coefficient for calcium in the same slag. Although oxygen is known to have a self-diffusion coefficient greater than aluminum and silicon in the same slag, this difference was explained on the basis that silicon is tied up as SiO_4^{4-} ions and aluminum as possibly AlO_3^{3-} ions which do not diffuse as easily as smaller O^{2-} ions (Turkdogan, 1955; Ward & Salmon, 1960). In contrast to the findings of Peter et al. (2005), these observations suggest that slag phase mass transfer rates play an integral role in reaction kinetics of industrial processes.

Kitamura and coworkers (1991) used a coupled reaction model (Robertson, 1984) to investigate the kinetics of hot metal dephosphorization and estimated slag phase mass transfer coefficients as ratios of the metal phase mass transfer correlation determined from their experiments. This idea is similar to the original suggestion by Robertson et al. (1984, 1984b), who employed the technique when modelling the experimental desulphurization work of Ramachandran et al. (1956) and Kim (1978), and in their own simultaneous desulphurization and dephosphorization experiments (Ohguchi et al., 1984). Kitamura and coworkers (1991) evaluated slag phase mass transfer coefficients in a similar manner as was done in this thesis by numerically selecting values that explained experimentally obtained dephosphorization and FeO compositional curves. Reported k_m / k_{sl} ratios were between 5-10, with the dependence of k_m and k_{sl} on temperature and stirring being almost the same. It is unclear from the work of Kitamura and coworkers (1991) whether the same k_{sl} values that were determined from fitting the dephosphorization and FeO concentration curves were valid for other slag components.

Figure 4-47 to 4-49 summarize the key k_m / k_{sl} mass transfer ratios used for modelling heats 11, 23, and 40. To the authors' knowledge this is the first time that separate k_m / k_{sl} ratios have been used to describe the different slag-metal equilibria reactions. An important finding of the study is that constant mass transfer ratios were found by and large sufficient for describing the state within the LMF. As shown in Figure 4-49, the slag phase mass transfer constant for FeO required updating 12 minutes after deoxidation due to the addition of aluminum into the ladle. The mass transfer rate constant was then subsequently held constant for the remainder of the simulation.

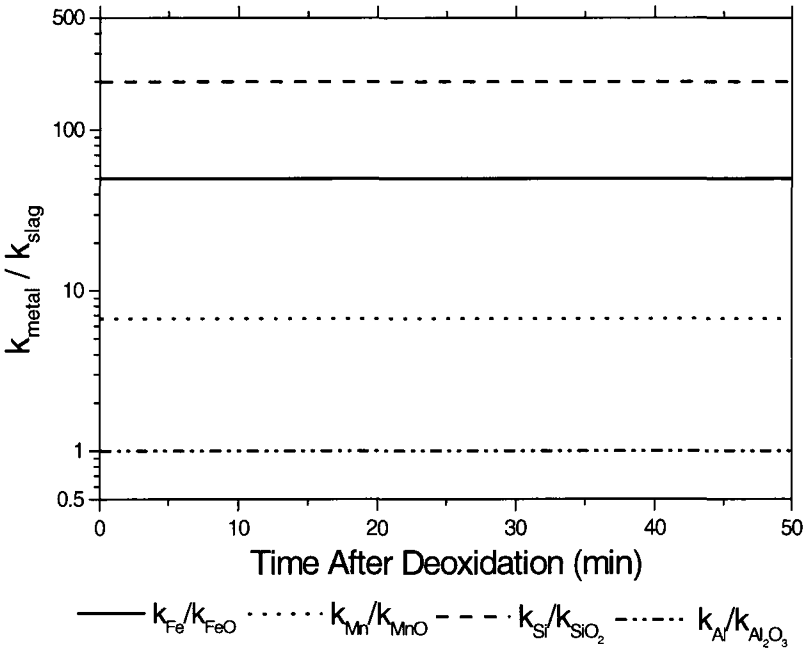

Figure 4-47: k_m / k_{sl} mass transfer ratio profile for Heat 11.

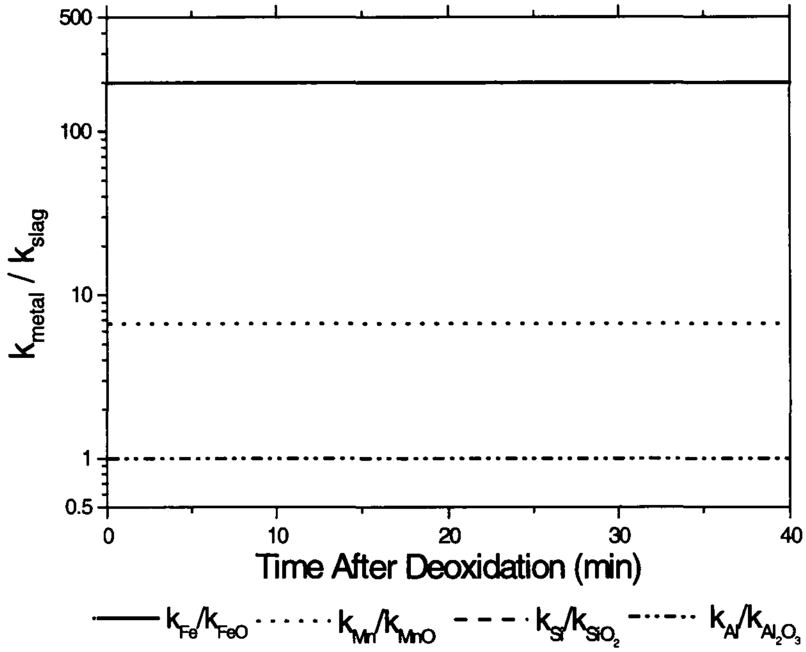

Figure 4-48: k_m / k_{sl} mass transfer ratio profile for Heat 23.

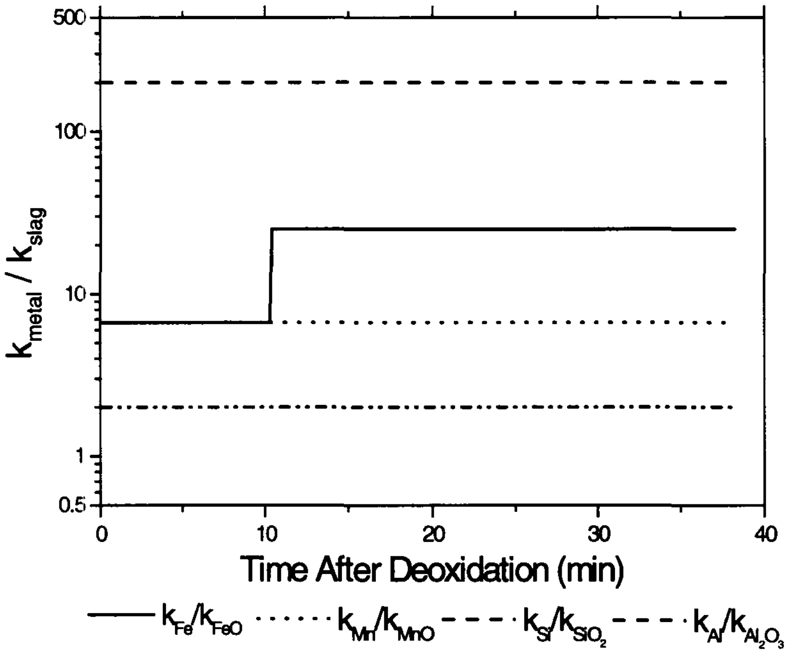

Figure 4-49: k_m / k_{sl} mass transfer ratio profile for Heat 40.

The good agreement between model predictions and experimental results (Figure 4-38 to 4-42) serve to substantiate the assumption of separate k_m / k_{sl} mass transfer ratios for the different slag-metal equilibria reactions considered in this work. Table 4-8 presents a summary of the slag phase mass transfer coefficients statistics for all experimental heats sampled. Variation within the data was due to process conditions within the ladle, namely: initial slag and metal compositions, stirring rate, and electrical arcing.

Table 4-8: Slag phase mass transfer ratio summary statistics

	k_m^{Fe} / k_{sl}^{FeO}	k_m^{Mn} / k_{sl}^{MnO}	k_m^{Ti} / $k_{sl}^{TiO_2}$	k_m^{Si} / $k_{sl}^{SiO_2}$	k_m^{Al} / $k_{sl}^{Al_2O_3}$
Average	115	7	200	125	1
Std Dev	65	1.25	-	55	0.25
Min	7	4	200	25	1
Max	200	13	200	200	2.5

The fitted FeO mass transfer ratios determined from this study during non-arcing conditions and with greater than 1wt% FeO content in slag were found to be in general agreement with the previously published results of Kitamura et al. (1991). It was observed, however, that significantly higher k_m / k_{sl} mass transfer ratios for FeO were required to fit the experimental plant data during periods of electrical arcing and for slag FeO contents less than 1wt%. The influence of electrical arcing on the oxygen potential within the melt was presented previously in Section 4.5.2.1 where the dissolved oxygen content was found to increase at a rate of 0.11 ppm / minute of power on time and FeO content in slag was reported to have increased 80% of the time. While current study results are unable to explain the kinetics of oxygen absorption during electrical heating, it would seem probable that arc heating has a similar effect on oxygen as has previously been reported for nitrogen (Takada & Nakamura, 1978; Kaneko, Sano & Matsushita, 1976; Kemeny, McLean & Sommerville, 1986; Meredith & Stenkvist, 1986). These researchers demonstrated that nitrogen first dissociates in the presence of electric arcs into its atomic form before being readily absorbed into the molten steel.

An interesting outcome from the study was that MnO behaviour in slag was accurately described using a near constant k_m / k_{sl} mass transfer ratio, and at no time during the industrial trials did its content in slag (in contrast to the FeO content) increase during electrical heating. While it is difficult to reach firm conclusions on the basis of this observation, one possible explanation for the preferential reoxidation of FeO over MnO may be due to the significantly higher iron activity in liquid steel as compared with dissolved manganese.

The following slag phase mass transfer coefficient correlations were evaluated using linear regression from the fitted mass transfer ratio results. Reported slag phase mass transfer coefficients have units of volume per unit of time (m^3/sec).

i) Mass Transfer Coefficient Correlation for FeO:

$$\log\left(k_{sl}^{FeO}\right) = -4.467 + 0.02\varepsilon + 0.36\left(wt\%FeO\right) - 0.47\left(Power\ On/Off\right)$$
$$\left(R^2 = 0.65\right) \tag{4-78}$$

ii) Mass Transfer Coefficient Correlation for MnO:

$$k_{sl}^{MnO} = [-73.28 + 8.86\varepsilon] \text{ x } 10^{-5} \quad (R^2 = 0.91) \tag{4-79}$$

iii) Mass Transfer Coefficient Correlation for Al_2O_3:

$$k_{sl}^{Al_2O_3} = [-465.5 + 85.82\varepsilon] \text{ x } 10^{-5} \quad (R^2 = 0.89) \tag{4-80}$$

As shown by equation 4-78, the mass transfer coefficient correlation for FeO was found in reasonable agreement with plant data, where stirring power, FeO content in slag, and an indicator variable for electrical heating were the independent variables. The $(Power\ On/Off)$ indicator variable was assumed to have a value of 1 during arcing periods and 0 during non-arcing periods. As is evident from their correlation coefficients having values near unity, the mass transfer coefficient correlations for MnO and Al_2O_3 are well modeled using stirring power as the only independent variable. Numerous attempts to derive a relationship for the mass transfer coefficient of SiO_2 as a function of process conditions were unsuccessful. As a result, an average slag phase mass transfer coefficient for SiO_2 is recommended for future studies:

$$k_{sl}^{SiO_2} = 3.06 \text{ x } 10^{-4} \text{ m}^3\text{/sec} \tag{4-81}$$

4.7.3. Application of the Model in a Control System

This chapter has presented a detailed process model for describing the kinetics within an industrial ladle metallurgical furnace. The model is based on fundamental principles but also dependent on slag-metal mass transfer correlations that were estimated using plant data. Under optimal process conditions, the model allows for the accurate and continuous real-time estimation of parameters that would otherwise go unmeasured or infrequently measured. Further benefits from the proposed model include the improvement of alloy addition and the development of optimum deslagging practices.

The primary drawback of the kinetic model, however, is the empirical nature of the slag-metal phase mass transfer correlations that were introduced to approximate relationships where determination of the true mechanisms were either too complicated or unavailable. Figure 4-50 to 4-52 compare the experimentally determined and kinetic model results using the developed mass transfer correlations. While these results remain in overall satisfactory agreement with the experimental data, it is apparent that significant prediction errors (most probably for Si-SiO_2 concentrations) may occur when extrapolating the model to new grades or process conditions. As such, Chapter 6 of this thesis introduces the Kalman filter, a state estimation algorithm capable of modelling plant-model mismatch, as a potential means for improving kinetic model performance.

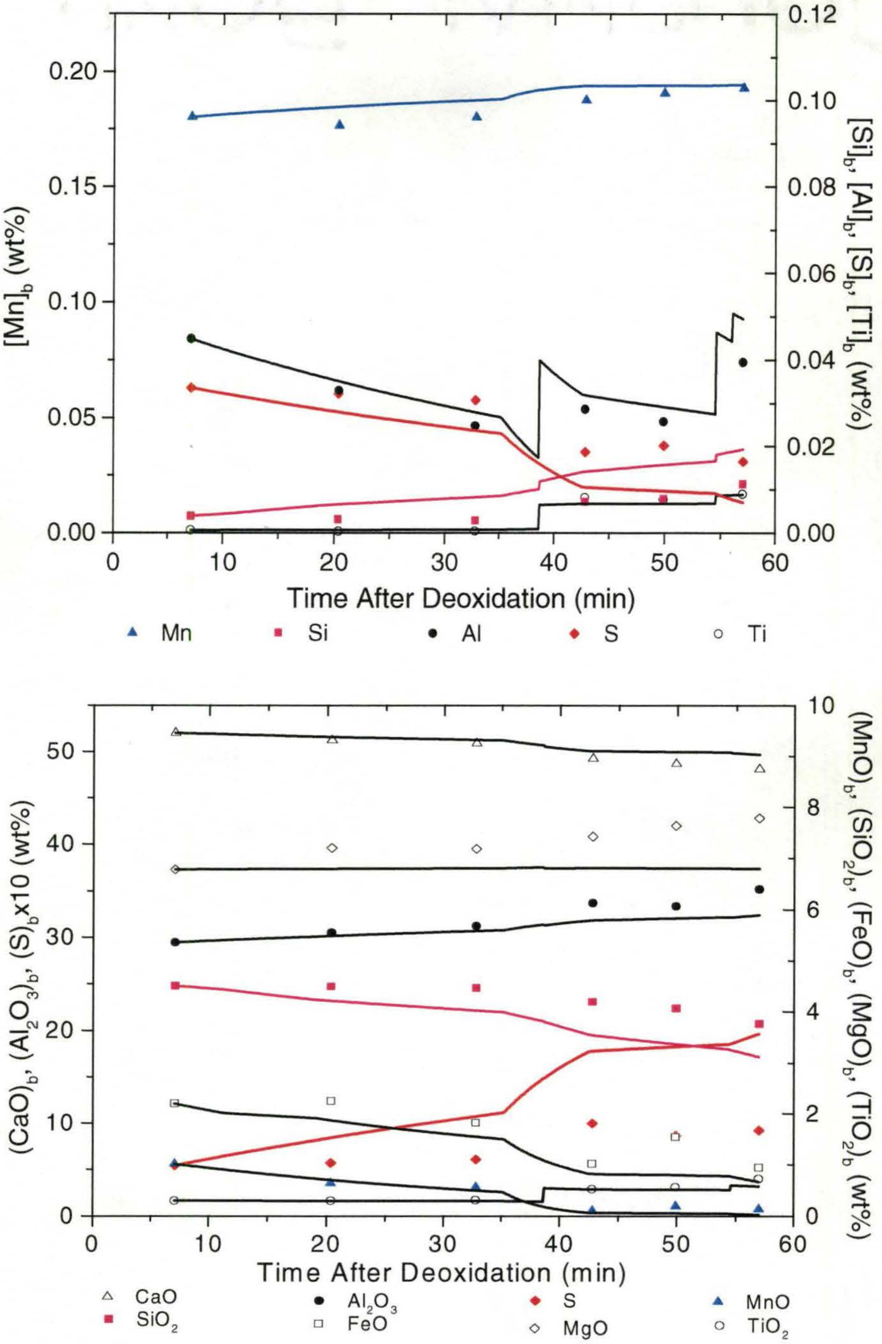

Figure 4-50: Comparison of experimental and model predicted results for Heat 11 using empirically derived slag phase mass transfer correlations. (top) Steel concentration profile, (bottom) slag concentration profile.

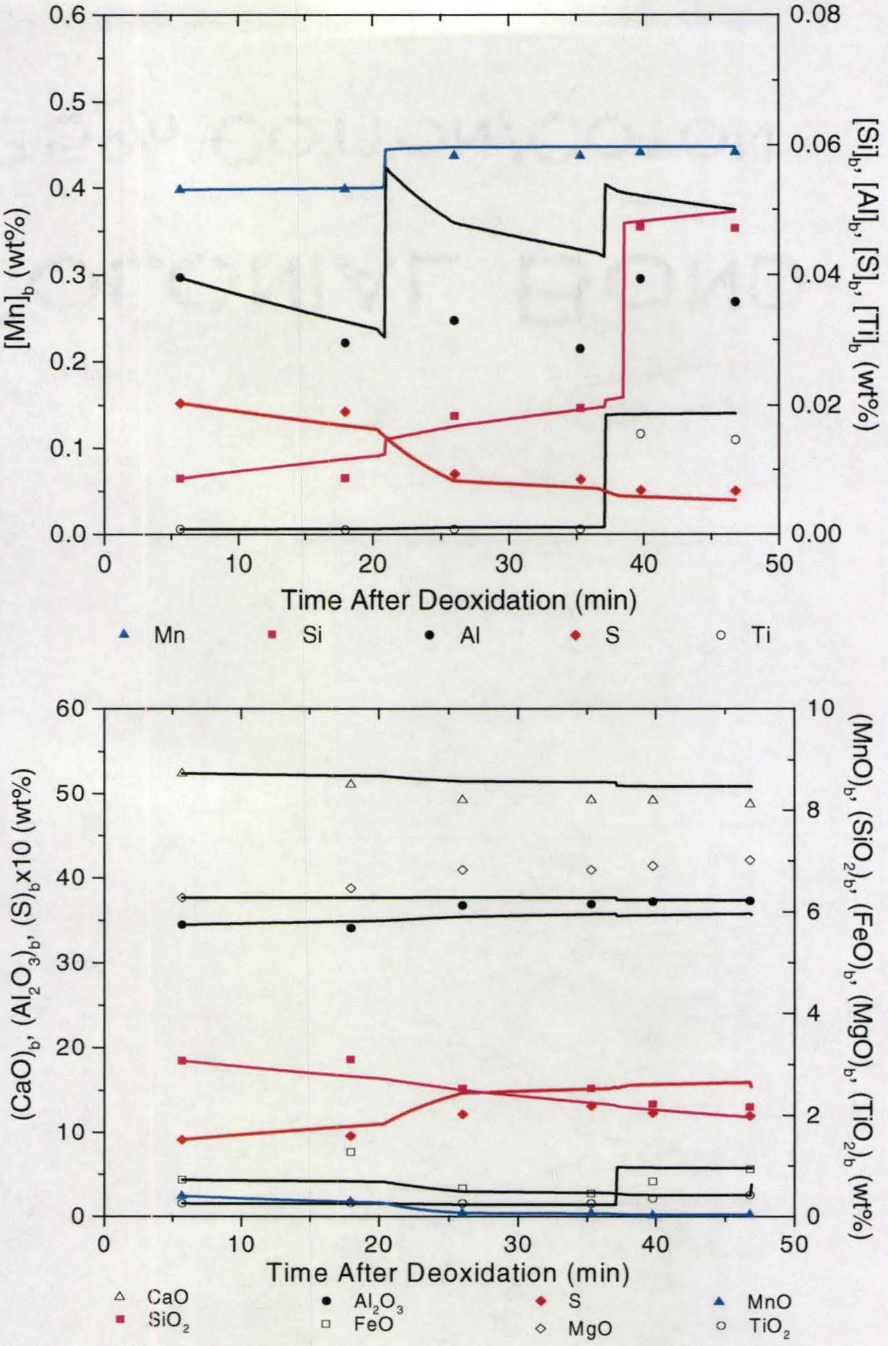

Figure 4-51: Comparison of experimental and model predicted results for Heat 23 using empirically derived slag phase mass transfer correlations. (top) Steel concentration profile, (bottom) slag concentration profile.

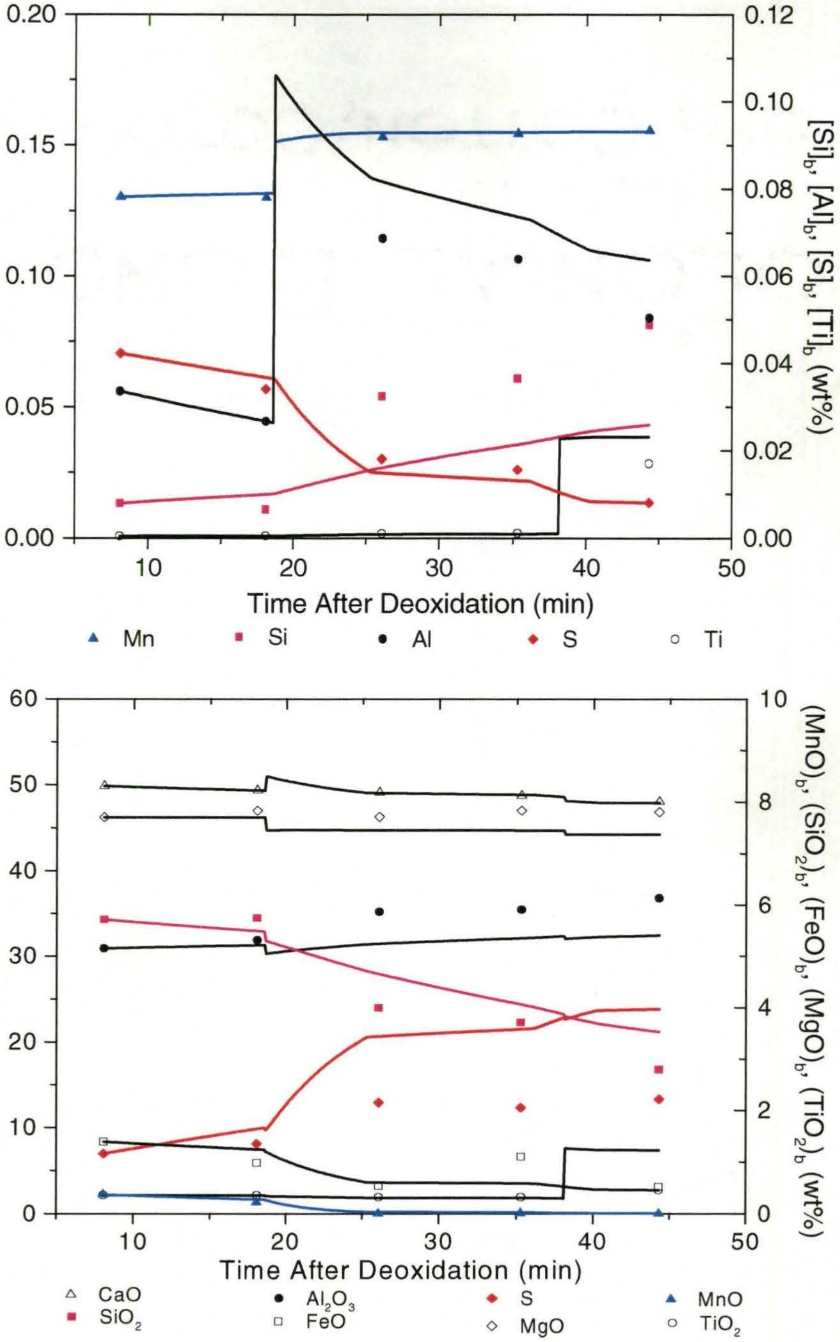

Figure 4-52: Comparison of experimental and model predicted results for Heat 40 using empirically derived slag phase mass transfer correlations. (top) Steel concentration profile, (bottom) slag concentration profile.

Chapter 5

NON-METALLIC INCLUSIONS

5.1. Introduction

Steelmaking is a process of controlled oxidation. In some unit operations (BOF & EAF) oxygen is introduced to selectively oxidize unwanted elements, while in other unit operations (LMF & VD) oxygen is removed by the addition of deoxidizers. It is largely a result of the deoxidation practice that inclusions form in steel. The two main categories of non-metallic inclusions are: indigenous and exogenous. The former group occurs as a result of reactions taking place in steel, whereas the latter group results from unintended process events. While the presence of inclusions in steel is inevitable, efforts are generally taken to minimize and control their properties in order to limit problems during liquid metal handling operations and to enhance the mechanical properties of steel (Kay & Junpu, 1988). Key areas of research on the subject of non-metallic inclusions include: inclusion formation, growth, evolution, and modification. Despite the significant amount of research work undertaken, the subject of non-metallic inclusions remains frequently misunderstood. Hilty & Kay (1985) attributed the resulting confusion both to the inherent complexity of the subject matter and in large part on the connotation attendant on the word 'inclusions' itself. In the context of this thesis, inclusions will be considered as a form of slag.

The objective of this chapter is to better elucidate the behaviour of non-metallic inclusions during ladle refining. The effect of different process operating conditions on inclusion behaviour will be discussed, and a comparison of the inclusion characteristics between calcium treated and non-calcium treated aluminum killed industrial heats will be undertaken. Secondary goals of this chapter are to review the application of a simple method for determining calcium modified inclusion composition in the absence of microscopic identification techniques. Inherent uncertainties when developing inclusion models will also be discussed.

5.2. Literature Review

5.2.1. Thermodynamics of Deoxidation

Deoxidation is achieved within the steelmaking industry via the addition of deoxidants. Added deoxidants (M) have a strong affinity for oxygen and lower its residual content according to the following generalized reaction:

$$x\underline{M} + y\underline{O} = M_xO_y \tag{5-1}$$

where the equilibrium constant for equation 5-1 may be expressed as:

$$K_{M_xO_y} = \frac{a_{M_xO_y}}{h_M{}^x h_O{}^y} \tag{5-2}$$

The activity of the precipitated deoxidation product in equation 5-2 is represented by $a_{M_xO_y}$, while the Henrian activities for oxygen and added deoxidant in steel are given as h_O and h_M. Commonly used deoxidants within the industry include, manganese, silicon and aluminum. Figure 5-1 summarizes the deoxidizing power of selected deoxidants. The observed non-linearity of the equilibrium curves in Figure 5-1 may be attributed to the interaction of solute elements in steel. Deoxidation by a single element is regarded as simple deoxidation, whereas complex deoxidation involves the addition of multiple deoxidizers. Frequently used industrial deoxidizer combinations include: Si-Mn, Si-Mn-Al, Ca-Si, and Ca-Si-Al. Advantages of complex deoxidation over simple deoxidation include lower attainable dissolved oxygen contents and larger deoxidation products that facilitate inclusion removal (Ghosh, 2001).

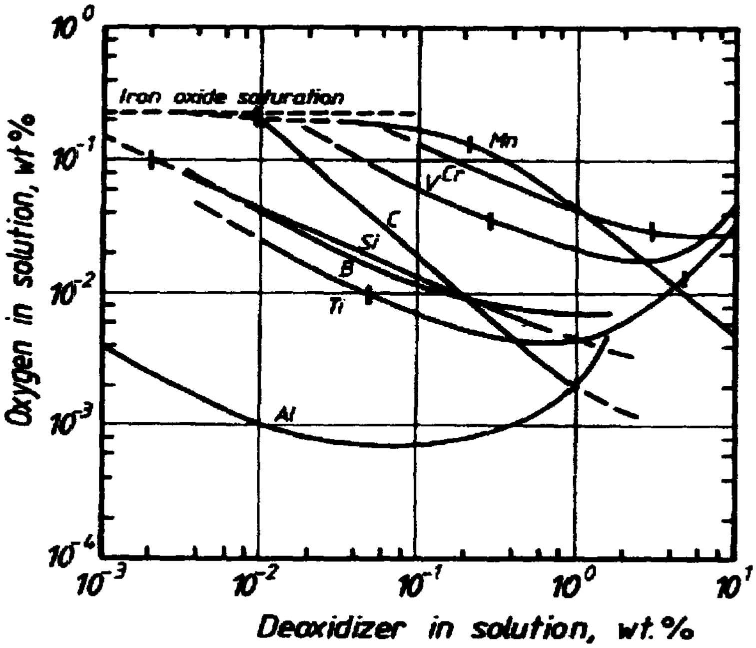

Figure 5-1: Deoxidation equilibria for selected deoxidizers. (Deo & Boom, 1993)

5.2.2. Lowering the Oxygen Activity in Steel

The total oxygen content of steel is considered as being comprised of two parts, the sum of the dissolved and bound (associated with inclusions) oxygen contents. Figure 5-2 illustrates the typical concentration behaviour profile for oxygen during the steelmaking process. As shown, and in accordance with equation 5-1, deoxidation results in the decrease of dissolved oxygen content. This decrease comes at the cost of increased oxide inclusions, which are generally slow to be removed from steel (Turkdogan, 1973; Engh et al., 1975; Lange, 1999). As seen in Figure 5-2, the total oxygen content is at its minimum when the content of non-metallic inclusions is also at its minimum. Further illustrated in Figure 5-2 is the increased frequency of inclusions in solid steel as compared to liquid steel. This difference is due to the lower oxygen solubility of solidified steel (Plockinger & Wahlster, 1960).

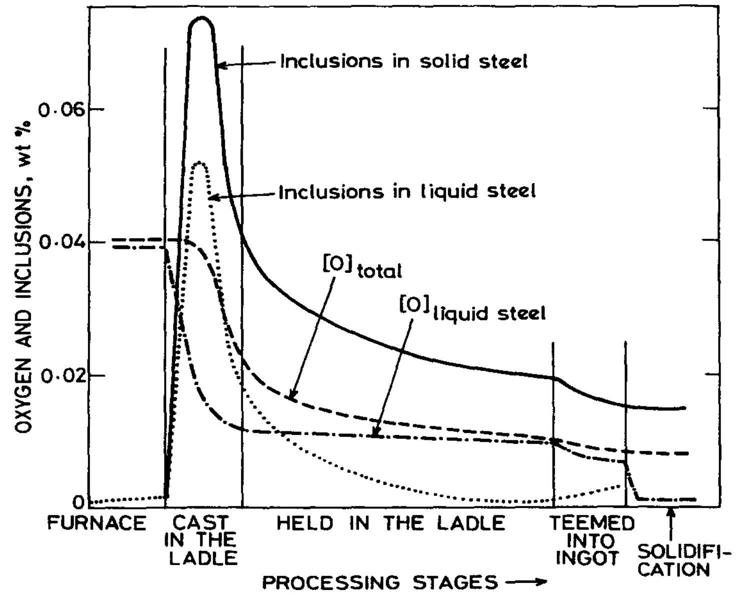

Figure 5-2: Change of oxygen and inclusion content of steel from furnace to ingot. (Plockinger & Wahlster, 1960)

A complicating factor in the effective control of oxygen within industrial operations concerns reoxidation. Reoxidation is the term used to describe the increase in steel oxygen content after deoxidation; the increase in oxygen content occurs due to the exchange of oxygen from regions of high oxygen potential to regions of low oxygen potential. Schwerdtferger (1993) identified the atmosphere, top slag, and refractory lining as possible sources of reoxidation. He further noted that stirring may, under sub-optimal conditions, promote reoxidation. In more recent work, Dekkers (2002) reported no proof of atmospheric reoxidation during his detailed investigation of inclusions on industrial sampled heats at Sidmar (Ghent, Belgium). However, it is unclear from the work of Dekkers (2002) whether electrical heating, which was demonstrated in Chapter 4 of this thesis to have a significant influence on the oxygen potential within the melt, occurred during his trials. Lange (1999) summarized the consequences of reoxidation as: (i) potential nucleation of new inclusions, (ii) uncontrolled variation of alloy composition in steel, (iii) increased probability of nozzle blockage, and (iv) poor desulphurization kinetics.

5.2.3. Influence of Inclusion Composition on Nozzle Clogging

The continuous casting of aluminum killed steels is subject to nozzle clogging problems due to the precipitation and sintering of solid alumina inclusions in nozzle refractories. Figure 5-3 presents an illustration of a typical accretion that may form within the submerged entry nozzle (SEN) and / or tundish nozzle.

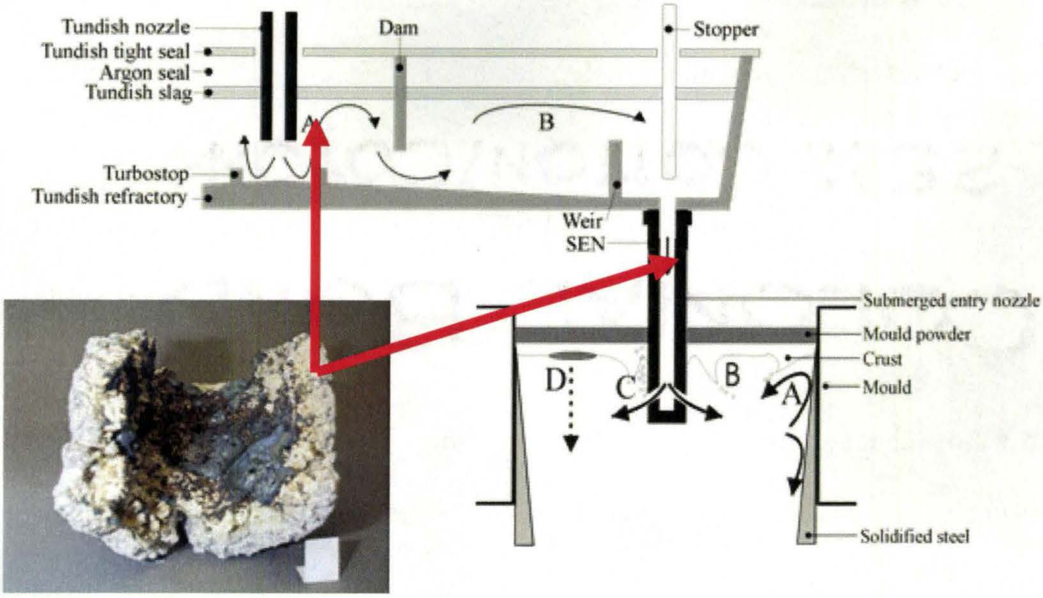

Figure 5-3: Illustration of a typical accretion and a schematic showing the location of nozzle clogging. (Dekkers, 2002)

One method to avoid the onset of nozzle clogging is to ensure that formed inclusions have melting points lower than that of bulk steel. This practice is called inclusion engineering and involves careful deoxidation and calcium treatment control. The importance of controlling calcium treatment is illustrated in Figure 5-4, which summarizes the experimental results of Faulring et al. (1979) who investigated the amount of steel tonnage capable of being cast prior to clogging as a function of the Ca/Al ratio. As seen in Figure 5-4, steel flow through the nozzle was consistently poor below a Ca/Al ratio of 0.1. As the ratio was raised between 0.1 and 0.14, Faulring et al. (1979) reported improved nozzle flow properties and the elimination of severe nozzle blockages. The major part of inclusions formed above a Ca/Al ratio of 0.14 were determined as being low melting point CaO-2Al$_2$O$_3$ and CaO-Al$_2$O$_3$ precipitates. An interesting outcome from the investigation of Faulring et al. (1979) was that magnesium contamination of steel was found to minimize the beneficial effects of calcium due to the formation of MgO.Al$_2$O$_3$ spinels.

Dekkers (2002), on the basis of chemical analysis results on accretions formed during the casting of a low carbon aluminum killed steel, attributed accretion formation to the reoxidation of steel after ladle metallurgy. The SEN was regarded as the most probable location of reoxidation. Dekkers (2002) further concluded that agglomeration of pre-existing deoxidation products played only a minor role with respect to clogging.

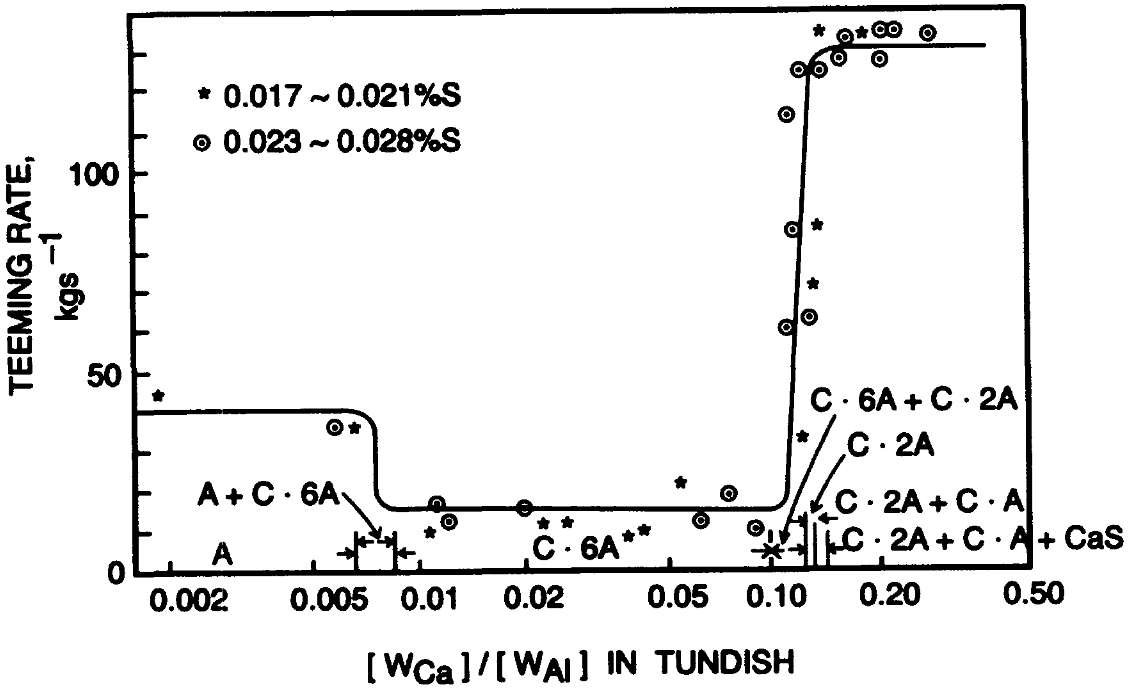

Figure 5-4: Effect of calcium on the flow of aluminum deoxidized steels through nozzles. (Faulring et al., 1979)

An alternative method of preventing nozzle clogging involves removing inclusions ahead of the submerged entry and / or tundish nozzles using a porous cermaic foam filter to entrap inclusions by filtration. While filters are currently in-use within the aluminum industry, steelmaking filters have not found wide-spread application (Lange, 1999).

5.2.4. Slag-Metal-Inclusion Equilibrium

Fuhr et al. (2007) demonstrated the influence of slag on the formation of non-metallic inclusions in steel by using BaO as a slag tracer in industrial trials undertaken at TenarisSiderca (Buenos Aires, Argentina). Results from their study revealed that approximately one third of large inclusions detected in the final product had traces of BaO within their composition. The authors attributed the large inclusions and the resulting presence of BaO to the onset of ladle slag emulsification during refining.

In addition to slag entrapment as being a physical source of inclusions in steel, numerous researchers have investigated the effect of chemical reactions taking place between slag, steel, and inclusions. In their work on slag-metal equilibria of stainless steels, Faral & Gaye (1984) computed and compared oxygen activities from the following equilibria reactions: $[Al]/(Al_2O_3)$, $[Fe]/(FeO)$, $[Mn]/(MnO)$, and $[Si]/(SiO_2)$ within a 30t vacuum argon / oxygen degassing (VAD / VOD) vessel. Slags in their study were reported as being comprised of furnace slag, deoxidation oxides, and added fluxes. Results indicated that slag-metal equilibrium was attained during the process and that stirring within the VOD / VAD was an integral parameter affecting equilibrium conditions.

More recently, Björkland et al. (2007) undertook an investigation to determine whether equilibrium conditions existed between slag, steel, and inclusions after deoxidation within an ASEA-SKF ladle furnace. Prior to refining, EAF slag carryover was removed and a synthetic slag was prepared. On the basis of their results, Björkland et al. (2007) reported that while equilibrium conditions existed between metal and inclusions, it did not exist between the slag and metal phase. This latter observation is significant in so much that it directly conflicts with a fundamental inclusion control assumption. As summarized by Suito & Inoue (1996), the whole purpose of using a synthetic top slag is that slag-metal equilibrium can be easily established. The production of such a chemically stable slag is a known precursor for inclusion engineering and enables the precise control of inclusion composition via a process called slag deoxidation.

5.2.5. Inclusion Engineering in Steelmaking

Inclusion engineering involves adjusting the composition of inclusions to prevent nozzle clogging and / or to enhance the mechanical properties of steel. According to Costa e Silva (2006) effective inclusion control involves three steps: (i) a good knowledge of how inclusions influence properties, (ii) definition of the desired inclusion product, and (iii) adjusting processing parameters to obtain these inclusions.

Suito & Inoue (1996) reviewed the subject of thermodynamic inclusion modelling by investigating the relations among the compositions of inclusion, steel, and top slag at 1873K in tire cord, valve spring, ultra low carbon sheet, bearing and sulphur free machining steels. Results from their work demonstrated the theoretical capability of thermodynamic models in determining inclusion composition. Steel-inclusion equilibrium was stated as a necessary assumption of inclusion engineering, where both top slag and refractory materials were found to have an influence on inclusion composition. Suito & Inoue (2006) further noted that in general only a partial state of equilibrium with respect to a certain element between steel-inclusion, slag-steel, refractory-slag, and refractory-steel has been observed in practice.

Subramanian & Kay (1988, 1997) investigated the contributions of manganese sulphides and various glassy oxides on the machinability performance of free cutting steels. The authors showed that steel machinability was greatly improved at moderate and higher cutting speeds by glassy oxide inclusions lubricating the tool-chip interface. On the basis of these results, Zhang et al. (2004) demonstrated a method to engineer glassy oxide inclusions in low carbon free cutting steels using a sub-regular solution model to calculate oxide activities. The developed inclusion model is based on slag-metal as well as melt-oxide inclusion equilibration and is reportedly used online within an industrial production line for the controlled production of glassy inclusions.

Continuing the previous work by Gaye et al. (1987), Gatellier and coworkers (1991) developed a model for predicting the composition of oxide and sulphide inclusions by assuming equilibrium between steel and inclusions as they precipitate. The method makes use of a recurrent procedure for complex equilibria calculation, combining mass balance equations and equilibrium calculations. As summarized by Gatellier et al. (1991), the model starts with an approximate composition of liquid oxide inclusions and uses a search pattern that progressively modifies inclusions composition in order to equate all the oxygen activities corresponding to the equilibrium value between the oxide components and the corresponding metal solutes. The possible precipitation of sulphides is checked at each step of the iteration. The procedure is reported to converge fairly rapidly and has reportedly been used to evaluate results in several French steel plants for various deoxidation practices.

5.3. Apparatus and Procedure

5.3.1. Experimental Sampling Procedure

The sampling methodology employed in the industrial trials at ArcelorMittal Dofasco was previously presented in Chapter 4 as Figure 4-11. Not shown in Figure 4-11 was that total oxygen samples were taken on 20 industrial heats using total oxygen sampling (TOS) probes from Heraeus Electro-Nite (Philadelphia, PA). All total oxygen samples were taken at identical process times as the metal and slag samples, and dissolved oxygen and temperature measurements. A schematic drawing of a TOS probe is presented as Figure 5-5.

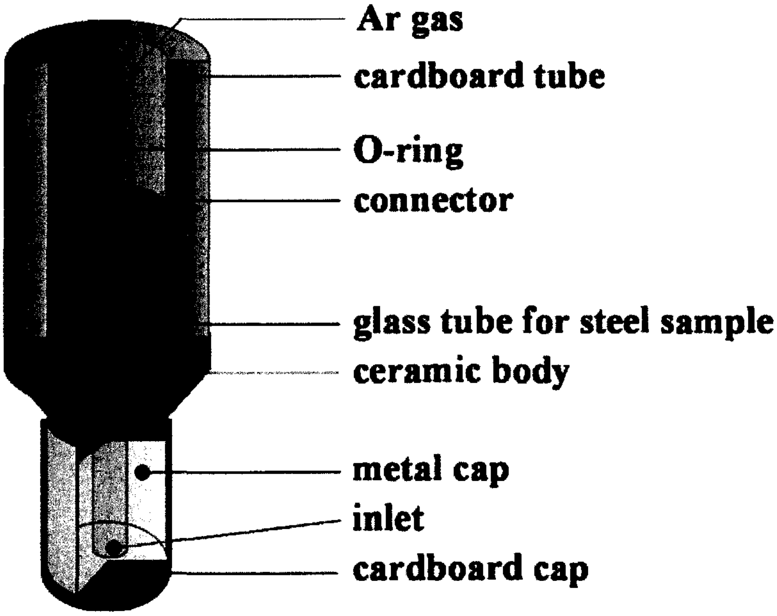

Figure 5-5: Schematic drawing of a Total Oxygen Sample (TOS) system probe. (Dekkers, 2002)

TOS samples were taken manually via the LMF slag door using a 4m long immersion lance connected to an argon gas line. The step-by-step sampling procedure was as follows:

- Slag door on ladle roof was opened.
- The TOS lance was immersed into liquid steel and held in a fixed position.
- Argon gas was blown through the sample probe and into the melt in order to prevent slag pick-up. After a 6 second waiting time, argon purging was stopped and the vacuum was applied allowing the sample to be taken.
- The TOS immersion lance was removed from the liquid steel.
- Slag door on ladle roof was closed.
- TOS pin samples (4mm diameter by 80 mm long) were removed from the probe and quenched in a water bath.

Total oxygen analysis on all pin samples was carried out within the Iron and Steel laboratory at ArcelorMittal Dofasco using a TC04 Leco analyzer. Sample preparation involved first using a file to carefully remove any surface oxide layer and then sectioning each pin sample into three approximate 1 gram pieces for separate analysis. Each 1 gram sample plug was then placed in a graphite crucible and heated within the TC04 Leco analyzer, where oxides contained within the sample were reduced by excess carbon to form carbon monoxide (CO) gas. The CO gas was subsequently oxidized to carbon dioxide (CO_2) by using a helium gas stream to sweep the evolved CO gas over a copper oxide filament contained within an OMI^{TM} indicating purifier. Oxygen contained as CO_2 was then measured within the analyzer using an infrared detection cell. In all cases, a minimum of two burns were obtained and averaged for each TOS pin sample (± 5ppm). Blank correction and selected control standards were used to calibrate the TC04 Leco analyzer.

TOS probe pin samples from Heraeus Electro-Nite (Philadelphia, PA) were used for determining total oxygen content within the study instead of the standard double thickness 'lollipop' type samples due to their shorter sample preparation times and increased reliability. In their work, Tieknik and coworkers (1994) reported a 30% average lower total oxygen value when using the TOS probe instead of the standard production samples. The observed lower values were attributed to the argon flushing mechanism within the TOS probes offering reduced oxygen pickup and slag entrapment as compared to the double thickness 'lollipop' type samplers. The findings of Tieknik and co-workers (1994) may help to explain the "shot-gun" pattern results observed by Peter et al. (2005) who used the double thickness 'lollipop' type samples for analyzing total oxygen contents from their industrial trials.

5.3.2. Inclusion Analysis

Industrial 'lollipop' steel samples were sent to RJ Lee Group (Monroeville, PA) and analyzed using a computer-controlled scanning electron microscope (CCSEM) known as the Automated Steel Cleanliness Analysis Tool (ASCAT). CCSEM provides simultaneous measurement of individual inclusion size, shape, and elemental composition by combining an ASPEX Instruments scanning electron microscope (SEM), an x-ray analyzer, and a digital scan generator operated under computer control. As summarized by Story et al (2004) the developed technique is capable of analyzing hundreds of inclusions in a steel sample in a matter of minutes.

Inclusions were detected on the polished steel sample by moving the electron beam in discrete increments across the sample. At each point, the computer controlled SEM paused and allowed the resultant backscattered signal to be compared against a pre-set threshold level, where signals exceeding the threshold signified the location of an inclusion. If no inclusions were found at a given spatial coordinate location the electron beam was moved. If, however, inclusions were identified, then the electron beam was moved across the indentified inclusions in a pre-set pattern using a more closely spaced grid point density to determine their size (all inclusions greater than 1μm in size were identified). The elemental composition of inclusions within the sample was determined by X-ray analysis, where the generated spectrum was interpreted by the computer to establish the elemental inclusion composition. The following elements were identified by CCSEM analysis: oxygen, magnesium, aluminum, silicon, sulphur, chlorine, potassium, calcium, titanium, chromium and manganese. The reader is referred to Story et al. (2004) and Ahlborg et al. (2003) for more detailed reviews on the sample preparation and analytical techniques.

5.4. Experimental Results

5.4.1. Total Oxygen Content

Measured total oxygen content values versus time after deoxidation are presented as Figure 5-6 and 5-7 for both the aluminum killed non-calcium treated heats and calcium treated heats. The average total oxygen content from the first sample taken after deoxidation was found to be 44.7 ± 13.8ppm for the aluminum killed non-calcium treated heats, and 32.3 ± 9.0ppm for the aluminum killed calcium treated heats. All total oxygen measurements ranged between 16.3 and 86.4ppm. As was similarly observed by Dekkers (2002), inclusions were removed from steel within about 15-20 minutes after deoxidation, after which the total oxygen content remained about constant.

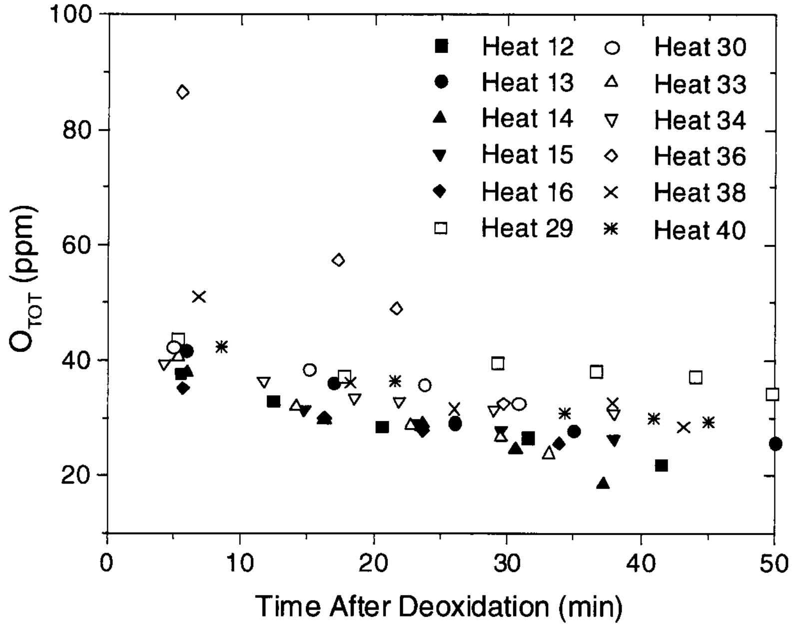

Figure 5-6: Total oxygen content concentration profile in aluminum killed non-calcium treated steel.

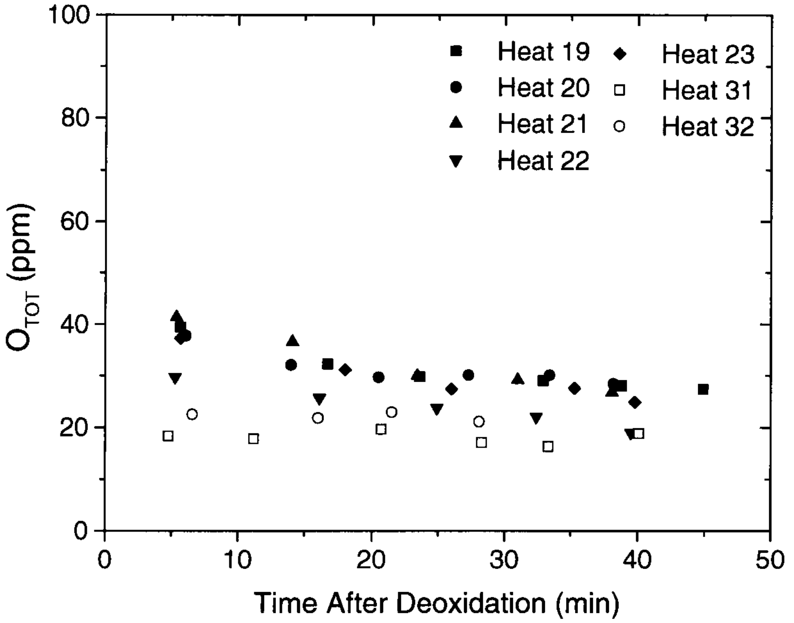

Figure 5-7: Total oxygen content concentration profile in aluminum killed calcium treated steel.

Inclusion removal rate constants were calculated from the results of Figure 5-6 and 5-7 on the assumption of the following first order rate equation:

$$[O]=\left([\mathrm{O}]_{\mathrm{i}}-[\mathrm{O}]_{eq}\right)\exp(-Kt)+[\mathrm{O}]_{eq} \tag{5-3}$$

where $[\mathrm{O}]_{\mathrm{i}}$ and $[\mathrm{O}]_{\mathrm{eq}}$ are the initial and equilibrium oxygen concentrations in steel, K is the inclusion removal rate constant, A is the inclusion-metal interfacial area, and V is the steel volume. The equilibrium total oxygen concentration is assumed as the total oxygen content at the end of treatment time, which was usually at a constant level. If the assumptions made in the derivation of the rate equation 5-3 are valid, then a plot of $\ln\left([O]-[\mathrm{O}]_{eq}/[\mathrm{O}]_{\mathrm{i}}-[\mathrm{O}]_{eq}\right)$ versus time must show a straight line, where the slope of the line represents the inclusion removal rate constant. This is demonstrated in Figure 5-8 where all the points for different initial total oxygen contents in steel are found generally linear and of identical slope, indicating that inclusion removal is first order and independent of the initial total oxygen content. The only omissions from Figure 5-8 were those measurements having registered an increase in total oxygen content from the previous sample. Figure 5-9 summarizes the inclusion removal rate constants as a function of bath stirring power. The shown relationship is observed fairly scattered and may be attributed to reoxidation and measurement uncertainties.

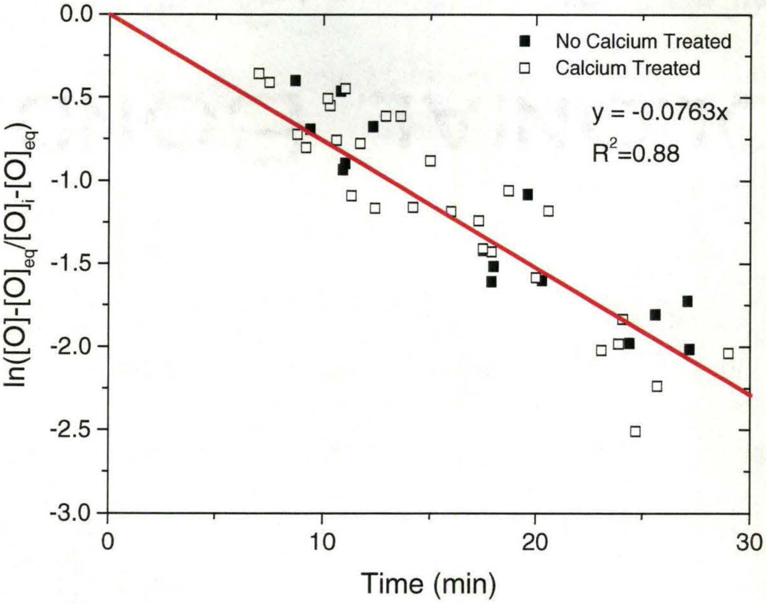

Figure 5-8: $\ln\left([O]-[\mathrm{O}]_{eq}/[\mathrm{O}]_{\mathrm{i}}-[\mathrm{O}]_{eq}\right)$ versus time plot for different initial total oxygen contents in steel.

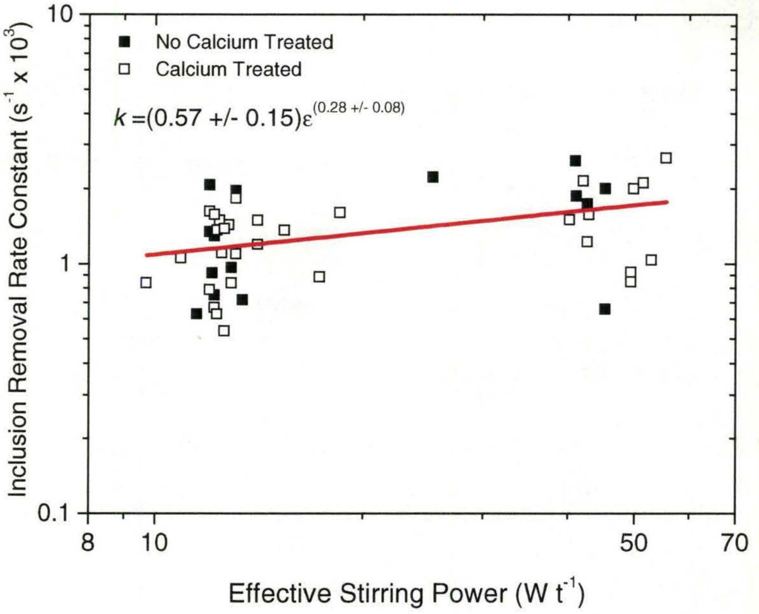

Figure 5-9: Relation between the inclusion removal rate constant and stirring energy.

5.4.2. Inclusion Distribution and Chemical Analysis

Over eighty metal samples from fifteen different heats were sent to RJ Lee Group (Monroeville, PA) and examined by CCSEM. Samples were taken from both aluminum killed non-calcium treated and calcium treated heats. In addition, samples from a separate trial undertaken by ArcelorMittal Dofasco investigating nozzle clogging at the caster were also analyzed by RJ Lee Group (Monroeville, PA). Results from both trials have been included within this thesis.

Representative statistical summary plots generated by RJ Lee Group (Monroeville, PA) are presented as Figure 5-10 and 5-11 for non-calcium treated heats and as Figure 5-12 and 5-13 for calcium treated heats. In all cases, the shown Ca-Al-Mg ternary diagram represents the respective atomic percentages of elemental Ca, Al, and Mg contents within the analyzed inclusions. As shown in Figure 5-10 and 5-12, inclusions were found to be of predominately pure alumina type immediately after deoxidation. In regard to non-calcium treated heats, inclusion analysis results on end of heat samples revealed that the initial alumina inclusions had been fluxed with magnesium by up to 40 atom%, Figure 5-11. End heat samples from calcium treated heats were found to have lower magnesium content inclusions, consisting mostly of calcium aluminates.

5.4.3. Area Fractions of Inclusions

Representative summary plots showing the inclusion area fraction changes of both total and the most common types of inclusions identified within aluminum killed non-calcium treated and calcium treated heats are presented as Figure 5-14 and 5-15. The gradual decrease in total area fraction of inclusions immediately following deoxidation was observed in all heats and was found independent of process conditions (i.e. low argon flowrate with arcs off, low argon flowrate with arcs on, and high argon flowrate with arcs off). These findings are in general agreement with the earlier reported total oxygen results (Figure 5-6 and 5-7) and indicate that the inclusion removal rate at the beginning of refining is faster than the inclusion generation rate. Inclusion removal and generation rates appear to reach a steady state towards the later stages of refining.

As was characteristic of all aluminum killed non-calcium treated heats, Al_2O_3 and $MgO.Al_2O_3$ spinels were the two most common types of inclusions (both in terms of number count and area fraction) identified by CCSEM. Perhaps the most striking feature of Figure 5-14 is the abruptness of the transition time between Al_2O_3 and spinel inclusions. As will be discussed later, the Al_2O_3 / spinel transition was found dependent on top slag composition and occurred anywhere from mid to late in the refining cycle.

Inclusion area fraction change within calcium treated heats was found far more irregular than for the non-calcium treated heats. A greater number of inclusion types coexisted within analyzed calcium treated samples with no discernible pattern existing between inclusions and process conditions. For instance, the area fraction of (Ca,Mn)S inclusions was often highest at lower bulk sulphur contents in steel despite expectations to the contrary. It is believed that much of the inclusion variability within calcium treated heats is associated with the unpredictable calcium recovery rates from calcium silicide (CaSi) addition.

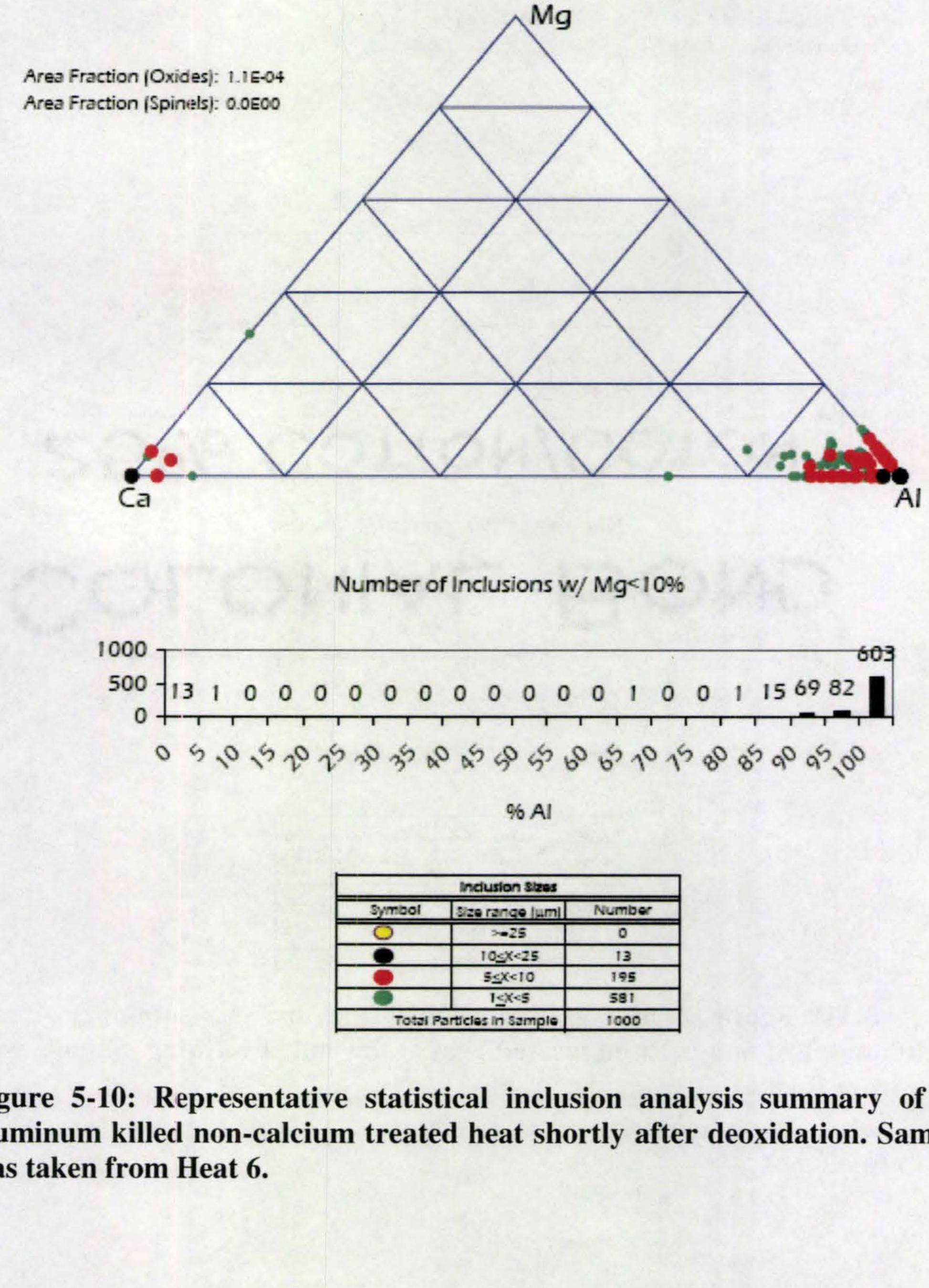

Inclusion Sizes		
Symbol	Size range [μm]	Number
○	>=25	0
●	10≤X<25	13
●	5≤X<10	195
●	1≤X<5	581
Total Particles in Sample		1000

Figure 5-10: Representative statistical inclusion analysis summary of an aluminum killed non-calcium treated heat shortly after deoxidation. Sample was taken from Heat 6.

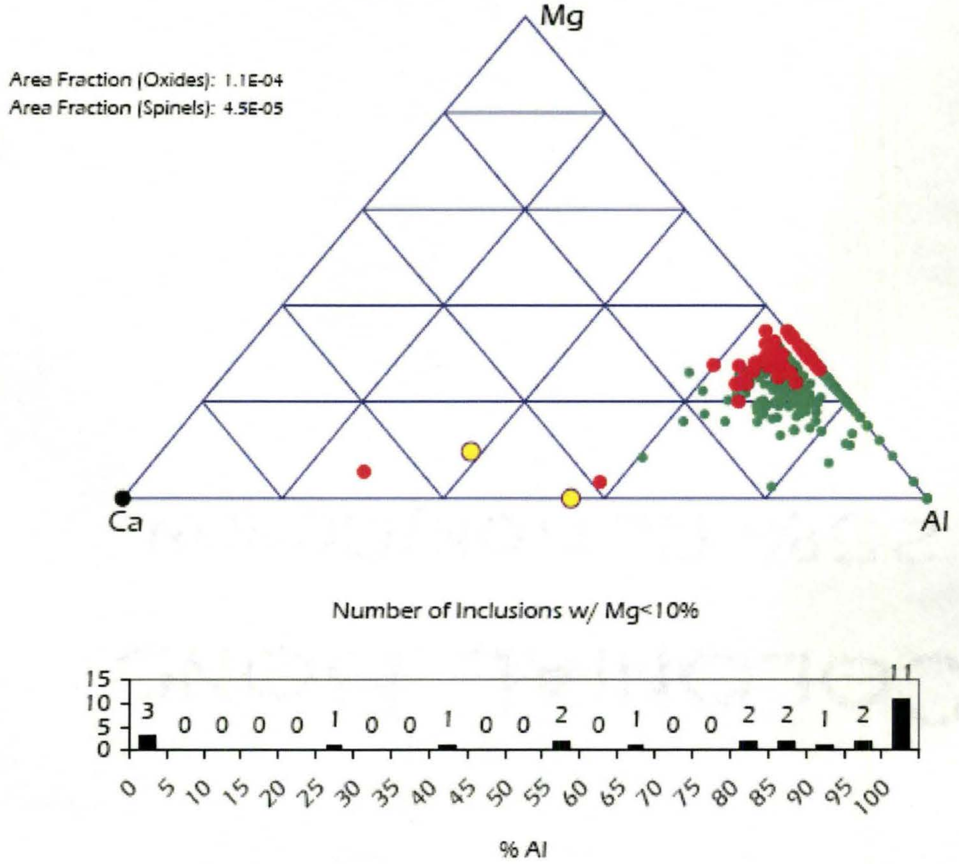

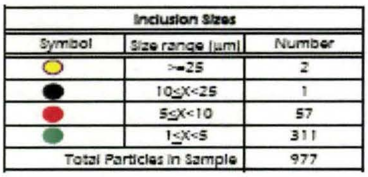

Inclusion Sizes		
Symbol	Size range (µm)	Number
🟡	>=25	2
⚫	10≤X<25	1
🔴	5≤X<10	57
🟢	1≤X<5	311
Total Particles in Sample		977

Figure 5-11: Representative statistical inclusion analysis summary of an aluminum killed non-calcium treated heat at the end of refining. Sample was taken from Heat 6.

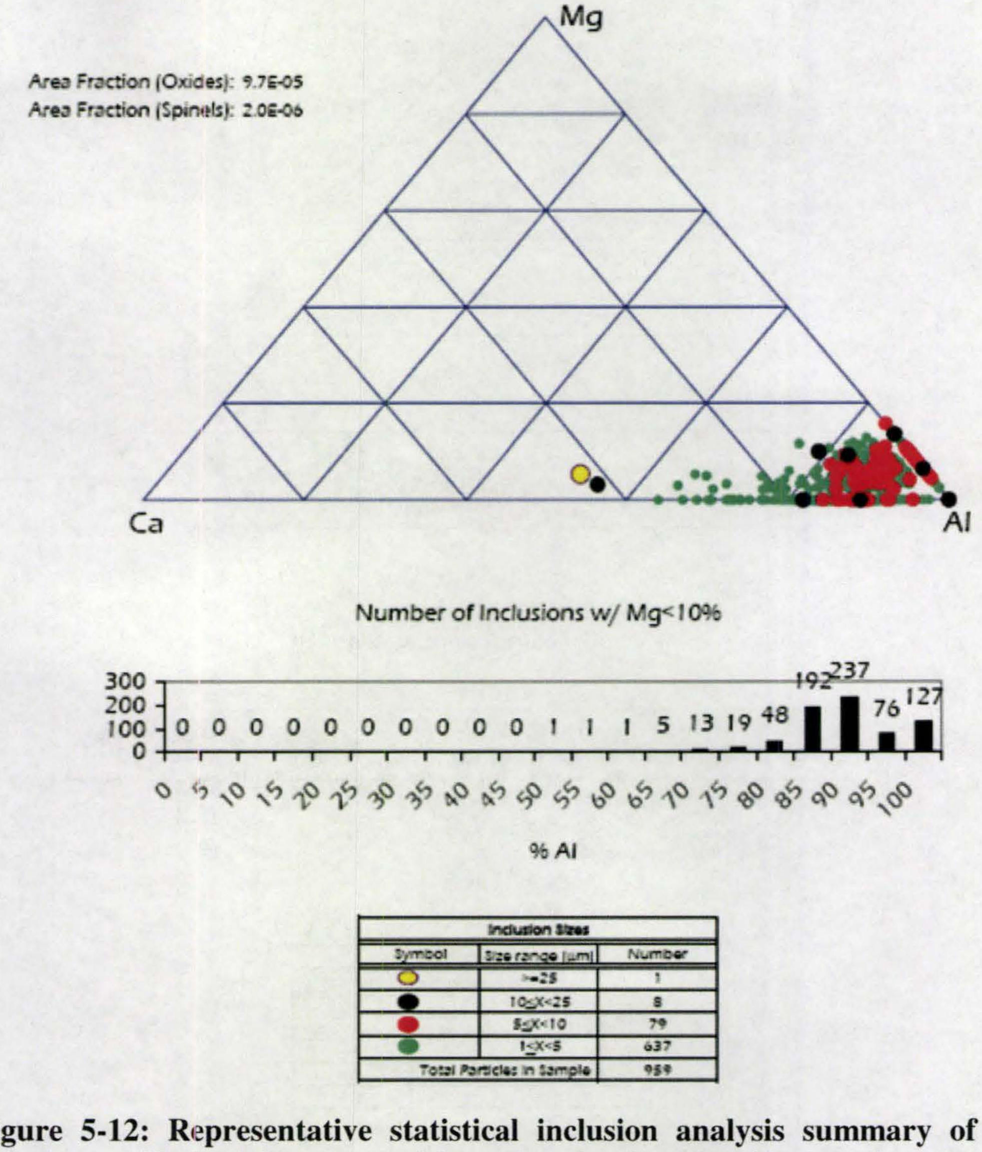

Inclusion Sizes		
Symbol	Size range [µm]	Number
○	>=25	1
●	10≤X<25	8
●	5≤X<10	79
●	1≤X<5	637
Total Particles in Sample		959

Figure 5-12: Representative statistical inclusion analysis summary of an aluminum killed calcium treated heat shortly after deoxidation. Sample was taken from Heat 19.

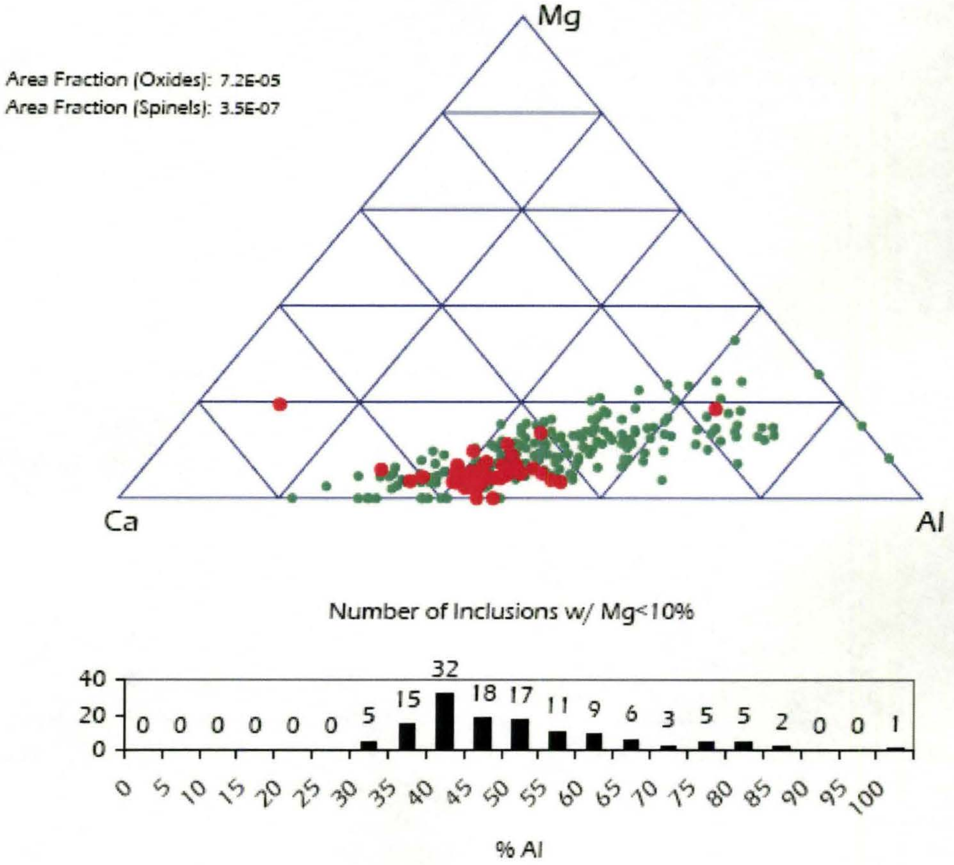

Inclusion Sizes		
Symbol	Size range (µm)	Number
🟡	>=25	0
⚫	10≤X<25	0
🔴	5≤X<10	43
🟢	1≤X<5	204
Total Particles in Sample		806

Figure 5-13: Representative statistical inclusion analysis summary of an aluminum killed calcium treated heat at the end of refining. Sample was taken from Heat 19.

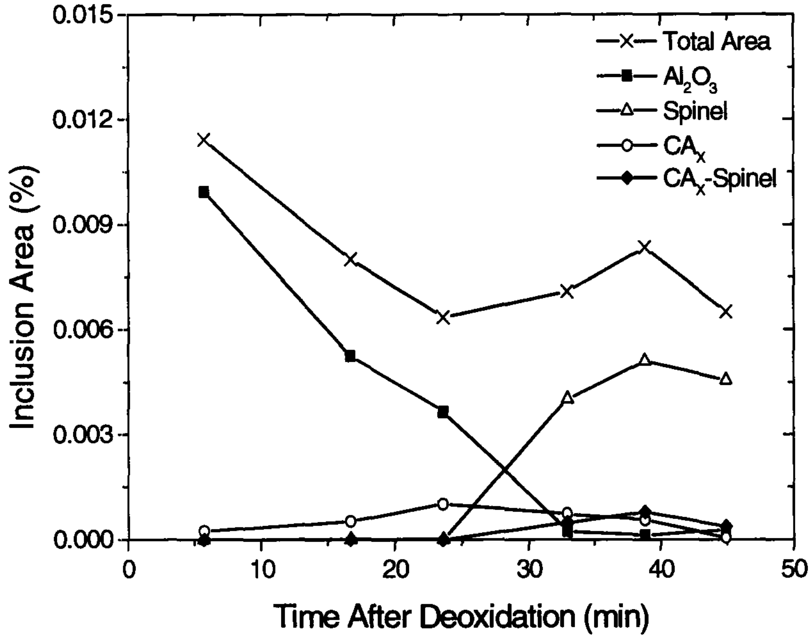

Figure 5-14: Representative summary of the area fraction changes for total and most common types of inclusions within an aluminum killed non-calcium treated heat (Heat 6).

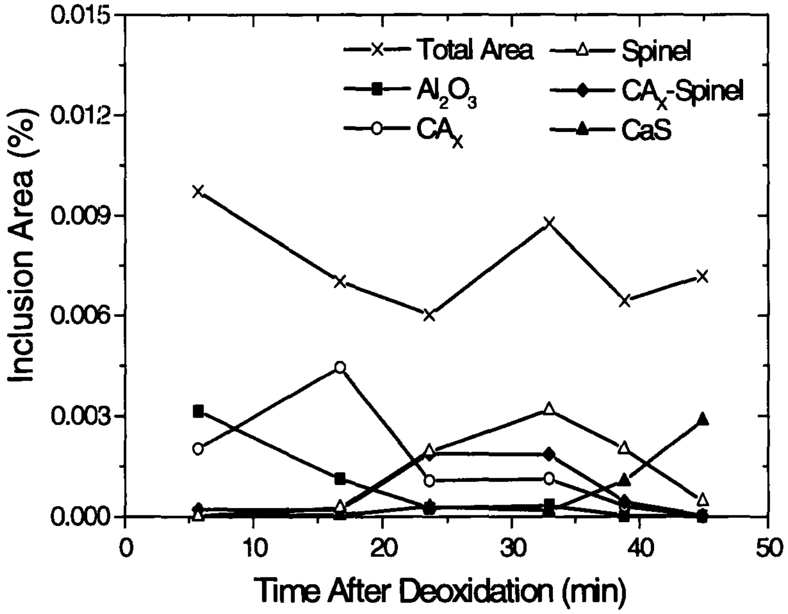

Figure 5-15: Representative summary of the area fraction changes for total and most common types of inclusions within an aluminum killed calcium treated heat (Heat 19).

5.4.4. Inclusion Size Distribution

Figure 5-16 and 5-17 summarize the inclusion size distribution results for all heats analyzed by RJ Lee Group (Monroeville, PA) as a function of process time. Inclusion average volumetric diameter was calculated using Underwood's method (1968), equation 5-4. A key assumption of Underwood's method (1968) is that particles are assumed spherical in shape.

$$d_i^v = \left(\frac{\pi}{2}\right) d_i^a \qquad (5\text{-}4)$$

where d_i^a is the average area diameter of inclusions determined by X-ray analysis:

$$d_i^a = \sum_{j=1}^{N} n_i d_i \Big/ \sum_{j=1}^{N} n_i \qquad (5\text{-}5)$$

It is seen from Figure 5-16 and 5-17 that inclusions from non-calcium and calcium treated heats have similar average volumetric diameters. Volumetric diameters of inclusions from non-calcium treated heats ranged from 5.6 to 8.2μm with an average of 6.8μm. In comparison, calcium treated inclusions had volumetric diameters ranging from 4 to 6.72μm with an average of 5.4μm. In agreement with the findings of Dekkers (2002) there appears to be no significant effect of ladle process conditions on inclusion size.

5.4.5. Inclusion Chemistry

As mentioned earlier, inclusion analysis results from RJ Lee Group (Monroeville, PA) reported inclusion composition as elemental atomic percentages only. However, in order to make accurate inferences as to which process variables or factors influence inclusion composition, the elemental inclusion analysis results require conversion to oxide and sulphide compositions. The conversion approach proposed by Lu (1991) for the determination of oxy-sulphide inclusions from particular elemental constituents was used in this study on the basis of the following general formula:

$$\left(CaO.wAl_2O_3.xMgO.ySiO_2.zMnO\right)\underline{.rCaS.qMnS} \qquad (5\text{-}6)$$

where the oxide phase was taken as the term within the parenthesis and the underlined term as the calcium-manganese sulphide. During the calculation process, manganese and calcium contents were first determined by satisfying the stoichiometric requirements for sulphur in the sulphide phase, with the remaining manganese and calcium contents being use to determine the oxide compositions. The relative stoichiometric coefficients (w, x, y, z, r and q) in equation 5-6 were computed on the assumption of 1 mole of CaO. Inclusion composition was then subsequently determined on both a mol fraction and wt% basis. Table 5-1 summarizes a sample calculation of inclusion composition.

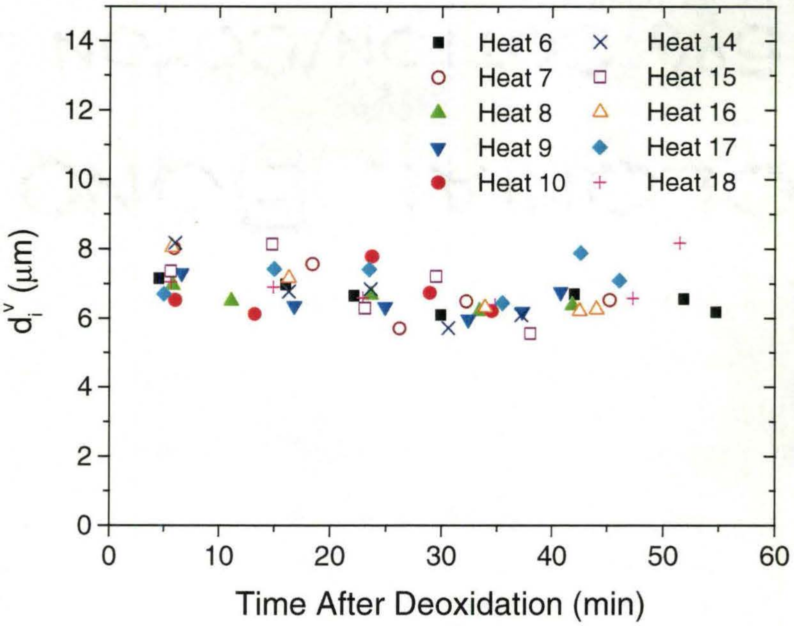

Figure 5-16: Change of the average volumetric diameter of inclusions during LMF refining of aluminum killed non-calcium treated heats.

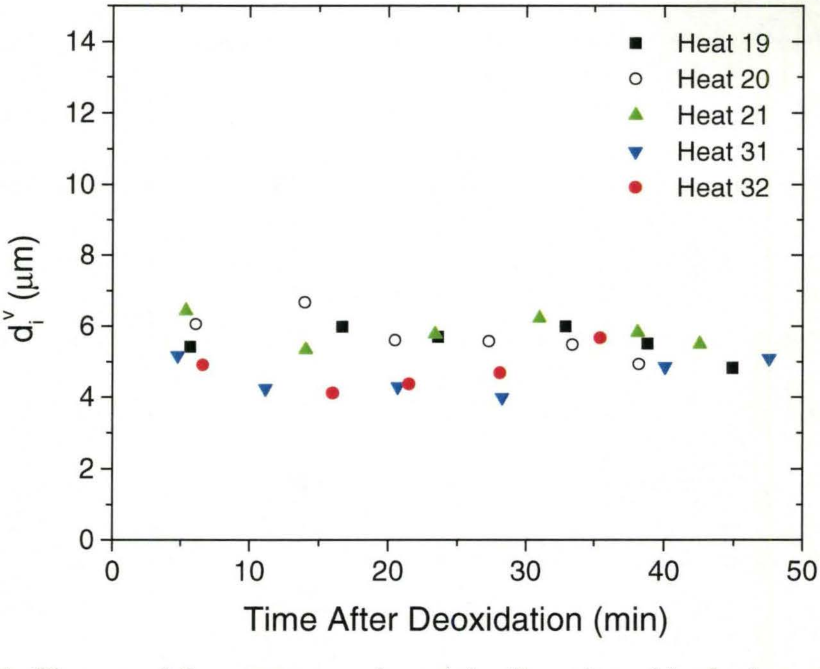

Figure 5-17: Change of the average volumetric diameter of inclusions during LMF refining of aluminum killed calcium treated heats.

Table 5-1: Sample inclusion composition determination calculation (mole%)

Inclusion Formula	$(CaO.wAl_2O_3.xMgO.ySiO_2.zMnO).\underline{rCaS.qMnS}$
Relative molar ratios of each component: $CaO/Al_2O_3/MgO/SiO_2/MnO/CaS/MnS$	1 / 2x / y / z / q (Based on 1 mole of CaO)
EDS molar % of above ratios:	8.27 / 74.2 / 10.6 / 1.15 / 0 / 0 / 2.86
Calculated values of w, x, y, z, r and q:	w = 8.97 x = 1.28 y = 0.14 z = 0 r = 0 q = 0.35
Calculated mole % of each component in the inclusion:	X_{CaO} = 8.53 % X_{Al2O3} = 76.4 % X_{MgO} = 10.9 % X_{SiO2} = 1.19 % X_{MnO} = 0 X_{CaS} = 0 X_{MnS} = 2.94 %

5.5. Discussion

5.5.1. Slag-Metal Oxygen Activity Variation within the LMF

Figure 5-18 to 5-20 summarize the oxygen activity variation observed during treatment within the LMF at ArcelorMittal Dofasco. Figure 5-18 and 5-19 correspond to aluminum killed non-calcium treated heats, while Figure 5-20 is representative of aluminum killed calcium treated heats (where ferrosilicon was added on tap at the EAF). Oxygen activity within each figure was calculated on the basis of the Al, Mn, and Si steel-slag equilibria reactions using the thermodynamic data summarized in Table 4-4. The unified interaction parameter model and cell model were used for computing the steel and slag phase activities. Steel and slag samples were taken according to the experimental procedure outlined in Section 4.3.3, where the initial oxygen activity immediately after deoxidation has been clearly labelled in each figure. An ideal linear fit is drawn in each plot and data points falling on or near to this line represents perfect or near perfect equilibrium conditions. It is recommended that the detailed LMF sampling results contained in Appendix F be used for interpreting Figure 5-18 to 5-19.

The observed steady decrease in $[Mn]/(MnO)$ oxygen activity in Figure 5-18 and 5-19 was found characterisitic of all aluminum killed non-calcium treated heats and is explained by considering the slag phase. Tapped from the EAF, ladle slag during the industrial trials was found to have a high reducible oxide content, Table 4-7. This high (FeO + MnO) slag content results in an elevated oxygen potential within the melt and consequently yields the initial non-equilibrium conditions observed in Figure 5-18 and 5-19. As shown, it was only after the (FeO + MnO) content in slag was reduced below approximately 1wt% that a state of partial equilibrium was established between the $[Mn]/(MnO)$ and $[Si]/(SiO_2)$ reactions. The gradual attainment of parital equilibrium between slag and metal observed within the trials at ArcelorMittal Dofasco follows a similar behaviour first reported by Faral & Gaye (1984).

In contrast to the aluminum killed non-calcium treated heats, the aluminum killed calcium treated heats (Figure 5-20) were found to have attained a state of partial equilibrium between $[Mn]/(MnO)$ and $[Si]/(SiO_2)$ immediately after deoxidation at the ladle. Upon review of the various conditions between the two different heats, it appears likely that the rapid attainment of equilibrium within the aluminum killed calcium treated heats was due to the FeSi added at EAF tapping having reduced the (FeO + MnO) slag content prior to deoxidation at the LMF. In all cases, the oxygen activity calculated from the $[Al]/(Al_2O_3)$ equilibrium reaction was found initially out of equilibrium and generally tended towards equilibrium with each succeeding sample taken. Faral & Gaye (1984) attributed this behaviour to the aluminum being directly added and dissolved within the steel without first reacting with the slag phase. This observation is believed valid and is supported by the trials undertaken at ArcelorMittal Dofasco, where mid-stream aluminum additions into the steel (under large ladle eye conditions) had the effect of pushing the calculated $[Al]/(Al_2O_3)$ oxygen activity further away from equilibrium.

5.5.2. Effect of Top Slag on the Magnesium Content of Inclusions

Also shown in Figure 5-18 to 5-20 are the average inclusion concentration profiles for the different heats as a function of ladle refining time. In comparing these composition profiles to the associated oxygen activity plots it becomes apparent that the attainment of partial equilibrium between $[Mn]/(MnO)$ and $[Si]/(SiO_2)$ is associated with elevated MgO inclusion contents. More specifically, in Figure 5-18 a distinct step-increase in the MgO inclusion content is seen between the third and fourth samples taken. A similar increase in inclusion MgO content was observed at the end of the refining cycle in Figure 5-19. In regard to Figure 5-20, the MgO inclusion content was at its highest concentration at the

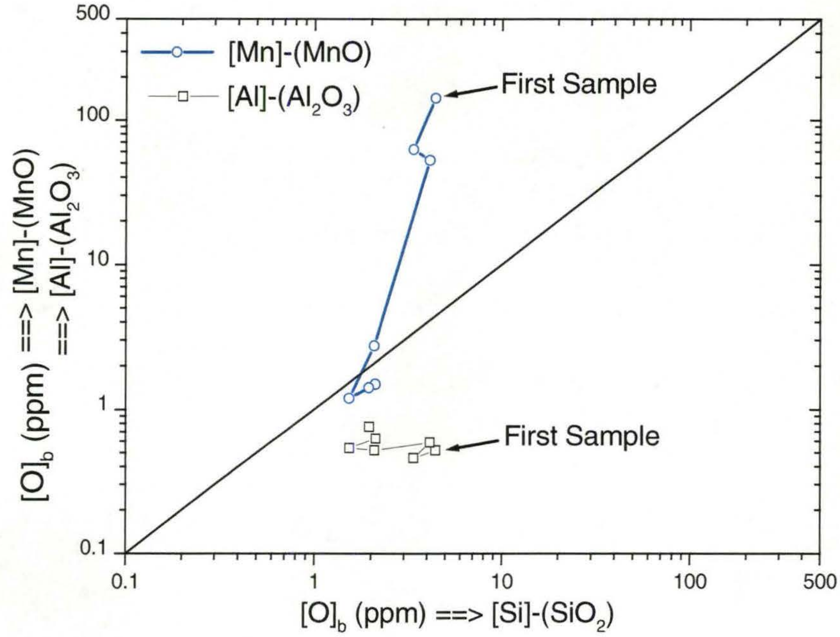

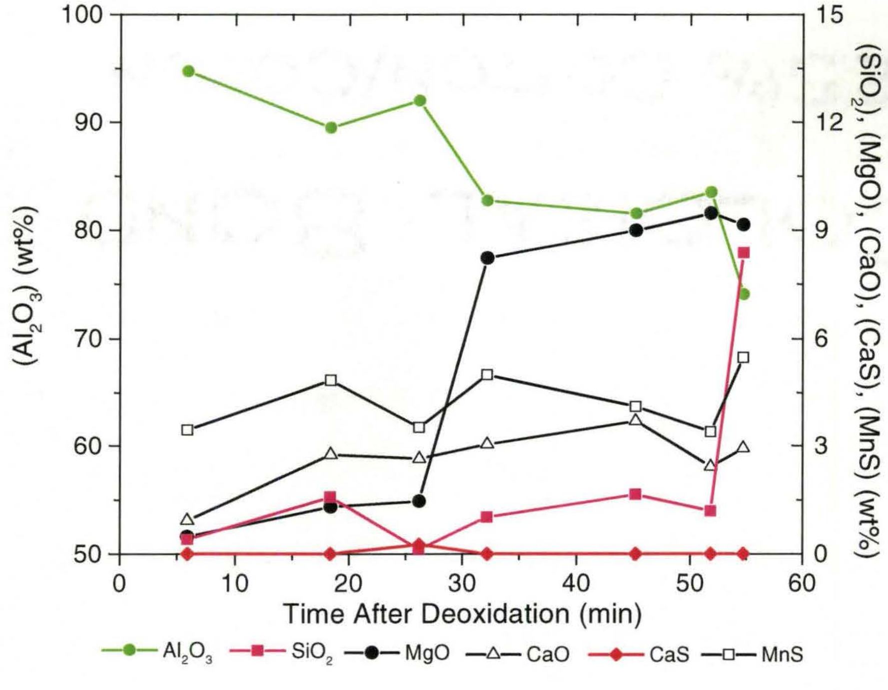

Figure 5-18: (top) Computed oxygen activity evolution within the LMF according to respective Al, Mn, and Si equilibria reactions between slag-metal (Heat 6); (bottom) Inclusion concentration profile (Heat 6).

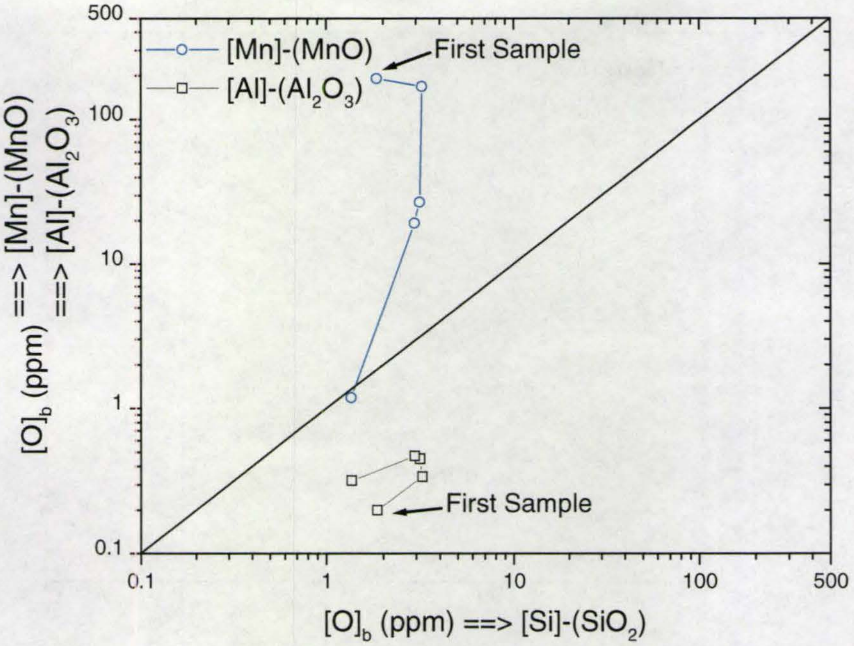

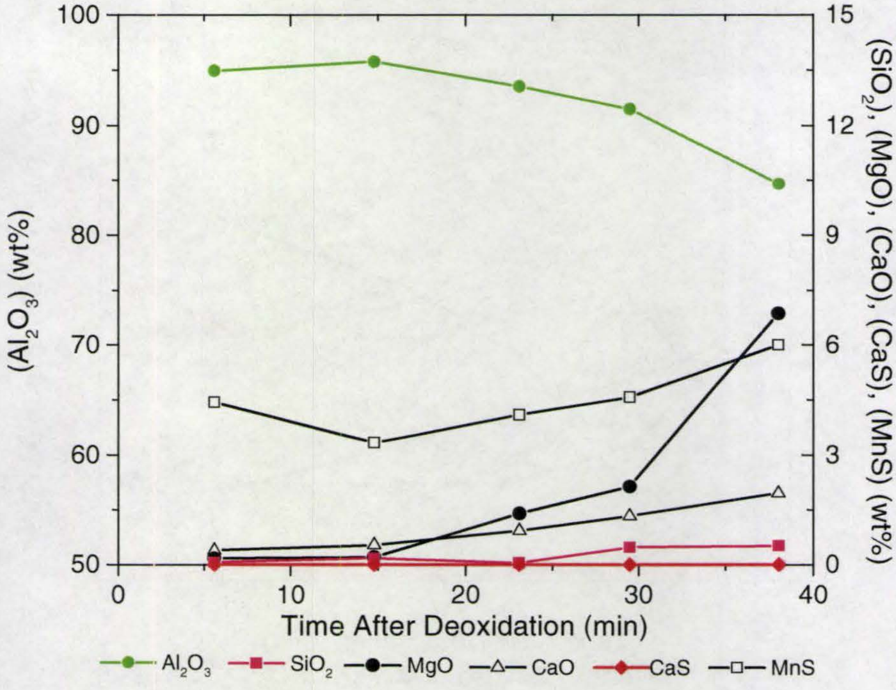

Figure 5-19: (top) Computed oxygen activity evolution within the LMF according to respective Al, Mn, and Si equilibria reactions between slag-metal (Heat 15); (bottom) Inclusion concentration profile (Heat 15).

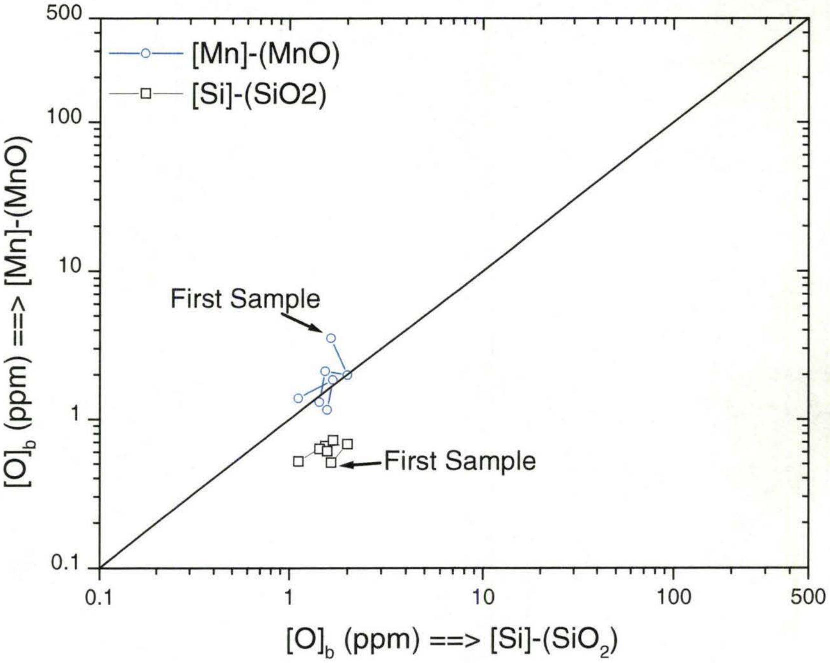

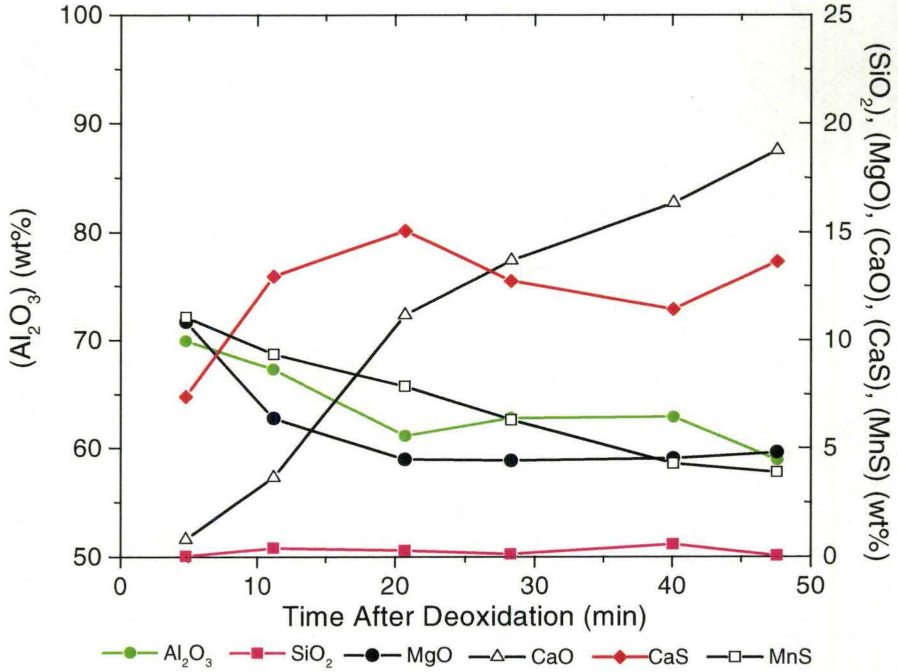

Figure 5-20: (top) Computed oxygen activity evolution within the LMF according to respective Al, Mn, and Si equilibria reactions between slag-metal (Heat 31); (bottom) Inclusion concentration profile (Heat 31).

start of processing. In each case, elevated MgO inclusion content levels only occurred after a state of slag-metal partial equilibrium had been established. These observations were found representative of nearly every heat sampled.

Story et al. (2005) have recently reviewed the factors affecting spinel inclusion formation in the steelmaking process. In their paper, the authors assert that the magnesium responsible for spinel formation originates during ladle processing, where the following potential sources of magnesium were identified: (i) as an impurity in added aluminum, (ii) refractory, and (iii) ladle slag. Results from the work of Story et al. (2005) indicated that spinel formation was promoted by electrical arcing within the LMF and for slags having lower levels of reducible oxides, particularly FeO.

On the basis of the results from Story et al. (2005) and the early finding within this thesis that the combined (FeO + MnO) content in slag influences the attainment of slag-metal partial equilibrium, an attempt was made to relate the average MgO incluson content as measured by RJ Lee Group (Monroeville, PA) to the top slag conditions during ladle refining. Figure 5-21 summarizes the results and clearly indicates that the (FeO + MnO) content of slag has a pronounced influence on the average MgO inclusion content. As shown, spinels are less likely to form under highly oxidizing slags, but their formation becomes much more favourable below a (FeO + MnO) content of approximately 1wt%. From Figure 5-21 it is seen that MgO inclusion content of both aluminum killed non-calcium treated and calcium treated heats exhibit a similar dependence on top slag (FeO + MnO) content.

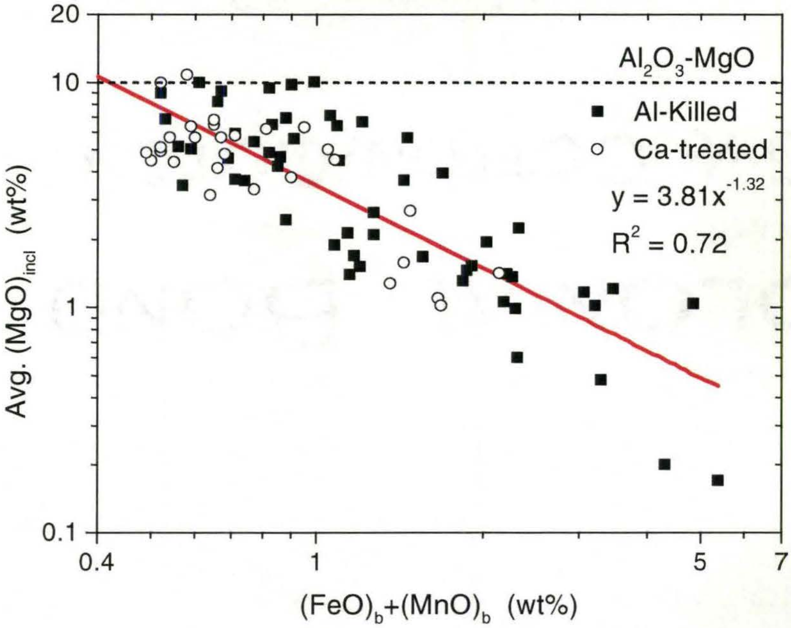

Figure 5-21: Effect of slag (FeO + MnO) content on the average MgO inclusion content within aluminum killed non-calcium treated (■) and calcium treated (○) heats.

In contrast to the results of Story et al. (2005), no relation was found between electrical arcing at the LMF and spinel formation. Further, while magnesium was present as an impurity in added aluminum and may promote spinel formation in some heats, it was not a precondition for spinel formation. Figure 5-22 presents the Al-Mg-O equilibrium diagram that was reproduced using the thermodynamic data of Nadif et al. (1986) and the cell model for calculating the thermodynamic activity of $MgO.Al_2O_3$ spinels.

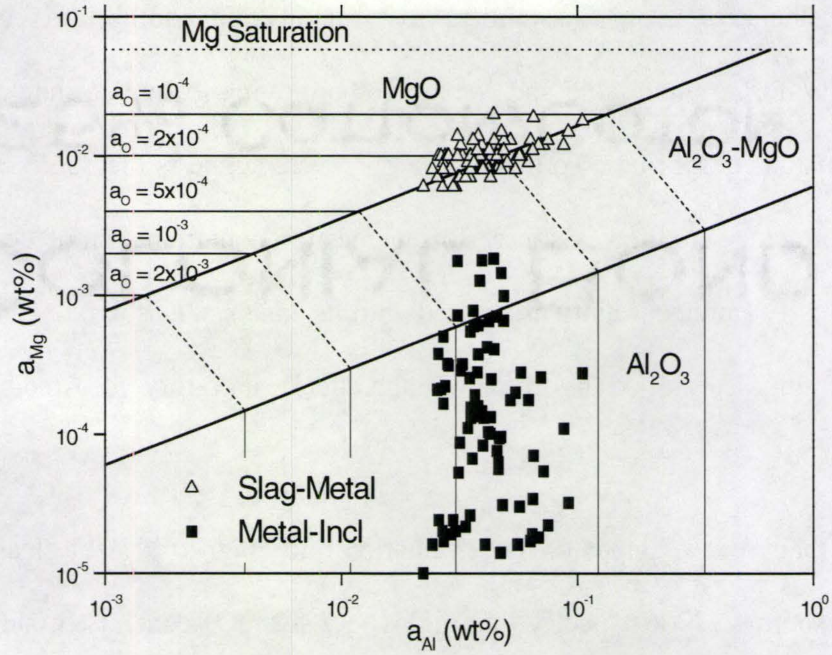

Figure 5-22: Al-Mg-O equilibrium diagram in liquid steel at 1,600°C (reproduced using the thermodynamic data of Nadif & Gatellier, 1986). Dissolved magnesium levels were calculated on the basis of slag-metal (Δ), and metal-inclusion (■) equilibrium.

As shown in Figure 5-22, for a given oxygen level the equilibrium phase changes from MgO, MgO.Al_2O_3, to Al_2O_3 with increasing aluminum content. Dissolved magnesium contents in steel for each heat sampled were determined using bulk slag, metal, and inclusion chemical analysis results on the assumption of slag-metal and metal-inclusion equilibrium. In regard to the assumption of slag-metal equilibrium, calculated dissolved magnesium contents ranged between 50 and 200ppm, with MgO being the most stable phase. A separate analysis of starting ladle slag compositions at ArcelorMittal Dofasco using the cell model (Section 3.4.6) confirms MgO as a stable phase within the slag, where slag MgO levels were determined as being approximately 15% on average (on an absolute not weight basis) above its slag saturation point. The dissolved magnesium content calculated from assuming metal-inclusion equilibrium changes significantly during processing and appears to be moving towards a state of slag-metal-inclusion equilibrium. To this end, Figure 5-22 suggests that ladle slag and possibly refractory are the key sources of magnesium contamination of steel. Due to the difficulty and uncertainty associated with its analysis, dissolved magnesium content is not determined by the iron and steel laboratory at ArcelorMittal Dofasco.

In their review paper on the evaluation and control of steel cleanliness, Zhang & Thomas (2006) specify that high (FeO + MnO) contents in slag are a key reason for the formation of slivers in as cast product. It is also well documented that high (FeO + MnO) contents in slag, reduce steel cleanliness by reoxidation and may even spoil an effective calcium treatment (Ahlborg, 2001). Yet a further disadvantage of high (FeO + MnO) slag contents was elucidated in Figure 4-29, where highly oxidizing slags were shown to yield low sulphur partition ratios that adversely influence desulphurization kinetics. To this end, it would seem obvious that minimizing slag carryover and targeting a highly reducing top slag during ladle refining would be the optimal practice within industry. However, consideration of Figure 5-21 in combination with the previously discussed findings of Faulring et al. (1979), where magnesium contamination of steel was found to minimize the effect of calcium treatment due to the formation of $MgO.Al_2O_3$ spinels, suggests that operation under reducing slags may potentially expedite nozzle clogging at the caster. Clearly, as suggested by Story et al. (2005), there appears to be an optimum operating window for (FeO + MnO) slag content that depends on factors such as whether the heat is calcium treated or is a surface-quality critical grade.

5.5.3. Calcium Modification of Alumina Inclusions

Figure 5-23 presents the equilibrium diagram for Al-Ca-O in steel at 1600°C that was reproduced using the cell model and the thermodynamic data of Nadif & Gatellier (1986). The diagram illustrates that several ppm of dissolved calcium in steel is required to form liquid calcium aluminate inclusions within the normal range of steelmaking oxygen and aluminum activities. In regard to the standard operating practice at ArcelorMittal Dofasco, calcium is injected as CaSi wire deep into the metal bath at the end of refining once sulphur content in steel is at or within target specification.

Slag-metal and inclusion-metal equilibrium points shown in Figure 5-23 were determined from plant data following a similar approach as was detailed in Section 5.5.2. As seen, calcium activity assuming slag-metal equilibrium is typically 2-3 orders of magnitude greater than the values calculated by assuming inclusion-metal equilibrium. Analysis of the ladle slag composition at ArcelorMittal Dofasco using the cell model revealed that slag was generally close to CaO staturation, being present at levels of 90-95% of saturation. From Figure 5-23, it is apparent from the low levels of dissolved calcium activity calculated from non-calcium treated heats, that top slag has little to no influence on the calcium content in steel. In contrast to the low dissolved calcium contents from assuming inclusion-metal equilibrium on non-calcium treated heats, dissolved calcium levels of a few tenths of a ppm were calculated from the inclusion composition results of Ca-treated heats before deliberate calcium additions. It should be noted that similar high levels of calcium were reported by Faral & Gaye (1984) in their investigation on slag-metal equilibria. Further, these findings are in agreement with the experimental results of Lu (1991). The longer times required for establishing equilibrium within the non-calcium treated heats (Figure 5-18 and 5-19) may serve as a possible explanation for the calculated low calcium levels within non-calcium treated heats.

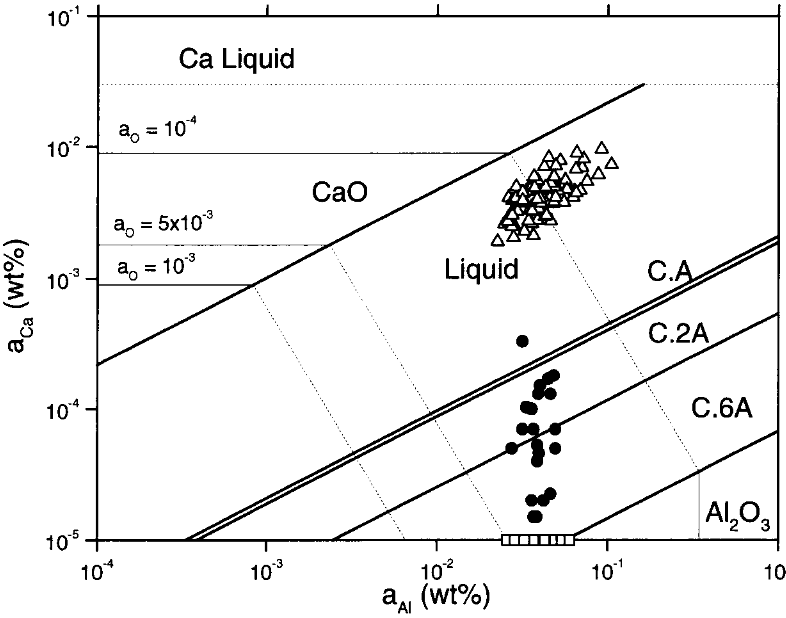

Figure 5-23: Al-Ca-O equilibrium diagram in liquid steel at 1,600°C (reproduced using the thermodynamic data of Nadif & Gatellier, 1986). Dissolved Ca levels were calculated on the basis of slag-metal (Δ), and metal-inclusion equilibrium for non-Ca treatment (□) and Ca-treated heats (●).

An attempt was made, using the thermodynamic models (i.e. unified interaction parameter model and cell model) previously reviewed in Chapter 3, at developing an inclusion control model for potential use as an online control tool at the ladle furnace at ArcelorMittal Dofasco. The model framework was based on the work of Zhang et al. (2004), and Gatellier and coworkers (1991). While the inclusion model developed was able to duplicate the published results of Zhang et al. (2004) for free cutting steels, it was unsuccessful in modelling the plant results contained within this thesis.

Several of the key factors found limiting the successful application of the inclusion model to the industrial trials at ArcelorMittal Dofasco was recently the subject of a discussion by Ghosh (2001). Ghosh (2001) notes that uncertainties in the thermodynamic data, melt homogenization, sampling and analysis of laboratory measurements yields experimental data suffering from scatter and irreproducibility. Figure 5-24 demonstrates the effect of these uncertainties on inclusion modelling using the thermodynamic data summarized in Table 5-2. The equilibrium constant expression by Gatellier & Olette (1979) was used for calculating the iso-activity line for aluminum in Figure 5-24 (top), while that by the Steelmaking Data Sourcebook (1988) was used for Figure 5-24 (bottom). In both cases the equilibrium data for Ca-CaO by Nadif & Gatellier (1986) was used for determining the iso-activity lines for calcium.

As shown, significant differences result in the computation of aluminum iso-activity lines despite what appears to be only a minimal difference in the equilibrium constant expressions presented in Table 5-2. While not illustrated in Figure 5-24, a far greater variability was observed when comparing the iso-activity lines for calcium using the widely different equilibrium constant relations available within the literature. On the basis of these results, the accuracy of thermodynamic inclusion model predictions within an industrial operation remains unclear. Ghosh (2001) appears to support this finding in his text, commenting that while thermodynamic predictions are expected to be valuable, very little experimental verification of these predictions has been sufficiently demonstrated within the literature.

Table 5-2: Thermodynamic data for slag-metal reactions

Reaction	ΔG^o (J)	log K	Reference
$Al_2O_3 = 2[Al] + 3[O]$	1,200,070 - 393.3T 1,225,000 - 393.8T	$-62,675/T + 20.54$ $-63,980/T + 20.57$	Gatellier et al.(1979) *
$CaO = [Ca] + [O]$	491,190 - 146.5T	$-30,110/T + 11.40$	Nadif et al.(1986)

* The Japan Society for the Promotion of Science: The 19th Committee on Steelmaking (1988)

Uncertainties in the thermodynamic data aside, a further problem encountered when attempting to implement an inclusion control model within an industrial operation is the issue of time. While a steel sample is generally taken after calcium injection, operational demands at the caster frequently require ladles to be shipped from the LMF prior to chemical analysis results being returned from the iron and steel laboratory. It follows that steelmakers have only one opportunity to correctly modify inclusions in steel, and that predictions from an inclusion model dependent on chemical analysis results as an input are of little

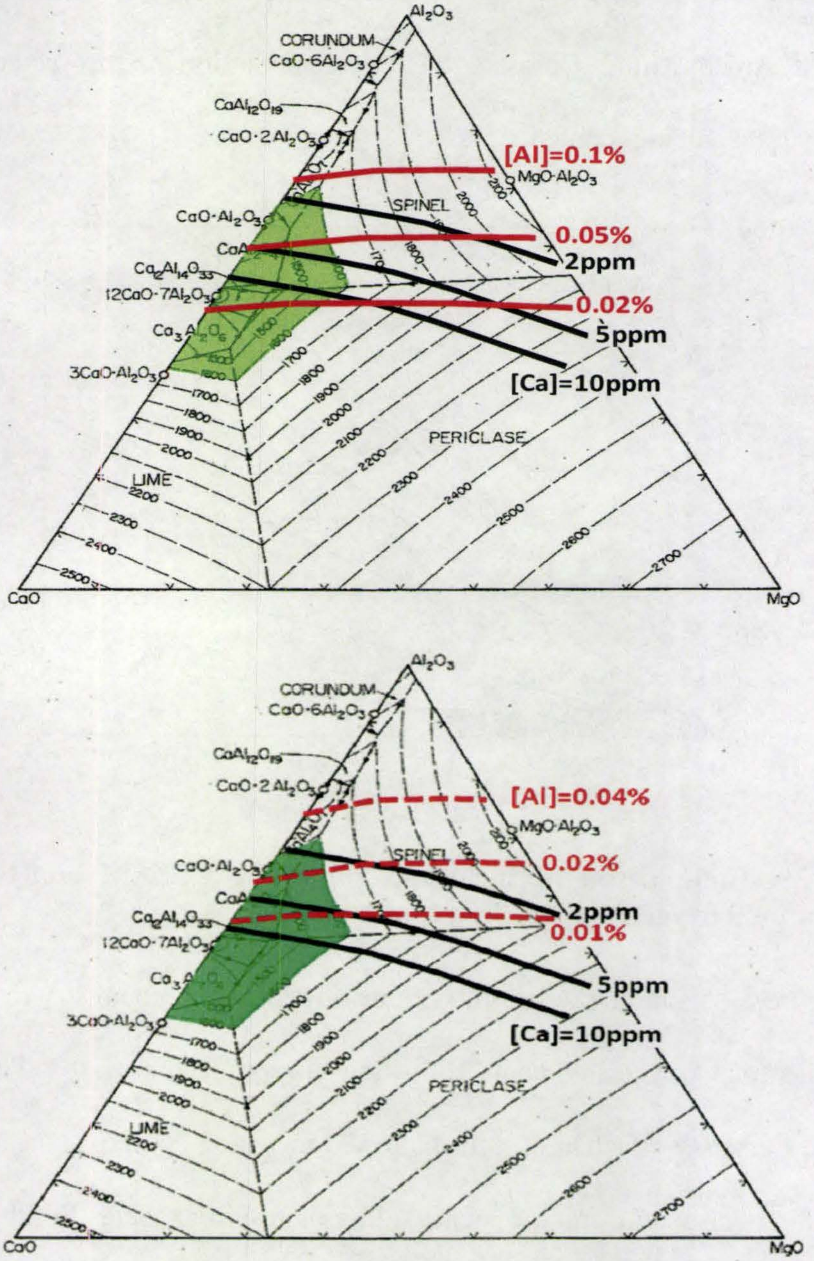

Figure 5-24: Iso-residual aluminum and calcium contents in steel in equilibration with CaO-MgO-Al_2O_3 slag system during ladle refining at 1600°C and 2ppm [O].

value after the fact. An additional impediment limiting the implementation of inclusion models concerns the actual measurement of the soluble calcium content in steel. At ArcelorMittal Dofasco, the atomic emission spectrometer (AES) returns only total calcium contents.

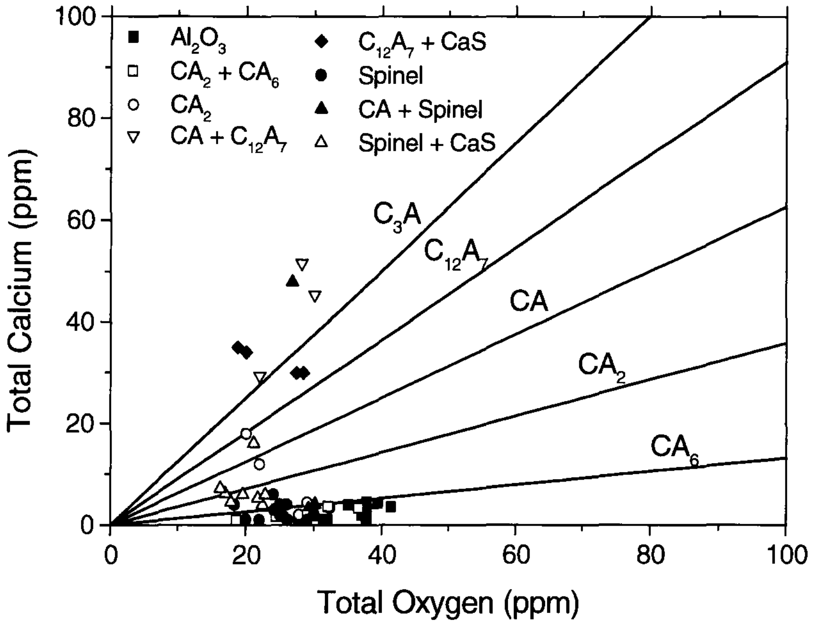

Figure 5-25: Comparison of inclusions found by CCSEM analysis as a function of total oxygen and calcium contents.

Figure 5-25 summarizes results comparing inclusion chemistry to the total calcium and total oxygen contents following an approach used by Turkodgan (1988) and Larsen & Fruehan (1990). Indicated inclusion compositions represent the most dominant inclusion type identified by inclusion analysis. Solid lines are drawn for the stochiometric relationships of various calcium aluminates. While the amount of calcium associated with sulphur is neglected in Figure 5-25, Turkdogan (1988) isolated characteristic regions for both high and low sulphur as a function of total oxygen and calcium contents using numerous industrial samples. Although the accuracy between the inclusions found and the stoichiometric lines is admittedly less than the agreement reported by Larsen & Fruehan (1990) for their laboratory melts, the results do demonstrate that the method provides a resonable approximation of oxide inclusions in the absence of microscopic examination.

Chapter 6

EXTENDED KALMAN FILTER

6.1. Introduction

The first step in process control involves the representation of a process in terms of manageable equations. The second step involves determining how to manage these equations in order to establish the optimum control action at any given time. In regards to metallurgical operations, the principal problem limiting the implementation of the latter step has been that reliable process models are generally unavailable (Soliman et al., 1974). It follows that a good physical understanding of the process and the development of proven mathematical models are necessary prerequisites for the implementation of on-line state estimation and control schemes.

The situation in regard to the ladle metallurgical furnace has been defined in Chapter 4, where a multi-component kinetic model was developed for estimating the state of the LMF. While good agreement was demonstrated between the developed multi-component kinetic model and experimental results, the process model alone is not typically sufficient as a control system. Theoretical models serve only to approximate reality, being unable to account for measurement and experimental observation errors resulting from natural process fluctuations and / or limitations of measurement devices. As process model predictions are invariably uncertain, plant-model mismatch if gone unchecked may lead to significant error propagation causing poor process control and plant economics.

State estimation is the process of determining the state from the output measurements given a dynamic model of the system (Muske & Edgar, 1996), where the state is the minimum amount of information necessary at the current time to uniquely determine the dynamic behaviour of the system at all future times given the inputs and parameters. The purpose of any state estimator is to feed-back information from the process to update the state estimates from the model, and thereby track the effect of these disturbances on all the states (Gagnon & MacGregor, 1991).

This chapter is intended to introduce the extended Kalman filter as a state estimator for modelling measurement noise within a ladle metallurgical furnace. While used extensively within the chemical engineering field the extended Kalman filter has largely been ignored by metallurgists. A secondary objective of this chapter is to stimulate research interest in the application of the Kalman filter for controlling metallurgical operations.

6.2. Literature Review

6.2.1. Application of the Extended Kalman Filter (EKF)

As summarized by Grewal & Andrews (2001), the EKF has found applications ranging from process control, navigation, and flood prediction. From a process control perspective, there have been a limited number of examples of EKF application to batch / semi-batch processes within the literature, with most of these applications being focused on the control of polymerization and fermentation reactors within the chemical industry (Gilles, 1986; Gilles, 1987).

Among the few studies regarding the application of the extended Kalman filter to metallurgical systems were a series of papers by Wells and coworkers (Wells, 1970; and Wells & Wismer, 1971). The objective of these studies was to determine the feasibility of applying the extended Kalman filter to a basic oxygen furnace (BOF) for estimating temperature and carbon within the molten bath. A detailed kinetic model consisting of 24 differential equations was developed for the BOF (Wells, 1970) and was subsequently used to simulate synthetic plant data, Figure 6-1.

As neither discrete nor continuous sensors were available to measure composition and temperature within the molten bath at the time of the study, the authors assumed that only the partial pressure of carbon monoxide in the exhaust gas was measurable. Wells (1970) then used the EKF for estimating carbon and temperature from the noisy carbon monoxide measurements. Given the uncoupled nature of many of the differential equations within the 24th order process model, Wells (1970) simulated the EKF using a simplified process model having only four state variables, namely: carbon, temperature, carbon monoxide partial pressure, and bath oxygen composition. Figure 6-2 summarizes the comparison between the 4th order model, 24th order model, and Kalman filter results.

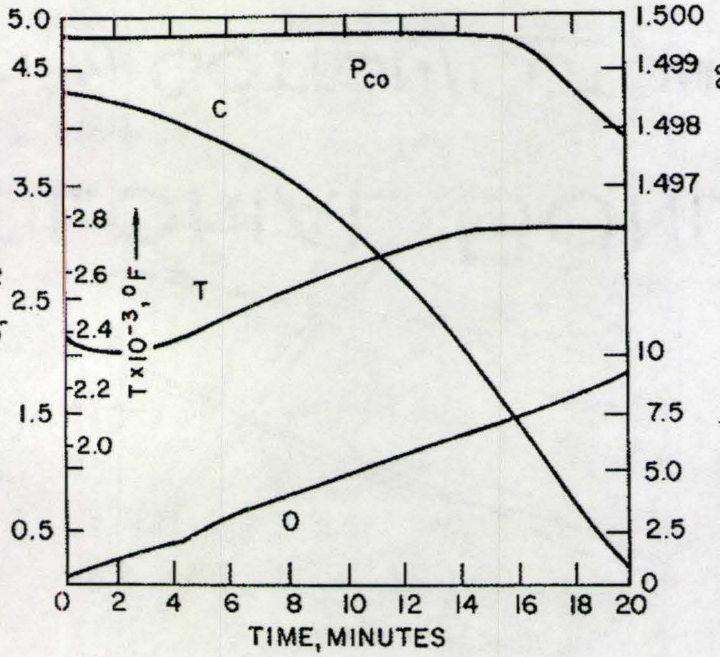

Figure 6-1: Summary concentration and temperature profiles within the BOF. Shown results were calculated using the full (24 differential equation) BOF kinetic model. (Wells, 1970)

On the basis of Figure 6-2, Wells (1970) concluded that the results from the 4th order model for the partial pressure of carbon monoxide and oxygen were good relative to the 24th order model (see Figure 6-1), but that the agreement between temperature and carbon was generally poor. A similar observation was made regarding Kalman filter performance, and it was noted that the 'forgetting' rate of the filter increased after 15 minutes. To improve the predictive performance of the filter, Wells (1970) considered the effect of hypothetical and discrete temperature and carbon measurements within the bath at 15 minutes. The results of the simulation are presented as Figure 6-3, from which Wells (1970) reasoned that Kalman filter performance was acceptable after the additional measurement information was introduced.

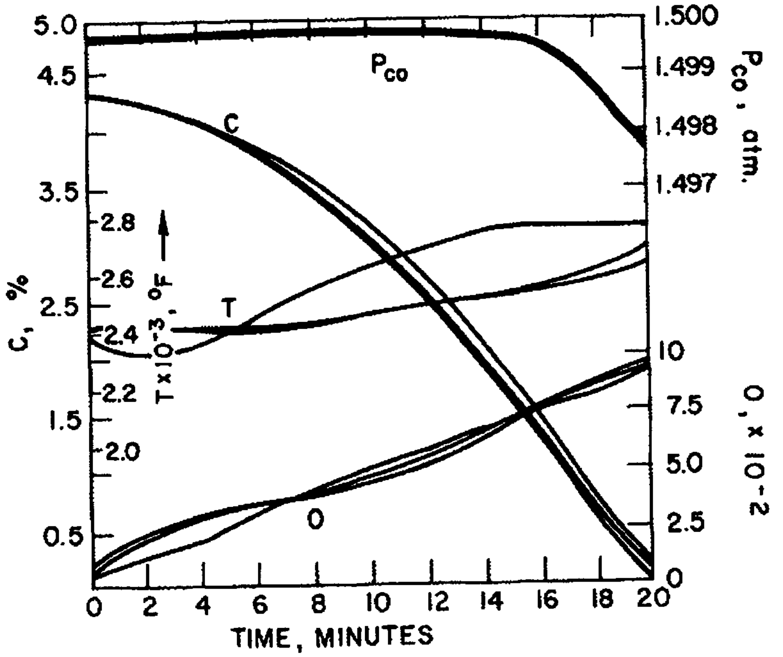

Figure 6-2: Comparative results of 4th order model, 24th order model and Kalman filter results. (Wells, 1970)

Following the work of Wells (1970) and Wells & Wismer (1971), Soliman et al. (1974) applied the extended Kalman filter in combination with a process model for describing bath temperature and composition trajectories within the argon-oxygen decarburization (AOD) stainless steel process. The process model used in their study was originally developed by Asai & Szekely (1974a, 1974b) and had previously been demonstrated to provide reasonable estimates of bath temperature and composition trajectories in both laboratory and industrial scale systems. Dissolved elements considered in the study include oxygen, carbon, chromium and silicon. The chemical kinetics of all these reactions were assumed fast, while equilibrium was assumed established at the slag-metal interface. Bulk slag and metal compositions were subsequently updated by solving first order differential equations. A simplifying assumption in the model was that slag and metal phases were assumed thoroughly mixed, such that no concentration gradients existed in the bulk phase. An extended Kalman filter was applied to the process assuming several levels of measurements possible (continuous and discrete), and for a range of measurement and process noises. Figure 6-4 summarizes selected results from the work of Soliman et al. (1974) for the case of different discrete sensor set measurements.

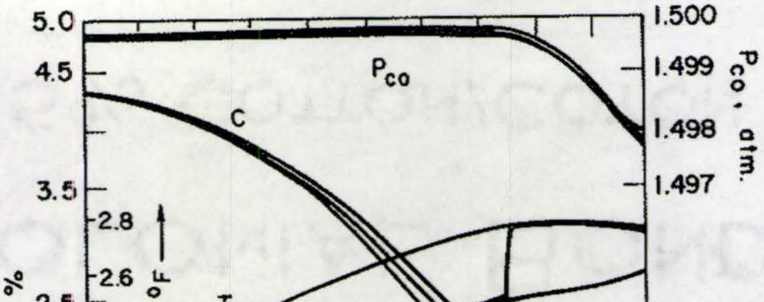

Figure 6-3: Comparative results of 4th order model, 24th order model and Kalman filter results. Discrete temperature and carbon measurements were assumed taken at 15 minutes. (Wells, 1970)

From their results, Soliman et al. (1974) concluded that while sampling of the full melt composition (carbon, chromium, and silicon) provided for the best state estimates, rather good estimates were still obtainable using temperature measurements only. From a practical viewpoint, the authors suggested that combining the filter with existing measurement hardware would give a very reliable on-line estimate of the bath composition within an industrial operation.

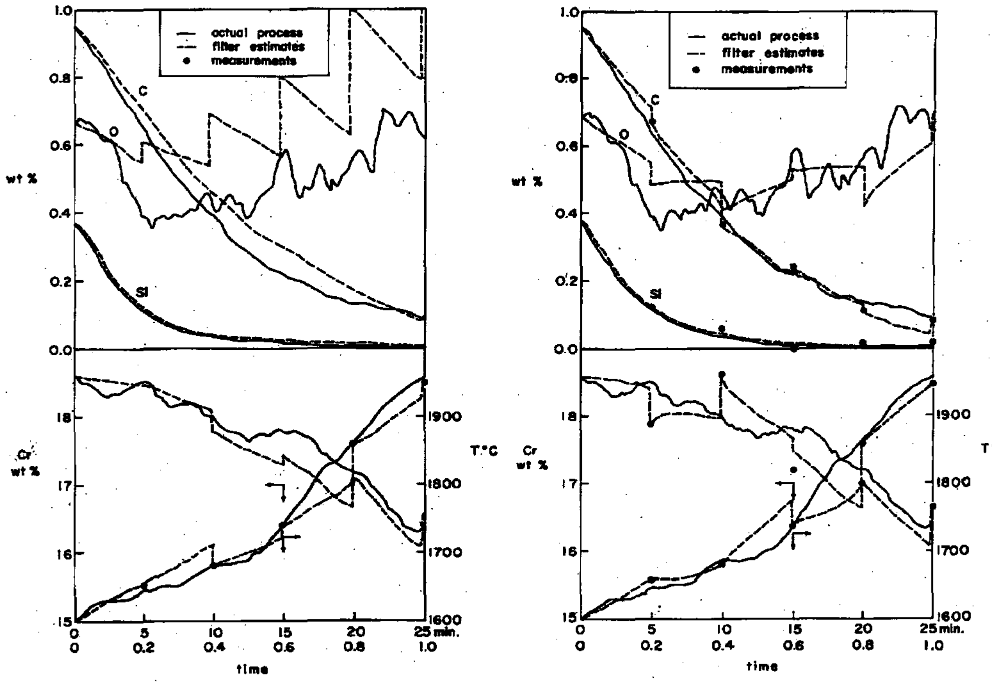

Figure 6-4: The filter performance with (left) discrete (5 min intervals) temperature measurements, (right) discrete (5 min intervals) temperature, carbon, chromium, and silicon measurements. (Soliman et al., 1974)

As summarized by Kozub & MacGregor (1992), a common error in judgment when formulating extended Kalman filters is neglecting the incorporation of non-stationary disturbance and / or parameter states needed to eliminate bias between the true and model predicted response when non-ideal prediction mismatch situations arise. Kozub & MacGregor (1992) further state that when making this type of mistake, the designer often attempts to mask the problem by increasing the noise associated with the process states, resulting in a noisy state estimator that hides the bias problem. In regards to the work of Wells (1970, 1971) and Soliman et al. (1974), neither researcher incorporated such non-stationary states. As shown in Figure 6-3 and 6-4 the end result from applying a Kalman filter in combination with developed process models in the absence of such non-stationary states was a proportional type of state estimator having none of the integral action necessary to eliminate bias. The inherent assumption being made by Wells (1970) and Soliman et al. (1974) is that the only way the true process can deviate from the model is by a zero mean, random component. As the whole purpose of the Kalman filter is to track the real process when non-stationary disturbances or model parameter mismatches occur, it follows that the inclusion of stochastic states are a necessary component in any real industrial application where imprecise models are usually applied and unmeasurable disturbances exist (Kozub & MacGregor, 1992; Gagnon & MacGregor, 1991).

6.2.2. Metallurgical Sensors

Process measurements play an integral role in the accuracy of predictive models. In regards to metallurgical operations, measurements are typically made using rapid and in situ consumable sensors for dissolved oxygen activity and temperature. There are no known direct or continuous steel and / or slag composition measuring methods in use today in steel plants. However, as summarized by Brooks and Subagyo (2002), and Carlsson et al. (1986) sensor development remains a well researched area within the metallurgical literature. These methods involve non-contact approaches such as (Carlsson et al., 1986): (i) sparking of the liquid iron bath and direct analysis via optical fiber, (ii) atomizing at the surface and using a plasma burner for analysis, and (iii) using a laser-beam projected at the surface giving a micro-plasma capable of being analyzed in a spectrometer. Clearly, improved sensors combined with improved process control models allow for the potential optimization of LMF practices.

The most successful commercial sensor currently in use within the steel industry is the oxygen activity probe, such as the Celox oxygen probe from Heraeus Electro-Nite (Philadelphia, PA). As previously described in Chapter 4 (Section 4.3.4.3), the Celox probe uses an empirical correlation to estimate dissolved oxygen activity within the steel bath from measured EMF and temperature readings. The EMF reading from the Celox probe has also being related to the dissolved aluminum content in steel on the assumption that the formed deoxidation product is pure Al_2O_3. However, as reported by Turkdogan (2001a), no detailed study has been made to evaluate the uncertainty limits of this approximation. Iwase and coworkers (1988), conducted research to develop a silicon EMF probe for the in situ measuring of silicon (Si) levels in liquid metals. Due to the lack of thermodynamic data on the effect of all other components on the silicon activity, however, a rigorous theoretical interpretation of the measurements has not been possible. Instead, an empirical correlation based on plant tests was derived between the percentage of silicon in hot metal and probe EMF readings. Following the work of Iwase et al. (1988), Gomyo et al. (1993) tested the performance of a double layered, three-phase zirconia electrolyte in both a laboratory and plant setting. Figure 6-5 summarizes the good agreement between sensor and laboratory measured results from the No. 1 blast furnace of Kure Works, Nisshin Steel.

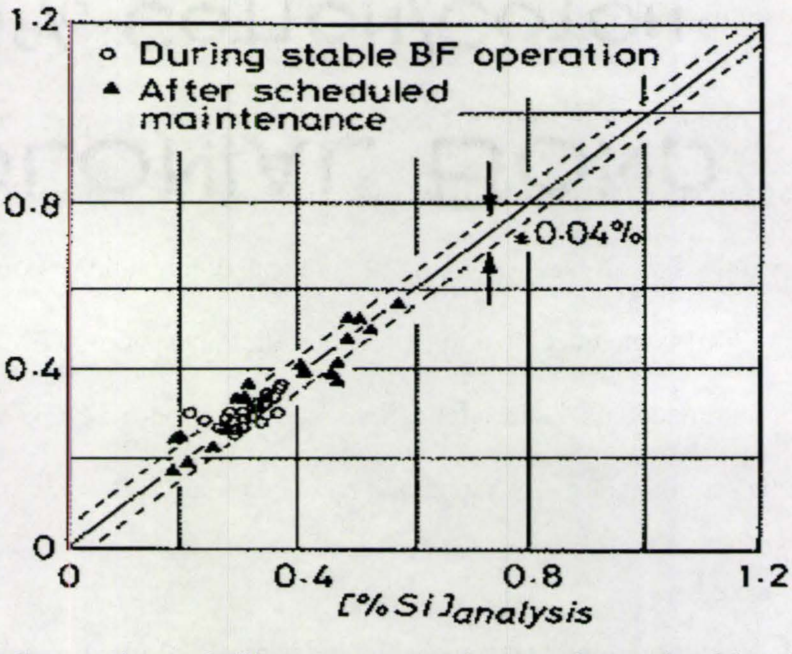

Figure 6-5: Comparison of silicon concentrations as determined by chemical analysis with those by silicon sensor. Results were obtained at the No. 1 blast furnace of Kure Works, Nisshin Steel. (Gomyo et al., 1993)

In his work on the development of sensors for measuring the solute contents of liquid ferrous and non-ferrous metals, Turkdogan (2001a, 2001b) proposed using glassy calcium alumino-silicate (containing approximately 38wt% CaO, 42wt% SiO_2, and 20wt% Al_2O_3) as an electrolyte in the EMF sensor with an appropriate reference electrode material selected based upon the type of solute element being measured, Table 6-1. On the basis of this design concept and citing the satisfactory results of many laboratory experiments using alumino-silicates as electrolytes in EMF concentration cells, Turkogan (2001a) secured a patent for detecting the concentrations of metallic elements Al, C, Ca, Cr, Mg, Si and for the gaseous elements H_2, O_2, S_2, N_2, and P_2 in liquid metals using disposable EMF sensors. It is unclear whether any of the listed sensors are currently commercially available.

As a logical extension to the proposed single EMF probe, Turkdogan (2001a) highlighted the possibility of incorporating two or more EMF probes within a single sensor base. Possible theoretical combinations considered by Turkdogan (2001a) included, a silicon, sulphur, and phosphorous EMF probe for blast furnace runner and ladle applications and a carbon, oxygen, and sulphur EMF probe combination for application in various stages of steelmaking operations.

Table 6-1: Recommended reference electrodes material for different solute elements being measured (Turkdogan, 2001a)

Solutes	Reference Electrode Materials	Melting Point (^oC)
Al in steel	NiAl	1639
C in steel & hot metal	Graphite	3800
Cr in steel	Cr	1903
Si in steel & hot metal	$Mo + Mo_3Si$	2070
O in steel	$Cr + Cr_2O_3$	1903 / 2265
N in steel & hot metal	Ti + TiN	1660 / 2950
S in steel & hot metal	Ti + TiS	1660 / 1927
P in steel & hot metal	Th + ThP	1775 / 2950

Suggesting an alternative to consumable probes, Chiba et al. (1993) demonstrated the application of a method termed 'hotspot radiation spectrometry' for the direct measurement of manganese in molten iron. The approach is based on the measurement of atomic emission radiated at a locally heated area of molten iron and provides for the real-time measurement of manganese concentration during decarburizing within a converter. Figure 6-6 presents a schematic diagram of the experimental system used in their laboratory trials. Analytical results obtained by this method were found in good agreement with those obtained by conventional means. It remains unclear from their work, however, whether hotspot radiation spectrometry is capable of measuring other solute contents.

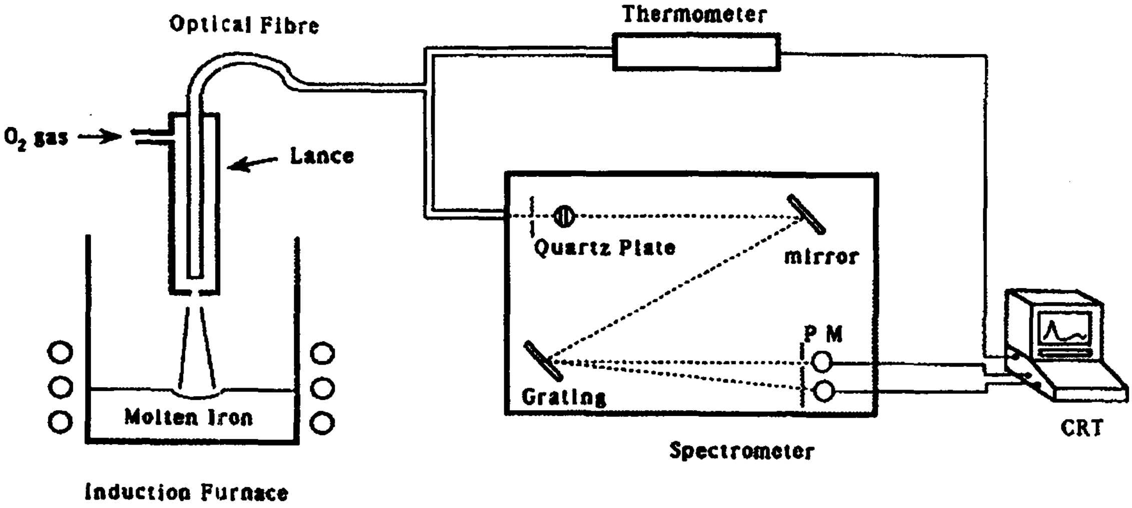

Figure 6-6: Schematic diagram of laboratory experimental system. (Chiba et al., 1993)

Turkdogan (2000) further proposed using slag-oxygen sensors to measure oxide activities (FeO, SiO_2, and CaO) of steelmaking slags. The slag-oxygen sensor conceived by Turkdogan (2000) consists of two dissimilar electrodes that result in an oxygen potential difference when immersed in molten slag, registering an open circuit cell EMF. While these sensors are by and large conceptual in nature, Heraeus Electro-Nite (Philadelphia, PA) has developed a sensor (Quick-Slag®) for measuring the activity of FeO in slag (Iwase et al., 2004). The sensor was extensively tested at the U.S. Steel Mon Valley (PA) Works (Meszaros et al., 1997), and proved to be an acceptable tool for accurate prediction of FeO content in slag, Figure 6-7.

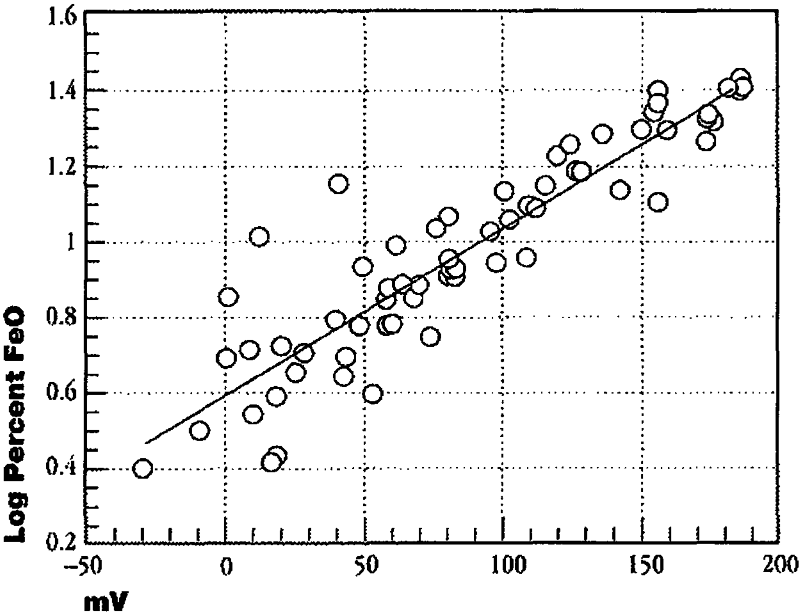

Figure 6-7: Corresponding slag activity probe millivolt readings were correlated to predict the slag FeO content. (Meszaros et al., 1997)

In parallel to the development of in situ measurement probes, significant research and development efforts have resulted in the commercialization of bench-top spectrometers. PANalytical's (Almelo, The Netherlands) new MiniPal 4 energy-dispersive XRF bench-top spectrometer system was successfully installed within the LMF pulpit on both the KBOM and EAF streams at

ArcelorMittal Dofasco. The bench-top spectrometer system is used by LMF operators and allows for the non-destructive, multi-element analysis of slag to international standards such as ASTM, ISO and DIN.

6.3. Mathematical Formulation

6.3.1. Introduction

As previously stated, the first step in modelling a system involves the representation of a process in terms of manageable equations. For metallurgical systems, these equations generally take the form of mass and energy balances and may be represented in continuous time by the following notation:

$$\dot{x}_i = f_i\left(x_i, u_i, t_i\right) \tag{6-1}$$

where x_i represents the set of dependent variables that influence the rate of change of $\dot{x}_i$, and u_i denotes the input variables that influence $\dot{x}_i$. Equation 6-1 relates the non-linear state equations at the current time step to the state of a future time step. First order differential equations of this type may be written for each major dependent variable in the process. Taken together the differential equations define the state vector:

$$\dot{x} = \left[\dot{x}_1 \ldots \dot{x}_i \ldots \dot{x}_n\right]^T \tag{6-2}$$

where n denotes the number of state variables in the process equations. The term state is defined as the minimum amount of information necessary at the current time to uniquely determine the dynamic behaviour of the system at all future times if the values of future independent variables are known. As summarized by Wells & Wismer (1970), while real processes are represented by an infinite number of states, dynamic process models usually only consider 10 or fewer state variables. To account for the incompleteness or process uncertainty of process models, a zero-mean Gaussian white noise vector is introduced as w:

$$\dot{x} = f\left(x,u,t\right) + w \tag{6-3}$$

A set of observation equations must be included in the process equations to define the control system completely. In the most general case the observations are non-linear combinations of the state variables and may be written as:

$$y = h\left(x,u,t\right) + v \tag{6-4}$$

where y is an n-dimensional vector of process observations that are related to the state, and v is a n-dimensional vector representing random sensor noise.

Since the state estimator will be used in real-time on a process control computer, discretized non-linear differential equations are to be used as:

$$\hat{x}_{t_{k+1}|t_k} = f\left(\hat{x}_{t_k|t_k}, u_{t_k}\right) + w_{t_k} \tag{6-5}$$

$$y_{t_k+1} = h\left(\hat{x}_{t_k+1|t_k}, u_{t_k}\right) + v_{t_k} \tag{6-6}$$

where t_k denotes discretized time, $t = t_k \Delta T$, and ΔT is the sampling interval.

6.3.2. Extended Kalman Filter

The extended Kalman filter (EKF) is the most commonly used method for estimating the state of a non-linear system. The theory behind the EKF is well known and understood. Based on the Kalman filter theory for linear systems (Kalman, 1960), the extended Kalman filter (Jazwinski, 1970) consists of a set of recursive time varying equations that are used for obtaining the updated values of the state vector from the available measurements. Extended Kalman filter equations may be considered as two groups: (i) time update (process model) equations, and (ii) measurement update equations:

Time Update Equations:

$$\hat{x}_{t_k+1|t_k} = f\left(\hat{x}_{t_k|t_k}, u_{t_k}\right) \tag{6-7}$$

$$y_{t_k+1} = h\left(\hat{x}_{t_k+1|t_k}, u_{t_k}\right) \tag{6-8}$$

$$P_{t_k+1|t_k} = \Phi_{t_k} P_{t_k|t_k} \Phi_{t_k}^T + R_w \tag{6-9}$$

Measurement Update Equations:

$$\hat{x}_{t_k+1|t_k+1} = \hat{x}_{t_k+1|t_k} + K_k\left(y_{t_k+1} - \hat{x}_{t_k+1|t_k}\right) \tag{6-10}$$

$$P_{t_k+1|t_k+1} = \left(I - K_{t_k} H_{t_k}\right) P_{t_k+1|t_k} \tag{6-11}$$

where

$$\Phi_{t_k} = \left(f_{t_k}\right)_{\hat{x}_{x_{t_k}|t_k}} = \left.\frac{\partial f_{t_k}}{\partial x_{t_k}}\right|_{\hat{x}_{x_{t_k}|t_k}} \tag{6-12}$$

$$H_{t_k} = \left(g_{t_k}\right)_{\hat{x}_{x_{t_k}|t_k}} = \left.\frac{\partial h_{t_k}}{\partial x_{t_k}}\right|_{\hat{x}_{x_{t_k}|t_k}} \tag{6-13}$$

$$R_w = E\left[w_k w_j^T\right] = R_w \delta_{kj} \tag{6-14}$$

$$R_v = E\left[v_k v_j^T\right] = R_v \delta_{kj} \tag{6-15}$$

where $P_{t_k|t_k}$ is the state covariance matrix, I is the identity matrix, Φ_{t_k} is the Jacobian matrix of x with respect to x in the state vector, H_{t_k} is the observation matrix, R_w and R_v are the process model and measurement covariance matrices, E denotes expected value operator, and δ_{kj} is the Kronecker delta function. The Kalman filter gain K_{t_k} is given by:

$$K_{t_k} = P_{t_k+1|t_k} H_{t_k}^T \left(H_{t_k} P_{t_k+1|t_k} H_{t_k}^T + R_v\right)^{-1} \tag{6-16}$$

The essential idea behind the EKF is to use the full non-linear differential equation model to obtain predicted state $\hat{x}_{t_k+1|t_k}$, and then to use the ordinary Kalman filter on the locally linearized process model, incorporating measurement results to obtain the updated state estimate $\hat{x}_{t_k+1|t_k+1}$. Figure 6-8 presents a schematic illustration showing the recursive nature of the EKF algorithm. As seen, when new observations y_{t_k+1} become available, the state estimates are iteratively updated using equation 6-10. While solution of the EKF equations is relatively straightforward, the uncertainty surrounding added Gaussian white noise terms w_{t_k} and v_{t_k} increases implementation difficulty.

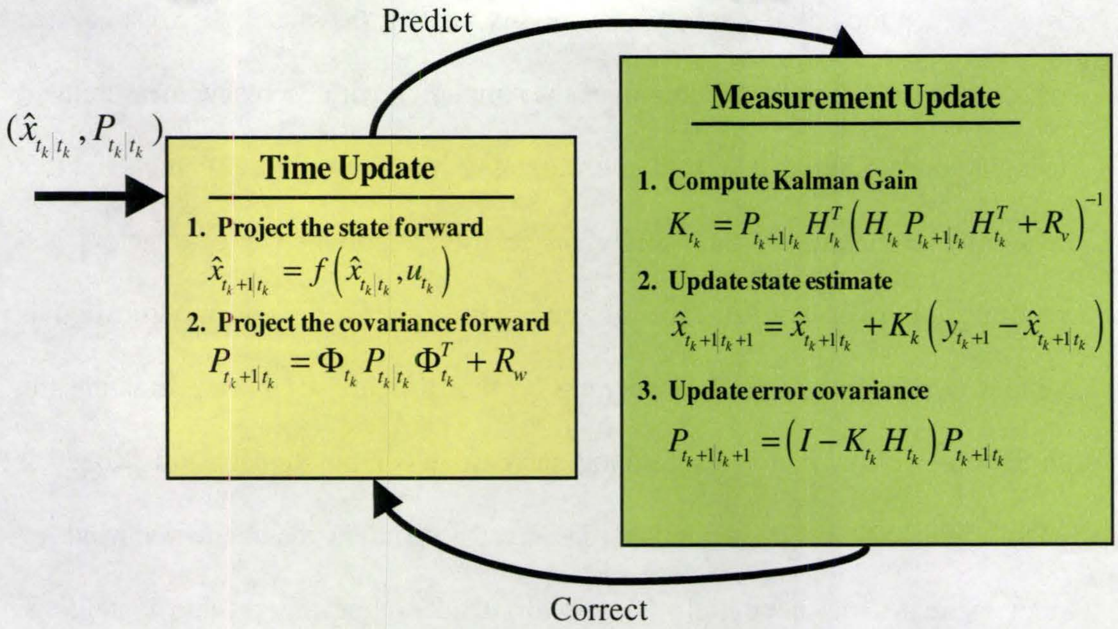

Figure 6-8: Schematic illustration of the extended Kalman filter. (adapted from Welch & Bishop, 2001)

6.3.3. Significance of Filter Parameters

The initial state vector $(\dot{x})$, the initial covariance matrix $\left(P_{t_k|t_k}\right)$, and the covariance matrices $(R_w$ and $R_v)$ are all parameters requiring specification by the designer when implementing an extended Kalman filter. The initial state estimate and covariance matrix determine the speed of the EKF filter response, while R_w and R_v determine its response characteristics. As summarized by Kozub & MacGregor (1992), if a serious error is made when selecting these parameters then the extended Kalman filter may provide poor biased estimates of the non-linear states.

When the initial state vector is poorly known, Jazwinski (1970) suggested restarting the EKF at the beginning of the simulation with each new measurement using an update initial state estimate. Kozub & MacGregor (1992) employed this reiterative technique in their study on semi-bath polymerization reactors and reported improved convergence of state estimates. While this modification is simple in principle, it may, depending on the difficulty of back-estimating the initial state vector, lead to a substantial increase in computational effort (Kozub & MacGregor, 1992). Gagnon (1990) used yet a different technique for handling poor estimates of the initial state vector. Under poor initial state conditions, Gagnon (1990) specified a larger initial covariance matrix $\left(P_{t_k|t_k}\right)$ and relied heavily on process measurements over the first few estimates to gain reasonable values of the state vector. The initial state covariance matrix estimate reflects the degree of confidence in the initial state estimate, where large values result in elevated Kalman gains thereby ensuring rapid convergence to reasonable values of the state vector.

Figure 6-9 and 6-10 illustrate the tuning potential of the Kalman filter using a simple example reproduced from Welch & Bishop (2001). As seen in Figure 6-9, if the process noise covariance (R_w) is small relative to the measurement noise covariance (R_v), it indicates that process measurements are imprecise and that the measurement update corrections will be small. Conversely, if as shown in Figure 6-10, the measurement noise covariance is decreased relative to the process noise covariance, then measurements become relatively noise free and the deviation between measured output and filter predicted output will be small. More specifically, the filter becomes dependent on current observations. As noted by Wells (1970), many practical methods for tuning the Kalman filter have been suggested, however, no analytical method for selecting these parameters has yet been obtained.

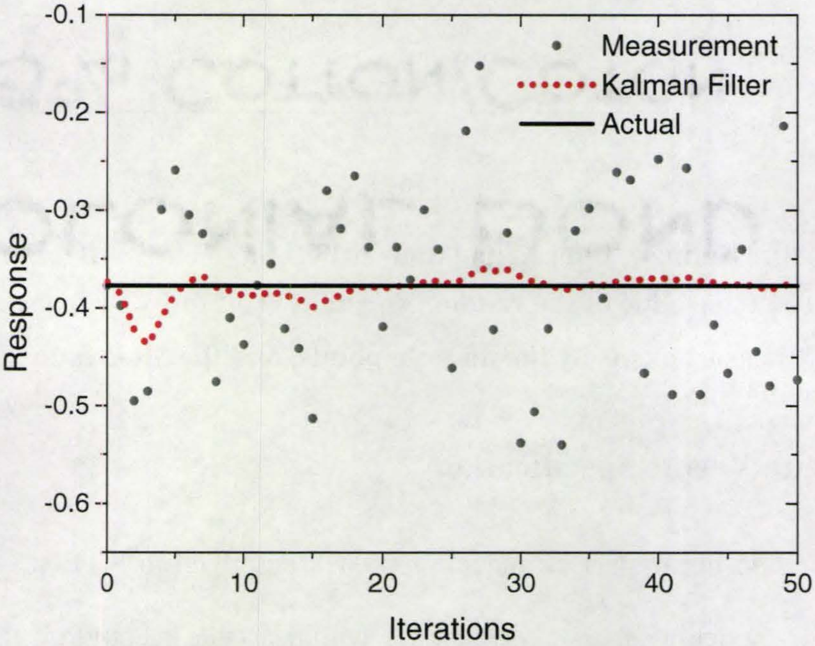

Figure 6-9: Kalman filter simulation where $\underline{R}_w = 1e^{-5}$, $\underline{R}_v = 0.01$, and $\underline{P}_{0|0} = 1$. The true value of the random constant is given by the constant solid line, noisy measurements by the discrete points, and the filter estimate by the dotted moving line.

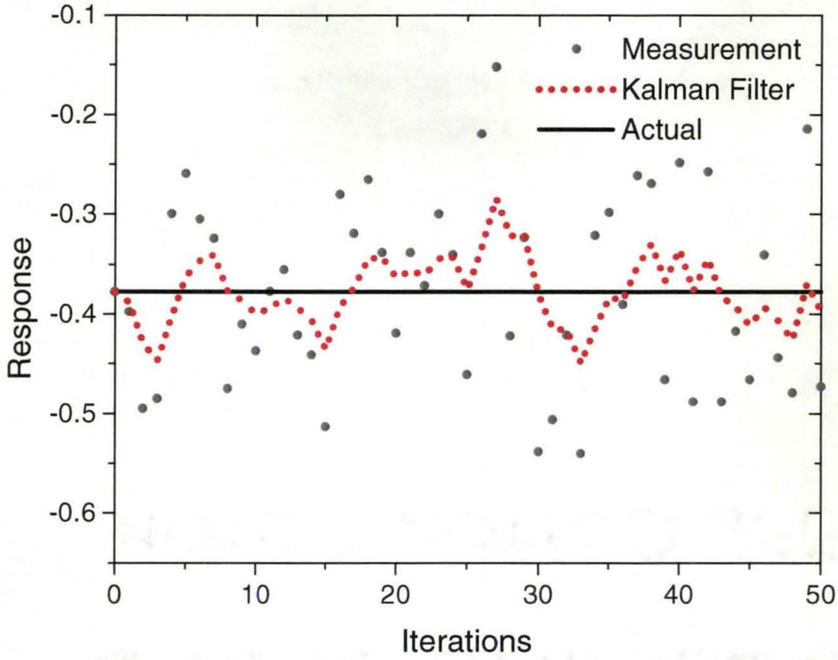

Figure 6-10: Kalman filter simulation where $\underline{R}_w = 1e^{-5}$, $\underline{R}_v = 1e^{-4}$, and $\underline{P}_{0|0} = 1$. The true value of the random constant is given by the constant solid line, noisy measurements by the discrete points, and the filter estimate by the dotted moving line.

6.3.4. State Vector Specification

The non-linear state estimation approach described in Section 6-3-2 will be used for modelling measurement noise within a ladle metallurgical furnace. The complete state vector consists of both deterministic and stochastic components. The deterministic states result from the non-linear differential equations defined for the multi-component kinetic model, and consist of the following 15 state component vector:

$$x^d = \left[X_{Mn}\ X_{Al}\ X_{Si}\ X_S\ X_{Ti}\ X_O\ X_{CaO}\ X_{Al_2O_3}\ X_S\ X_{MnO}\ X_{SiO_2}\ X_{FeO}\ X_{MgO}\ X_{TiO_2}\ T \right]^T \tag{6-17}$$

where

X_{Mn} : Concentration of manganese in steel (mol fraction)
X_{Al} : Concentration of aluminum in steel (mol fraction)
X_{Si} : Concentration of silicon in steel (mol fraction)
X_{S} : Concentration of sulphur in steel (mol fraction)
X_{Ti} : Concentration of titanium in steel (mol fraction)
X_{O} : Concentration of oxygen in steel (mol fraction)
X_{CaO} : Concentration of lime in slag (mol fraction)
$X_{Al_2O_3}$: Concentration of alumina in slag (mol fraction)
X_{S} : Concentration of sulphur in slag (mol fraction)
X_{MnO} : Concentration of manganese oxide in slag (mol fraction)
X_{SiO_2} : Concentration of silica in slag (mol fraction)
X_{FeO} : Concentration of wustite in slag (mol fraction)
X_{MgO} : Concentration of magnesia in slag (mol fraction)
X_{TiO_2} : Concentration of titanium oxide in slag (mol fraction)
T : Temperature (K)

As previously discussed in Chapter 4, the major uncertainties in the developed multi-component kinetic model are the slag phase mass transfer correlations that were determined empirically by fitting the experimental results at ArcelorMittal Dofasco. As these parameters are invariably uncertain, a stochastic parameter is introduced $\left(x^S = \xi\right)$ in all slag phase first order differential equations to account for process disturbances and to arrive at bias free estimates:

$$\frac{dX_{MO_\sigma}}{dt} = \xi k_{sl}^{M_xO_y}\left(\frac{A}{V_{sl}}\right)\left(X^*_{MO_\sigma} - X^b_{MO_\sigma}\right) \tag{6-19}$$

As the dynamics of stochastic disturbances are generally unknown, it is common to assume that they follow simple non-stationary random walk behaviour (Kozub & MacGregor, 1992; Gagnon & MacGregor, 1991):

$$x^S_{t_k+1} = x^S_{t_k} + w^S_{t_k} \tag{6-18}$$

where $w^S_{t_k}$ is random white noise and represents the amount of change occurring in the stochastic states between sampling intervals. The one-step-ahead prediction of the stochastic state is given by:

$$\hat{x}^S_{t_k+1|t_k} = \hat{x}^S_{t_k|t_k} \tag{6-20}$$

Combining the deterministic and stochastic states into a single augmented state vector gives:

$$x_k = \left[x_k^d \; x_k^S\right]^T \tag{6-21}$$

6.3.5. Computation of the Transition Matrix

In the case of non-linear models, the full non-linear differential equation process model is used to obtain the predicted state (equation 6-7). As such, the transition matrix is used within the extended Kalman filter only to update the error covariance matrix (equation 6-9) and consequently the Kalman gain (equation 6-16). The transition matrix is defined by the Jacobian of the differential process model equations and may be expressed in simplified form as:

$$\Phi_{t_k} = \left(\begin{array}{c|c} \Phi_{t_k}^{D} & \Phi_{t_k}^{S} \\ \hline 0 & I \end{array} \right) \tag{6-22}$$

where $\Phi_{t_k}^{D}$ is the Jacobian of the deterministic states, $\Phi_{t_k}^{S}$ the Jacobian of the stochastic states, and I is the identity matrix.

Computation of the Jacobian matrix was found by numerical differentiation using the multi-component kinetic model developed in Chapter 4. As determination of the transition matrix very computationally intense, it is desirable to avoid re-calculating the transition matrix at each time step. Gagnon (1990) determined that a converged, steady-state Kalman gain calculated using a constant transition matrix about the initial conditions yielded results that were very close to those obtained for a time varying transition matrix. Filter performance was also found to be relatively insensitive to the Kalman gain. It should be noted that continuous computation of the transition matrix is considered far more critical for linear Kalman filters, as the transition matrix is also used within the prediction step for updating the state vector.

A computer code developed in MATLAB$^{\text{TM}}$ was used for solving the transition matrix within this work. The partial differential equations within the Jacobian matrix were solved numerically using the central difference method as follows:

$$\Phi_{ij} = \frac{\delta x_i}{\delta x_j} = \frac{\left[x_i\left(x, x_j + \Delta x_j\right) - x_i\left(x, x_j - \Delta x_j\right)\right]}{2\Delta x_j} \qquad (6\text{-}23)$$

6.3.6. Computation of the Observation Matrix

Measured process variables are related to the state vector by the following measurement equation:

$$y_{t_k+1} = H_{t_k} \hat{x}_{t_k+1|t_k} + v_{t_k} \qquad (6\text{-}24)$$

The precision of the corrected state vector depends on the precision of the measurements (R_v) and on the number and type of measurements used $\left(H_{t_k}\right)$. If the observation matrix has rank equivalent to the dimension of the state vector then the system is fully observable, indicating that model states can be estimated from a finite set of measurements. Observability was first introduced by Kalman (1960) to describe state-output relationships in linear dynamic systems.

In order to demonstrate the capability of the EKF in simulating the operation of an industrial LMF, it was assumed that direct measurements of all deterministic states were instantaneously available online. It was also assumed that sensor noise was at precision levels currently attainable within a modern iron and steel laboratory. The effect of sensor selection and sampling frequency will be assessed in the following section.

6.4. Results & Discussion

The extended Kalman filter was applied to the process using several levels of measurements possible. All simulations were illustrated in the following way: (i) the solid line represents the real value of the variable under study, (ii) the dotted line represents the Kalman filter estimate of the variables, and (iii) the discrete dots symbolize the measurements taken.

6.4.1. EKF Simulation Studies

The objective of this section is to investigate the ability of the extended Kalman filter in correcting for model errors (i.e. incorrect model structure, poor parameter estimates, incorrect assumptions, etc.) using different sensor set combinations and tuning parameter variances. As previously discussed, the primary uncertainties in the developed multi-component kinetic model are slag-metal mass transfer correlations. Figures 4-50 to 4-52 illustrate that the empirical nature of these correlations may result in significant plant-model mismatch, where the Al and Si contents in metal and the SiO_2 contents in slag were the most variable states. As such, the filter was applied to the process assuming several levels of measurements possible. It is assumed that the multi-component kinetic model summarized in Chapter 4 of this thesis is correct, and that the initial state estimate was perfectly known in all cases.

6.4.1.1. Case 1 – Si and SiO_2 Measurements at 5min Intervals

This simulation involving the measurement of Si and SiO_2 at 5min intervals was found to yield the most satisifactory results and is therefore considered as the 'Base Case'. Following the approach by Kozub & MacGregor (1992) the diagonal elements of R_w for the deterministic states were initially selected to allow for approximate 10% maximum error in the model equations at each sampling period. For the non-stationary state $\left(x^S = \xi\right)$ the covariance diagonal element of R_w was selected by repeated simulations until an acceptable compromise had been achieved between the smoothness of the estimation and the rapidity of tracking. It was found that the following values led to acceptable EKF performance:

$$R_w = [0.001, 0.001, 0.001, 0.001, 0.001, 0.0001, 0.5, 0.5, 0.05, 0.05, 0.2, 0.05, 0.01, 0.1, 25, 20]^T \tag{6-25}$$

The precision of the measurements (R_v) was set to:

$$R_v = [0.0001, 0.05]^T \tag{6-26}$$

Although these measurement precisions are attainable in a modern iron and steel laboratory, it is unlikely that they would be attainable within the process environment. The diagonal elements of the initial covariance matrix $\left(P_{t_k|t_k}\right)$ were chosen to reflect the expected variance of the initial state estimates where:

$$P_0 = [0.01, 0.01, 0.01, 0.01, 0.01, 0.01, 0.01, 0.01, 0.01, 0.01, 0.01, 0.01, 0.01, 0.01, 1]^T \tag{6-27}$$

If a serious error in judgment is made in selecting R_w, R_v or P_0 the extended Kalman filter may yield poor estimates of the non-linear states. As a result, the general practice of selecting these values requires much insight and repeated simulation to arrive at an acceptable set of tuning parameters.

Figure 6-11 summarizes the performance of the filter for the base case simulation. In comparison with Figure 4-52 it is seen that the EKF arrives at improved end-point composition estimates for nearly all steel and slag phase components, where only the end-point sulphur content was slightly negatively impacted. Of particular importance in Figure 6-11 is the effect of the stochastic parameter on model estimates. At each 5min sample point, the EKF updates the stochastic parameter, which consequently influences the rate of mass transfer within the slag phase. Figure 6-11 illustrates that although the EKF appears to converge quite quickly (t = 25min) on the appropriate slag phase mass transfer constant, the change in stirring conditions within the ladle at t = 35min results in the significant deviation in the Si and SiO_2 contents. It is only after a sample is taken during the high flow conditions that the EKF is able to correct for the change in stochastic parameter and improve the state estimates.

An interesting outcome from Figure 6-11 is the ability of the EKF to influence non-measured states. Although only Si and SiO_2 measurements were taken during this base case simulation, the inclusion of the stochastic parameter had a favourable influence on the Al / Al_2O_3 composition curves as compared with the process model results in Figure 4-52.

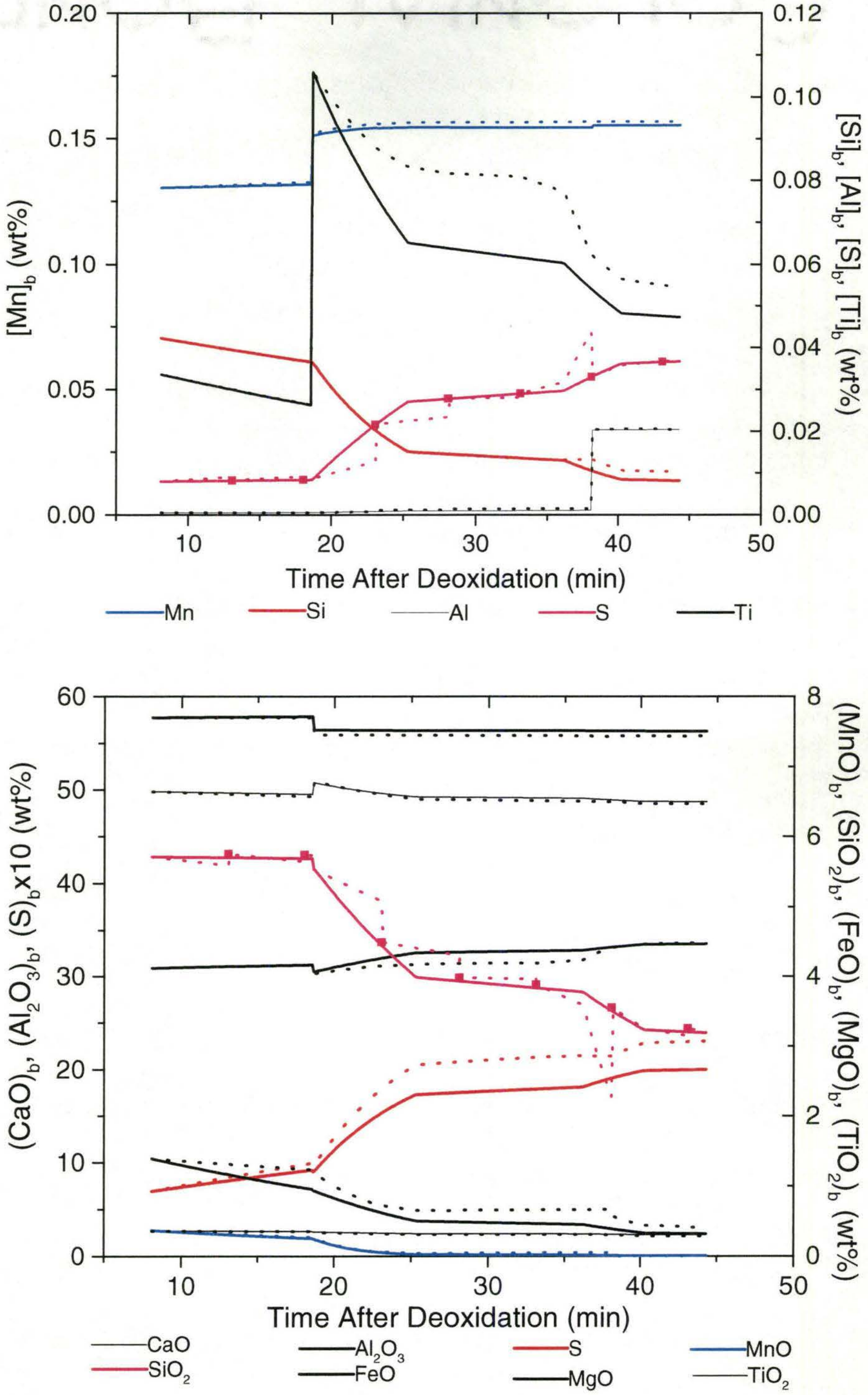

Figure 6-11: Case 1 simulation comparing the experimental and extended Kalman filter predicted results for Heat 40: (——) actual, (-----) predicted, (■) measurement. (top) Steel concentration profile, (bottom) slag concentration profile.

6.4.1.2. Case 2 – SiO_2 Measurements at 5min Intervals

In this case, it is assumed that only the SiO_2 measurements were available at 5min intervals. Results from the simulation are presented as Figure 6-12. While this case results in an improved end-point Al content over Case 1, it also yields negative end-point sulphur in steel and MnO in slag contents. Such physically impossible predictions using the EKF have previously been reported within the literature. In recent research work, Haseltine & Rawlings (2003) demonstrated that application of the extended Kalman filter does not ensure the elmination of divergerence problems. Using a simple gas phase reversible reaction, Haseltine & Rawlings (2003) showed that the extended Kalman filter resulted in a negative partial pressure estimate for one gas species. The basis for extended Kalman filter failure was attributed to its convergence at a local minimum of the probability density function due to a poor initial guess of the state (Haseltine & Rawlings, 2003). To prevent the negative partial pressures, Haseltine & Rawlings (2003) recommend optimally constraining the states using the moving horizon estimation algorithm.

In contrast to the conclusions of Haseltine & Rawlings (2003), the divergence problems encountered within the current simulation may be attributed to the fact that a single stochastic parameter is being used to describe the uncertainty in all slag phase mass transfer correlations. It follows that separate stochastic parameters would ideally be useful in describe the behaviour of each slag-metal reaction. Unfortunately, these requirements are unable to be met from an observability stand-point (Gagnon & MacGregor, 1991). More specifically, the number of non-stationary disturbances must be equal to or less than the number of independent measurements. As a result, it is generally impossible to account for all types of disturbances or modelling errors.

Figure 6-13 illustrates the effect of tuning the EKF using R_w^S. The variance of the stochastic state in this simulation was 20 times smaller than the initial base case simulation. As shown, while using a reduced stochastic state improves the end-point sulphur content the reduced stochastic state is, in general, very slow in responding to the data. In fact, the current simulation yields results very similar to those of Figure 4-52 where the process model was used in the absence of the EKF.

6.4.1.3. Case 3 – Base Case with $R_w^S = 5R_w^S{}_{\text{BASE CASE}}$

This simulation demonstrates the effect of increasing the variance of the stochastic state by 5 times over than the initial base case simulation. As shown in Figure 6-14, a higher stochastic variance forces the filter to adapt to disturbances faster but results in noisier estimates. A further consequence of increasing the stochastic parameter variance was that the EKF predicted a negative FeO content at approximately 40minutes after deoxidation. The primary reason for the negative composition prediction was again due to the inability of a single stochastic parameter being unable to account for all possible disturbances within the process.

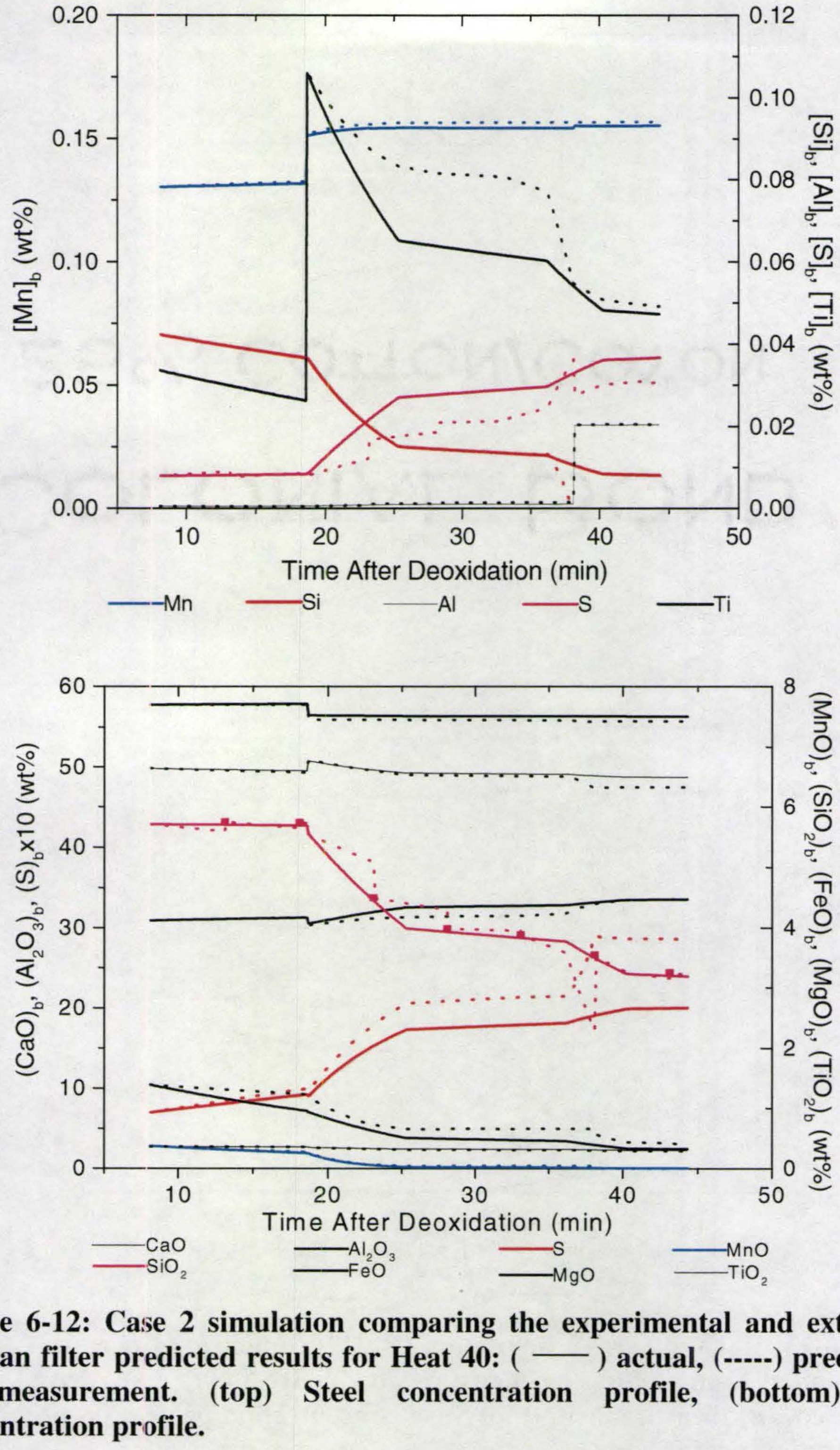

Figure 6-12: Case 2 simulation comparing the experimental and extended Kalman filter predicted results for Heat 40: (——) actual, (-----) predicted, (■) measurement. (top) Steel concentration profile, (bottom) slag concentration profile.

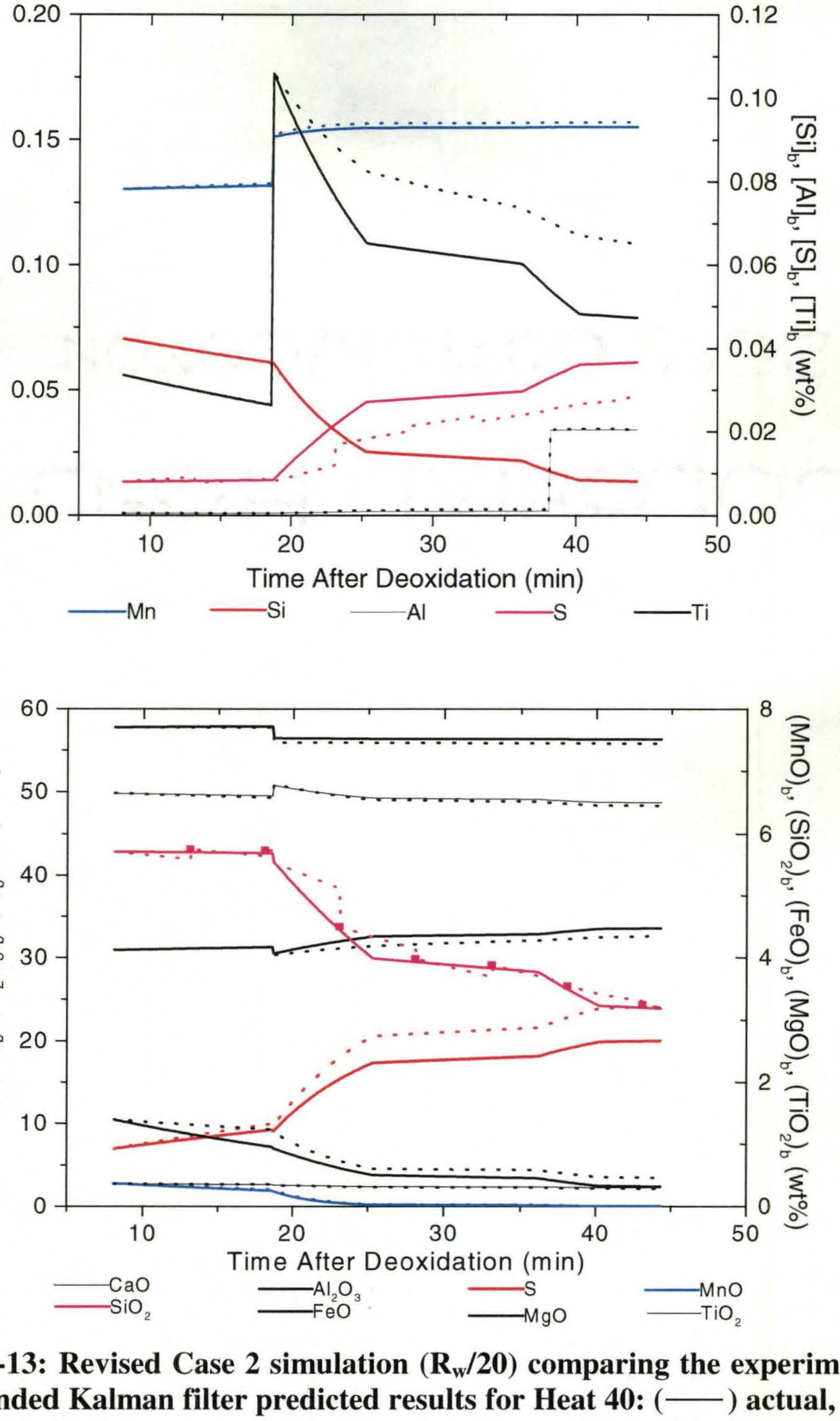

Figure 6-13: Revised Case 2 simulation ($R_w/20$) comparing the experimental and extended Kalman filter predicted results for Heat 40: (——) actual, (-----) predicted, (■) measurement. (top) Steel concentration profile, (bottom) slag concentration profile.

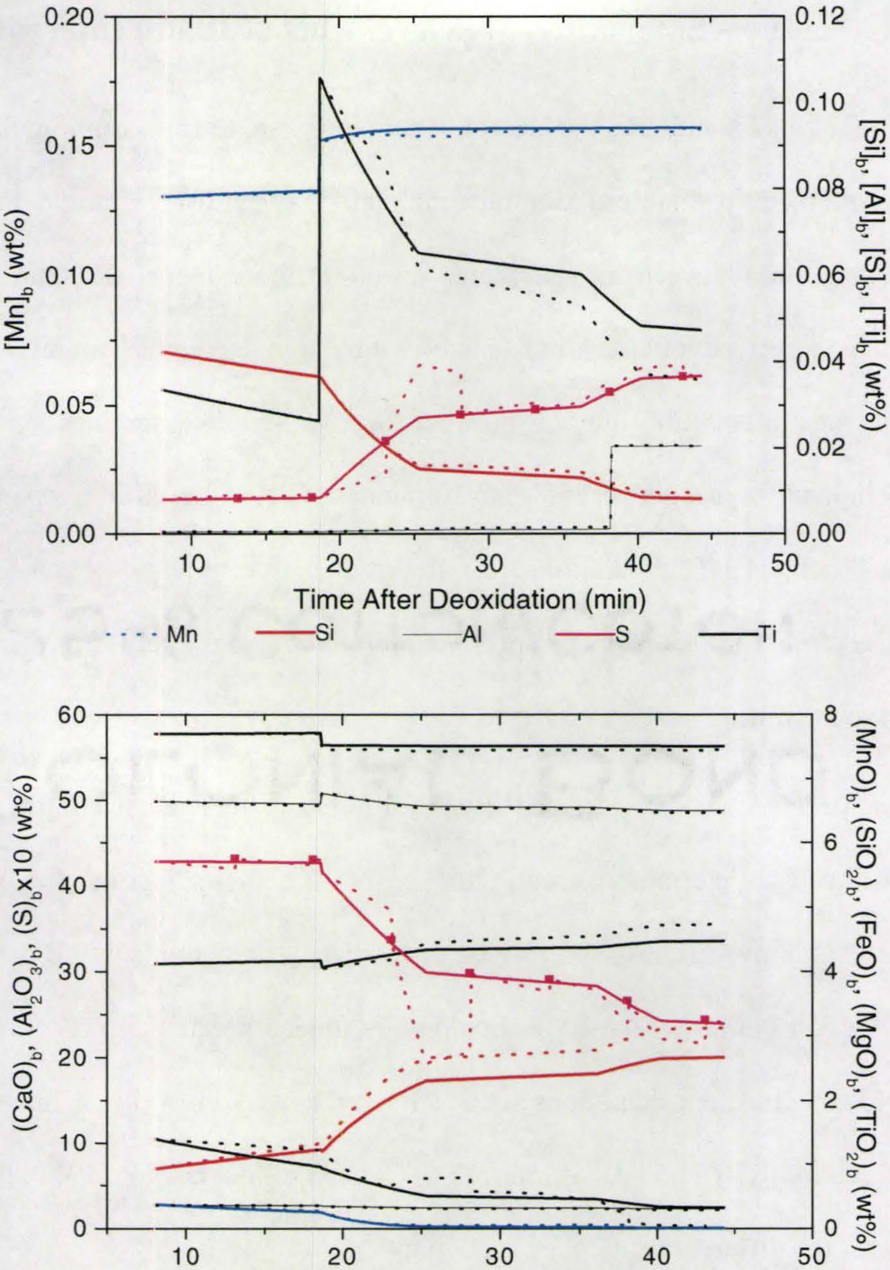

Figure 6-14: Case 3 simulation ($5R_w$) comparing the experimental and extended Kalman filter predicted results for Heat 40: (——) actual, (-----) predicted, (■) measurement. (top) Steel concentration profile, (bottom) slag concentration profile.

6.4.1.4. Case 4 – Si and SiO_2 Measurements at 10min Intervals

In this final simulation the base case conditions are re-run assuming Si and SiO_2 measurements available at 10minute intervals. As seen from Figure 6-15, the long interval time between measurements results in the extended Kalman filter being unable to effectively track most states with a high degree of certainty. As a result, the maximum time interval between Si and SiO_2 measurements would therefore appear to be between 5 and 10minutes. Given the current operating conditions at the LMF, a sampling rate fewer than five minutes is considered impractical from an operator perspective and more than likely from a cost perspective as well.

While not considered in this thesis, different mathematical criteria have been developed to determine the optimum sensor set combination and frequency relative to some overall cost and / or quality objective function. Future optimal sensor selection studies for the LMF should work to incorporate these criterions to account for practical considerations such as the price of a sensor, its maintenance cost, and reliability. The reader is referred to Gagnon & MacGregor (1991) for an overview of the different techniques available.

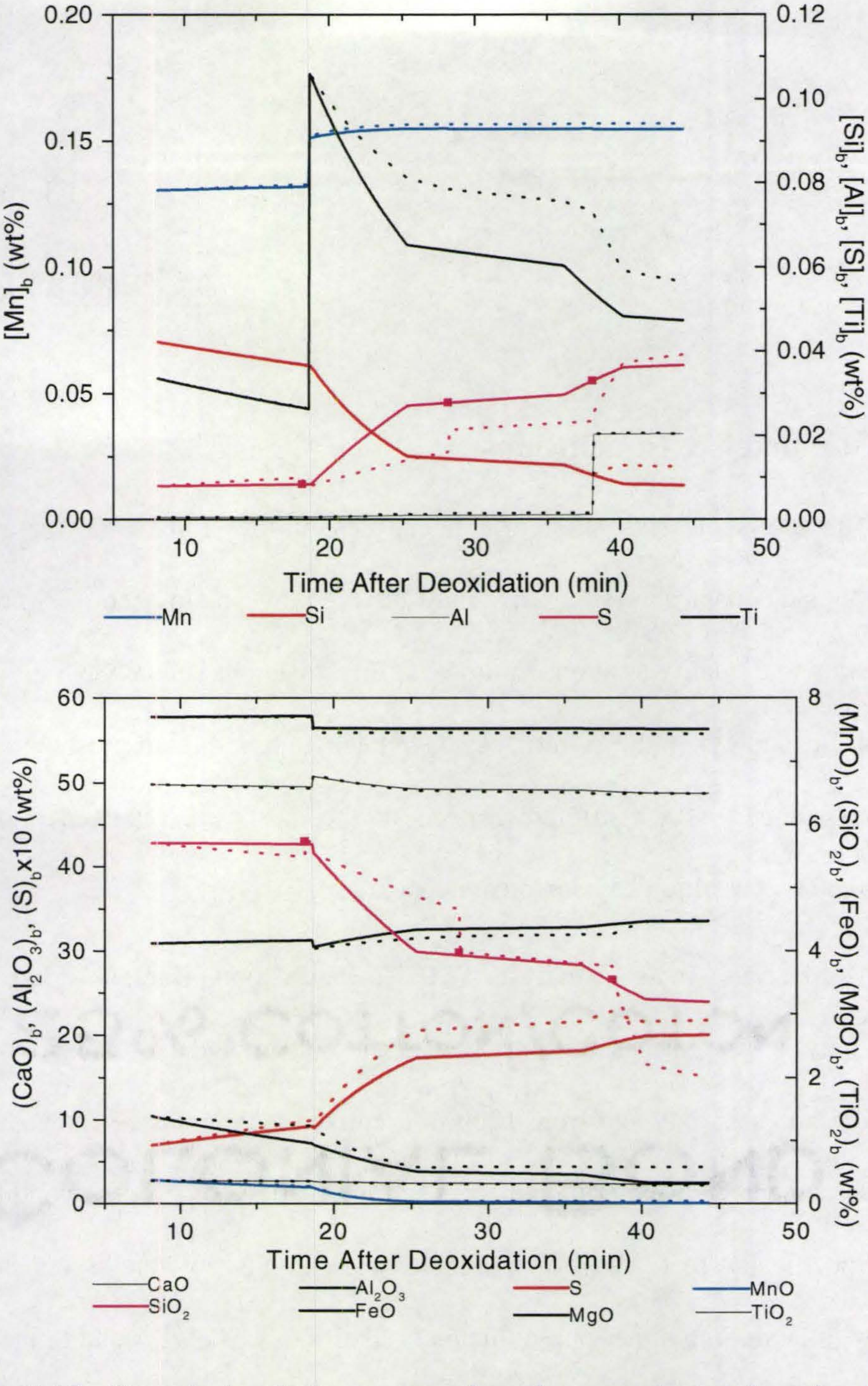

Figure 6-15: Case 4 simulation comparing the experimental and extended Kalman filter predicted results for Heat 40: (——) actual, (-----) predicted, (■) measurement. (top) Steel concentration profile, (bottom) slag concentration profile.

Chapter 7

CONCLUSIONS

7.1. Summary & Conclusions

The thesis presents studies and analyses of the framework for a first generation ladle control system that may be used by steelmakers for process optimization and quality assurance purposes. Five different subjects pertaining to the control of ladle metallurgy furnaces have been addressed and presented in an integrated manner. These different aspects of the thesis are arranged into five major chapters, for which key conclusions include:

1. Multivariate Image Analysis (MIA), based on principal component analysis, was successfully applied to the cold model laboratory work of Krishnapisharody and Irons (2006). Predicted ladle eye size showed good agreement with experimental results for a variety of process conditions. Specifically, that ladle eye size increases with gas flowrate and decreases with increasing upper phase thickness. Eye size was also found to increase with increasing lower phase depth.
2. The MIA approach was able to provide rapid on-line estimates of the ladle eye area. MIA was, however, sensitive to lighting conditions and image

pre-processing was required on images to improve model prediction results.

3. Preliminary work using a 780nm bandpass filter has proven MIA capable of successfully detecting ladle eyes within an industrial steelmaking ladle.
4. Evaluation of the unified interaction parameter model (UIPM) revealed that the solvent activity coefficient equation originally derived by Pelton & Bale (1986) was not a unique solution, but one of an infinite number of possible solutions.
5. The cell model is capable of accurately predicting the thermodynamic properties of multi-component slags within the system SiO_2-TiO_2-Ti_2O_3-Cr_2O_3-Al_2O_3-Fe_2O_3-CrO-FeO-MnO-MgO-CaO-S. Moreover, the model was found as a valuable tool having application within kinetic and inclusion model studies.
6. Numerical procedures and previously unpublished equations have been presented enabling cell model extension to poly-anionic slags. The model is, however, dependent on tuning parameters (including energy of interaction, energy of formation, energy of stability, enthalpy and entropy of melting energies) that have either not been published and / or evaluated.
7. The Delta Dist L sensor from Heraeus Electro-Nite (Philadelphia, PA) allows for slag depth to be measured quickly and accurately in an industrial ladle.

8. A method has been introduced using the AMEPA slag detection system in combination with the Delta Dist L sensors to provide an online estimate of slag carryover from the EAF. Work is ongoing to incorporate the results of this work into plant operations. Immediate benefits include the development of optimum deslagging practice, while future benefits include improvement of alloy addition practices and the development of an integrated ladle control system.
9. A process model was developed to describe the kinetics of coupled multi-component slag-metal reactions within an industrial ladle metallurgical furnace at ArcelorMittal Dofasco, assuming that the rates were mixed-transport controlled.
10. The sampling practice employed at ArcelorMittal Dofasco for this study proved effective in isolating the differences between process events: (i) low argon flowrate with arcs off, (ii) low argon flowrate with arcs on, and (iii) high argon flowrate with arcs off.
11. Dissolved oxygen contents decreased in a step-wise manner immediately after deoxidation. Preliminary inclusion analysis results indicate that deoxidation products undergo transformation from pure alumina to spinel and less frequently to calcium aluminates when calcium treatment is employed.

12. Electrical heating appears to have a significant influence on the oxygen potential within the steel and slag phases. The significant volume of oxygen pick-up seen during periods of power-on time may serve as one possible explanation for the occurrence of sulphur reversion during periods of electrical heating.

13. Measured bulk sulphur partition coefficients were observed to be dependent on slag FeO content. A comparative analysis of four different methods used to calculate the sulphur partition ratio revealed widely different results.

14. The dissolved oxygen content in aluminum killed steel is controlled by the inclusions. Good agreement was found when calculating dissolved oxygen concentration assuming equilibrium with dissolved aluminum and pure alumina inclusions.

15. The mass transfer capacity coefficient for sulphur was found to increase with stirring power (ε) in proportion to $\varepsilon^{1.4\pm0.09}$. The relation was accurate in describing desulphurization during all process events in an argon-gas stirred ladle.

16. The assumption that slag phase mass transfer coefficients were proportional to the metal phase mass transfer capacity coefficient correlations for sulphur proved effective in modelling the industrial results at ArcelorMittal Dofasco.

17. Slag phase mass transfer coefficient correlations for MnO, FeO, and Al_2O_3 were determined by linear regression from the fitted mass transfer ratio results. Numerous attempts to derive a relationship for the mass transfer coefficient of SiO_2 as a function of process conditions were unsuccessful, and an average slag phase mass transfer coefficient for SiO_2 is recommended for future studies.

18. Model predictions showed that as much as 30% sulphur on average contained in steel (5.9 kg of sulphur / tonne of slag) fails to report to the slag phase and may be lost during refining to the atmosphere, refractory and / or inclusions.

19. Inclusion removal rate followed first order reaction kinetics. Inclusion removal rate constants were found dependent on stirring power within the melt in proportion to $\dot{\varepsilon}^{0.28 \pm 0.08}$. The relationship had a high standard deviation, which may be a result of reoxidation occurring during refining and / or measurement uncertainties.

20. Elevated MgO concentration levels were found present in inclusions only after a state of slag-metal partial equilibrium had been established between slag and metal. Spinels were found less likely to form under highly oxidizing slags, but their formation was observed much more favourable below a (FeO + MnO) content of approximately 1wt%.

21. Results from this study suggest that ladle slag and possibly refractory are the key sources of magnesium contamination of steel.
22. Uncertainty in thermodynamic data for Al-Al_2O_3 and Ca-CaO equilibrium reactions was the key factor limiting the development of an inclusion model for potential use as an online control tool at ArcelorMittal Dofasco.
23. An approach comparing the CCSEM determined inclusion composition results to the total calcium and total oxygen contents in steel was found capable of providing a resonable approximation of oxide inclusion composition in the absence of microscopic examination.
24. Process models serve only to approximate reality. State estimators improve model predictions by updating model estimates using measurement data and by tracking the effect of disturbances on states. In the present work, an extended Kalman filter was developed. Simulations showed that better results could be achieved than for a process model alone, but was very sensitive to the type of sample and frequency.
25. It has been demonstrated that the uncertainties associated with the developed slag phase mass transfer coefficient correlations could be described by simple non-stationary random walk behaviour.

7.2. Future Work

This project resulted in an increased knowledge of the operation and control of the ladle metallurgical furnace. Identified areas requiring further research are summarized below.

7.2.1. Multivariate Image Analysis

Future work is aimed at installing an argon cooled housing for the camera on the ladle furnace roof. A camera in a fixed position on the ladle furnace roof would facilitate the continuous and unobstructed measurement of ladle eye area under all process conditions. Further, it would enable additional research into using the eye area measurement feedback signal to control argon flow, or in using the direct eye measurement to infer temperature or slag condition (Subagyo & Brooks, 2002), and potentially as an input variable to metallurgical models. At a minimum, a ladle eye sensor would have the operational benefits listed in Chapter 2.

With regard to incorporating the ladle eye measurement into metallurgical models, preliminary work has been undertaken to describe the absorption and desorption of nitrogen across the gas-metal ladle eye area interface. A mixed transport controlled nitrogen model has been developed and considers two possible locations for nitrogen absorption or desorption: (i) the bubble interface of the injected gas, and (ii) the free surface (ladle eye). In advance of full-scale industrial trials, the developed model has been validated against the published nitrogen desorption laboratory work of Takahashi et al. (1987a, 1987b). Figures 7-1 and 7-2 summarize the comparison between model predicted and experimental results over a wide range of process conditions, where shown figures specify the location site and degree of nitrogen removal during a given experimental condition. As seen, model predictions are in excellent agreement with the experimental results of Takahashi et al. (1987a, 1987b), substantiating its potential future use within an industrial operation.

As far as the author is aware, investigations into ladle freeboard gas composition (O_2, N_2, and Ar) as a function of process conditions have either not been undertaken or are not available within the literature. As such, it is therefore recommended that work be undertaken to define ladle freeboard conditions during refining before any attempt is made at integrating ladle eye area measurements within metallurgical process models.

7.2.2. Cell Model Development

Chapter 3 of this thesis has summarized a step-by-step procedure for developing the cell model, a two sub-lattice statistical thermodynamic model capable of accurately predicting the thermodynamic properties of multi-component slags within the system SiO_2-TiO_2-Ti_2O_3-Cr_2O_3-Al_2O_3-Fe_2O_3-CrO-FeO-MnO-MgO-CaO-S. While necessary equations allowing for the extension of the model to polyanionic equations were presented, the model is, however,

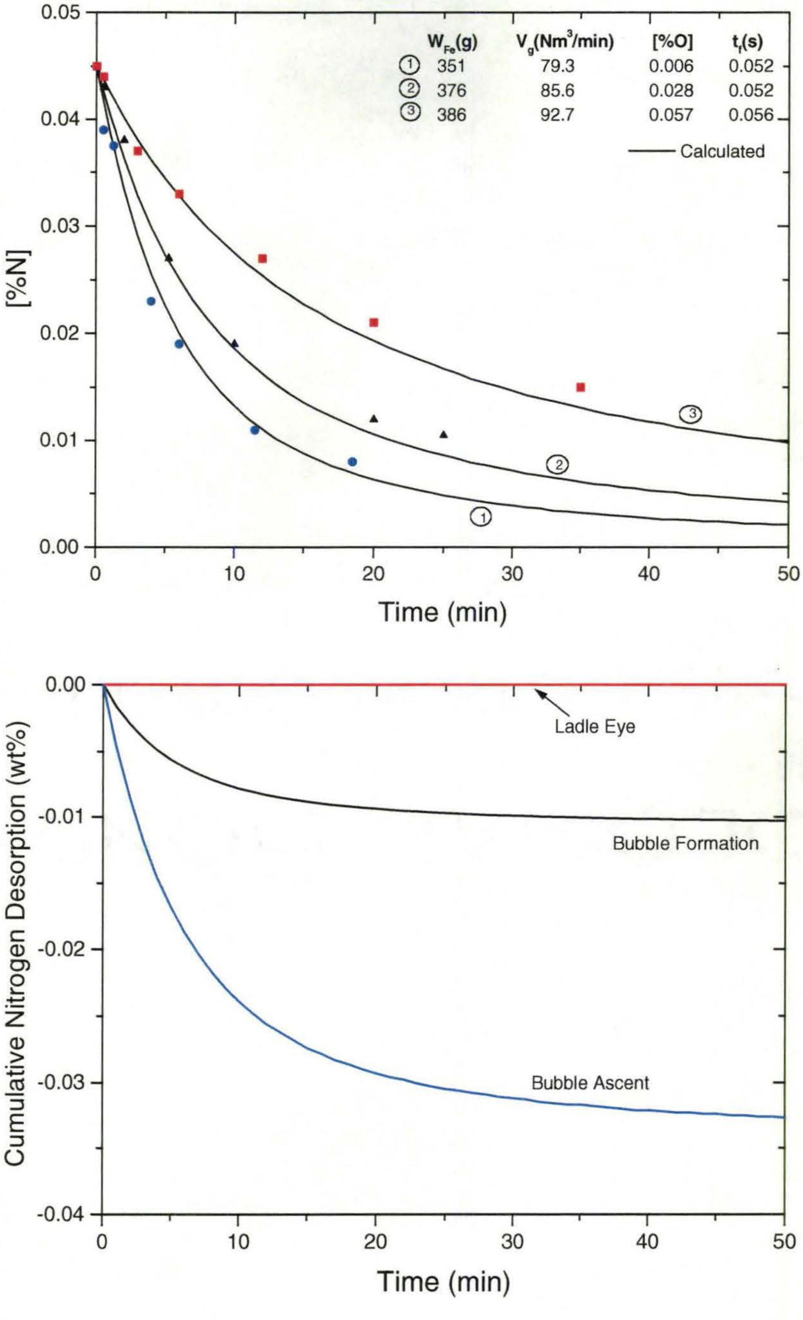

Figure 7-1: Change in nitrogen concentration with time (Upper); Location of nitrogen removal (Lower) considering nitrogen desorption across the bubble interface only.

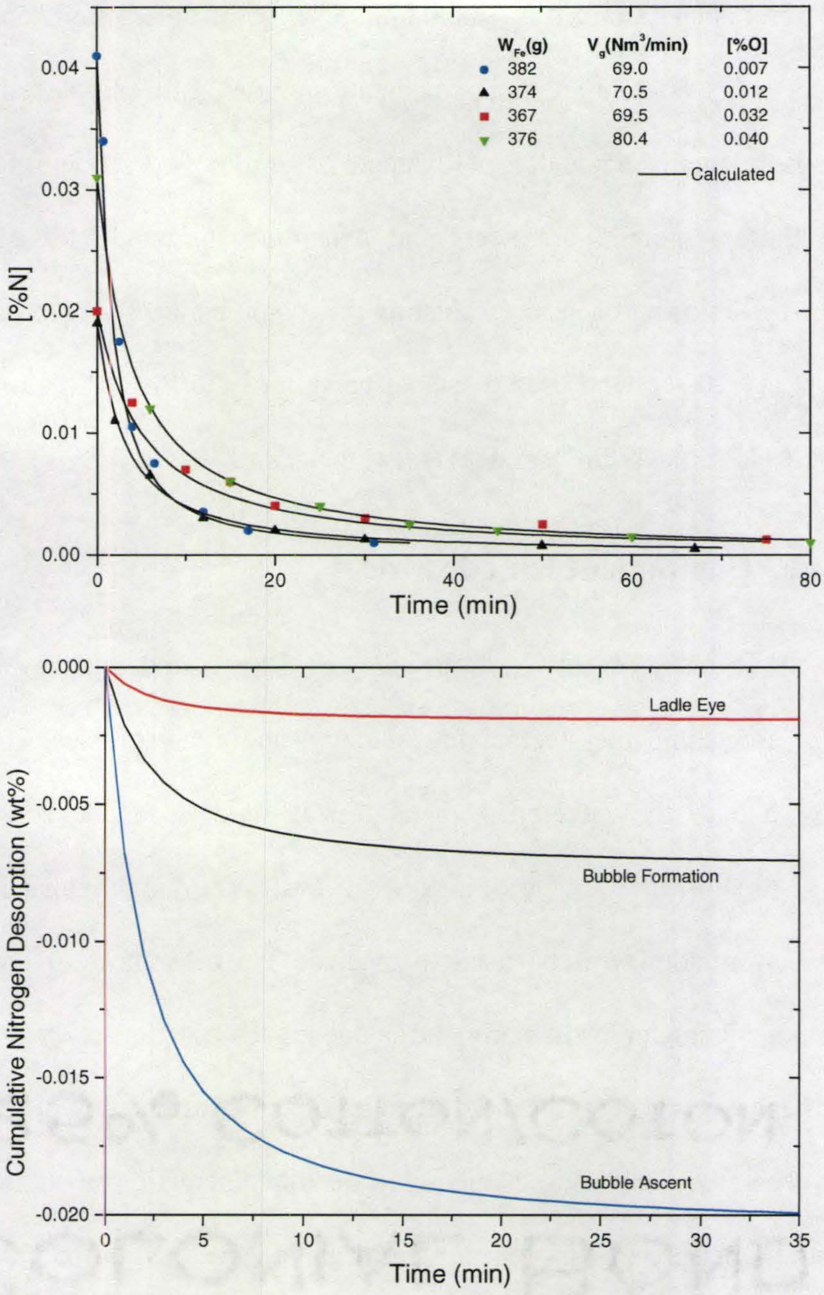

Figure 7-2: Change in nitrogen concentration with time (Upper); Location of nitrogen removal (Lower) considering nitrogen desorption across the bubble interface only.

dependent on tuning parameters (including: energy of interaction, energy of formation, energy of stability, enthalpy and entropy of melting energies) that have either not been published and / or evaluated. Future work should focus on evaluating these required parameters and extending the model to additional oxides. One possible approach for evaluating the model parameters was presented by Zhang et al. (2007), who used a special version of the PARROT program in the Thermo-Calc (Stockholm, Sweden) software package.

7.2.3. Multi-Component Kinetic Model

As the primary objective of this project is to commercialize a control package for use within the steelmaking industry, additional full-scale trials are needed to validate the developed metallurgical models. Work is currently underway at ArcelorMittal Dofasco to gather heat data from approximately 10-20 heats. This information will be used to evaluate the robustness of the multi-component kinetic model in simulating heats outside the training set on an off-line basis. The next stage of the project will then involve the formulation of an overall ladle control strategy and subsequent full-scale implementation of the model at ArcelorMittal Dofasco. In addition to plant trials at ArcelorMittal Dofasco, it is expected that work will be undertaken at a second operating plant to verify the model for different grades and under different operating conditions.

While the steel industry is the primary focus of the ladle control system technology, alternative applications within the non-ferrous industry will be explored. One potential application concerns the refining of ferronickel. Most commonly produced via the rotary kiln – electric furnace (RKEF), crude ferronickel from the electric arc furnace contains impurities such as sulphur, carbon, silicon, chromium and possibly phosphorus that must be removed to levels satisfying target market specifications. Presently, ferronickel refining is performed in ladles (20-60t) in a process similar to the ladle metallurgical furnace. Application of the model to non-ferrous systems may, however, require its extension to include different slag-metal equilibrium reactions.

Heat data contained within this thesis is currently the subject of a separate analysis at McMaster University using multi-block multi-way partial least squares (PLS). The PLS methods developed by Flores-Cerillo and MacGregor (2002, 2004) offer an alternative solution to real-time control. These multivariate statistical process control methods have been shown successful in modelling industrial data for both the off-line and on-line monitoring of batch operations. The key drawback of this method, however, is that due to its empirical nature the developed model is limited to the data for which the model was built on.

7.2.4. Extended Kalman Filtering / Sensor Optimization

Most metallurgical processes are dependent on operator skill and manual procedures in achieving operational objectives. Two factors are largely responsible for the current lack of online control: (i) the complex nature of metallurgical processes, and (ii) very little work has been undertaken within the metallurgical literature to incorporate available measurements in on-line state estimation and control schemes. Chapter 6 of this thesis presented a non-linear state estimation technique based on the extended Kalman filter for modelling process disturbances and maintaining improved ladle metallurgy furnace control. Several case studies were undertaken in order to demonstrate the filter effectiveness. On the basis of this work, a research area having potential significant benefits to the steel industry involves using the extended Kalman filter to identify what existing or non-existent sensors render the process observable. Research and development efforts could then be focused on developing any non-existent sensors identified from this work. It follows that sensor selection and optimization (i.e. sampling time, placement, etc.) is a previously unexplored research area within metallurgical systems.

A further area of potential benefit to the metallurgical industry involves assigning economic weights to various process uncertainties, after which an overall optimization formulation could then be used to minimize a process cost objective function. A similar type of investigation was recently completed by MacRosty (2005) in the modelling, optimization, and control of an electric arc furnace.

BIBLIOGRAPHY

Ahlborg, K. (2001). Seven Ways to Shut Down the Caster. *Steelmaking Conference Proceedings* (pp. 861-869). Baltimore, MD: Iron and Steel Society.

Ahlborg, K., Fruehan, R., Potter, M., Badger, S., & Casuccio, G. (2003). Inclusions in Aluminum-Killed Steel with varying Calcium Additions. *ISSTech Conference Proceedings*, (pp. 177-1 94).

Andersson, A., Jonsson, L., & Jonsson, P. (2000). A Thermodynamic and Kinetic Model of Reoxidation and Desulphurisation in the Ladle Furnace. *Iron and Steel Institute of Japan* , *40* (11), 1080-1088.

Asai, S., & Szekely, J. (1974). Decarburization of Stainless Steels: Part 1. A Mathematical Model for Laboratory Scale Results. *Metallurgical Transactions* , 651-657.

Asai, S., Kawachi, M., & Muchi, I. (1983). Mass Transfer Rate in Ladle Refining Processes. *SCANINJECT III, 3rd International Conference on Injection Metallurgy* (pp. 12:1-12-29). Lulea, Sweden: MEFOS.

Baerts, C. (1992). *Patent No. 5,156,799.* United States Patent.

Bale, C., & Pelton, A. (1990). The Unified Interaction Parameter Formalism: Thermodynamic Consistency and Applications. *Metallurgical Transactions A* , *21A*, 1997-2002.

Battle, T., & Pehlke, R. (1986). Kinetics of Nitrogen Absorption / Desorption by Liquid Iron and Iron Alloys. *Ironmaking and Steelmaking* , *13* (4), 176-189.

Baxes, G. (1996). *Digital Image Processing: Principles and Applications.* New York: John Wiley & Sons.

Bharati, M. (2002). *Multivariate image analysis and regression for industrial process monitoring and product quality control.pdf.* McMaster University: PhD Thesis.

Bharati, M. (1997). *Multivariate Image Analysis for Real-Time Process Monitoring.* McMaster University: M.Eng. Thesis.

Bharati, M., & MacGregor, J. (1998). Multivariate Image Analysis for Real-Time Process. *Ind. Eng. Chem. Res.* , *37* (12), 4715-4724.

Bharati, M., & MacGregor, J. (2003). Softwood Lumber Grading Through On-Line Multivariate Image Analysis. *Ind. Eng. Chem. Res.*, *42* (21), 5345-5353.

Bjorkland, J., Andersson, M., & Jonsson, P. (2007). Equilibrium Between Slag, Steel, and Inclusions During Ladle Treatment: Comparison with Production Data. *Ironmaking and Steelmaking*, *34* (4), 312-324.

Bodsworth, C. (1972). *Physical Chemistry of Iron and Steel Manufacture 2nd Edition.* London: Longman.

Bristow, D., Carter, R., Frakes, H., Lewis, D., Mang, J., Sattelberger, S., et al. (2000). *Ferroalloys & Alloying Additives Handbook: 2nd Edition.* New York : Shieldalloy Metallurgical Corporation.

brochure, H. E.-N. (2007). Electro-Nite 2-in-1 Combination Sensor.

Brooks, G. A., & Subgayo. (2003). Ladle Eye Detection using Multivariate Image Analysis. *ISSTech Conference Proceedings* (pp. 843-852). Indianapolis, IN: The Iron and Steel Society.

Brooks, G., & Subagyo. (2002). Advances in Ladle Metallurgy Control . *Advances in Ladle Metallurgy Control, Proceedings of the International Symposium on Ladle and Tundish Metallurgy* (pp. 41-53). Montreal, Canada: MetSoc.

Carlsson, G., Lehner, T., Brunner, M., & Thoren, T. (1986). Instrumentation for Ladle Metallurgical Control. *SCANINJECT IV: Part 1, 4th International Conference on Injection Metallurgy* (pp. 11:1-11:37). Lulea, Sweden: MEFOS.

Chang, L., & Goldman, K. (1948). Kinetics of the Transfer of Sulphur Across a Slag-Metal Interface. *Transactions AIME*, *176*, 309-329.

Chiba, K., Ono, A., Saeki, M., Yamauchi, M., Kanamoto, M., & Ohno, T. (1993). Development of Direct Analysis Method for Molten Iron in Converter - Hotspot Radiation Spectrometry. *Ironmaking and Steelmaking*, *20* (3), 215-220.

Conejo, A., Lara, F., Macias-Hernandez, M., & Morales, R. (2007). Kinetic Model of Steel Refining in a Ladle Furnace. *Steel Research*, *78* (2), 141-150.

Costa e Silva, A. (2006). Thermodynamic Aspects of Inclusion Engineering. *Rare Metals*, *25* (5), 412-419.

da Silva, W., Bergman, D., & Lindfors, N. (1993). Slag Carryover in Oxygen Converters: An International Review. *Steel Technology International*, 91-95.

Darken, L. (1958). *The Physical Chemistry of Steelmaking* . (J. Elliott, Ed.) New York: Technology Press and Wiley.

Darken, L. (1967b). Thermodynamics of Binary Metallic Solutions. *TMS-AIME* , *239*, 80-89.

Darken, L. (1967a). Thermodynamics of Ternary Metallic Solutions. *TMS AIME* , *239*, 90-96.

De Hemptinne, X., Eyring, H., & Ree, T. (1961). The Electrochemical Theory of Smelting and Related Reactions. In G. St Pierre, *The Physical Chemistry of Process Metallurgy Part 1* (pp. 65-93). New York: Interscience.

Dekkers, R. (2002). *Non-Metallic Inclusions in Liquid Steel.* Katholieke Universiteit Leuven: PhD Thesis.

Deng, J., & Oeters, F. (1990). Mass Transfer of Sulfur from Liquid Iron into Lime Saturated CaO-Al2O3-MgO-SiO2 Slags. *Steel Research* , *40* (10), 438-448.

Deo, B., & Boom, R. (1993). *Fundamentals of Steelmaking Metallurgy.* New York: Prentice Hall International.

Deo, B., & Grieveson, P. (1986). Kinetics of Desulphurization of Molten Pig Iron. *Steel Research* , *57* (10), 514-519.

Derge, G., Philbrook, W., & Goldman, K. (1950). Mechanism of Sulphur Transfer between Carbon-Saturated Iron and CaO-SiO2-Al2O3 Slags. *Transactions AIME* , *188*, 1111-1119.

Duffy, J., & Ingram, M. (1971). Establishment of an Optical Scale for Lewis Basicity in Inorganic Oxyacids, Molten Salts, and Glasses. *Journal of the American Chemical Society* , *93*, 6448-6455.

Ebneth, G., & Pluschkel, W. (1985). Dimensional analysis of the vertical heterogeneous buoyant plume. *Steel Research* , *56*, 513–518.

Electro-Nite, H. (2007). Personal Communication.

El-Kaddah, N., & Szekely, J. (1983). Turbulence and Agitation in Ladle Metallurgical Operations. *Scaninject III - Proceedings from the International Conference on Injection Metallurgy* (pp. 5:1–5:32.). Lulea, Sweden: MEFOS.

Elliott, J., & Gleiser, M. (1960). *Thermochemistry for Steelmaking* (Vol. 1). Reading, Mass.: Addison-Wesley Pub. Co.

Engh, T., & Lindskog, N. (1975). A Fluid Mechanical Model of Inclusion Removal. *Scandinavian Journal of Metallurgy*, *4*, 49-58.

Eriksson, L., Johansson, E., Kettaneh-Wold, N., Trygg, J., Wikström, C., & Wold, S. (2001). *Multi- and Megavariate Data Analysis Part I: Basic Principles and Applications.* Umeå, Sweden: Umetrics.

Esbensen, K., & Geladi, P. (1989). Strategy of Multivariate Image Analysis (MIA). *Chemometrics and Intelligent Laboratory Systems*, *7*, 67–86.

Faral, M., & Gaye, H. (1984). Metal Slag Equilibria. *2nd International Symposium on Metallurgical Slags and Fluxes* (pp. 159-179). Warrendale, PA: Metallurgical Society of AIME.

Faulring, G., Farrell, J., & Hilty, J. (1979). Steel Flow Through Nozzles: Influence of Calcium. *Electric Furnace Conference* (pp. 57-66). Detroit, MI: AIME.

Fincham, C., & Richardson, F. (1954). The Behaviour of Sulphur in Silicate and Aluminate Melts. *Proceedings of the Royal Society of London*, *A223*, 40-62.

Flood, H., & Knapp, W. (1963). Acid-Base Equilibria in the System PbO-SiO2. *Journal of the American Ceramic Society*, *46* (2), 61-65.

Fuhr, F., Torga, G., Medina, F., & Cicutti, C. (2007). Application of Slag Tracers to Investigate Source of Non-Metallic Inclusions. *Ironmaking and Steelmakin*, *34* (6), 463-470.

Gagnon, L. (1990). *State Estimation and Sensor Selection for a Continuous Emulsion Polyermisation Reactor.* McMaster University, Hamilton Ontario: Master's Thesis.

Gagnon, L., & MacGregor, J. (1991). State Estimation for Continuous Emulsion Polyermerization. *The Canadian Journal of Chemical Engineering*, 648-656.

Gaskell, D. (2003). *Introduction to the Thermodynamics Of Materials (4th Edition).* New York: Taylor & Francis Publishing Inc..

Gaskell, D. (1967). *The Densities of Liquid Silicates Containing Iron Oxide at 1410 C.* McMaster University : Ph.D. Thesis.

Gatellier, C., & Olette, M. (1979). Aspects fondamentaux des Reactions Entre Elements Metalliques et Elements Non Metalliques dan les Aciers Liquides. *Rev. Metall.*, *6*, 377-386.

Gatellier, C., Gaye, H., Lehmann, J., Pontoire, J., & Castro, F. (1991). Control of Complex Inclusions During Metallurgical Treatments on Liquid and Solid Steels. *74th Steelmaking Conference* (pp. 827-834). Washington, DC: Iron and Steel Society.

Gaye, H. (1971). *Computer Applications to the Thermodynamics of Multicomponent Solutions.* Carnegie-Mellon University: PhD Thesis.

Gaye, H., & Coulomet, D. (Mars 1984). Donnees Thermodynamiques et Cinetiques Relatives a Certain Materiaux Siderigiques. *ECSC Report n°. 7210-CF/301* .

Gaye, H., & Lehman, J. (1997). Modelling of Slag Thermodynamic Properties from Oxides to Oxisulphides. *Molten Slags, Fluxes and Salts '97 Conference* (pp. 27-34). Sydney, Australia: Metallurgical Society of AIME.

Gaye, H., & Riboud, P. (Novembre 1981). Donnees Experimentales sur les Activities des Constituants de Laitiers. *Report CECA n° 7210-CA/3/303* .

Gaye, H., & Welfringer, J. (1984). Modelling of the Thermodynamic Properties of Complex Metallurgical Slags. *2nd International Symposium on Metallurgical Slags and Fluxes* (pp. 357-373). Warrendale, PA: Metallurgical Society of AIME.

Gaye, H., Gatellier, C., Nadif, M., Riboud, P., Saleil, J., & Faral, M. (1987). Slags and Inclusions Control in Secondary Steelmaking. *Rev. Metall., Cah. Inf. Tech., , 84* (11), 759–771.

Gaye, H., Lehmann, J., Matsumiya, T., & Yamada, W. (1992). A Statistical Thermodynamic Model of Slags: Applications to Systems Containing S, F, P2O5 and Cr Oxides. *4th International Conference on Molten Slags and Fluxes* (pp. 103-108). Sendai, Japan: Iron and Steel Institute of Japan.

Geiger, G. H., & Poirer, D. R. (1980). *Transport Phenomena in Metallurgy.* Reading, MA: Addison Wesley.

Geladi, P., & Grahn, H. (1996). *Multivariate Image Analysis.* Baffins Lane, Chichester: John Wiley & Sons Inc.

Ghosh, A. (2001). *Secondary Steelmaking: Principles and Applications.* New York: CRC Press.

Gilles, E. (1987). Model Based Techniques for Controlling Processes in Chemical Engineering. *10th World Conference on Automatic Control*, (pp. 239-253). Munich, Germany.

Gilles, E. (1986). Some New Approaches for Controlling Complex Processes in Chemical Engineering . *Proceedings of the Third International Conference on Chemical Process Control.* Asilomar, California.

Goldman, K., Derge, G., & Philbrook, W. (1954). Effect of Si, Mn, P, Al, C, Ni, and Cu on the Mechanism of Sulphur Transfer Across a Slag-Metal Interface. *Transactions AIME , 200,* 534-540.

Golub, G., & Van Loan, C. (1996). *Matrix Computations.* Baltimore, M.D.: John Hopkins University Press.

Graham, K., & Irons, G. (2008). Integrated Control in the Ladle Metallurgy Furnace. *SCANMET III, 3rd International Conference on Process Development in Iron and Steelmaking.* Lulea, Sweden.

Grewal, M., & Andrews, A. (2001). *Kalman Filtering : Theory and Practice Using MATLAB.* New York: John Wiley & Sons.

Guggenheim, G. (1952). *Mixtures.* Oxford: Oxford University Press.

Gustafson, T. (2006). *Personal Communication* .

Harris, T. (1980). *Topics in Stochastic Control with Applications to a Tubular Reactor.* McMaster Univeristy, Hamilton Ontario: PhD Thesis.

Haseltine, E. &.-W. (2003). A Critical Evaluation of Extended Kalman Filtering and Moving Horizon Estimation.

Haseltine, E., & Rawlings, J. (2003). *A Critical Evaluation of Extended Kalman Filtering and Moving Horizon Estimation.* University of Wisconsin: Texas-Wisconsin Modeling and Control Consortium.

Hatch, G., & Chipman, J. (1949). Sulphur Equilibria between Iron Blast Furnace Slags and Metal. *Transactions AIME , 185,* 274-284.

Heraeus Electro-Nite brochure. (2008). *Delt-Dist L: Slag Thickness and Freeboard Measurement* .

Herasymenko, P. (1938). Electrochemical Theory of Slag–Metal Equilibria. Part I – Reactions of Manganese and Silicon in Acid Open Heart Furnace. *Transactions of the Faraday Society , 34,* 1245–1254.

Herasymenko, P. (1938). Electrochemical Theory of Slag–Metal Equilibria. Part II – The Reactions of Chromium in the Acid Open Hearth Furnace. *Transactions of the Faraday Society , 34,* 1254-1257.

Hilty, D., & Kay, D. (1985). Inclusions in Steel. In *Electric Furnace Steelmaking* (pp. 237-251). Warrendale, PA: Iron and Steel Society.

Höskuldsson, H. (1996). *Prediction Methods in Science and Technology. Vol. 1, Basic Theory.* Copenhagen: Thor Publishing.

Iguchi, M., Miyamoto, K., Yamishita, S., Iguchi, D., & ZeZe, M. (2004). Spout Eye Area in Ladle Refining Process. *Iron and Steel Institute of Japan* , *44* (3), 636-638.

Inoue, R., & Suito, H. (1994). Calcium Desulfurization Equilibrium in Liquid Iron. *Steel Research* , *65* (10), 403-409.

Ishida, J., Yamaguchi, K., Sugiura, S., Yamano, K., Hayakawa, S., & Demukai, N. (1981). Effects of Stirring by Gas Blowing on Metallurgical Reactions. *Denki-Seiko* , *52*, 2-8.

Itoh, H., Hino, M., & Ban-ya, S. (1997). Deoxidation Equilibria of Magnesium in Liquid Iron. *Tetsu-to-Hagane* , *83* (10), 623-628.

Iwase, M., Abe, H., & Iritani, H. (1988). Tri-phasic Zirconia Electrolyte for the In-situ Determinations of Silicon Activities in Hot Metal. *Steel Research* , *59* (10), 433-437.

Iwase, M., McLean, A., Katogi, K., Kikuchi, Y., and Wakimoto, K. (2004). Evalution and Control of Iron and Steelmaking Slags Through Electrochemical FeO Sensors, *VIII International Conference on Molten Slags Fluxes and Salts*, The South African Institute of Mining and Metallurgy, 787-796.

Jackson, J. (1991). *A User's Guide to Principal Component Analysis.* New York: John Wiley and Sons Inc.

Jahnsen, E. (n.d.). *Personal Communication* , 2006.

Jazwinski, A. (1970). *Stochastic Processes and Filtering Theory.* New York: Academic.

JFE 21st Century Foundation. (n.d.). *An Introduction to Iron and Steel Processing*. Retrieved from World Wide Web Edition: http://jfe-21st-cf.or.jp

Jolliffe, I. (2002). *Principal Component Analysis.* New York: Springer Verlag.

Jonsson, L. D. (1998). A New Approach to Model Sulphur Refining in a Gas-stirred Ladle – A Coupled CFD and Thermodynamic Model. *Iron and Steel Institute of Japan* , *38* (3), 260-267.

Jonsson, P., & Jonsson, L. (2001). The Use of Fundamental Process Models in Studying Ladle Refining Operations. *Iron and Steel Institute of Japan , 41* (11), 1289-1302.

Kalman, R. (1960). A New Approach to Linear Filtering and Prediction Problems. *ASME Trans. J. Basic Eng. , 82D* (35), 35-45.

Kaneko, K., Sano, N., & Matsushita, Y. (1976). Decarburization and Denitrogenization of Iron and Iron-Chromium Alloys by Plasma Jet of Hydrogen-Argon Gas Mixture. *Transaction ISIJ , 16*, 680-687.

Kapoor, M., & Frohberg, M. (1973). Theoretical Treatment of Activities in Silicate Melts. In *Chemical Metallurgy of Iron and Steel* (pp. 17-22). London: Iron and Steel Institute.

Kawai, Y., & Mori, K. (1982). *Tetsu-to-Hagane , 68*, A21-A24.

Kawai, Y., Shinozaki, N., & Mori, K. (1982). Rate of Transfer of Manganese Across Metal-Slag Interface and Interfacial Phenomena. *Canadian Metallurgical Quarterly , 21* (4), 385-391.

Kay, D., & Junpu, J. (1988). Slag Models and Inclusion Engineering in Steelmaking. *3rd International Conference on Molten Slags and Fluxes* (pp. 1-13). University of Strathclyde: Institute of Metals.

Kay, D., & Subramanian, S. (1986). Inclusions in Calcium Treated Steels. *Proceedings of the Second International Symposium on the Effects and Control of Inclusions and Residuals in Steel* (pp. 25-43). Toronto, Canada: Metallurgical Society of CIM.

Kemeny, F., McLean, A., & Sommerville, I. (1986). Gas-Slag-Metal Reactions in Plasma-Arc Induction Furnace Refining. *Proceed of the 6th Proc. Tech. Conf., 5th International Iron and Steel Conference. 6*, pp. 725-733. Washington, D.C.: ISS.

Kim, Y. (1978). *Kinetics of Sulphur Transfer from Carbon Saturated Iron to Slags.* University of Strathclyde: Ph.D. Thesis.

Kitamurat, S.-Y., Kitamura, T., Aida, E., Sakomura, R., Kaneko, T., & Nuibe, T. (1991). Development of Analysis and Control Method for Hot Metal Dephosphorization Process by Computer Simulation. *Iron and Steel Institute of Japan , 31* (11), 1329-1335.

Kiukkola, K., & Wagner, C. (1957). Measurements on Galvanic Cells Involving Solid Electrolytes. *Journal of the Electro-Chemical Society , 104*, 379–387.

Korber, F., & Oelsen, W. (1933). *Mitt. Kaiser-Wilhem Inst. Eisenforsch*, *15*, 272.

Kourti, D., MacGregor, J., & Dunn, K. (2006). *MACCMIA - Software for Multivariate Image Analysis*. Retrieved from McMaster University Website: http://macc.mcmaster.ca/maccmia/maccmia.htm

Kozub, D., & MacGregor, J. (1989). State Estimation and Control for Semibatch Polymerization Reactors. *AIChe Meeting, San Francisco*.

Krishnapisharody, K. (2007). *Model Studies of Fluid Mechanic Interactions Between Steel and Slag in Gas-Stirred Ladles*. McMaster University: PhD Thesis.

Krishnapisharody, K., & Irons, G. (2007). A Study of Spouts on Bath Surfaces from Gas Bubbling: Part I. Experimental Investigation. *Metallurgical and Materials Transactions*, *38B*, 367-375.

Krishnapisharody, K., & Irons, G. (2006). Modeling of Slag Eye Formation over a Metal Bath Due to Gas Bubbling. *Metallurgical and Materials Transactions B*, *37B*, 763-772.

Krishnapisharody, K., & Irons, G. (2006). Modeling of Slag Eye Formation over a Metal Bath Due to Gas Bubbling. *Metallurgical and Materials Transactions B*, *37B*, 763-772.

Kubaschewski, O., & Alcock, C. (1979). *Metallurgical Thermochemistry Fifth Edition*. London: Pergamon Press.

Lange, K. (1999). Thermodynamic and Kinetic Aspects of Secondary Steelmaking Processes. *International Materials Review*, *33* (2), 53-89.

Larsen, K., & Fruehan, R. (1990). Calcium Modification of Oxide Inclusions. *Iron & Steelmaker*, *17* (7), 45-52.

Lehmann, J., & Gaye, H. (1992-1993). Modeling of Thermodynamic Properties of Sulphur Bearing Metallurgical Slags. *Rev. Int. Hautes. Temper. Refract.*, *28*, 81-90.

Liu, J. (2004). *Machine Vision for Process Industries: Monitoring, Control, and Optimization of Visual Quality of Processes and Products*. McMaster University: PhD Thesis.

Lu, D. (1992). *Kinetics, Mechanisms and Modelling of Calcium Treatment of Steel*. McMaster University: Ph.D. Thesis.

Lu, W.-K. (1971). Some Applications of Irreversible Thermodynamics to Slag/Metal Reactions. *Transactions of the Iron and Steel Institute of Japan* , *11*, 32-39.

Lupis, C. (1981). *Chemical Thermodynamics of Materials.* New York: Elsevier Science Publishing Co. Inc.

Lupis, C., & Elliott, J. (1966). Generalized Interaction Coefficients. *Acta Metallurgica* , *14*, 529-538.

MacRosty, R. (2005). *Modelling, Optimization, and Control of an Electric Arc Furnace.* McMaster University, Hamilton Ontario: Ph.D. Thesis.

Marshall, A., & Martin, R. (1992). *Computer Vision, Models, and Inspection.* Singapore: World Scientific Publishing.

Masson, C. (1965). An Approach of the Problem of Ionic Distribution in Liquid Silicates. *Proceedings of the Royal Society of London* , *A287*, 201-221.

Masson, C. (1972). Thermodynamics and Constitution of Silicate Slags. *Journal of the Iron and Steel Institute* , 89-96.

Mazumdar, D., & Evans, J. (2004). A Model for Estimating Exposed Plume Eye Area in Steel Refining Ladles Covered with Thin Slag. *Metallurgical and Materials Transactions B* , *35B*, 400-404.

Meredith, D., & Stenkvist, S. (1986). Single Electrode DC Arc Furnace Operation at Florida Steel Corporation. *Electric Furnace Conf. Proceeds. 44*, pp. 43-47. Dallas, TX: AIME.

Meszaros, G., Docktor, D., Stone, R., Carr, C., Kemeny, F., Lawrence, L., et al. (1997). Implementation of a Ladle Slag Oxygen Activity Sensor to Optimize Ladle Slag Practices at the U.S. Steel Mon Valley Works. *Iron & Steelmaker* , *24* (7), 33-39.

Meszaros, G., Estocin, J., Marquat, R., Kemeny, E., & Walker, D. (2000). Development and Application of the DepthWaveTM Slag Depth Measuring System. *Iron and Steelmaker* , 31.

Mills, K., & Keene, B. (1987). Physical Properties of BOS Slags. *International Materials Reviews* , *21* (1-2), 1-120.

Monaghan, B., Pomfret, R., & Coley, K. (1998). The Kinetics of Dephosphorization of Carbon-Saturated Iron Using an Oxidizing Slag. *Metallurgical and Materials Transactions B* .

Moore, J. (1990). *Chemical Metallurgy.* London, UK: Butterworths.

Muske, K., & Edgar, T. (1996). Nonlinear State Estimation. In M. Henson, & D. Seborg (Eds.), *Nonlinear Process Control* (pp. 311-370). Englewood Cliffs, NJ: Prentice Hall.

Nadif, M., & Gatellier, C. (1986). Influence d'une Addition de Calcium ou de Magnesium sur la Solubilite de l'Oxygen et du Soufre dan l'Acier Liquid. *Revue de Metallurgie - CIT* , 377-394.

Oeters, F., Plushkell, W., Steinmetz, E., & Wilhelmi, H. (1988). Fluid Flow and Mixing in Secondary Metallurgy. *Steel Research* , *59* (5), 192-201.

Ohguchi, S., Robertson, D., Deo, B., Grieveson, P., & Jeffes, J. (1984). Simultaneous Dephosphorization and Desulphurization of Molten Pig Iron. *Ironmaking and Steelmaking* , *11* (4), 202-213.

Pan, Y., & Brooks, G. (2004). *Unpublished Research* .

Pelton, A., & Bale, C. (1986). A Modified Interaction Parameter Formalism for Non-Dilute Solutions. *Metallurgical and Materials Transactions A* , *17A*, 1211-1215.

Peter, J., Peaslee, K., Robertson, D., & Thomas, B. (2005). Experimental Study of Kinetic Processes During the Steel Treatment at Two LMFs. *AIST Tech Conference Proceedings*, (pp. 959-973).

Plockinger, E., & Wahlster, M. (1960). *Stahl Eisen* , 659-669.

Pluschkell, W. (1981). Grundoperationen Pfannenmetallurgischer. *Stahl und Eisen* , *101*, 97-102.

Pomfret, R., & Grieveson, P. (1983). The Kinetics of Slag-Metal Reactions. *Canadian Metallurgical Quarterly* , *22* (3), 287-299.

Pratt, J. (1990). Applications of Solid Electrolytes in Thermodynamic Studies of Materials: A Review. *Metallurgical and Material Transactions A* , *21* (5), 1223-1250.

Prosensus. (2008, March 19). *Software for Colour Image Segmentation.* Retrieved from World Wide Web Edition: http://www.prosensus.ca/software/proportion/ProPortion_manual.pdf

Ramachandran, S., King, T., & Grant, N. (1956). Rate and Mechanism of the Sulfur Transfer Reaction. *Transactions AIME* , *11*, 1549-1558.

Rankin, G., & Wright, F. (1915). The Ternary System CaO-Al2O3-SiO2. *Am. J. Sci. (4th Series)*, *39*, 1-79.

Rao, B., & Gaskell, D. (1981). The Thermodynamic Properties of Melts in the System MnO-SiO2. *Metallurgical and Materials Transactions B*, *12B*, 311-317.

Ray, W., & J., S. (1973). *Process Optimization - with Applications in Metallurgy and Chemical Engineering.* John Wiley & Sons.

Rein, R. H., & Chipman, J. (1965). Activities in the Liquid Solution SiO2-CaO-MgO-Al2O3 at 1600°C. *Trans. AIME*, *233*, 415–425.

Riboud, P., & Lucas, L. (1981). Influence of Mass Transfer Upon Surface Phenomena in Iron- and Steelmaking. *Canadian Metallurgical Quarterly*, *20* (2), 199 - 208.

Richardson, F. (1974). *Physical Chemistry of Melts in Metallurgy.* London, UK: Academic Press.

Robertson, D. (1995). The Computation of the Kinetics of the Reactions Between Multiple Phases. *TMS EPD Congress* (pp. 347-361). Warrendale, PA: TMS.

Robertson, D., Deo, B., & Ohguchi, S. (1984). Multicomponent Mixed-Transport Control Theory for Kinetics of Coupled Slag/Metal and Slag/Metal/Gas Reactions: Application to Desulphurization of Molten Iron. *Ironmaking and Steelmaking*, *11* (1), 41-55.

Rosenfeld, A. (2001). From Image Analysis to Computer Vision: An Annotated Bibliography, 1955-1979. *Computer Vision and Image Understanding*, *84*, 298-214.

Schneck, H. (1945). *Physical Chemistry of Steelmaking.* London, UK: Iron and Steel Industrial Research Council.

Schwerdtfeger, K. (1983). Present State of Oxygen Control in Aluminum Deoxidized Steel. *Arch. Eisen.*, *54*, 87.

Sigworth, G., & Elliott, J. (1974). The Thermodynamics of Liquid Dilute Iron Alloys. *Metal Science*, *8*, 298-310.

Soliman, M., Ray, W., & Szekely, J. (1974). Applications of Non-Linear Filtering to the Stainless Steel Decarburization Process. *Int. J. Control*, *20* (4), 641-653.

(1998). Steelmaking and Refining Volume. In R. J. Fruehan (Ed.), *"Making Shaping.* Pittsburgh PA: AISE Foundation.

Story, S., Piccone, T., Fruehan, R., & Potter, M. (September 2004). Inclusion Analysis to Predict Casting Behavior. *Iron & Steel Technology* , 163-1 69.

Story, S., S.M., S., Fruehan, R., Casuccio, G., Potter, M., & Lersch, T. (September 2005). Application of Rapid Inclusion Identification and Analysis. *Iron & Steel Technology* , 41-49.

Subagyo, Brooks, G., Waterfall, S., & Sun, S. (2002). Inferential Model of Desulfurization for Ladle Metallurgy. *Electric Furnace Conference Proceedings*, (pp. 819-827).

Subagyo, S., & Brooks, G. (2004). *Patent No. PCT/CA2003/001053.* Canada.

Subgayo, & Brooks, G. A. (2003). Advanced Image Analysis of Molten Slag for Process Control. *Yazawa International Symposium. 1*, pp. 475-483. San Diego, CA: TMS Annual Meeting.

Subgayo, Brooks, G., & Irons, G. (2003). Spout Eyes Area Correlation in Ladle Metallurgy. *Iron and Steel Institute of Japan , 43* (2), 262-263.

Subramanian, S., & Kay, D. (1988). Inclusion Engineering for the Improved Machinability of Medium Carbon Steels. *Proceedings of Inclusions and their Influence on Material Behaviour.* Chicago: ASM International.

Subramanian, S., & Kay, D. (1997). Microstructural Engineering for Enhanced Machinability. *38th Mechanical Working and Steel Processing Conference.* Warrendale, PA: Iron and Steel Society.

Suito, H., & Inoue, R. (1996). Thermodynamics on Control of Inclusions Composition in Ultra-Clean Steels. *Iron and Steel Institute of Japan , 36* (5), 528-536.

Swamy, K. (1996). *Application of Theoretical and Physical Models to Smelting and Refining.* University of Missouri-Rolla: Ph.D. Thesis.

Szatvanyi, G., Duchesne, C., & Bartolacci, G. (2006). Multivariate Image Analysis of Flames for Product Quality and Combustion Control in Rotary Kilns. *Ind. Eng. Chem. Res. , 45*, 4706-4715.

Szekely, J., & Asai, S. (1974). Decarburization of Stainless Steel: Part II. A Mathematical Model and a Process Optimzation for Industrial Scale Systems. *Metallurgical Transactions* , 1573-1580.

Szekely, J., Evans, J., & Brimacombe, J. (1988). *Physical and Mathematical Modeling of Primary Metals Processing Operations.* New York: John Wiley & Sons Inc.

Takahashi, M., Matsuda, H., Sano, M., & Mori, K. (1987). Rate Controlling Mechanism of Nitrogen Desorption by Ar Injection into Molten Iron. *Transactions of the Iron and Steel Institute of Japan , 27,* 626-632.

Takahashi, M., Sano, M., Mori, K., & Hirasawa, M. (1987). Enhanced Nitrogen Desorption from Molten Iron by Combined Ar Injection and Blowing. *Transaction of the Iron and Steel Institute of Japan , 27,* 633-637.

Taylor, C. (Ed.). (1985). *Electric Furnace Steelmaking, Iron and Steel Society.* Warrendale, PA: Iron and Steel Society.

Temkin, M. (1945). Mixtures of Fused Salts as Ionic Solutions. *Acta Physicochimica U.R.S.S. , 4,* 411–420.

The Japan Society for the Promotion of Science: The 19th Committee on Steelmaking. (1988). *Steelmaking Data Sourcebook.* Tokyo, Japan: Gordon and Breach Science Publishers.

Tiekink, W., Brockhoff, J., & Maes, R. (1994). Total Oxygen Measurements at Hoogovens Ijmuiden BOS. No.2. *77th Steelmaking Conference Proceeding* (pp. 49-51). Warrendale, PA: ISS.

Toop, G., & Samis, C. (1962). Activities of Ions in Silicate Melts. *TMS-AIME* , 878-887.

Toop, G., & Samis, C. (1962). Some New Ionic Concepts of Silicate Slags. *Canadian Metallurigical Quarterly , 1* (2), 129-152.

Turkdogan, E. (2001a). *Patent No. 6,328,867 B1.* United States Patent.

Turkdogan, E. (1973). *Chemical Metallurgy of Iron and Steel.* London, UK: Iron and Steel Institute.

Turkdogan, E. (1996). *Fundamentals of Steelmaking.* London, UK: The University Press, Cambridge.

Turkdogan, E. (1988). Metallurgical Consequences of Calcium Retention in Liquid and Solid Steel. *Calcium Treatment Symposium* (pp. 3-13). London: The Institute of Metals.

Turkdogan, E. (2001). Novel Concept of Disposable EMF Sensors for In Situ Measurements of Solute Contents of Liquid Metals in Metal-Refining Processes. *Scandinavian Journal of Metallurgy*, *30*, 193-203.

Turkdogan, E. (2000). Theoretical Concept on Slag-Oxygen Sensors to Measure Oxide Activities Related to FeO, SiO2, and CaO Contents of Steelmaking Slags. *Ironmaking and Steelmaking*, *27* (1), 32-36.

Turkdogan, E., & Grieveson. (1962). Transfer of Sulfur or Oxygen from a Low to a High Chemical Potential through an Ionic Membrane. *Transactions of the Metallurgical Society of AIME*, *224*, 316-323.

Turkdogan, E., Hancock, R., & Pearson, J. (1955). Desulphurization of Carbon-Saturated Iron: Influence of SIlicon, Manganese, and Aluminum. *Journal of the Iron and Steel Institute*, *179*, 338-341.

Underwood, E. (1968). In R. de Hoff, & F. Rhines (Eds.), *Quantitative Microscopy.* New York: McGraw-Hill.

Wagner, C. (1952). *Thermodynamics of Alloys.* Cambridge, MA: Addison-Wesley.

Ward, R., & Salmon, K. (1960). The Kinetics of Sulphur Transfer from Iron to Slag. *Journal of the Iron and Steel Institute*, *196*, 393-403.

Ward, R., & Salmon, K. (1963). The Kinetics of Sulphur Transfer from Iron to Slag. *Journal of the Iron and Steel Institute*, *201*, 222-227.

Welch, G., & Bishop, G. (2001). *An Introduction to the Kalman Filter.* Chapel Hill, NC: University of North Carolina.

Wells, C. (1970). Optimum Estimation of Carbon and Temperature in a Simulated BOF. *Joint Automatic Control Conference* (pp. 7-18). Atlanta, Ga.: American Automatic Control Council.

Wells, C., & Wismer, D. (1971). Advances in Process Control Applications. *Advanced Control Systems*, *8*, 217-252.

Wilkinson, D. (2000). *Mass Transport in Solids and Fluids.* London: Cambridge University Press.

Wilson, W., & McLean, A. (1980). *Desulfurization of Iron and Steel and Sulfide Shape Control*. Warrendale, PA: Iron & Steel Society of AIME.

Winkler, T., & Chipman, J. (1946). An Equilibrium Study of the Distribution of Phosphorous between Liquid Iron and Basic Slags. *Transactions AIME*, *167*, 111-133.

Wold, H. (1966). Estimation of Principal Components and Related Models by Iterative Least Squares. *In Multivariate Analysis (Ed., P.R. Krishnaiah)*, 391-420.

Wold, S. (1978). Cross Validitory Estimation of the Number of Components in Factor and Principal Component Models. *Technometrics*, *20*, 397-405.

Wold, S., Geladi, P., Esbensen, K., & Ohman, J. (1987). Multi-way Principal Component and PLS Analysis. *Journal of Chemometrics*, *1*, 41-56.

Yokokawa, T., & Niwa, K. (1969). Free Energy of Solution in Binary Silicate Melts. *Transactions of the Japan Institute of Metals*, 3-7.

Yokokawa, T., & Niwa, K. (1969). Free Energy of Solution in Binary Silicate Melts. *Transactions of the Japan Institute of Metals*, 81-86.

Yonezawa, K., & Schwerdtfeger, K. (1999). Spout Eyes Formed by an Emerging Gas Plume at the Surface of a Slag-Covered Metal Melt. *Metallurgical and Materials Transactions B*, *30B*, 655-660.

Young, R., Duffy, J., Hassall, G., & Xu, Z. (1992). Use of Optical Basicity Concept for Determining Phosphorous and Sulphur Slag-Metal Partitions. *Ironmaking and Steelmaking*, *19* (3), 201-219.

Yu, H., & MacGregor, J. (2003). Multivariate Image Analysis and Regression for Prediction of Coating Content and Distribution in the Production of Snack Foods. *Chemometrics and Intelligent Laboratory Systems*, *67*, 125–144.

Zhang, L., & Thomas, B. (2006). State of the Art in the Control of Inclusions During Steel Ingot Casting. *Metallurgical and Materials Transactions B*, *37B*, 733-761.

Zhang, L., Jahanshahi, S., Sun, S., Chen, C., Bourke, B., Wright, S., et al. (2002). CSIRO's Multiphase Reaction Models and Their Industrial Applications. *Journal of Minerals, Metals & Materials Society*, *54* (11), 51-56.

Zhang, L., Sun, S., & Jahanshahi, S. (2007). An Approach to Modeling Al2O3 Containing Slags with the Cell Model. *Journal of Phase Equilibria and Diffusion*, *28* (1), 121.

Zhang, Z., Roelofs, H., Lemgen, S., Urlau, U., & Subramanian, S. (2004). Application of Thermodynamic Model for Inclusion Control in Steelmaking to Improve the Machinability of Low Carbon Free Cutting Steels. *Steel Research*, *75* (5), 314-321.

Appendix A

CELL MODEL EQUATIONS

The free energy of mixing of a slag containing components SiO_2-TiO_2-Ti_2O_3-Cr_2O_3-Al_2O_3-Fe_2O_3-CrO-FeO-MnO-MgO-CaO-S can be determined from:

$$G^M = \sum_{i,j,k} W_{ij}^k R_{ij}^k + 2RT\sum_{i,k} R_{ii}^k \ln Q_{ik} \sum_{i=1}^{m-1} a_i - RT\left(D_i \ln\left(\frac{D_i}{V_i}\right) - D_{i+1}\ln\left(\frac{D_{i+1}}{V_i}\right)\right)$$
$$-2RT\sum_{i=1}^{m} Vi \ln\left(\frac{V_i}{D_1}\right) - \sum_{i,j,k} R_{ij}^k \ln\left(\frac{R_{ij}^k}{D_1}\right) \qquad \text{(A-1)}$$

where:

$m = number\ of\ cations\ ;\ \ p = number\ of\ anions$

$$\left.\begin{matrix} u_{ik}\ (i = 1\ldots m; k = 1\ldots p) \\ v_{ik}\ (i = 1\ldots m; k = 1\ldots p) \end{matrix}\right\} Stoichiometric\ Coefficients\ of : (M_i)_{u_{ik}}\ (A)_{v_{ik}}$$

$a_i = u_{ik} / v_{ik}$

$R_{ij}^k = number\ of\ cells\ i - k - j$

$X_{ik}\ mole\ fraction\ of\ (M_i)_{u_{ik}}\ (A_k)_{v_{ik}}$

$$V_i = \sum_k v_{ik} X_{ik} \qquad V^k = \sum_i v_{ik} X_{ik} \qquad D_i = \sum_{j=i}^{m} V_j \qquad \text{(A-2)}$$

$$RT\ln Q_{ik} = \frac{1}{D_1}\left(\sum_j V_j E_{ij}^k + \sum_l V^l E_i^{k\,l}\right) \qquad \text{(A-3)}$$

The number of cells R_{ij}^k is subject to the following mass balance and partition function maximization constraints:

Mass Balance Constraints:

$$\text{Cations:} \quad \sum_{j,k} R_{ij}^k = V_i \qquad \text{(A-4)}$$

$$\text{Anions:} \quad \sum_{i,j} R_{ij}^k = V^k \qquad \text{(A-5)}$$

Partition Function Maximization Constraints:

$$\begin{aligned}
&R_{ii}^1 R_{jj}^1 = \left(R_{ij}^1 / P_{ij}^1\right)^2 && i,j = 1\ldots m \\
&R_{ii}^1\left(R_{11}^k / R_{11}^1\right) = \left(R_{ii}^k / P_{ii}^k\right) && i = 1\ldots m, k = 2\ldots p \\
&R_{ii}^1 R_{jj}^1\left(R_{11}^k\right)^2 = \left(R_{11}^1\right)^2\left(R_{ij}^k / P_{ij}^k\right)^2 && i,j = 1\ldots m, k = 2\ldots p
\end{aligned} \qquad \text{(A-6)}$$

$$\begin{aligned}
with\ RT\ln\left(P_{ij}^k\right) &= W_{11}^k - \left(1-\delta_{ij}\right)\left(W_{ii}^k + W_{jj}^k\right) - W_{ij}^k \\
&+ RT\ln\left(Q_{i1}Q_{j1}\left(\frac{Q_{1k}}{Q_{11}}\right)^2\right) - 2\delta_{ij} RT\ln Q_{ik}
\end{aligned} \qquad \text{(A-7)}$$

Appendix B

CELL MODEL EXAMPLE

In order to demonstrate cell model capability, the following section contains the calculation results from a worked example having a slag composition of 55wt% CaO, 35wt% Al_2O_3, and 10wt% SiO_2 at 1873K. The step-by-step summary is intended to facilitate steelmakers in developing the model.

Example (55%, CaO, 35wt% Al_2O_3, 10wt% SiO_2) at 1873K:

1. Determination of Cell Fractions (R_{ij}^{k})

(I) Pre-Calculation:

1) Mole Fraction (X_i):

$$X = \begin{bmatrix} 0.111663 & 0 & 0.230306 & 0 & 0 & 0 & 0 & 0 & 0.658031 \\ 0 & 0 & 0 & 0 & 0 & 0 & 0 & 0 & 0 \end{bmatrix}$$

2) Interaction Energy (E_{ij}^{k}):

$$E_{ij}^{k} = \begin{bmatrix} 0 & -3000 & -3662.53 \\ -3000 & 0 & -6651.53 \\ -3662.52 & -6651.53 & 0 \end{bmatrix}$$

3) Formation Energy (W_{ij}^{k}):

$$W_{ij}^{k} = \begin{bmatrix} 0 & 2000 & -12500 \\ 2000 & 0 & -7809.08 \\ -12500 & -7809.08 & 0 \end{bmatrix}$$

4) Cation Vector (V_i):

$$V_i = \begin{bmatrix} 0.223327 & 0.690917 & 0.658031 \end{bmatrix}$$

5) Anion Vector (V_k):

$$V^k = \begin{bmatrix} 1.572274 \end{bmatrix}$$

6) O^{2-} Available (D_i):

$$D_i = \begin{bmatrix} 1.572274 & 1.348948 & 0.658031 \end{bmatrix}$$

7) Q_{ik}-vector:

$$Q_{ik} = \begin{bmatrix} 0.464858 & 0.473346 & 1 \end{bmatrix}$$

8) P_{ij}^k-matrix:

$$P_{ij}^k = \begin{bmatrix} 1 & 0.128568 & 13.361303 \\ 0.128568 & 1 & 3.857985 \\ 13.361303 & 3.857985 & 1 \end{bmatrix}$$

(II) Calculation of Y_i, Y^k, and R_{ij}^k:

(A) Approximation (Algorithm 1)

1) Initialize Y_i, Y^k (Eq. XX)

$$Y_i = \begin{bmatrix} 0.178105 & 0.551013 & 0.524786 \end{bmatrix}$$

$$Y^k = \begin{bmatrix} 1 \end{bmatrix}$$

2) Solution @ z = 0

$$A = \begin{bmatrix} 1.432009 & 0.178105 & 0.178105 \\ 0.551013 & 1.804916 & 0.551013 \\ 0.524786 & 0.524786 & 1.778690 \end{bmatrix}$$

$$B' = \begin{bmatrix} -0.040990 & -0.189103 & -0.632713 \end{bmatrix}$$

$$B'' = \begin{bmatrix} -0.704126 & -0.366948 & -0.578398 \end{bmatrix}$$

$$Y' = \begin{bmatrix} 0.016179 & 0.000377 & -0.360603 \end{bmatrix}$$

$$Y'' = \begin{bmatrix} -0.46812 & -0.003611 & -0.186002 \end{bmatrix}$$

3) Non-Optimal Solution of Y_i and Y^k

$$Y_i = \begin{bmatrix} 0.069241 & 0.524565 & 0.177499 \end{bmatrix}$$

$$Y^k = \begin{bmatrix} 1 \end{bmatrix}$$

(B) Refinement (Algorithm 2)

1) Converged Solution

$$A = \begin{bmatrix} 2.892754 & 0.010206 & 1.060625 \\ 0.067903 & 1.836328 & 2.037608 \\ 2.666090 & 0.769815 & 3.497309 \end{bmatrix}$$

$$B' = \begin{bmatrix} 5.302\text{e-}12 & -1.076\text{e-}13 & 1.296\text{e-}11 \end{bmatrix}$$

$$Y' = \begin{bmatrix} 7.457\text{e-}14 & -5.440\text{e-}12 & 4.848\text{e-}12 \end{bmatrix}$$

2) Optimal Solution of Y_i and Y^k

$$Y_i = \begin{bmatrix} 0.079380 & 0.528153 & 0.199538 \end{bmatrix}$$

$$Y^k = \begin{bmatrix} 1 \end{bmatrix}$$

(C) Compute R_{ijk}^{k} using Y_i and Y^k

$$R_{ij}^{k} = \begin{bmatrix} 0.006301 & 0.005390 & 0.211635 \\ 0.005390 & 0.278945 & 0.406580 \\ 0.211635 & 0.406580 & 0.039815 \end{bmatrix}$$

Check that R_{ij}^{k} Satisfies Mass Balance Constraints:

$$\sum_{k}^{p}\sum_{j}^{m} R_{ij}^{k} = V_i \quad --> \quad \begin{bmatrix}0.223327\\0.690917\\0.658031\end{bmatrix} = \begin{bmatrix}0.223327\\0.690917\\0.658031\end{bmatrix}$$

$$\sum_{i,j} R_{ij}^{k} = V^{k} \quad --> \quad [1.572274] = [1.572274]$$

2. Determination of Free Energy (G^M), Enthalpy (H^M), and Entropy (S^M)

The free energy expression shown in Appendix A can be alternatively expressed as:

$$G^{M} = -RT\ln(\Omega) = -RT\left(-\frac{\mathrm{E_{tot}}}{\mathrm{RT}} + \ln(g)\right) = \left(E_{form} + E_{\mathrm{int}}\right) - RT\left[\ln(P) + \ln(U) + \ln(U^{*})\right]$$

(I) Determination of G^M:

1) Ratio of Stoichiometric Coefficients

$$a_i = [0.5 \quad 0.6667 \quad 1]$$

2) Calculation of Total Energy - E_{tot}

$$E_{form} = \sum_{i,j,k} W_{ij}^{k} R_{ij}^{k} = [-11619.36]$$

$$E_{\mathrm{int}} = 2RT\sum_{i,k} R_{ii}^{k} \ln Q_{ik} = [-1588.99]$$

$$E_{tot} = E_{form} + E_{\mathrm{int}} = [-13208.36]$$

3) Calculation of Degeneracy - ln(g)

$$\ln(P) = \sum_{i=1}^{m-1} a_i \left(D_i \ln\left(\frac{D_i}{V_i}\right) - D_{i+1}\ln\left(\frac{D_{i+1}}{V_i}\right)\right) = [0.944]$$

$$\ln(U) = 2\sum_{i=1}^{m} Vi \ln\left(\frac{V_i}{D_1}\right) = [-3.154]$$

$$\ln\left(U^*\right) = -\sum_{i,j,k} R_{ij}^k \ln\left(\frac{R_{ij}^k}{D_1}\right) = [2.673]$$

$$\ln(g) = \ln(P) + \ln(U) + \ln\left(U^*\right) = [0.463]$$

4) Calculation of Free Energy of Mixing (G^M)

$$\ln(\Omega) = -\frac{\mathrm{E_{tot}}}{\mathrm{RT}} + \ln(g) = [4.012]$$

$$G^M = G_{ID} + G_{EX} = -RT\ln(\Omega) = [-14933.16]$$

$$G_{ID} = RT\sum_i X_i \ln(X_i) = [-3194.81]$$

$$G_{EX} = G^M - G_{ID} = [-11738.35]$$

(II) Determination of H^M, S^M:

$$H^M = E_{tot} = [-13208.36]$$

$$S^M = R\ln(g) = [0.920876]$$

Check that the solution for H^M and S^M are consistent:

$$G^M = H^M + TS^M = \text{-13208.36-1873}(0.920876) = \text{-14933.16}$$

3. Determination of Slag Activities and Activity Coefficients

(I) Determination of a_{liq}

1) Results for $-\Delta X_{CaO}$ (incremental decrease in CaO concentration; similar procedure

for Al_2O_3 required)

$$X_{low} = \begin{bmatrix} 0.111670 & 0 & 0.230306 & 0 & 0 & 0 & 0 & 0 & 0.658025 \\ 0 & 0 & 0 & 0 & 0 & 0 & 0 & 0 & 0 \end{bmatrix}$$

$$R_{low} = \begin{bmatrix} 0.006303 & 0.005391 & 0.211646 \\ 0.005391 & 0.278958 & 0.406568 \\ 0.211646 & 0.406568 & 0.039810 \end{bmatrix}$$

$$G^{M}{}_{low} = [\text{-}14933.28]$$

2) Results for $-\Delta X_{CaO}$ (incremental increase in CaO concentration ; similar procedure for Al_2O_3 required)

$$X_{high} = \begin{bmatrix} 0.111657 & 0 & 0.230306 & 0 & 0 & 0 & 0 & 0 & 0.658038 \\ 0 & 0 & 0 & 0 & 0 & 0 & 0 & 0 & 0 \end{bmatrix}$$

$$R_{high} = \begin{bmatrix} 0.006300 & 0.005389 & 0.211624 \\ 0.005389 & 0.278934 & 0.406593 \\ 0.211624 & 0.406593 & 0.039820 \end{bmatrix}$$

$$G^{M}{}_{high} = [\text{-}14933.05]$$

3) Computation of dG^M/dX_i

$$\frac{\delta G^M}{\delta X_{Al_2O_3}} = [9386.17] \qquad \frac{\delta G^M}{\delta X_{CaO}} = [17995.83]$$

4) Calculation of Activities (a_{liq} – Liquid Reference)

$$a_{liq} = \begin{bmatrix} 0.000420 & 0 & 0.005234 & 0 & 0 & 0 & 0 & 0 & 0.052893 \\ 0 & 0 & 0 & 0 & 0 & 0 & 0 & 0 & 0 \end{bmatrix}$$

(II) Determination of Activities (a_{sol} – Solid Reference)

$$a_{sol} = \begin{bmatrix} 0.000437 & 0 & 0.020867 & 0 & 0 & 0 & 0 & 0 & 0.307973 \\ 0 & 0 & 0 & 0 & 0 & 0 & 0 & 0 & 0 \end{bmatrix}$$

(III) Determination of Activity Coefficients

$$\gamma_{sol} = \begin{bmatrix} 0.0039 & 0 & 0.0906 & 0 & 0 & 0 & 0 & 0 & 0.4680 \\ 0 & 0 & 0 & 0 & 0 & 0 & 0 & 0 & 0 \end{bmatrix}$$

Appendix C

COUPLED MULTI-COMPONENT KINETIC MODEL

The following describes the derivation of the coupled multi-component kinetic model used Chapter 4 of this thesis. Equilibrium slag-metal reactions incorporated within the model include: Fe-FeO, Mn-MnO, CC-CaO, Mg-MgO, Si-SiO_2, Ti-TiO_2, Al-Al_2O_3. The developed model is based on the work of Robertson et al. (1984) and assumes mixed mass transport control, having a concentration gradient profile within the boundary layer defined by Figure 4-15.

Fe-FeO Equilibria Reaction

Consider the following equilibrium reaction at the slag-metal interface:

$$\{Fe\}+[O]=(FeO) \tag{C- 1}$$

The equilibrium constant for reaction C-1 may be expressed as:

$$\begin{aligned} K_{FeO} &= \frac{a_{FeO}}{a_{Fe}h_O} = \frac{\gamma^i_{FeO}X^i_{FeO}}{\gamma^i_{Fe}X^i_{Fe}f^i_O\left(wt\%O_i\right)} \\ &= \frac{\gamma^i_{FeO}X^i_{FeO}\left(0.5585\right)}{\gamma^i_{Fe}X^i_{Fe}f^i_O X^i_O MM_O} \end{aligned} \tag{C- 2}$$

Equation C-2 may be rearranged to yield an expression for the interfacial concentration of FeO on a mole fraction basis as:

$$X_{FeO}^{i} = \frac{K_{FeO}\gamma_{Fe}^{i} X_{Fe}^{i} f_{O}^{i} X_{O}^{i} MM_{O}}{\gamma_{FeO}^{i}(0.5585)} \tag{C- 3}$$

Assuming a state of local equilibrium at the interface allows the flux density equation for iron transfer between slag and metal to be stated as follows:

$$k_{m}^{Fe} C_{vm}\left(X_{Fe}^{b} - X_{Fe}^{i}\right) = k_{s}^{FeO} C_{vs}\left(X_{FeO}^{i} - X_{FeO}^{b}\right) \tag{C- 4}$$

$$X_{Fe}^{b} - X_{Fe}^{i} = \left(\frac{k_{s}^{FeO} C_{vs}}{k_{m}^{Fe} C_{vm}}\right)\left(X_{FeO}^{i} - X_{FeO}^{b}\right) \tag{C- 5}$$

Letting $k_{Fe}^{*} = k_{s}^{FeO} C_{vs} / k_{m}^{Fe} C_{vm}$ and rearranging gives:

$$X_{Fe}^{i} + k_{Fe}^{*} X_{FeO}^{i} = X_{Fe}^{b} + k_{Fe}^{*} X_{FeO}^{b} \tag{C- 6}$$

Substituting equation C-3 into equation C-6 and rearranging terms gives an expression for the interfacial concentration of Fe on a mole fraction basis:

$$X_{Fe}^{i} + k_{Fe}^{*}\left(\frac{K_{FeO}\gamma_{Fe}^{i} X_{Fe}^{i} f_{O}^{i} X_{O}^{i} MM_{O}}{\gamma_{FeO}^{i}(0.5585)}\right) = X_{Fe}^{b} + k_{Fe}^{*} X_{FeO}^{b} \tag{C- 7}$$

$$X_{Fe}^{i}\left(1 + k_{Fe}^{*}\left(\frac{K_{FeO}\gamma_{Fe}^{i} f_{O}^{i} X_{O}^{i} MM_{O}}{\gamma_{FeO}^{i}(0.5585)}\right)\right) = X_{Fe}^{b} + k_{Fe}^{*} X_{FeO}^{b} \tag{C- 8}$$

$$X_{Fe}^{i} = \frac{X_{Fe}^{b} + k_{Fe}^{*} X_{FeO}^{b}}{1 + k_{Fe}^{*} \beta X_{O}^{i}} \tag{C- 9}$$

where

$$\beta = \frac{K_{FeO}\gamma^{i}_{Fe} f^{i}_{O} MM_{O}}{\gamma^{i}_{FeO}(0.5585)} \tag{C- 10}$$

Mn-MnO Equilibria Reaction

Consider the following equilibrium reaction at the slag-metal interface:

$$[Mn]+[O]=(MnO) \tag{C- 11}$$

The equilibrium constant for reaction C-11 can be expressed as:

$$\begin{aligned} K_{MnO} &= \frac{a_{MnO}}{h_{Mn}h_{O}} = \frac{\gamma^{i}_{MnO} X^{i}_{MnO}}{f^{i}_{Mn}(wt\%Mn_{i}) f^{i}_{O}(wt\%O_{i})} \\ &= \frac{\gamma^{i}_{MnO} X^{i}_{MnO}(0.5585)^{2}}{f^{i}_{Mn} X^{i}_{Mn} f^{i}_{O} X^{i}_{O} MM_{O} MM_{Mn}} \end{aligned} \tag{C- 12}$$

Equation C-12 may be rearranged to yield an expression for the interfacial concentration of MnO on a mole fraction basis as:

$$X^{i}_{MnO} = \frac{K_{MnO} f^{i}_{Mn} X^{i}_{Mn} f^{i}_{O} X^{i}_{O} MM_{O} MM_{Mn}}{\gamma^{i}_{MnO}(0.5585)^{2}} \tag{C- 13}$$

Assuming a state of local equilibrium at the interface allows the flux density equation for manganese transfer between slag and metal to be stated as follows:

$$k^{Mn}_{m} C_{vm}\left(X^{b}_{Mn} - X^{i}_{Mn}\right) = k^{MnO}_{s} C_{vs}\left(X^{i}_{MnO} - X^{b}_{MnO}\right) \tag{C- 14}$$

$$X^{b}_{Mn} - X^{i}_{Mn} = \left(\frac{k^{MnO}_{s} C_{vs}}{k^{Mn}_{m} C_{vm}}\right)\left(X^{i}_{MnO} - X^{b}_{MnO}\right) \tag{C- 15}$$

Letting $k^{*}_{Mn} = k^{MnO}_{s} C_{vs} / k^{Mn}_{m} C_{vm}$ and rearranging gives:

$$X^{i}_{Mn} + k^{*}_{Mn}\, X^{i}_{MnO} = X^{b}_{Mn} + k^{*}_{Mn}\, X^{b}_{MnO} \tag{C- 16}$$

Substituting equation C-13 into equation C-16 and manipulating yields an expression for the interfacial concentration of Mn on a mole fraction basis as:

$$X^{i}_{Mn} + k^{*}_{Mn}\left(\frac{K_{MnO} f^{i}_{Mn} X^{i}_{Mn} f^{i}_{O} X^{i}_{O} MM_{O} MM_{Mn}}{\gamma^{i}_{MnO}\,(0.5585)^{2}}\right) = X^{b}_{Mn} + k^{*}_{Mn}\, X^{b}_{MnO} \tag{C- 17}$$

$$X^{i}_{Mn}\left(1 + k^{*}_{Mn}\left(\frac{K_{MnO} f^{i}_{Mn} f^{i}_{O} X^{i}_{O} MM_{O} MM_{Mn}}{\gamma^{i}_{MnO}\,(0.5585)^{2}}\right)\right) = X^{b}_{Mn} + k^{*}_{Mn}\, X^{b}_{MnO} \tag{C- 18}$$

$$X^{i}_{Mn} = \frac{X^{b}_{Mn} + k^{*}_{Mn}\, X^{b}_{MnO}}{1 + k^{*}_{Mn}\,\delta\, X^{i}_{O}} \tag{C- 19}$$

where

$$\delta = \frac{K_{MnO} f^{i}_{Mn} f^{i}_{O} MM_{O} MM_{Mn}}{\gamma^{i}_{MnO}\,(0.5585)^{2}} \tag{C- 20}$$

Ca-CaO Equilibria Reaction

Consider the following equilibrium reaction at the slag-metal interface:

$$[Ca] + [O] = (CaO) \tag{C- 21}$$

The equilibrium constant for reaction C-21 can be expressed as:

$$\begin{aligned} K_{CaO} &= \frac{a_{CaO}}{h_{Ca} h_{O}} = \frac{\gamma^{i}_{CaO} X^{i}_{CaO}}{f^{i}_{Ca}\left(wt\%Ca_{i}\right) f^{i}_{O}\left(wt\%O_{i}\right)} \\ &= \frac{\gamma^{i}_{CaO} X^{i}_{CaO}\,(0.5585)^{2}}{f^{i}_{Ca} X^{i}_{Ca} f^{i}_{O} X^{i}_{O} MM_{O} MM_{Ca}} \end{aligned} \tag{C- 22}$$

Equation C-22 may be rearranged to yield an expression for the interfacial concentration of CaO on a mole fraction basis as:

$$X_{CaO}^{i} = \frac{K_{CaO} f_{Ca}^{i} X_{Ca}^{i} f_{O}^{i} X_{O}^{i} MM_{O} MM_{Ca}}{\gamma_{CaO}^{i} (0.5585)^{2}} \tag{C- 23}$$

Assuming a state of local equilibrium at the interface allows the flux density equation for calcium transfer between slag and metal to be stated as follows:

$$k_{m}^{Ca} C_{vm} \left(X_{Ca}^{b} - X_{Ca}^{i} \right) = k_{s}^{CaO} C_{vs} \left(X_{CaO}^{i} - X_{CaO}^{b} \right) \tag{C- 24}$$

$$X_{Ca}^{b} - X_{Ca}^{i} = \left(\frac{k_{s}^{CaO} C_{vs}}{k_{m}^{Ca} C_{vm}} \right) \left(X_{CaO}^{i} - X_{CaO}^{b} \right) \tag{C- 25}$$

Letting $k_{Ca}^{*} = k_{s}^{CaO} C_{vs} / k_{m}^{Ca} C_{vm}$ and rearranging gives:

$$X_{Ca}^{i} + k_{Ca}^{*} X_{CaO}^{i} = X_{Ca}^{b} + k_{Ca}^{*} X_{CaO}^{b} \tag{C- 26}$$

Substituting equation C-23 into equation C-26 and manipulating yields an expression for the interfacial concentration of Ca on a mole fraction basis as:

$$X_{Ca}^{i} + k_{Ca}^{*} \left(\frac{K_{CaO} f_{Ca}^{i} X_{Ca}^{i} f_{O}^{i} X_{O}^{i} MM_{O} MM_{Ca}}{\gamma_{CaO}^{i} (0.5585)^{2}} \right) = X_{Ca}^{b} + k_{Ca}^{*} X_{CaO}^{b} \tag{C- 27}$$

$$X_{Ca}^{i} \left(1 + k_{Ca}^{*} \left(\frac{K_{CaO} f_{Ca}^{i} f_{O}^{i} X_{O}^{i} MM_{O} MM_{Ca}}{\gamma_{CaO}^{i} (0.5585)^{2}} \right) \right) = X_{Ca}^{b} + k_{Ca}^{*} X_{CaO}^{b} \tag{C- 28}$$

$$X_{Ca}^{i} = \frac{X_{Ca}^{b} + k_{Ca}^{*} X_{CaO}^{b}}{1 + k_{Ca}^{*} \theta X_{O}^{i}} \tag{C- 29}$$

where

$$\theta = \frac{K_{CaO} f_{Ca}^{i} f_{O}^{i} MM_{O} MM_{Ca}}{\gamma_{CaO}^{i} (0.5585)^2} \tag{C- 30}$$

Mg-MgO Equilibria Reaction

Consider the following equilibrium reaction at the slag-metal interface:

$$[Mg]+[O]=(MgO) \tag{C- 31}$$

The equilibrium constant for reaction C-31 can be expressed as:

$$\begin{aligned} K_{MgO} &= \frac{a_{MgO}}{h_{Mg} h_{O}} = \frac{\gamma_{MgO}^{i} X_{MgO}^{i}}{f_{Mg}^{i} (wt\%Mg_i) f_{O}^{i} (wt\%O_i)} \\ &= \frac{\gamma_{MgO}^{i} X_{MgO}^{i} (0.5585)^2}{f_{Mg}^{i} X_{Mg}^{i} f_{O}^{i} X_{O}^{i} MM_{O} MM_{Mg}} \end{aligned} \tag{C- 32}$$

Equation C-32 may be rearranged to yield an expression for the interfacial concentration of MgO on a mole fraction basis as:

$$X_{MgO}^{i} = \frac{K_{MgO} f_{Mg}^{i} X_{Mg}^{i} f_{O}^{i} X_{O}^{i} MM_{O} MM_{Mg}}{\gamma_{MgO}^{i} (0.5585)^2} \tag{C- 33}$$

Assuming a state of local equilibrium at the interface allows the flux density equation for magnesium transfer between slag and metal to be stated as follows:

$$k_{m}^{Mg} C_{vm} \left(X_{Mg}^{b} - X_{Mg}^{i} \right) = k_{s}^{MgO} C_{vs} \left(X_{MgO}^{i} - X_{MgO}^{b} \right) \tag{C- 34}$$

$$X_{Mg}^{b} - X_{Mg}^{i} = \left(\frac{k_{s}^{MgO} C_{vs}}{k_{m}^{Mg} C_{vm}} \right) \left(X_{MgO}^{i} - X_{MgO}^{b} \right) \tag{C- 35}$$

Letting $k^*_{Mg} = k_s^{MgO}\, C_{vs} \big/ k_m^{Mg}\, C_{vm}$ and rearranging gives::

$$X^i_{Mg} + k^*_{Mg}\, X^i_{MgO} = X^b_{Mg} + k^*_{Mg}\, X^b_{MgO} \tag{C- 36}$$

Substituting equation C-33 into equation C-36 and manipulating yields an expression for the interfacial concentration of Mg on a mole fraction basis as:

$$X^i_{Mg} + k^*_{Mg}\left(\frac{K_{MgO} f^i_{Mg} X^i_{Mg} f^i_O X^i_O MM_O MM_{Mg}}{\gamma^i_{MgO}(0.5585)^2}\right) = X^b_{Mg} + k^*_{Mg}\, X^b_{MgO} \tag{C- 37}$$

$$X^i_{Mg}\left(1 + k^*_{Mg}\left(\frac{K_{MgO} f^i_{Mg} f^i_O X^i_O MM_O MM_{Mg}}{\gamma^i_{MgO}(0.5585)^2}\right)\right) = X^b_{Mg} + k^*_{Mg}\, X^b_{MgO} \tag{C- 38}$$

$$X^i_{Mg} = \frac{X^b_{Mg} + k^*_{Mg}\, X^b_{MgO}}{1 + k^*_{Mg}\, \Omega\, X^i_O} \tag{C- 39}$$

where

$$\Omega = \frac{K_{MgO} f^i_{Mg} f^i_O MM_O MM_{Mg}}{\gamma^i_{MgO}(0.5585)^2} \tag{C- 40}$$

Si-SiO$_2$ Equilibria Reaction

Consider the following equilibrium reaction at the slag-metal interface:

$$[Si] + 2[O] = (SiO_2) \tag{C- 41}$$

The equilibrium constant for reaction C-41 can be expressed as:

$$K_{SiO_2} = \frac{a_{SiO_2}}{h_{Si} h_O^{\,2}} = \frac{\gamma^i_{SiO_2} X^i_{SiO_2}}{f^i_{Si}\left(wt\%Si_i\right)\left(f^i_O\left(wt\%O_i\right)\right)^2}$$

$$= \frac{\gamma^i_{SiO_2} X^i_{SiO_2} \left(0.5585\right)^3}{f^i_{Si} X^i_{Si} \left(f^i_O X^i_O\right)^2 \left(MM_O\right)^2 MM_{Si}} \qquad \text{(C- 42)}$$

Equation C-42 may be rearranged to yield an expression for the interfacial concentration of SiO_2 on a mole fraction basis as:

$$X^i_{SiO_2} = \frac{K_{SiO_2} f^i_{Si} X^i_{Si} \left(f^i_O X^i_O\right)^2 \left(MM_O\right)^2 MM_{Si}}{\gamma^i_{SiO_2} \left(0.5585\right)^3} \qquad \text{(C- 43)}$$

Assuming a state of local equilibrium at the interface allows the flux density equation for silicon transfer between slag and metal to be stated as follows:

$$k^{Si}_m C_{vm} \left(X^b_{Si} - X^i_{Si}\right) = k^{SiO_2}_s C_{vs} \left(X^i_{SiO_2} - X^b_{SiO_2}\right) \qquad \text{(C- 44)}$$

$$X^b_{Si} - X^i_{Si} = \left(\frac{k^{SiO_2}_s C_{vs}}{k^{Si}_m C_{vm}}\right)\left(X^i_{SiO_2} - X^b_{SiO_2}\right) \qquad \text{(C- 45)}$$

Letting $k^*_{Si} = k^{SiO_2}_s C_{vs} / k^{Si}_m C_{vm}$ and rearranging gives:

$$X^i_{Si} + k^*_{Si} X^i_{SiO_2} = X^b_{Si} + k^*_{Si} X^b_{SiO_2} \qquad \text{(C- 46)}$$

Substituting equation C-43 into equation C-46 and manipulating yields an expression for the interfacial concentration of Si on a mole fraction basis as:

$$X^i_{Si} + k^*_{Si}\left(\frac{K_{SiO_2} f^i_{Si} X^i_{Si} \left(f^i_O X^i_O\right)^2 \left(MM_O\right)^2 MM_{Si}}{\gamma^i_{SiO_2} \left(0.5585\right)^3}\right) = X^b_{Si} + k^*_{Si} X^b_{SiO_2} \qquad \text{(C- 47)}$$

$$X_{Si}^{i}\left(1+k_{Si}^{*}\left(\frac{K_{SiO_2} f_{Si}^{i}\left(f_{O}^{i}X_{O}^{i}\right)^{2}\left(MM_{O}\right)^{2}MM_{Si}}{\gamma_{SiO_2}^{i}\left(0.5585\right)^{3}}\right)\right)=X_{Si}^{b}+k_{Si}^{*}X_{SiO_2}^{b} \qquad \text{(C- 48)}$$

$$X_{Si}^{i}=\frac{X_{Si}^{b}+k_{Si}^{*}X_{SiO_2}^{b}}{1+k_{Si}^{*}\Phi\left(X_{O}^{i}\right)^{2}} \qquad \text{(C- 49)}$$

where

$$\Phi=\frac{K_{SiO_2} f_{Si}^{i}\left(f_{O}^{i}\right)^{2}\left(MM_{O}\right)^{2}MM_{Si}}{\gamma_{SiO_2}^{i}\left(0.5585\right)^{3}} \qquad \text{(C- 50)}$$

Ti-TiO$_2$ Equilibria Reaction

Consider the following equilibrium reaction at the slag-metal interface:

$$[Ti]+2[O]=(TiO_2) \qquad \text{(C- 51)}$$

The equilibrium constant for reaction C-51 can be expressed as:

$$\begin{aligned} K_{TiO_2} &= \frac{a_{TiO_2}}{h_{Ti}h_{O}^{2}}=\frac{\gamma_{TiO_2}^{i}X_{TiO_2}^{i}}{f_{Ti}^{i}\left(wt\%Ti_{i}\right)\left(f_{O}^{i}\left(wt\%O_{i}\right)\right)^{2}} \\ &= \frac{\gamma_{TiO_2}^{i}X_{TiO_2}^{i}\left(0.5585\right)^{3}}{f_{Ti}^{i}X_{Ti}^{i}\left(f_{O}^{i}X_{O}^{i}\right)^{2}\left(MM_{O}\right)^{2}MM_{Ti}} \end{aligned} \qquad \text{(C- 52)}$$

Equation C-52 may be rearranged to yield an expression for the interfacial concentration of TiO$_2$ on a mole fraction basis as:

$$X_{TiO_2}^{i}=\frac{K_{TiO_2} f_{Ti}^{i}X_{Ti}^{i}\left(f_{O}^{i}X_{O}^{i}\right)^{2}\left(MM_{O}\right)^{2}MM_{Ti}}{\gamma_{TiO_2}^{i}\left(0.5585\right)^{3}} \qquad \text{(C- 53)}$$

Assuming a state of local equilibrium at the interface allows the flux density equation for titanium transfer between slag and metal to be stated as follows:

$$k_m^{Ti}\,C_{vm}\left(X_{Ti}^b - X_{Ti}^i\right) = k_s^{TiO_2}\,C_{vs}\left(X_{TiO_2}^i - X_{TiO_2}^b\right) \qquad \text{(C- 54)}$$

$$X_{Ti}^b - X_{Ti}^i = \left(\frac{k_s^{TiO_2}\,C_{vs}}{k_m^{Ti}\,C_{vm}}\right)\left(X_{TiO_2}^i - X_{TiO_2}^b\right) \qquad \text{(C- 55)}$$

Letting $k_{Ti}^* = k_s^{TiO_2}\,C_{vs} / k_m^{Ti}\,C_{vm}$ and rearranging gives:

$$X_{Ti}^i + k_{Ti}^*\,X_{TiO_2}^i = X_{Ti}^b + k_{Ti}^*\,X_{TiO_2}^b \qquad \text{(C- 56)}$$

Substituting equation C-53 into equation C-56 and manipulating yields an expression for the interfacial concentration of Ti on a mole fraction basis as:

$$X_{Ti}^i + k_{Ti}^*\left(\frac{K_{TiO_2} f_{Ti}^i X_{Ti}^i \left(f_O^i X_O^i\right)^2 \left(MM_O\right)^2 MM_{Ti}}{\gamma_{TiO_2}^i\,(0.5585)^3}\right) = X_{Ti}^b + k_{Ti}^*\,X_{TiO_2}^b \qquad \text{(C- 57)}$$

$$X_{Ti}^i\left(1 + k_{Ti}^*\left(\frac{K_{TiO_2} f_{Ti}^i \left(f_O^i X_O^i\right)^2 \left(MM_O\right)^2 MM_{Ti}}{\gamma_{TiO_2}^i\,(0.5585)^3}\right)\right) = X_{Ti}^b + k_{Ti}^*\,X_{TiO_2}^b \qquad \text{(C- 58)}$$

$$X_{Ti}^i = \frac{X_{Ti}^b + k_{Ti}^*\,X_{TiO_2}^b}{1 + k_{Ti}^*\omega\left(X_O^i\right)^2} \qquad \text{(C- 59)}$$

where

$$\omega = \frac{K_{SiO_2} f_{Si}^i \left(f_O^i\right)^2 \left(MM_O\right)^2 MM_{Si}}{\gamma_{SiO_2}^i\,(0.5585)^3} \qquad \text{(C- 60)}$$

Al-Al_2O_3 Equilibria Reaction

Consider the following equilibrium reaction at the slag-metal interface:

$$2[Al]+3[O]=(Al_2O_3) \tag{C- 61}$$

The equilibrium constant for reaction C-61 can be expressed as:

$$\begin{aligned} K_{Al_2O_3} &= \frac{a_{Al_2O_3}}{h_{Al}{}^2 h_O{}^3} = \frac{\gamma^i_{Al_2O_3} X^i_{Al_2O_3}}{\left(f^i_{Al}\left(wt\%Al\right)\right)^2 \left(f^i_O\left(wt\%O\right)\right)^3} \\ &= \frac{\gamma^i_{Al_2O_3} X^i_{Al_2O_3}(0.5585)^5}{\left(f^i_{Al}X^i_{Al}\right)^2\left(f^i_O X^i_O\right)^3\left(MM_O\right)^3\left(MM_{Al}\right)^2} \end{aligned} \tag{C- 62}$$

Equation C-62 may be rearranged to yield an expression for the interfacial concentration of Al_2O_3 on a mole fraction basis as:

$$X^i_{Al_2O_3} = \frac{K_{Al_2O_3}\left(f^i_{Al}X^i_{Al}\right)^2\left(f^i_O X^i_O\right)^3\left(MM_O\right)^3\left(MM_{Al}\right)^2}{\gamma^i_{Al_2O_3}(0.5585)^5} \tag{C- 63}$$

Assuming a state of local equilibrium at the interface allows the flux density equation for aluminum transfer between slag and metal to be stated as follows:

$$k^{Al}_m C_{vm}\left(X^b_{Al}-X^i_{Al}\right)=2k^{Al_2O_3}_s C_{vs}\left(X^i_{Al_2O_3}-X^b_{Al_2O_3}\right) \tag{C- 64}$$

$$X^b_{Al}-X^i_{Al}=2\left(\frac{k^{Al_2O_3}_s C_{vs}}{k^{Al}_m C_{vm}}\right)\left(X^i_{Al_2O_3}-X^b_{Al_2O_3}\right) \tag{C- 65}$$

Letting $k^*_{Al}=k^{Al_2O_3}_s C_{Vs}/k^{Al}_m C_{Vm}$ and rearranging gives:

$$X^i_{Al}+2k^*_{Al}X^i_{Al_2O_3}=X^b_{Al}+2k^*_{Al}X^b_{Al_2O_3} \tag{C- 66}$$

Substituting equation C-63 into equation C-66 and manipulating yields a quadratic expression for the interfacial concentration of Al on a mole fraction basis as:

$$X_{Al}^{i\ 2} + \left(\frac{X_{Al}^{i}}{2k_{Al}^{*}\,\psi\left(X_O^i\right)^3} \right) - \left(\frac{X_{Al}^{b} + 2k_{Al}^{*} X_{Al_2O_3}^{b}}{2k_{Al}^{*}\,\psi\left(X_O^i\right)^3} \right) = 0 \tag{C- 67}$$

where

$$\psi = \left(\frac{K_{Al_2O_3}\left(f_{Al}^i\right)^2 \left(f_O^i\right)^3 \left(MM_O\right)^3 \left(MM_{Al}\right)^2}{\gamma_{Al_2O_3}^{i}\left(0.5585\right)^5} \right) \tag{C- 68}$$

Equation C-68 is solved using an initial guess for the interfacial oxygen content and iterating using the oxygen flux density equation below to until convergence has been obtained.

Oxygen Flux Density Equation

By coupling the slag-metal reactions for Fe-FeO, Mn-MnO, CC-CaO, Mg-MgO, Si-SiO_2, Ti-TiO_2, Al-Al_2O_3 an overall oxygen mass balance equation can be stated as:

$$\begin{aligned} k_M^O C_{vm}\left(X_O^b - X_O^i\right) = {} & k_S^{FeO} C_{vs}\left(X_{FeO}^i - X_{FeO}^b\right) + k_S^{MnO} C_{vs}\left(X_{MnO}^i - X_{MnO}^b\right) \\ & + k_S^{CaO} C_{vs}\left(X_{CaO}^i - X_{CaO}^b\right) + k_S^{MgO} C_{vs}\left(X_{MgO}^i - X_{MgO}^b\right) \\ & + 2k_S^{SiO_2} C_{vs}\left(X_{SiO_2}^i - X_{SiO_2}^b\right) + 2k_S^{TiO_2} C_{vs}\left(X_{TiO_2}^i - X_{TiO_2}^b\right) \\ & + 3k_S^{Al_2O_3} C_{vs}\left(X_{Al_2O_3}^i - X_{Al_2O_3}^b\right) \end{aligned} \tag{C- 69}$$

Dividing equation C-69 by $k_M^O C_{vm}$ gives:

$$\begin{aligned} X_O^b - X_O^i = {} & k_{Fe,O}^{*}\left(X_{FeO}^i - X_{FeO}^b\right) + k_{Mn,O}^{*}\left(X_{MnO}^i - X_{MnO}^b\right) \\ & + k_{Ca,O}^{*}\left(X_{CaO}^i - X_{CaO}^b\right) + k_{Mg,O}^{*}\left(X_{MgO}^i - X_{MgO}^b\right) \\ & + 2k_{Si,O}^{*}\left(X_{SiO_2}^i - X_{SiO_2}^b\right) + 2k_{Ti,O}^{*}\left(X_{TiO_2}^i - X_{TiO_2}^b\right) \\ & + 3k_{Al,O}^{*}\left(X_{Al_2O_3}^i - X_{Al_2O_3}^b\right) \end{aligned} \tag{C- 70}$$

where

$$\begin{gathered} k_{Fe,O}^{*} = \left(\frac{k_s^{FeO}\, C_{vs}}{k_m^O\, C_{vm}}\right);\; k_{Mn,O}^{*} = \left(\frac{k_s^{MnO}\, C_{vs}}{k_m^O\, C_{vm}}\right);\; k_{Ca,O}^{*} = \left(\frac{k_s^{CaO}\, C_{vs}}{k_m^O\, C_{vm}}\right); \\ k_{Mg,O}^{*} = \left(\frac{k_s^{MgO}\, C_{vs}}{k_m^O\, C_{vm}}\right);\; k_{Si,O}^{*} = \left(\frac{k_s^{SiO_2}\, C_{vs}}{k_m^O\, C_{vm}}\right);\; k_{Ti,O}^{*} = \left(\frac{k_s^{TiO_2}\, C_{vs}}{k_m^O\, C_{vm}}\right); \\ k_{Al,O}^{*} = \left(\frac{k_s^{Al_2O_3}\, C_{vs}}{k_m^O\, C_{vm}}\right) \end{gathered} \tag{C- 71}$$

Substituting in the equations for interfacial metal and oxide concentrations and rearranging yields the following equation:

$$\begin{aligned} 0 = {} & X_O^i + \left(\frac{B X_O^i}{1 + C X_O^i}\right) + \left(\frac{D X_O^i}{1 + E X_O^i}\right) + \left(\frac{F X_O^i}{1 + G X_O^i}\right) \\ & + \left(\frac{H X_O^i}{1 + I X_O^i}\right) + \left(\frac{2J\left(X_O^i\right)^2}{1 + K\left(X_O^i\right)^2}\right) + \left(\frac{2L\left(X_O^i\right)^2}{1 + M\left(X_O^i\right)^2}\right) \\ & + 3N\left(X_{Al}^i\right)^2\left(X_O^i\right)^3 - A \end{aligned} \tag{C- 72}$$

where

$$\begin{aligned} A = {} & X_O^b + k_{Fe,O}^{*}\, X_{FeO}^b + k_{Mn,O}^{*}\, X_{MnO}^b + k_{Ca,O}^{*}\, X_{CaO}^b \\ & + k_{Mg,O}^{*}\, X_{MgO}^b + 2k_{Si,O}^{*}\, X_{SiO_2}^b + 2k_{Ti,O}^{*}\, X_{TiO_2}^b + 3k_{Al,O}^{*}\, X_{Al_2O_3}^b \end{aligned} \tag{C- 73}$$

$B = k^*_{Fe,O}\beta\left(X^b_{Fe} + k^*_{Fe}\, X^b_{FeO}\right)$ (C- 74)

$C = k^*_{Fe}\beta$ (C- 75)

$D = k^*_{Mn,O}\delta\left(X^b_{Mn} + k^*_{Mn}\, X^b_{MnO}\right)$ (C- 76)

$E = k^*_{Mn}\delta$ (C- 77)

$F = k^*_{Ca,O}\theta\left(X^b_{Ca} + k^*_{Ca}\, X^b_{CaO}\right)$ (C- 78)

$G = k^*_{Ca}\theta$ (C- 79)

$H = k^*_{Mg,O}\Omega\left(X^b_{Mg} + k^*_{Mg}\, X^b_{MgO}\right)$ (C- 80)

$I = k^*_{Mg}\Omega$ (C- 81)

$J = k^*_{Si,O}\,\Phi\left(X^b_{Si} + k^*_{Si}\, X^b_{SiO_2}\right)$ (C-

82) $K = k^*_{Si}\,\Phi$ (C- 83)

$L = k^*_{Ti,O}\,\omega\left(X^b_{Ti} + k^*_{Ti}\, X^b_{TiO_2}\right)$ (C- 84)

$M = k^*_{Ti}\,\omega$ (C- 85)

$N = k^*_{Al,O}\,\psi$ (C- 86)

Equation C-72 is a non-linear equation can be solved using numerical methods. The Newton-Raphson method was used in this study and is given as:

$$x_{i+1} = x_i - \frac{f\left(x_i\right)}{f^{'}\left(x_i\right)}$$

$$
\begin{aligned}
f(x_i) = X_O^i &+ \left(\frac{B X_O^i}{1+C X_O^i}\right) + \left(\frac{D X_O^i}{1+E X_O^i}\right) + \left(\frac{F X_O^i}{1+G X_O^i}\right) \\
&+ \left(\frac{H X_O^i}{1+I X_O^i}\right) + \left(\frac{2J\left(X_O^i\right)^2}{1+K\left(X_O^i\right)^2}\right) + \left(\frac{2L\left(X_O^i\right)^2}{1+M\left(X_O^i\right)^2}\right) \\
&+ 3N\left(X_{Al}^i\right)^2\left(X_O^i\right)^3 - A
\end{aligned}
\tag{C- 87}
$$

$$
\begin{aligned}
f'(x_i) = 1 &+ \frac{B}{1+C X_O^i} - \frac{BC X_O^i}{\left(1+C X_O^i\right)^2} + \frac{D}{1+E X_O^i} - \frac{DE X_O^i}{\left(1+E X_O^i\right)^2} \\
&+ \frac{F}{1+G X_O^i} - \frac{FG X_O^i}{\left(1+G X_O^i\right)^2} + \frac{H}{1+I X_O^i} - \frac{HI X_O^i}{\left(1+I X_O^i\right)^2} \\
&+ \frac{4J X_O^i}{1+K X_O^i} - \frac{\left(4J X_O^i\right)\left(K X_O^{i2}\right)}{\left(1+K X_O^{i2}\right)^2} + \frac{4L X_O^i}{1+M X_O^i} \\
&- \frac{\left(4L X_O^i\right)\left(M X_O^{i2}\right)}{\left(1+M X_O^{i2}\right)^2} + 9LN\left(X_{Al}^i\right)^2\left(X_O^i\right)^2
\end{aligned}
\tag{C- 88}
$$

The developed routine should be iterated until both the interfacial concentrations for aluminum and oxygen have converged.

Appendix D

MODEL FOR ESTIMATING SLAG DENSITY

The following appendix details a slag density prediction model. The density model was used in combination with slag height measurements to estimate ladle slag mass and other relevant ladle heat properties.

Slag Density Model:

The developed model is that of Mills & Keene (1987), and is based on the widely accepted additive method for the estimation of slag densities. Slag molar volume is calculated from equation D-1 using the partial molar values shown in Table D-1.

$$V = X_1\bar{V}_1 + X_2\bar{V}_2 + X_3\bar{V}_3 + \ldots + X_n\bar{V}_n = \sum_{i=1}^{i=n} X_i\bar{V}_i \qquad \text{(D- 1)}$$

where V is the molar volume (cm^3/mol), X_i is the mole fraction of the i-th slag component, $\bar{V}_i$ is the partial molar volume (cm^3/mol) of the i-th component, and n is the number of slag components. Having calculated the molar volume, slag density is determined from the following equation:

$$\rho = \frac{M_1X_1 + M_2X_2 + M_3X_3 + \ldots + M_nX_n}{V} = \frac{\sum_{i=1}^{i=n} M_iX_i}{V} \qquad \text{(D- 2)}$$

where ρ is the slag density (g/cm^3), and M_i is the molecular weight (g/mol) of the i-th slag component.

To account for the variation of density with temperature, Mills & Keene (1987) evaluated the molar volume temperature dependencies (dV/dT) of numerous slag systems and recommended a mean relationship of 0.01 %/K.

Table D-1: Values for partial molar volume of various slag constituents at 1500°C

Constituent	**Partial Molar Volume (cm^{3}mol^{-1})**
Al_2O_3	$28.31 + 32(X_{Al2O3}) - 31.45\ (X_{Al2O3})^2$
CaF_2	31.3
CaO	20.7
FeO	15.8
Fe_2O_3	38.4
K_2O	51.8
MgO	16.1
MnO	15.6
Na_2O	33.0
P_2O_5	65.7
SiO_2	$19.55 + 7.966(X_{SiO2})$
TiO_2	24.0

References:

Mills, K., & Keene, B. (1987). Physical Properties of BOS Slags. *International Materials Reviews*, *21* (1-2), 1-120.

Appendix E

DETERMINATION OF OXYGEN ACTIVITY IN Si-Mn DEOXIDIZED STEEL

In Chapter 4 of this thesis it was demonstrated that the dissolved oxygen content in steel in aluminum killed heats was controlled by the inclusions when the activity of alumina is or close to unity. The following section outlines a procedure based on the work of Jahnsen (2006) and Gustafson (2008) that was developed for determining the dissolved oxygen content in iron-silicon-manganese deoxidized steels. Although the accuracy of the developed routine was unable to be validated within this thesis it has been substantiated by industrial trials by previous investigators (Jahnsen, 2006; Gustafson, 2008).

The model is developed on the assumption of inclusion-metal equilibrium, where the precipitated deoxidation products control the dissolved oxygen activity in steel. A key difference between this model and most inclusion models within the literature is that the activity coefficients of top slag components are not used within the developed routines to represent the activity coefficients of inclusion components. Instead, the model uses activity correlations that were developed using the cell model on the basis of the following binary systems: FeO-MnO, FeO-SiO_2, MnO-SiO_2. Using the activity data contained in Figure E-, E-2, and E-3 an algorithm can be developed to recursively determine the equilibrium oxygen activity for each added deoxidant (where the lowest value is assumed to control the oxygen potential).

FeO-MnO Equilibria Reaction:

Consider the following equilibrium reaction at the inclusion-metal interface:

$$\begin{array}{c}[Mn]+[O]=(MnO)\\ (FeO)=\{Fe\}+[O]\\ \hline [Mn]+(FeO)=\{Fe\}+(MnO)\end{array} \qquad \text{(E- 89)}$$

The equilibrium constant for reaction E-1 may be expressed as:

$$K_{MnOFeO}=\frac{h_{Mn}a_{FeO}}{a_{Fe}a_{MnO}} \qquad \text{(E- 90)}$$

Equation E-2 may be alternatively rearranged as:

$$\frac{a_{FeO}}{a_{MnO}}=\frac{K_{MnOFeO}a_{Fe}}{h_{Mn}} \qquad \text{(E- 3)}$$

Figure E-1 summarizes the activity correlations for FeO and MnO that were determined on the basis of equation E-3 for different temperatures using the cell model. Table E-1 presents a partial listing of FeO and MnO activities at 1550°C.

Table E-1: Partial listing of the cell model computed FeO and MnO activities at 1550°C.

$K_{FeO}*a_{Fe}$ / h_{Mn}	$\ln(K_{MnOFeO}*a_{Fe} / h_{Mn})$	X_{FeO}	a_{FeO}	a_{MnO}
0.133	-2.019	0.989	1	0.133
0.450	-0.798	0.887	0.818	0.368
0.694	-0.365	0.786	0.703	0.488
0.954	-0.047	0.685	0.614	0.585
1.257	0.229	0.585	0.540	0.678
1.632	0.490	0.485	0.475	0.775
2.122	0.752	0.385	0.415	0.880
2.813	1.034	0.285	0.356	1

FeO-SiO$_2$ Equilibria Reaction:

Consider the following equilibrium reaction at the inclusion-metal interface:

$$\begin{array}{r} [Si]+2[O]=(SiO_2) \\ 2(FeO)=2\{Fe\}+2[O] \\ \hline [Si]+2(FeO)=2\{Fe\}+(SiO_2) \end{array} \tag{E- 4}$$

The equilibrium constant for reaction E-4 may be expressed as:

$$K_{SiO_2FeO}=\frac{a_{Fe}{}^2 a_{SiO_2}}{h_{Si}a_{FeO}{}^2} \tag{E- 5}$$

Equation E-5 may be alternatively rearranged as:

$$\frac{a_{SiO_2}}{a_{FeO}{}^2}=\frac{K_{SiO_2FeO}h_{Si}}{a_{Fe}{}^2} \tag{E- 6}$$

Figure E-2 summarizes the activity correlations for FeO and SiO$_2$ that were determined on the basis of equation E-6 for different temperatures using the cell model. Table E-2 presents a partial listing of FeO and SiO$_2$ activities at 1550°C.

Table E-2: Partial listing of the cell model computed FeO and SiO$_2$ activities at 1550°C.

$K_{SiO2FeO}*h_{Si}/a_{Fe}{}^2$	$\ln(K_{SiO2FeO}*h_{Si}/a_{Fe}{}^2)$	X_{FeO}	a_{FeO}	a_{SiO2}
0.017	-4.069	0.966	1	0.017
0.223	-1.500	0.850	0.819	0.150
1.192	0.175	0.738	0.617	0.454
3.551	1.267	0.630	0.477	0.807
5.959	1.785	0.521	0.410	1

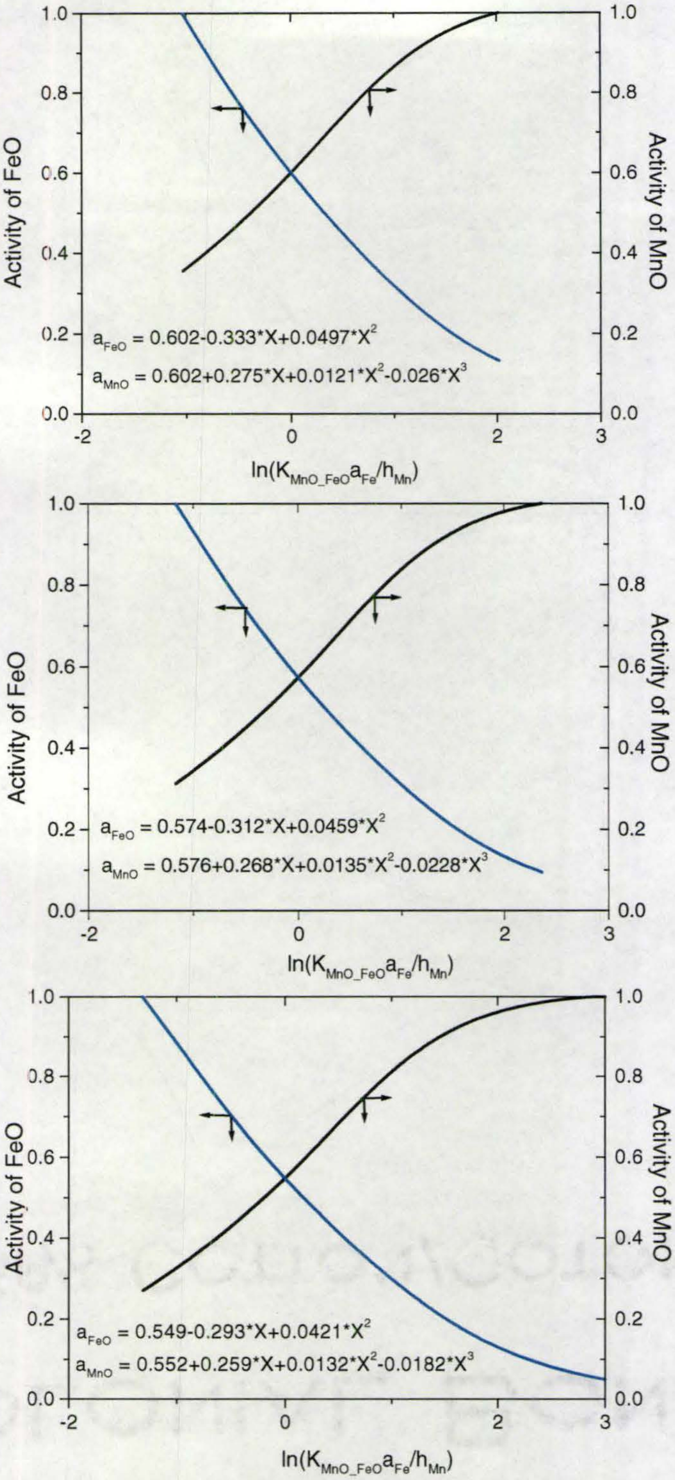

Figure E-1: Plots showing the variation in FeO and MnO activity as a function of $\ln(K_{MnOFeO}*a_{Fe}/h_{Mn})$ for different temperatures (top) 1550°C, (mid) 1600°C, (bottom) 1650°C.

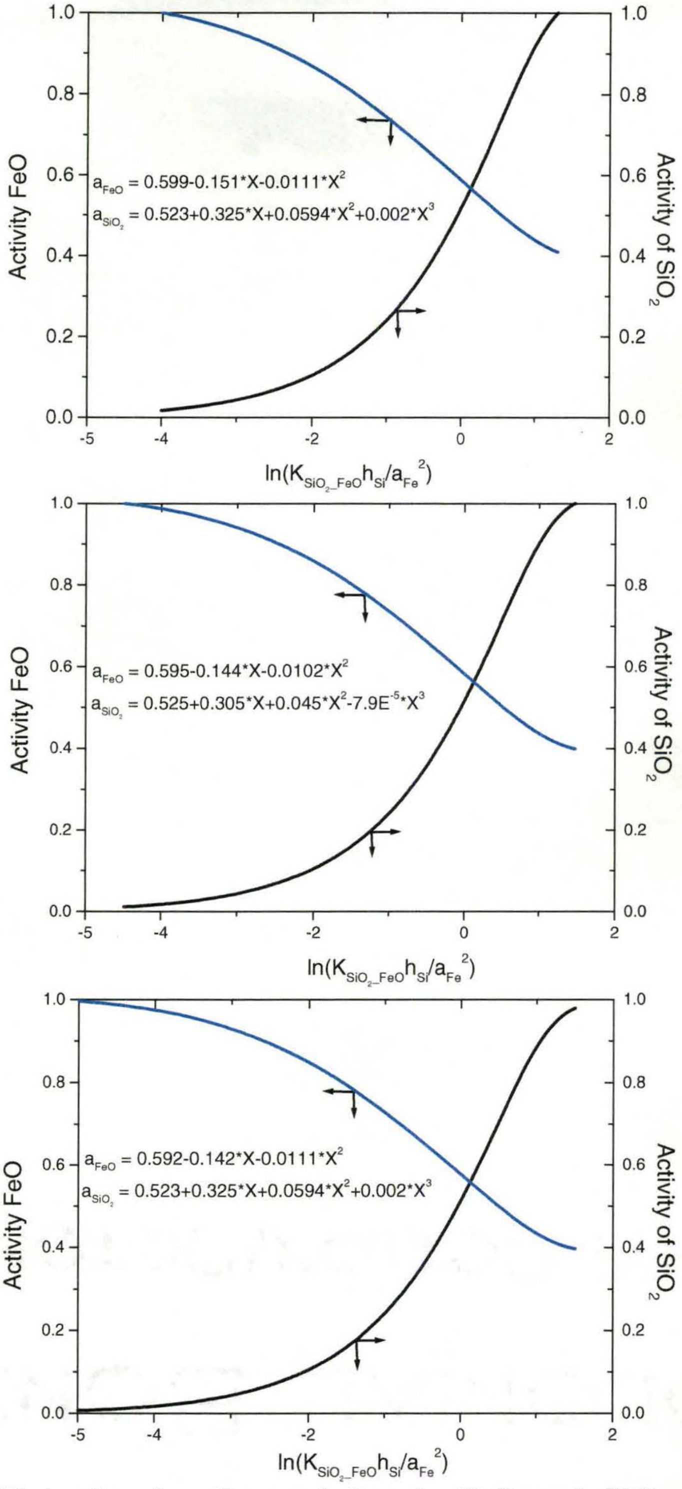

Figure E-2: Plots showing the variation in FeO and SiO_2 activity as a function of $\ln(K_{SiO2FeO} * h_{Si}/a_{Fe}^2)$ for different temperatures (top) 1550°C, (mid) 1600°C, (bottom) 1650°C.

MnO-SiO$_2$ Equilibria Reaction:

Consider the following equilibrium reaction at the inclusion-metal interface:

$$\begin{array}{l} [Si]+2[O]=(SiO_2) \\ \underline{\quad 2(MnO)=2[Mn]+2[O]} \\ [Si]+2(MnO)=2[Mn]+(SiO_2) \end{array} \qquad \text{(E- 7)}$$

The equilibrium constant for reaction E-7 may be expressed as:

$$K_{SiO_2MnO}=\frac{h_{Mn}{}^2 a_{SiO_2}}{h_{Si}a_{MnO}{}^2} \qquad \text{(E- 8)}$$

Equation E-8 may be alternatively rearranged as:

$$\frac{a_{SiO_2}}{a_{MnO}{}^2}=\frac{K_{SiO_2MnO}h_{Si}}{h_{Mn}{}^2} \qquad \text{(E- 9)}$$

Figure E-3 summarizes the activity correlations for MnO and SiO$_2$ that were determined on the basis of equation E-9 for different temperatures using the cell model. Table E-3 presents a partial listing of MnO and SiO$_2$ activities at 1550°C.

Table E-3: Partial listing of the cell model computed MnO and SiO$_2$ activities at 1550°C.

$K_{SiO2MnO}*h_{Si}/h_{Mn}{}^2$	$\ln(K_{SiO2MnO}*h_{Si}/h_{Mn}{}^2)$	X_{MnO}	a_{MnO}	a_{SiO2}
0.018719	-3.97822	0.78754	1	0.018719
0.47509	-0.74425	0.67893	0.5045	0.12092
0.095492	-2.34872	0.57398	0.21891	0.50184
0.017528	-4.04396	0.47252	0.12731	0.92469
0.013407	-4.31195	0.44471	0.11579	1

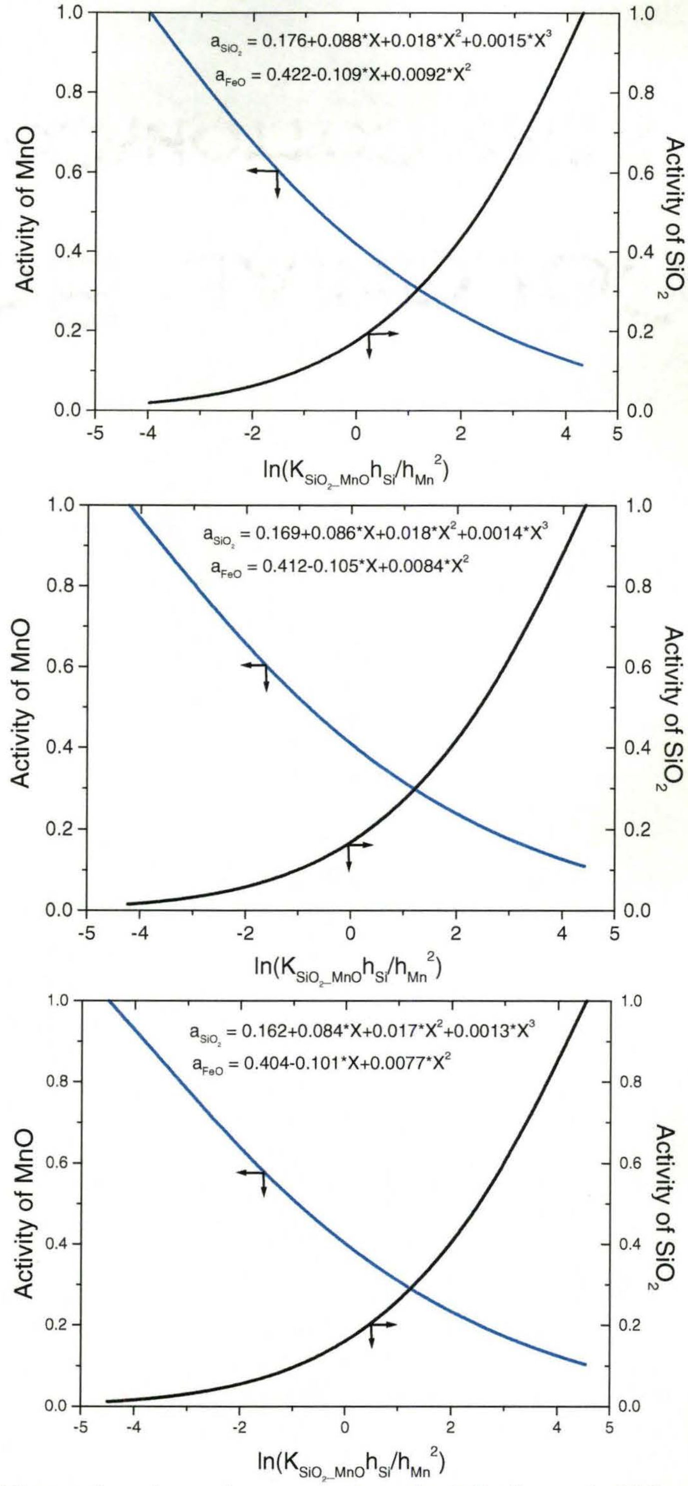

Figure E-3: Plots showing the variation in MnO and SiO$_2$ activity as a function of $\ln(K_{SiO2MnO}*h_{Si}/h_{Mn}^2)$ for different temperatures (top) 1550°C, (mid) 1600°C, (bottom) 1650°C.

Appendix F

LMF SAMPLING & MODELLING RESULTS

The following section summarizes the sampling methodology, experimental and simulated results for all 41 heats sampled during the industrial trials at ArcelorMittal Dofasco. Predicted results were simulated using the coupled multi-component kinetic model outlined in Chapter 4 in combination with the unified interaction parameter formalism and cell model summarized in Chapter 3. Steel and slag compositions were initialized using the chemical analysis measurement results taken after deoxidation. Metal phase mass transfer coefficients for all elements in steel were assumed to follow the empirical relation given in Figure 4-31, while slag phase mass transfer coefficients were calculated by fitting the ratio of $k_m^M \ / \ k_{sl}^{M_xO_y}$ to the experimental results.

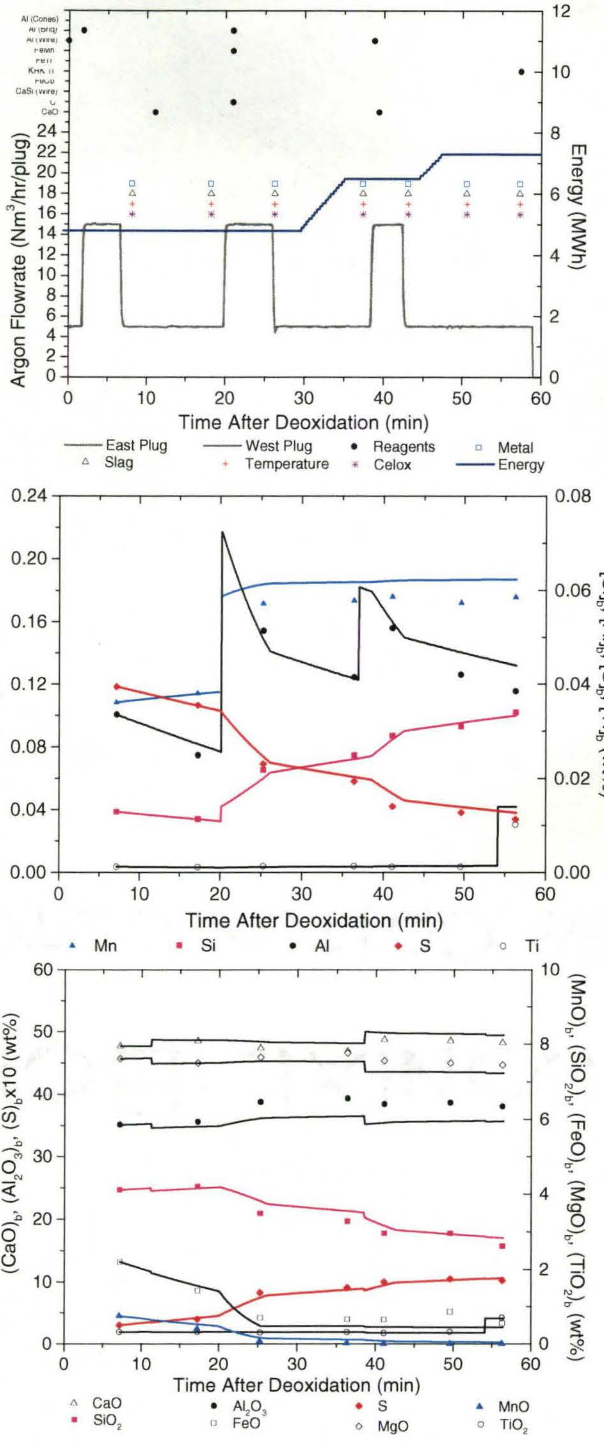

Figure F-1: (top) Heat 1 stirring, heating, and sampling procedure. Comparison of experimental and model predicted results for Heat 1 using fitted slag phase mass transfer coefficients. (middle) Steel concentration profile, (bottom) slag concentration profile.

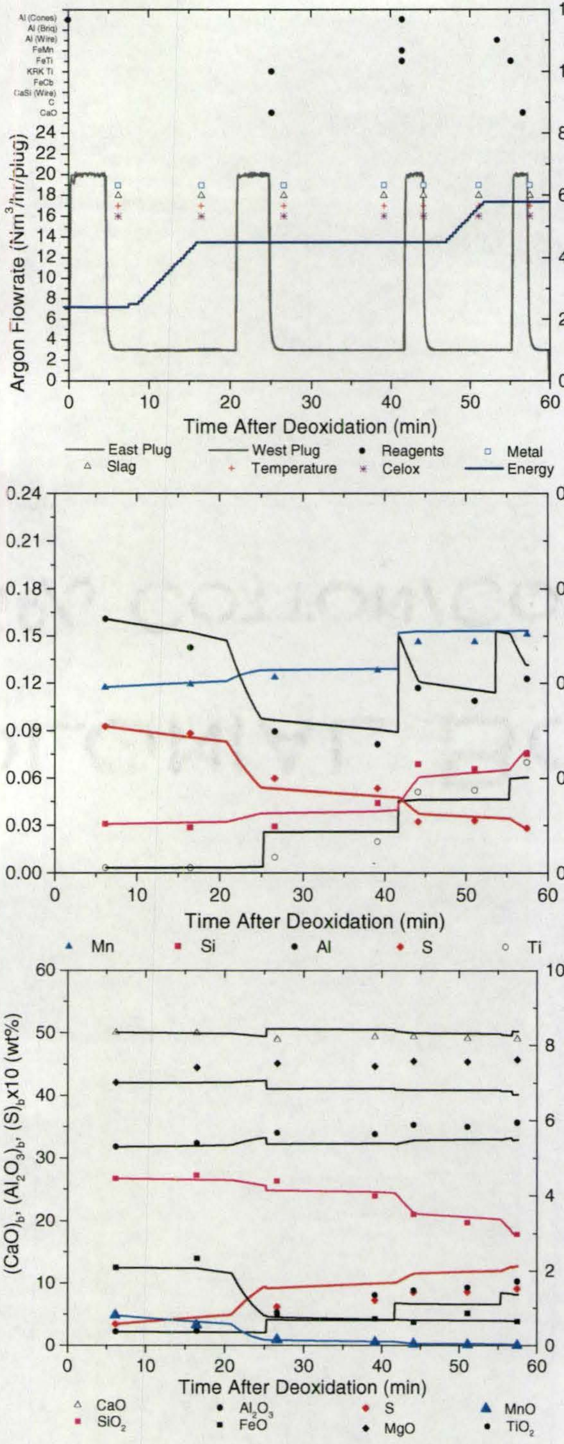

Figure F-2: Heat 2 stirring, heating, and sampling procedure. Comparison of experimental and model predicted results for Heat 2 using fitted slag phase mass transfer coefficients. (middle) Steel concentration profile, (bottom) slag concentration profile.

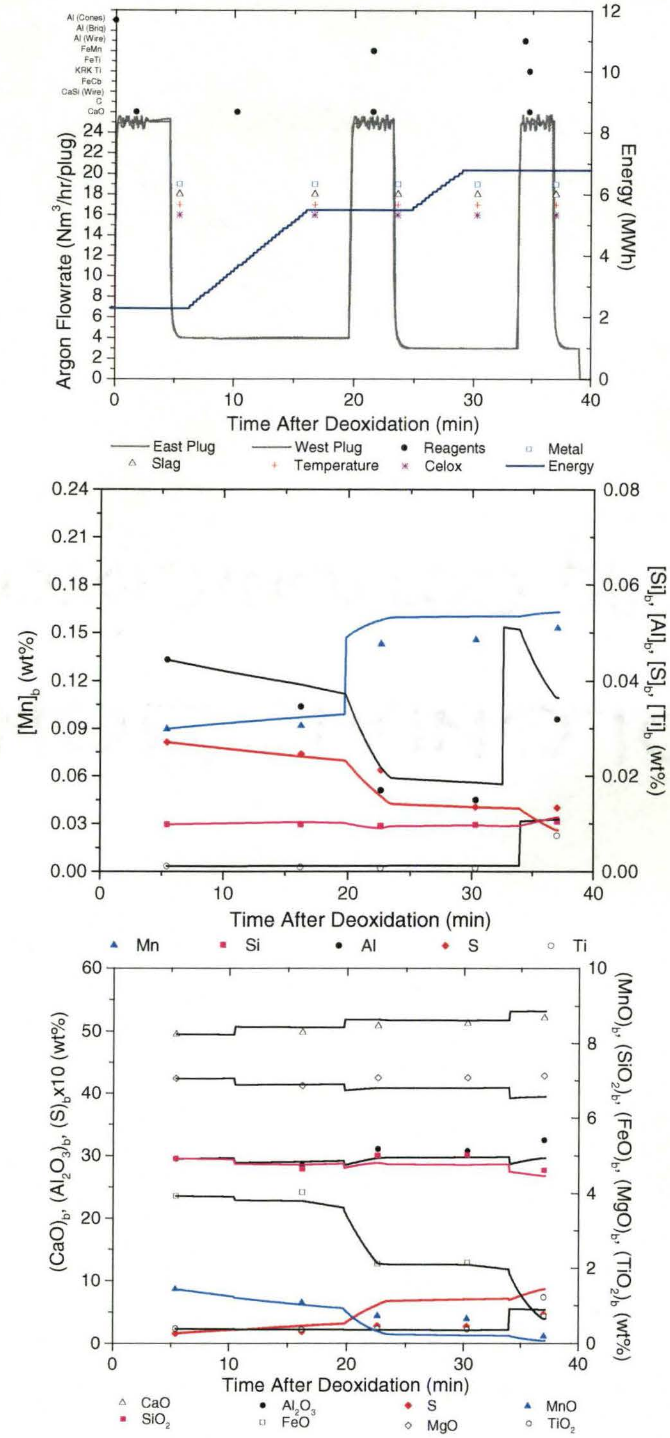

Figure F-3: Heat 3 stirring, heating, and sampling procedure. Comparison of experimental and model predicted results for Heat 3 using fitted slag phase mass transfer coefficients. (middle) Steel concentration profile, (bottom) slag concentration profile.

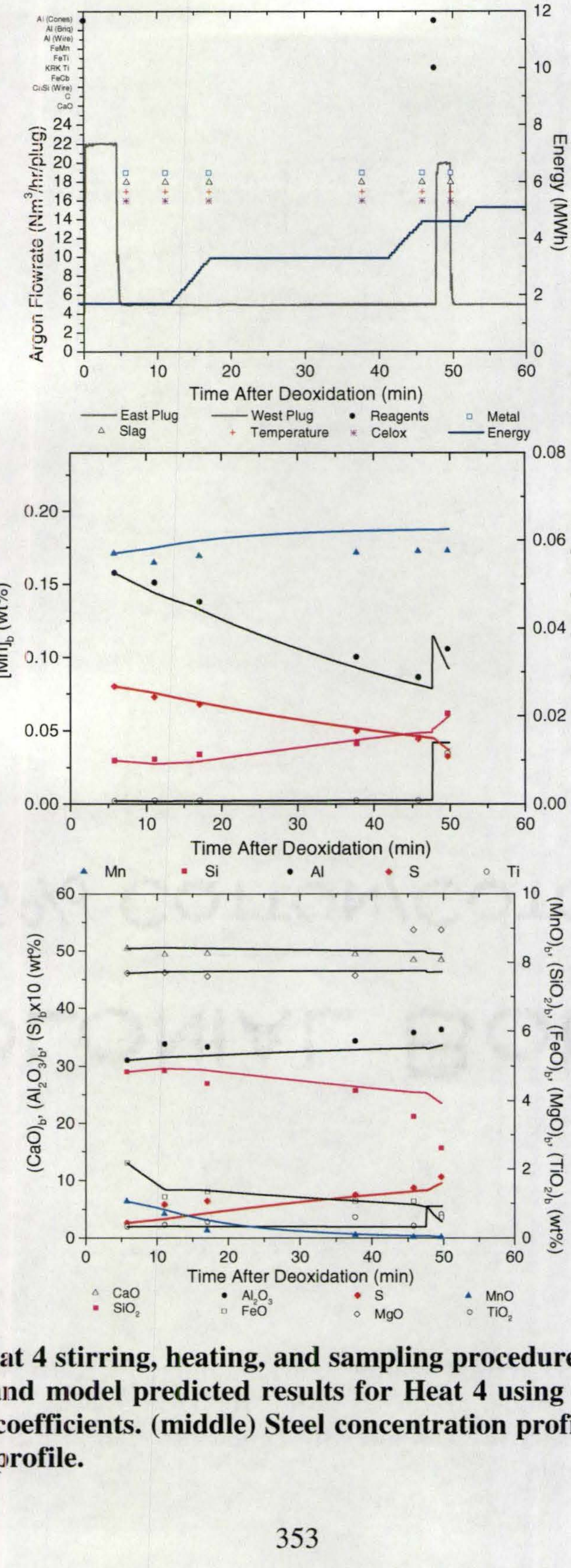

Figure F-4: Heat 4 stirring, heating, and sampling procedure. Comparison of experimental and model predicted results for Heat 4 using fitted slag phase mass transfer coefficients. (middle) Steel concentration profile, (bottom) slag concentration profile.

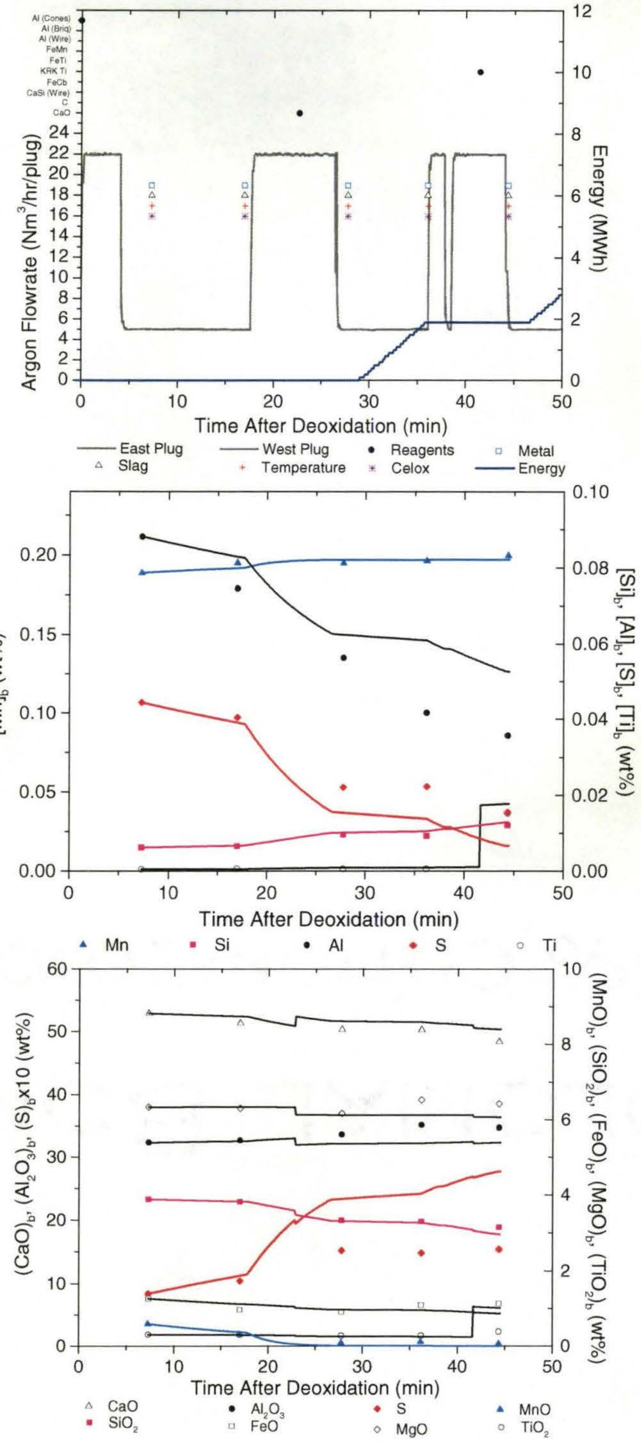

Figure F-5: Heat 5 stirring, heating, and sampling procedure. Comparison of experimental and model predicted results for Heat 5 using fitted slag phase mass transfer coefficients. (middle) Steel concentration profile, (bottom) slag concentration profile.

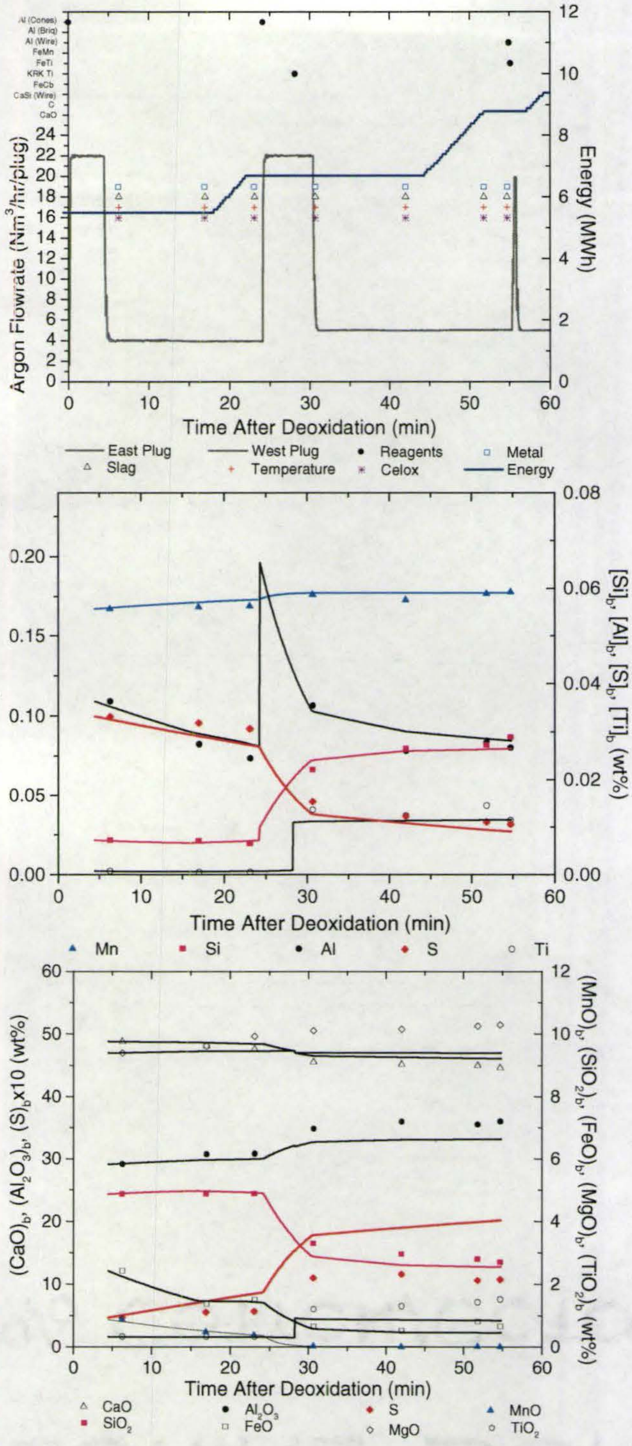

Figure F-6: Heat 6 stirring, heating, and sampling procedure. Comparison of experimental and model predicted results for Heat 6 using fitted slag phase mass transfer coefficients. (middle) Steel concentration profile, (bottom) slag concentration profile.

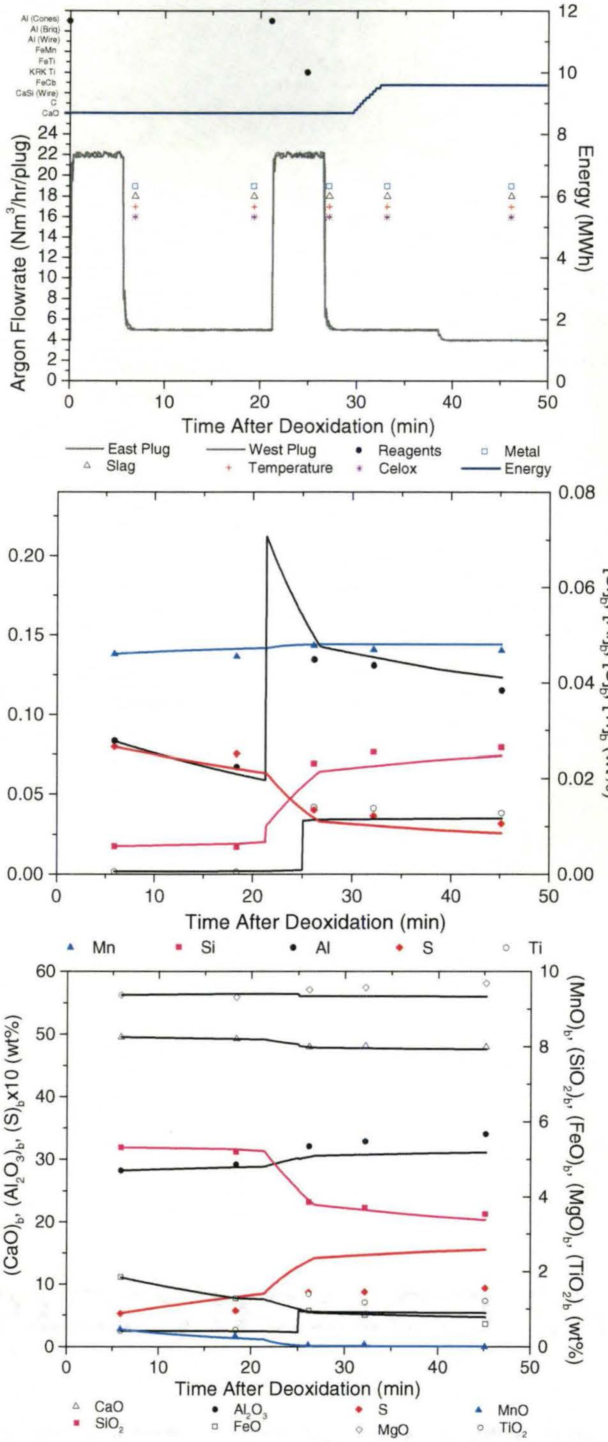

Figure F-7: Heat 7 stirring, heating, and sampling procedure. Comparison of experimental and model predicted results for Heat 7 using fitted slag phase mass transfer coefficients. (middle) Steel concentration profile, (bottom) slag concentration profile.

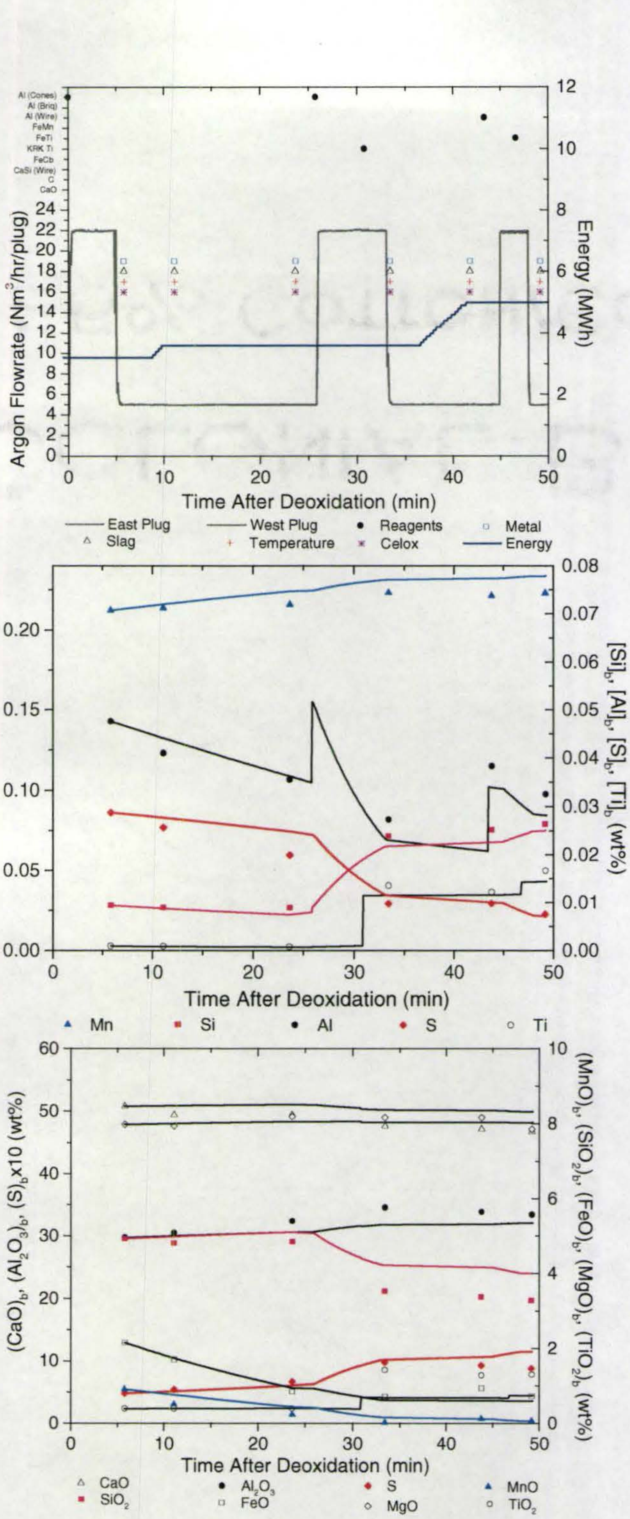

Figure F-8: Heat 8 stirring, heating, and sampling procedure. Comparison of experimental and model predicted results for Heat 8 using fitted slag phase mass transfer coefficients. (middle) Steel concentration profile, (bottom) slag concentration profile.

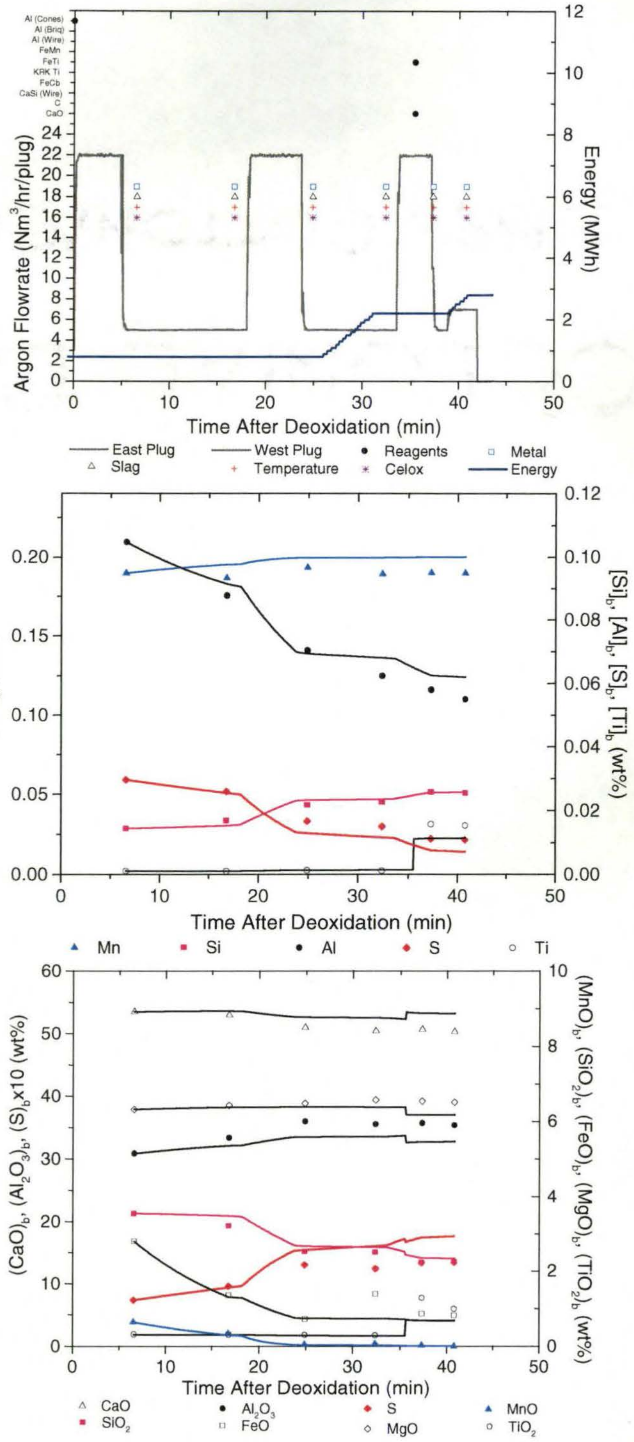

Figure F-9: Heat 9 stirring, heating, and sampling procedure. Comparison of experimental and model predicted results for Heat 9 using fitted slag phase mass transfer coefficients. (middle) Steel concentration profile, (bottom) slag concentration profile.

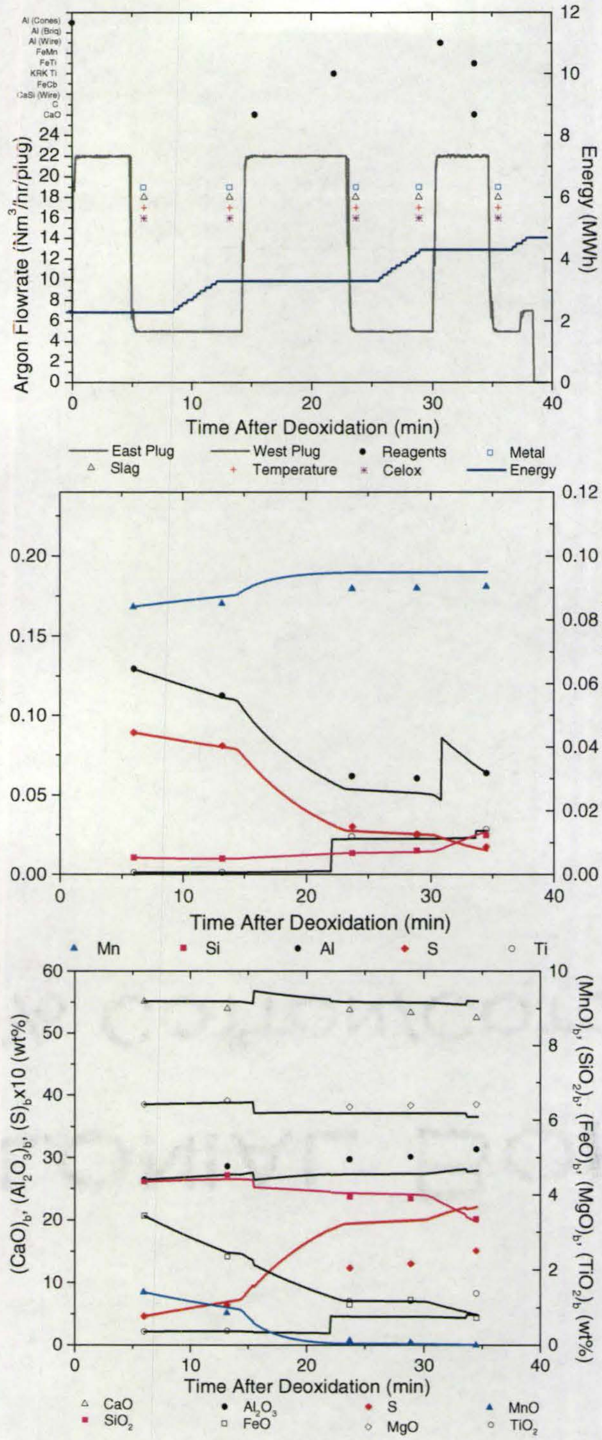

Figure F-10: Heat 10 stirring, heating, and sampling procedure. Comparison of experimental and model predicted results for Heat 10 using fitted slag phase mass transfer coefficients. (middle) Steel concentration profile, (bottom) slag concentration profile.

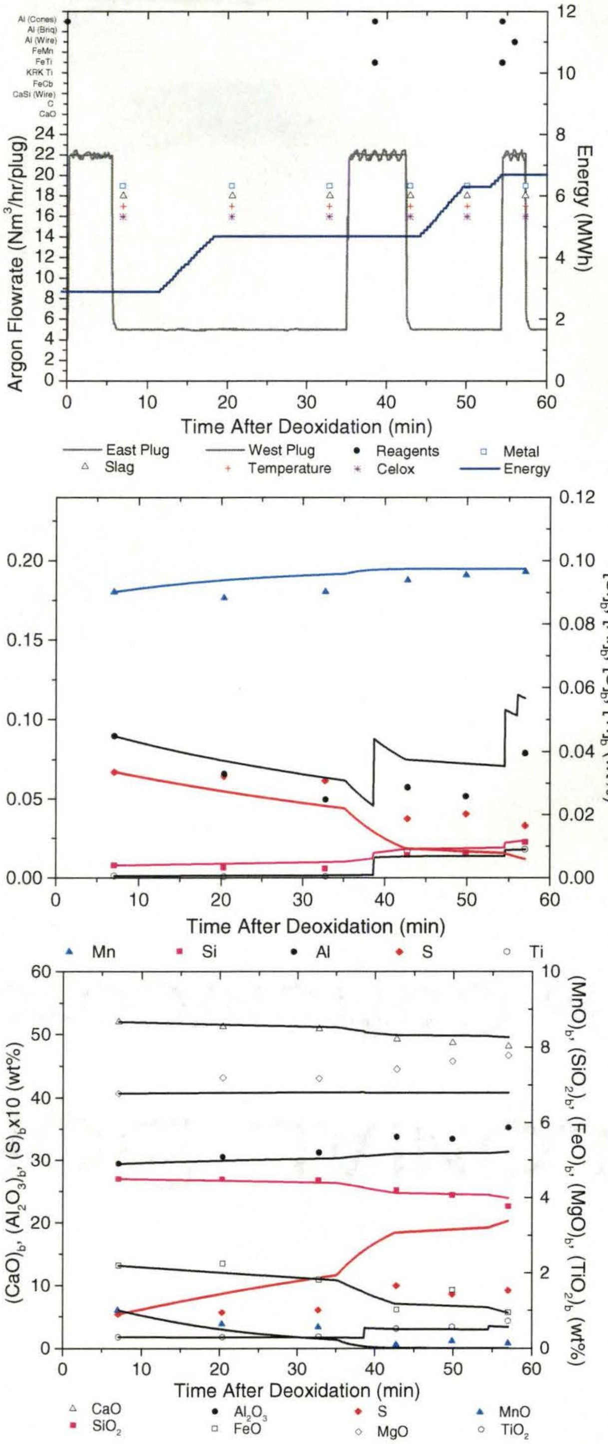

Figure F-11: Heat 11 stirring, heating, and sampling procedure. Comparison of experimental and model predicted results for Heat 11 using fitted slag phase mass transfer coefficients. (middle) Steel concentration profile, (bottom) slag concentration profile.

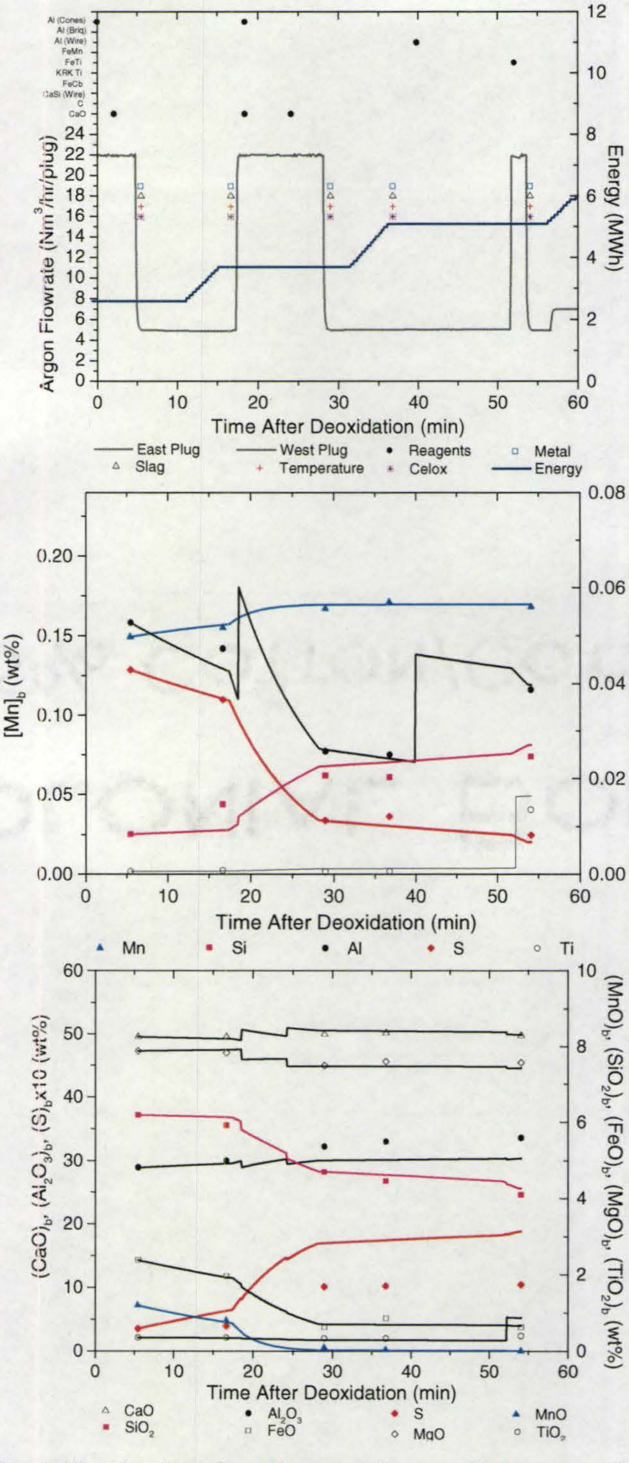

Figure F-12: Heat 12 stirring, heating, and sampling procedure. Comparison of experimental and model predicted results for Heat 12 using fitted slag phase mass transfer coefficients. (middle) Steel concentration profile, (bottom) slag concentration profile.

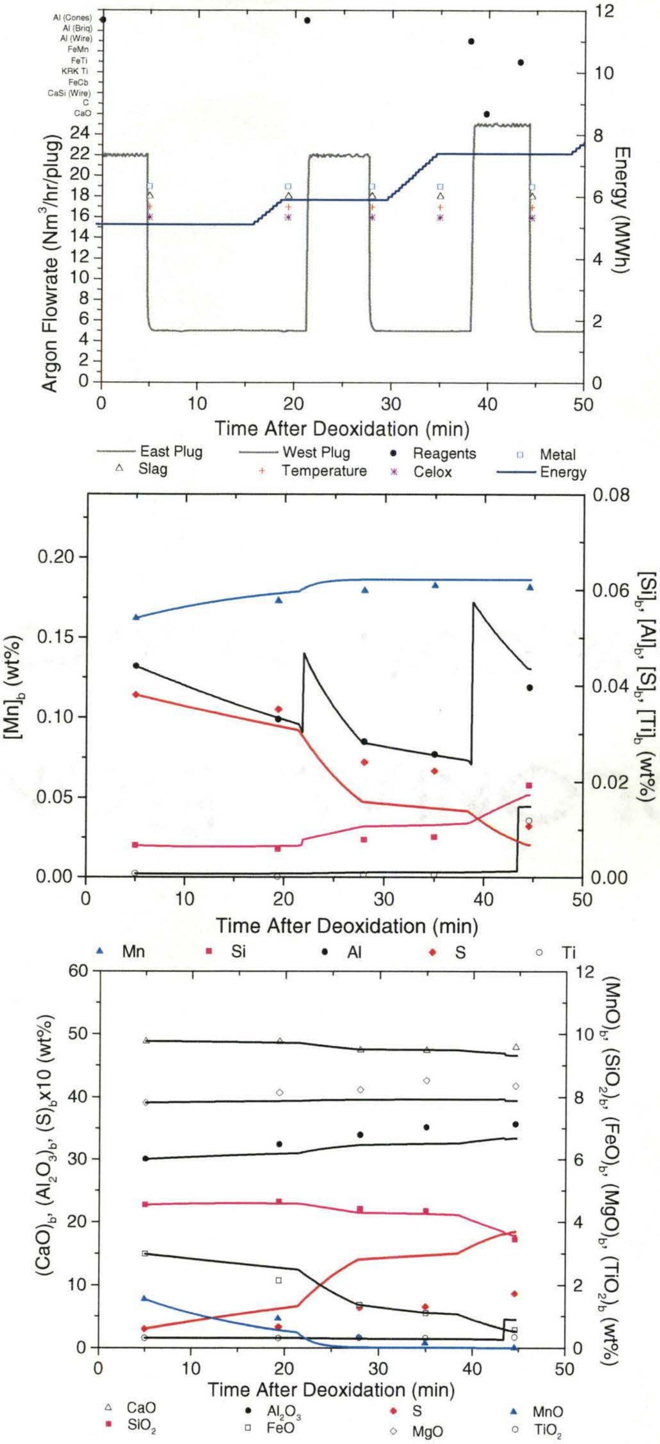

Figure F-13: Heat 13 stirring, heating, and sampling procedure. Comparison of experimental and model predicted results for Heat 13 using fitted slag phase mass transfer coefficients. (middle) Steel concentration profile, (bottom) slag concentration profile.

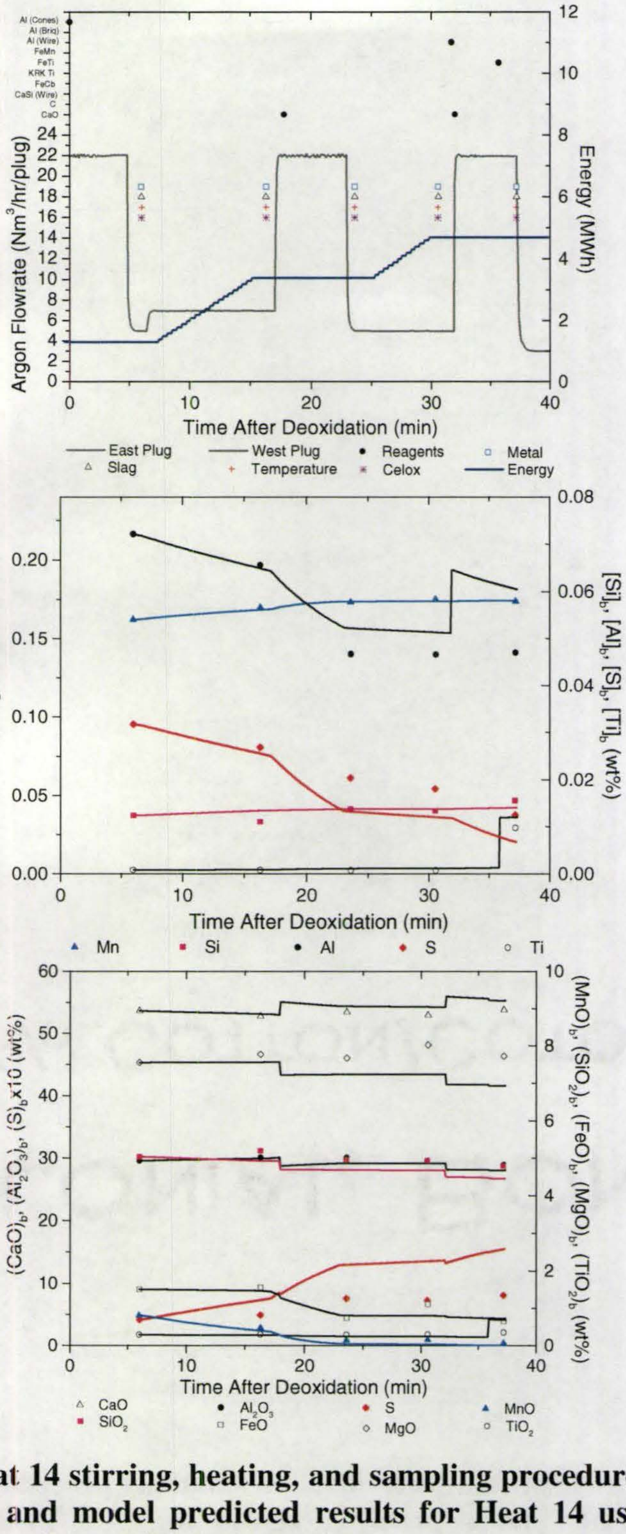

Figure F-14: Heat 14 stirring, heating, and sampling procedure. Comparison of experimental and model predicted results for Heat 14 using fitted slag phase mass transfer coefficients. (middle) Steel concentration profile, (bottom) slag concentration profile.

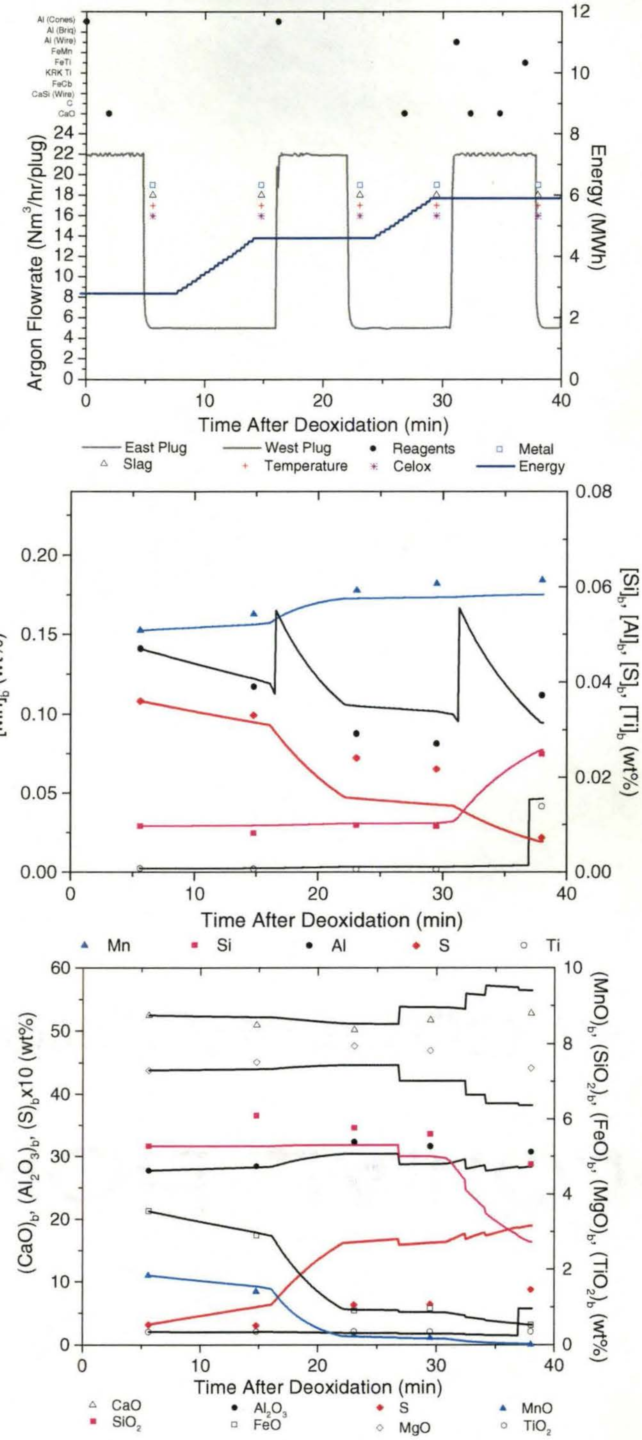

Figure F-15: Heat 15 stirring, heating, and sampling procedure. Comparison of experimental and model predicted results for Heat 15 using fitted slag phase mass transfer coefficients. (middle) Steel concentration profile, (bottom) slag concentration profile.

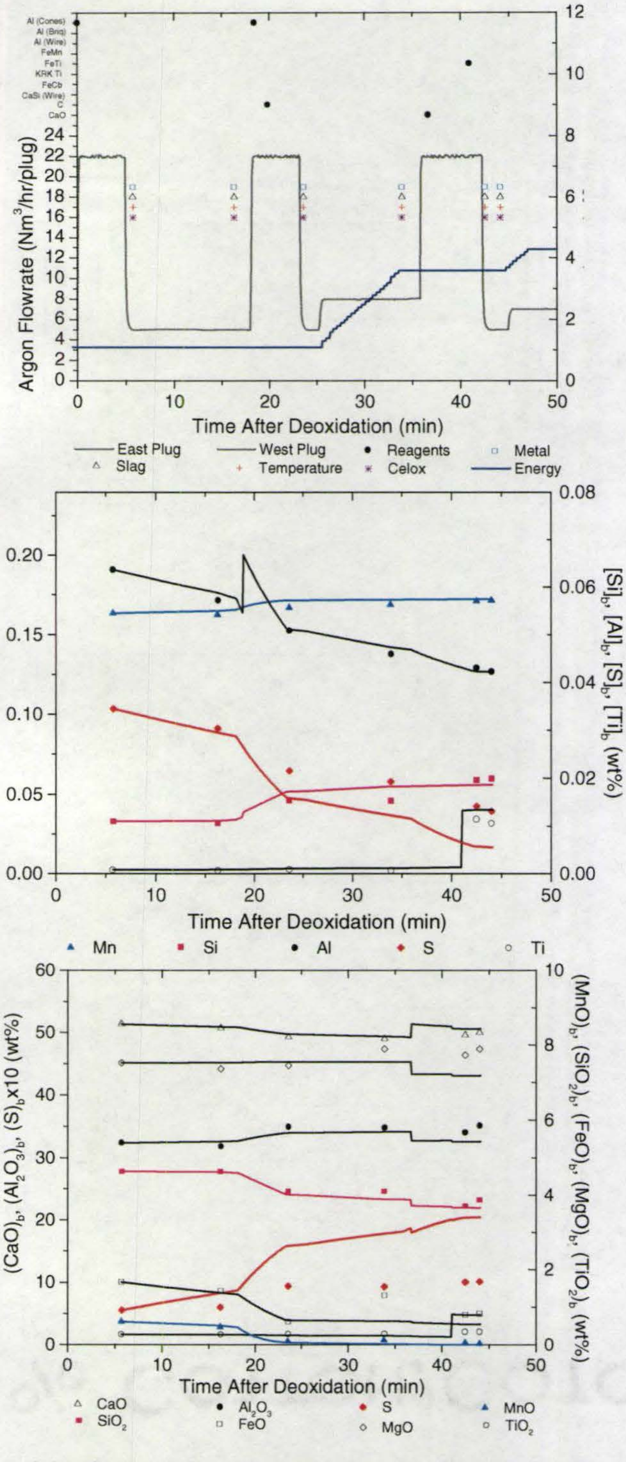

Figure F-16: Heat 16 stirring, heating, and sampling procedure. Comparison of experimental and model predicted results for Heat 16 using fitted slag phase mass transfer coefficients. (middle) Steel concentration profile, (bottom) slag concentration profile.

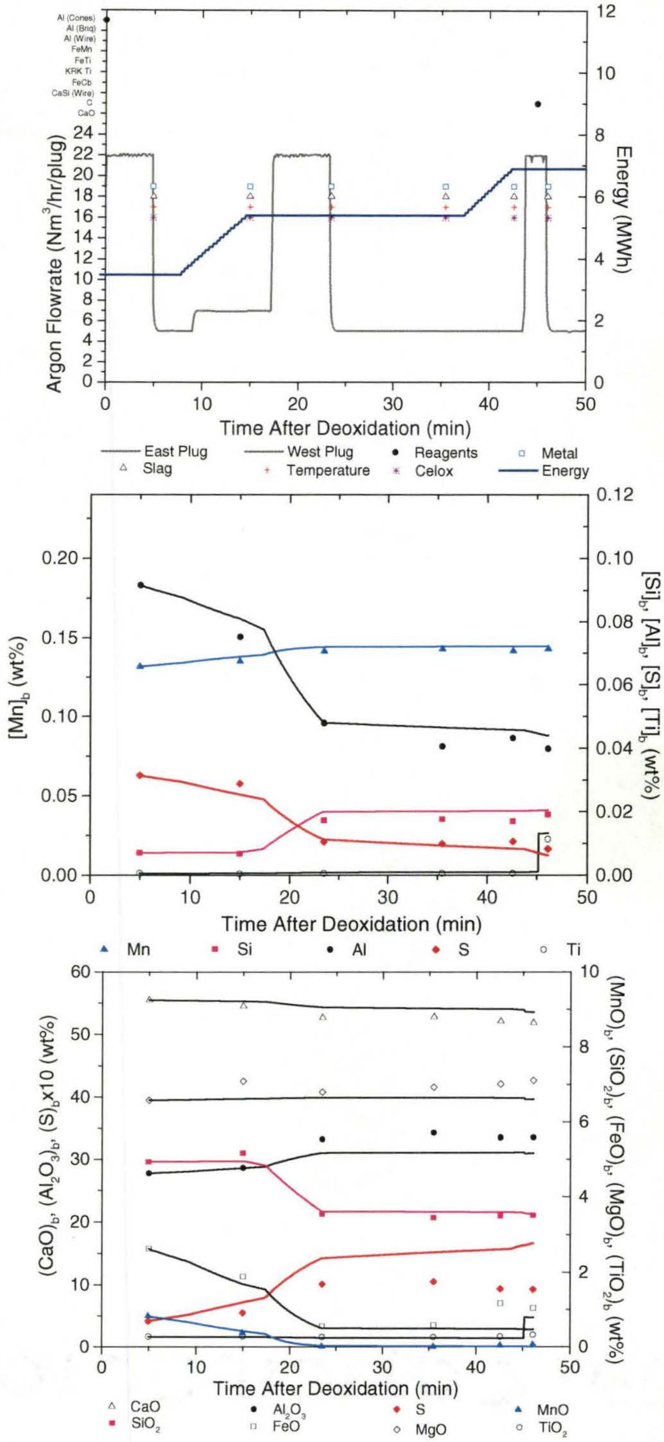

Figure F-17: Heat 17 stirring, heating, and sampling procedure. Comparison of experimental and model predicted results for Heat 17 using fitted slag phase mass transfer coefficients. (middle) Steel concentration profile, (bottom) slag concentration profile.

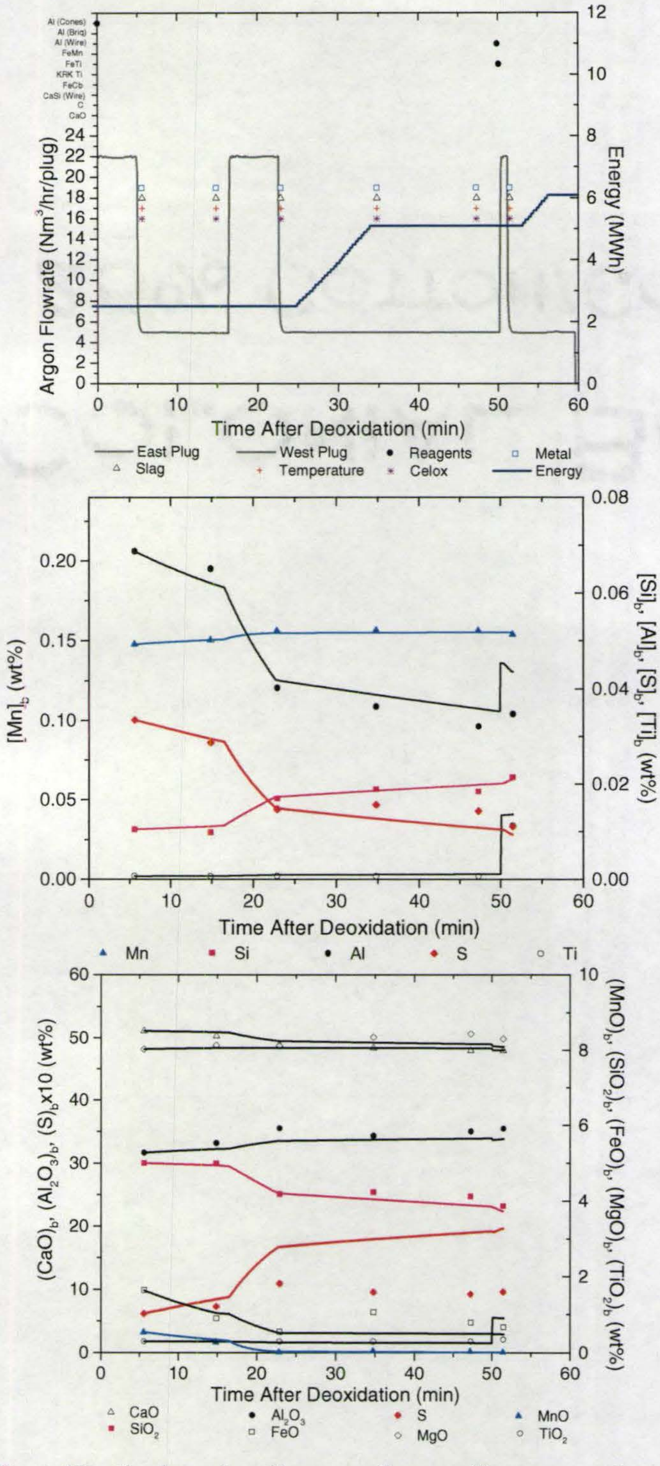

Figure F-18: Heat 18 stirring, heating, and sampling procedure. Comparison of experimental and model predicted results for Heat 18 using fitted slag phase mass transfer coefficients. (middle) Steel concentration profile, (bottom) slag concentration profile.

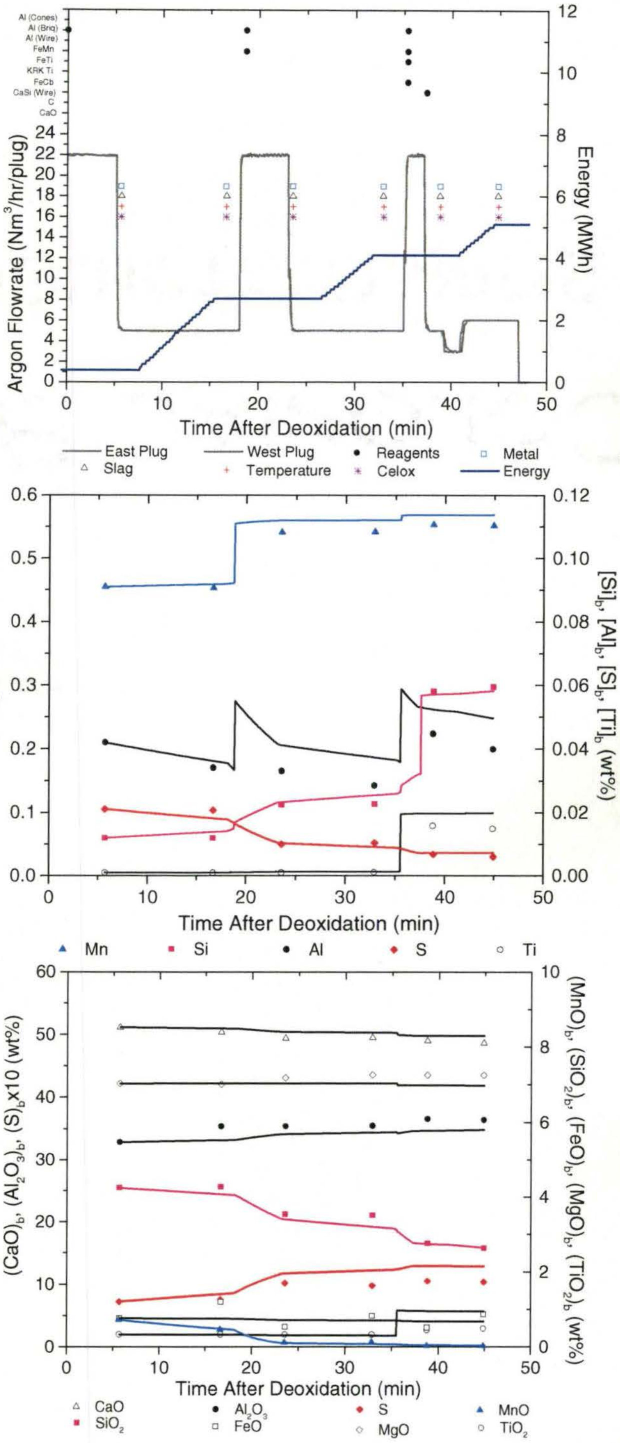

Figure F-19: Heat 19 stirring, heating, and sampling procedure. Comparison of experimental and model predicted results for Heat 19 using fitted slag phase mass transfer coefficients. (middle) Steel concentration profile, (bottom) slag concentration profile.

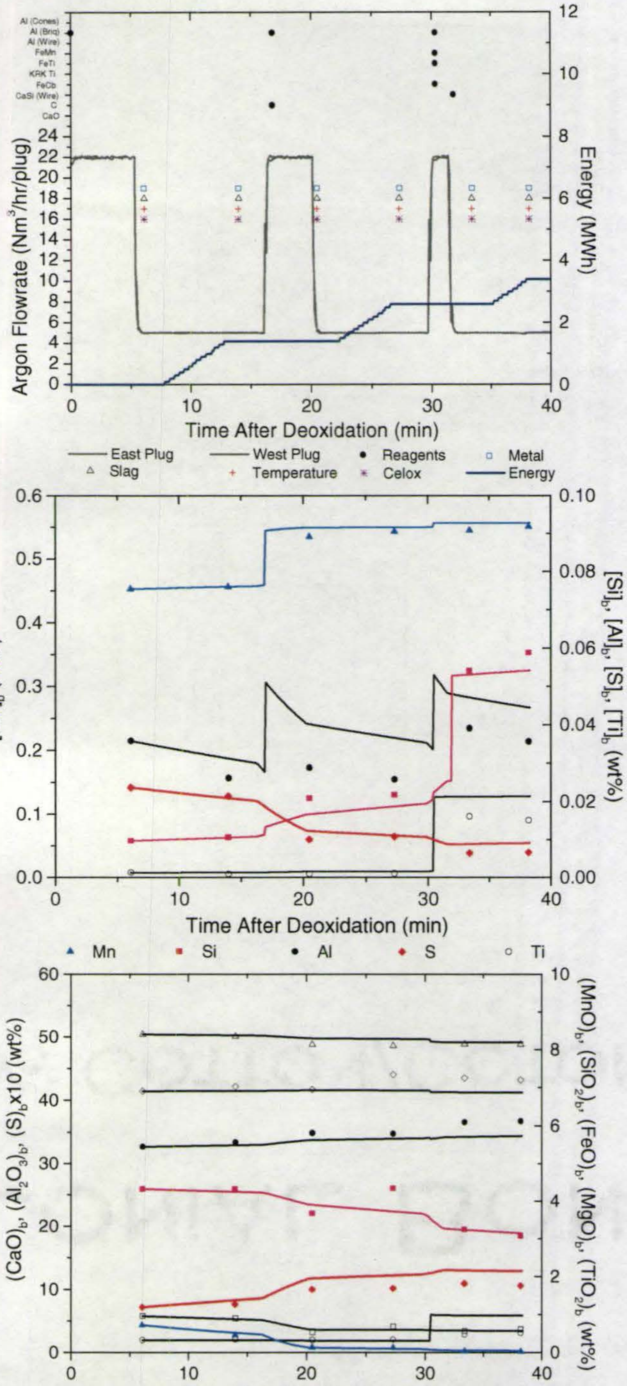

Figure F-20: Heat 20 stirring, heating, and sampling procedure. Comparison of experimental and model predicted results for Heat 20 using fitted slag phase mass transfer coefficients. (middle) Steel concentration profile, (bottom) slag concentration profile.

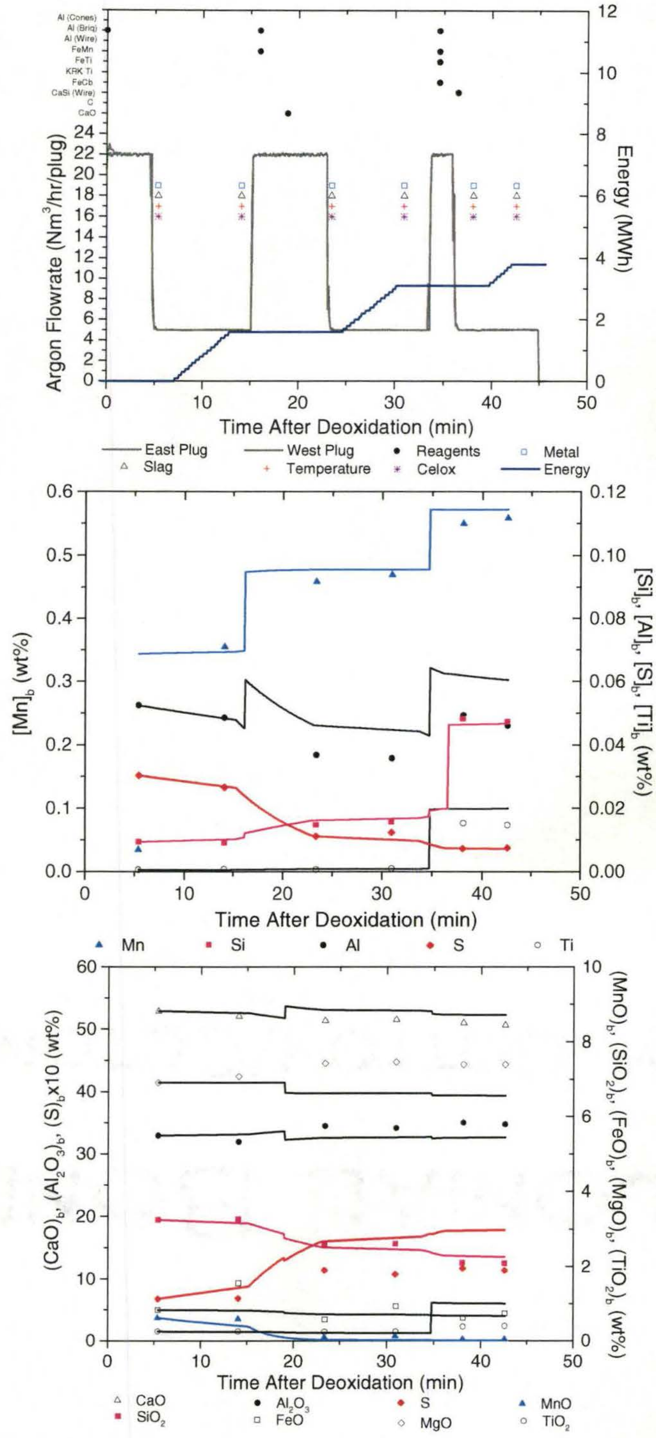

Figure F-21: Heat 21 stirring, heating, and sampling procedure. Comparison of experimental and model predicted results for Heat 21 using fitted slag phase mass transfer coefficients. (middle) Steel concentration profile, (bottom) slag concentration profile.

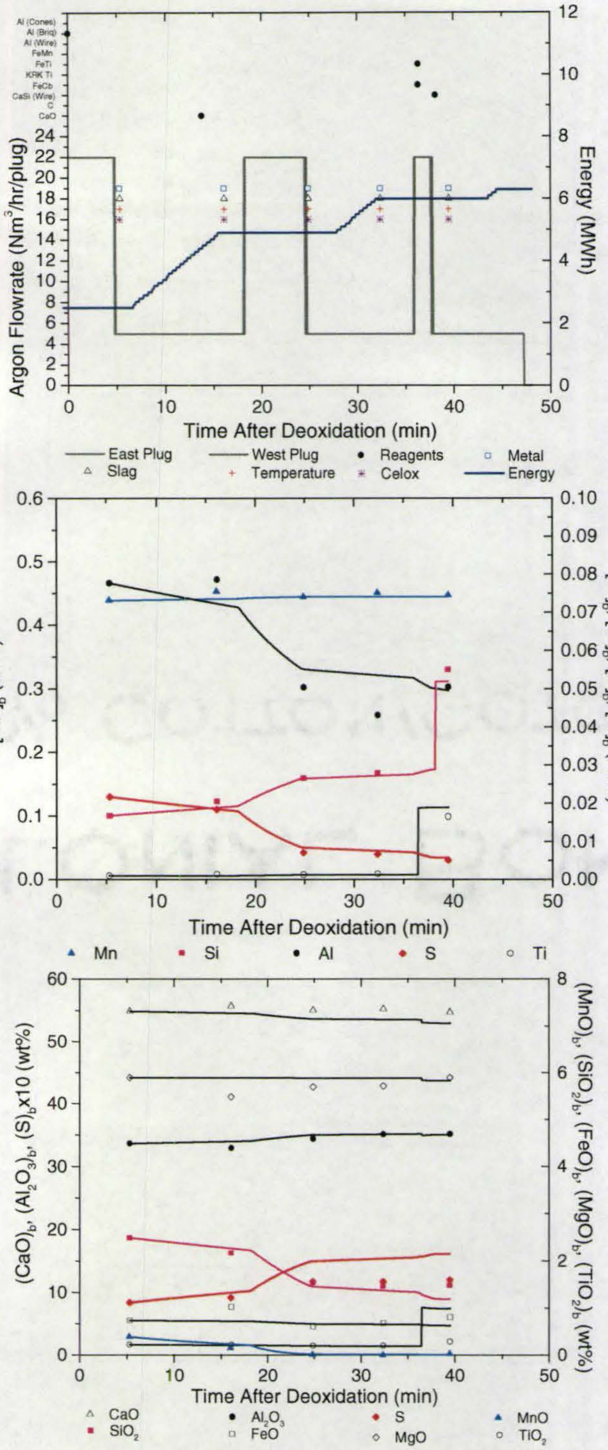

Figure F-22: Heat 22 stirring, heating, and sampling procedure. Comparison of experimental and model predicted results for Heat 22 using fitted slag phase mass transfer coefficients. (middle) Steel concentration profile, (bottom) slag concentration profile.

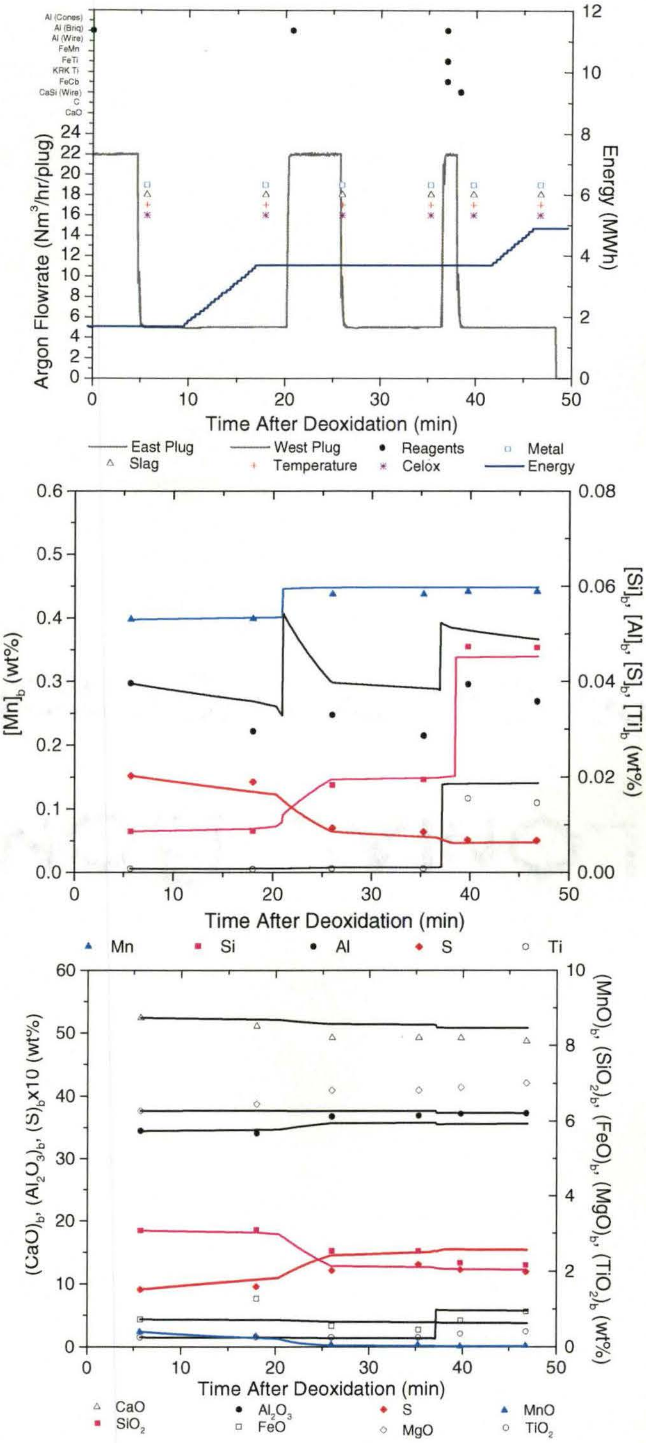

Figure F-23: Heat 23 stirring, heating, and sampling procedure. Comparison of experimental and model predicted results for Heat 23 using fitted slag phase mass transfer coefficients. (middle) Steel concentration profile, (bottom) slag concentration profile.

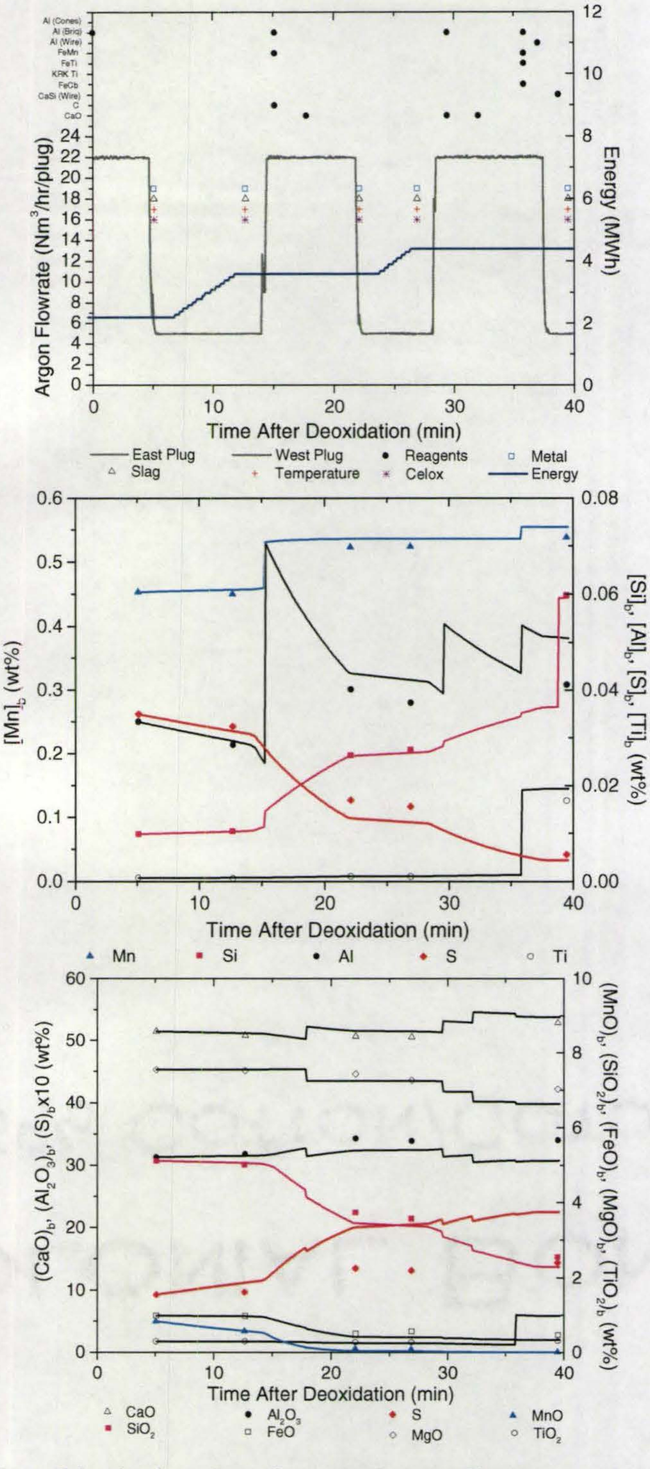

Figure F-24: Heat 24 stirring, heating, and sampling procedure. Comparison of experimental and model predicted results for Heat 24 using fitted slag phase mass transfer coefficients. (middle) Steel concentration profile, (bottom) slag concentration profile.

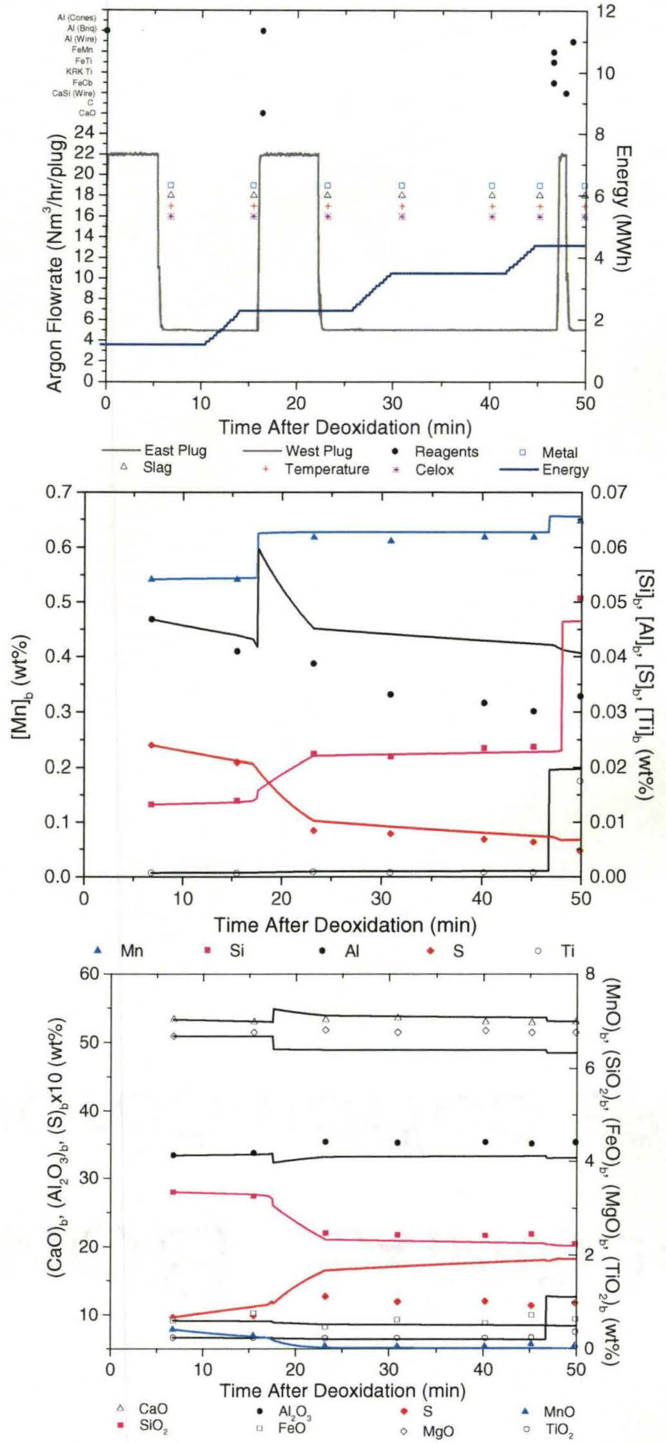

Figure F-25: Heat 25 stirring, heating, and sampling procedure. Comparison of experimental and model predicted results for Heat 25 using fitted slag phase mass transfer coefficients. (middle) Steel concentration profile, (bottom) slag concentration profile.

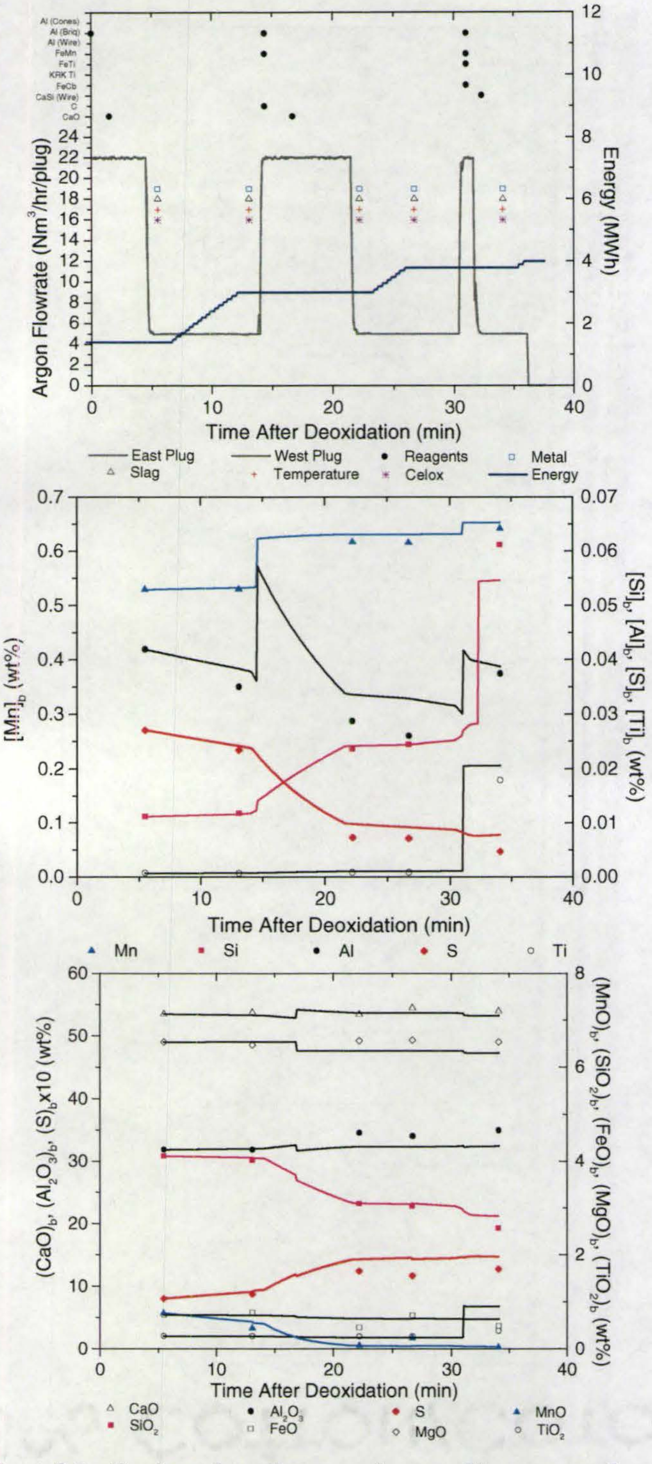

Figure F-26: Heat 26 stirring, heating, and sampling procedure. Comparison of experimental and model predicted results for Heat 26 using fitted slag phase mass transfer coefficients. (middle) Steel concentration profile, (bottom) slag concentration profile.

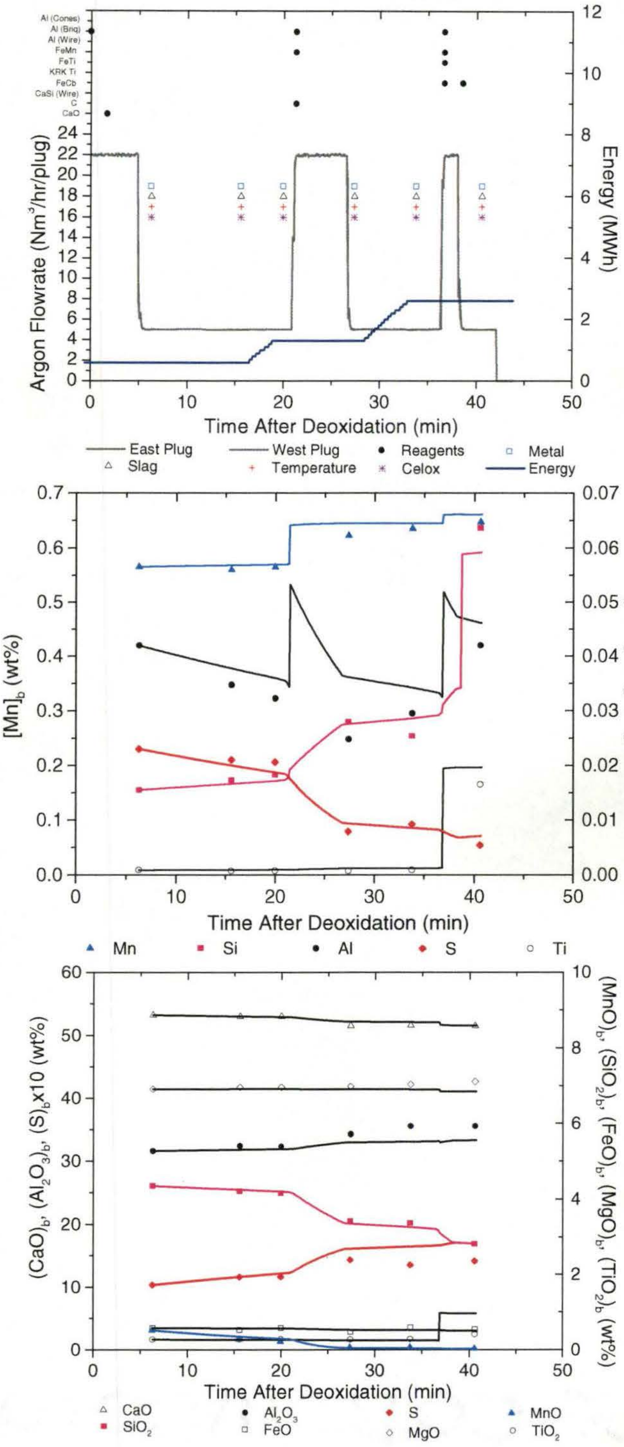

Figure F-27: Heat 27 stirring, heating, and sampling procedure. Comparison of experimental and model predicted results for Heat 27 using fitted slag phase mass transfer coefficients. (middle) Steel concentration profile, (bottom) slag concentration profile.

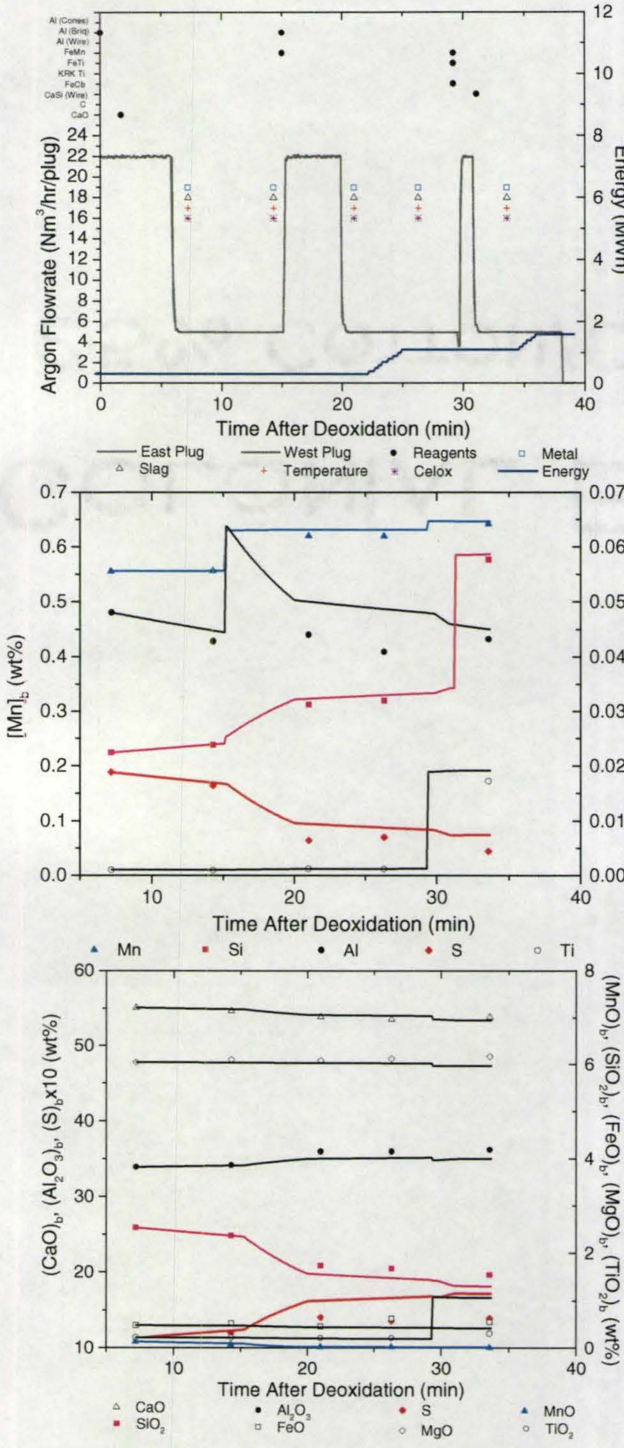

Figure F-28: Heat 28 stirring, heating, and sampling procedure. Comparison of experimental and model predicted results for Heat 28 using fitted slag phase mass transfer coefficients. (middle) Steel concentration profile, (bottom) slag concentration profile.

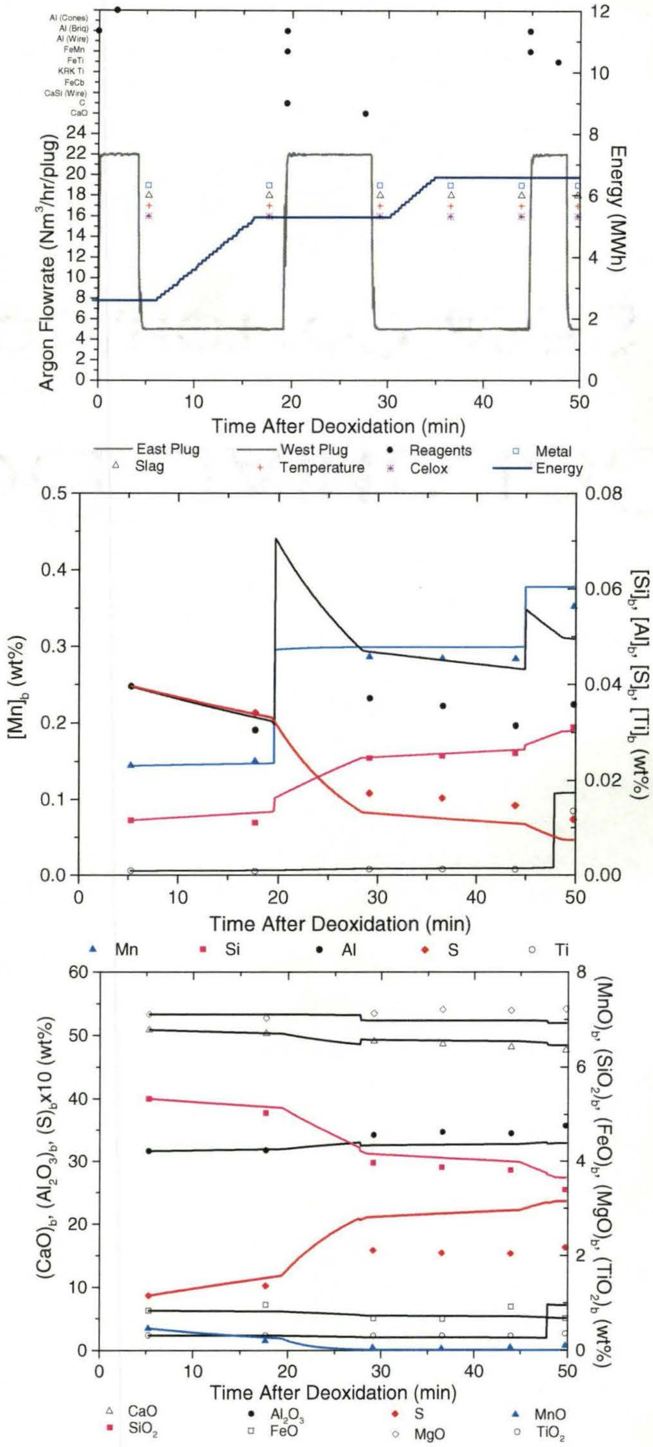

Figure F-29: Heat 29 stirring, heating, and sampling procedure. Comparison of experimental and model predicted results for Heat 29 using fitted slag phase mass transfer coefficients. (middle) Steel concentration profile, (bottom) slag concentration profile.

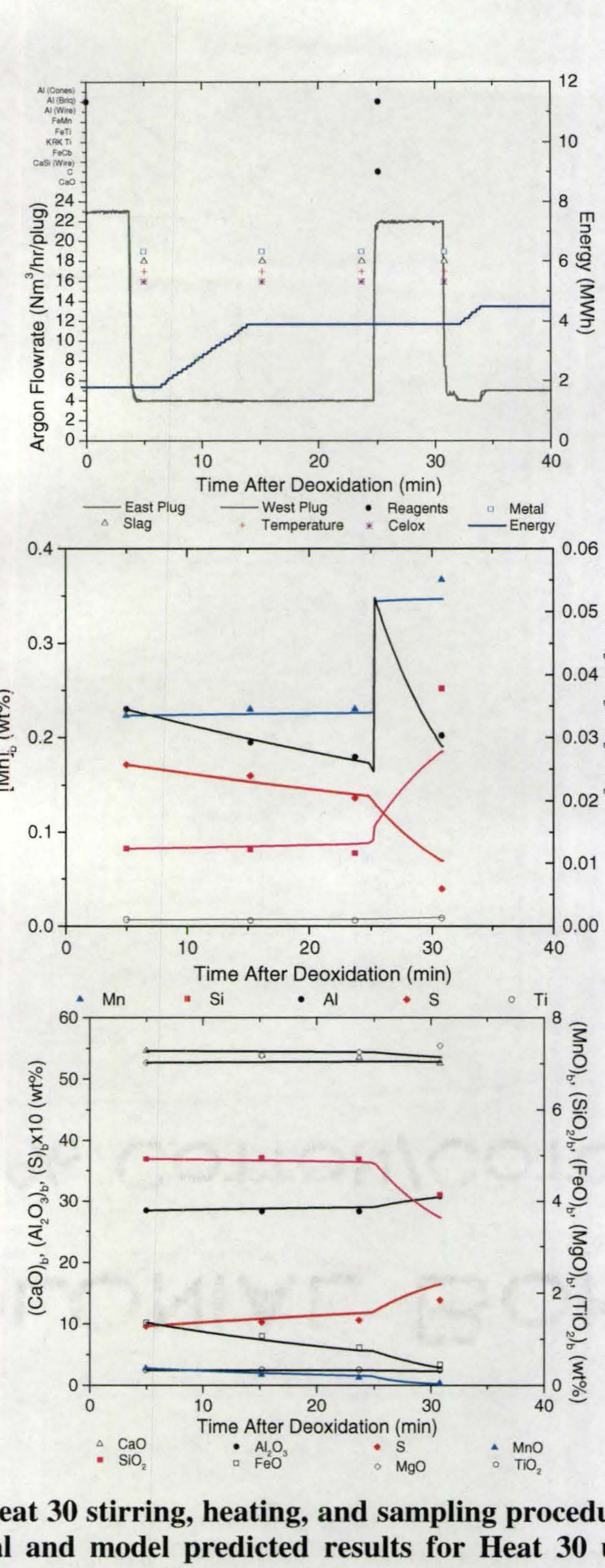

Figure F-30: Heat 30 stirring, heating, and sampling procedure. Comparison of experimental and model predicted results for Heat 30 using fitted slag phase mass transfer coefficients. (middle) Steel concentration profile, (bottom) slag concentration profile.

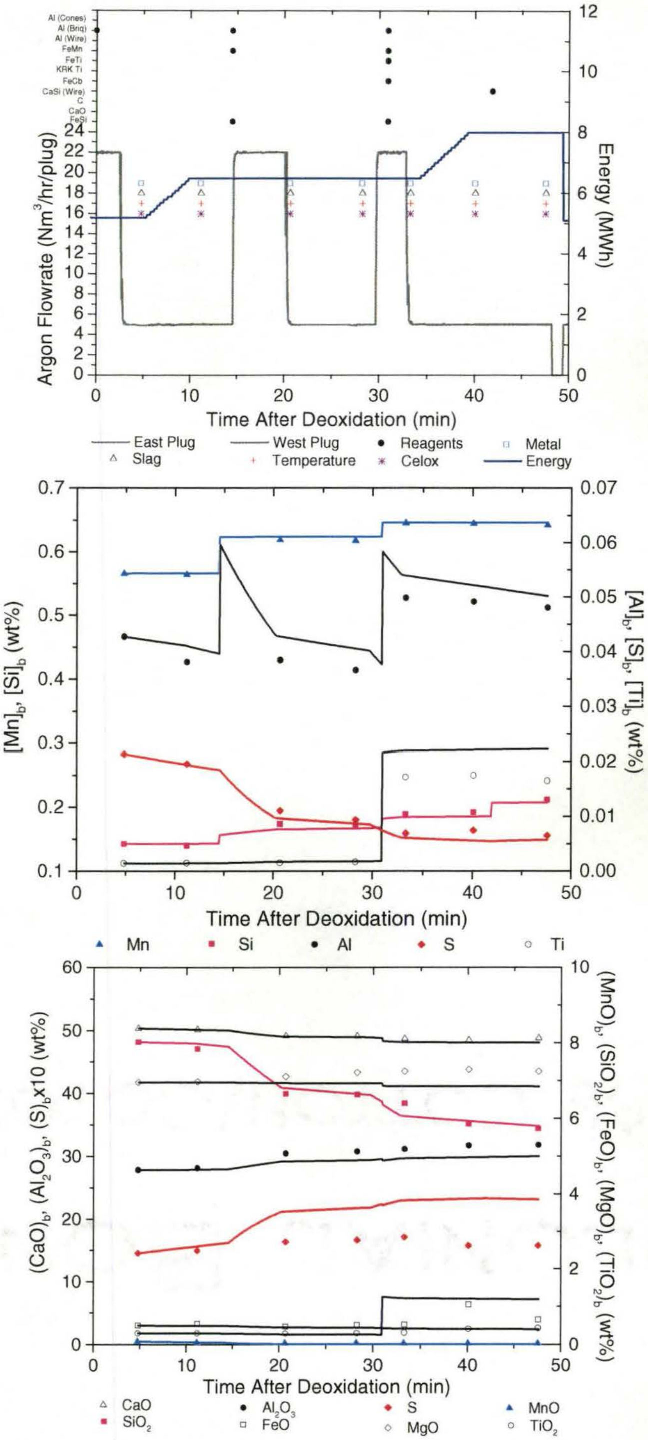

Figure F-31: Heat 31 stirring, heating, and sampling procedure. Comparison of experimental and model predicted results for Heat 31 using fitted slag phase mass transfer coefficients. (middle) Steel concentration profile, (bottom) slag concentration profile.

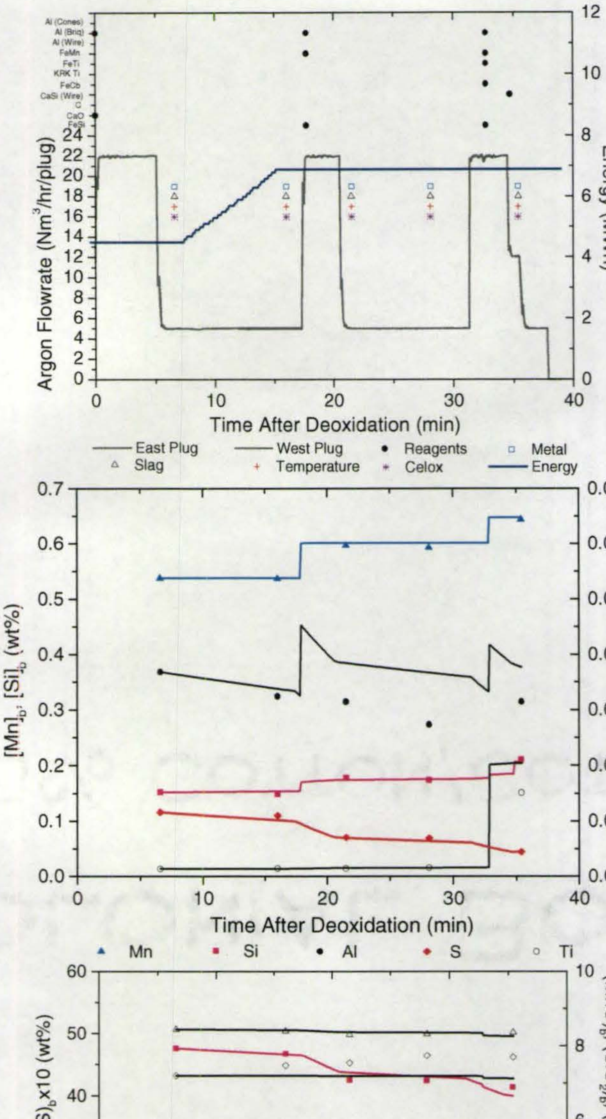

Figure F-32: Heat 32 stirring, heating, and sampling procedure. Comparison of experimental and model predicted results for Heat 32 using fitted slag phase mass transfer coefficients. (middle) Steel concentration profile, (bottom) slag concentration profile.

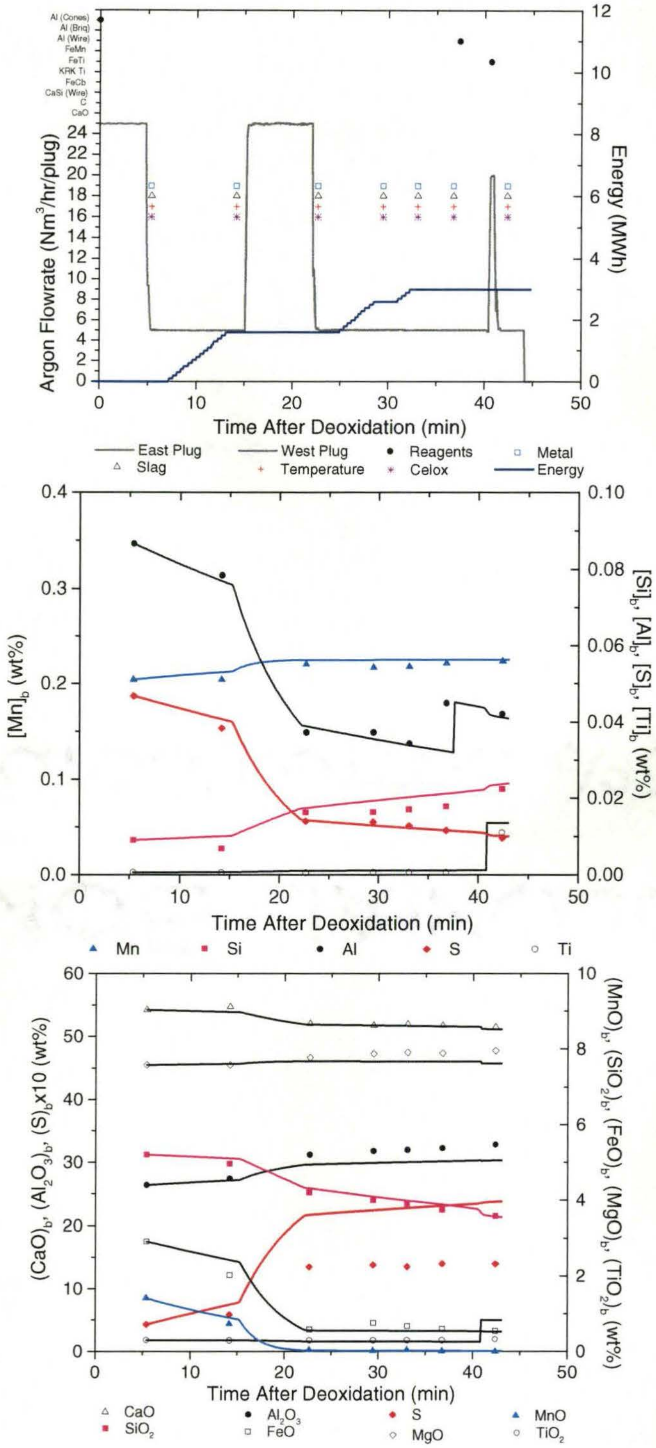

Figure F-33: Heat 33 stirring, heating, and sampling procedure. Comparison of experimental and model predicted results for Heat 33 using fitted slag phase mass transfer coefficients. (middle) Steel concentration profile, (bottom) slag concentration profile.

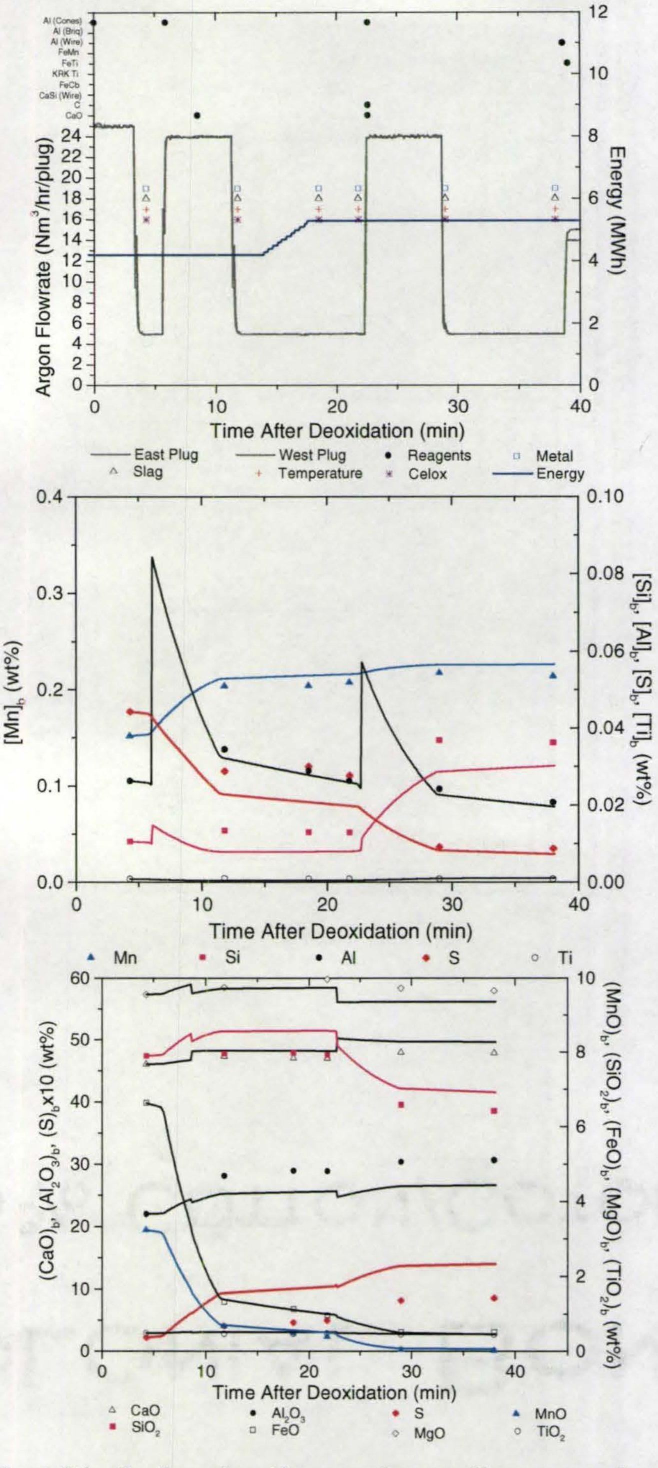

Figure F-34: Heat 34 stirring, heating, and sampling procedure. Comparison of experimental and model predicted results for Heat 34 using fitted slag phase mass transfer coefficients. (middle) Steel concentration profile, (bottom) slag concentration profile.

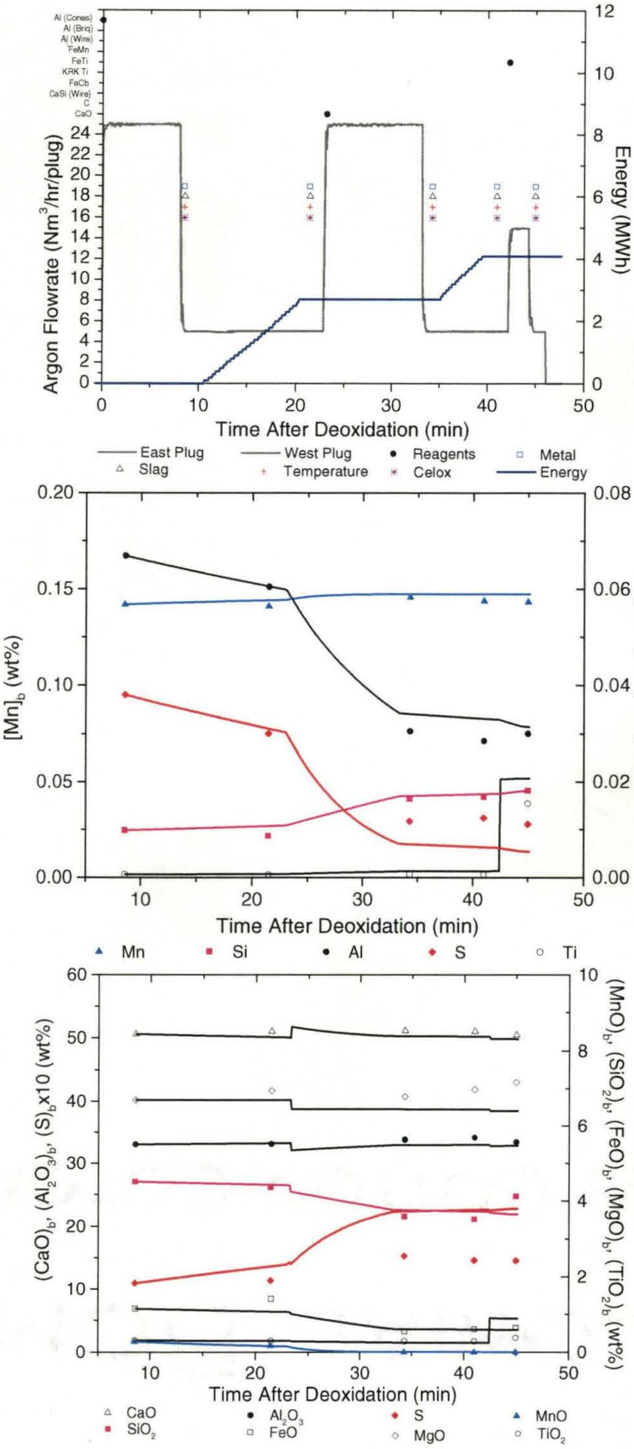

Figure F-35: Heat 35 stirring, heating, and sampling procedure. Comparison of experimental and model predicted results for Heat 35 using fitted slag phase mass transfer coefficients. (middle) Steel concentration profile, (bottom) slag concentration profile.

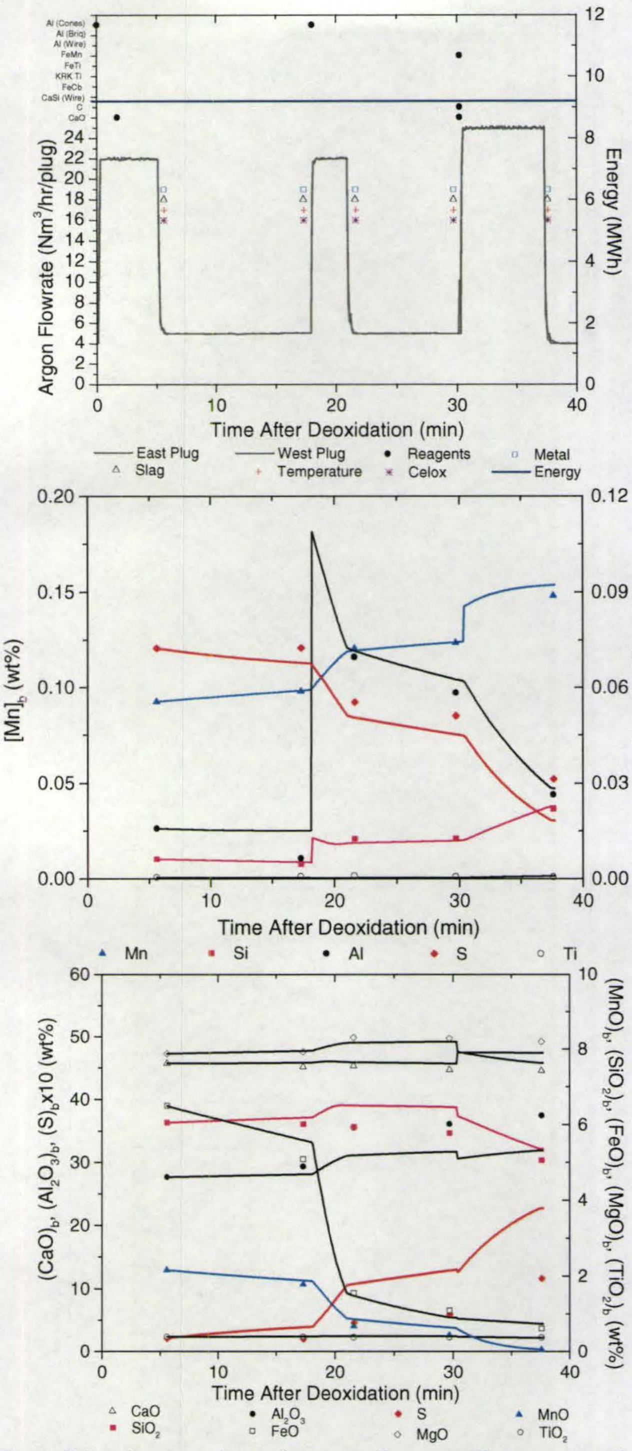

Figure F-36: Heat 36 stirring, heating, and sampling procedure. Comparison of experimental and model predicted results for Heat 36 using fitted slag phase mass transfer coefficients. (middle) Steel concentration profile, (bottom) slag concentration profile.

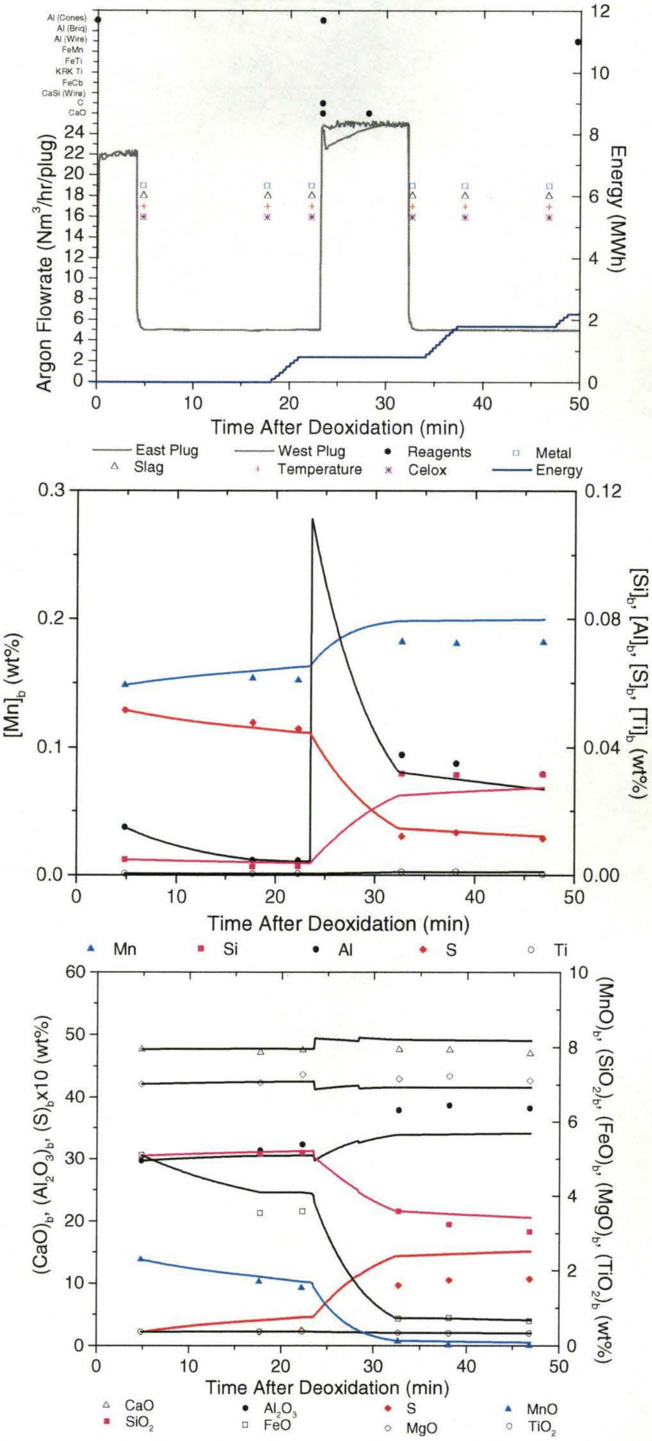

Figure F-37: Heat 37 stirring, heating, and sampling procedure. Comparison of experimental and model predicted results for Heat 37 using fitted slag phase mass transfer coefficients. (middle) Steel concentration profile, (bottom) slag concentration profile.

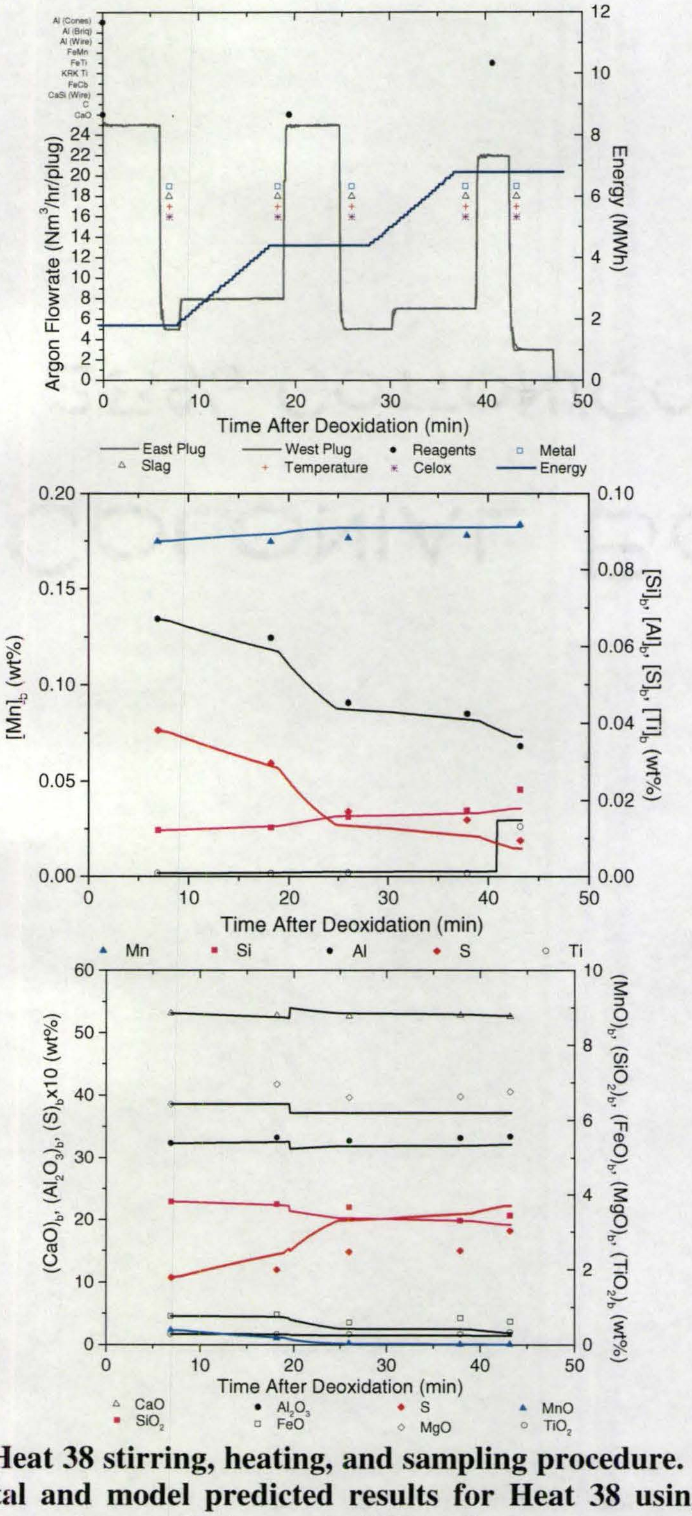

Figure F-38: Heat 38 stirring, heating, and sampling procedure. Comparison of experimental and model predicted results for Heat 38 using fitted slag phase mass transfer coefficients. (middle) Steel concentration profile, (bottom) slag concentration profile.

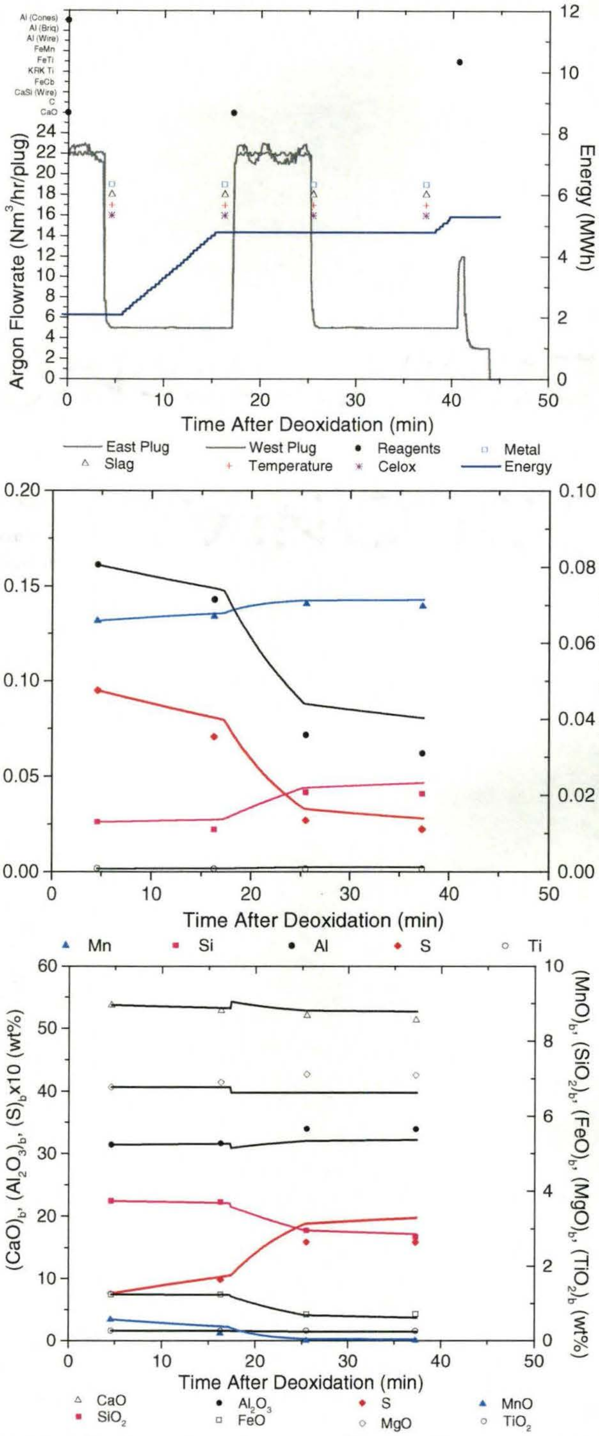

Figure F-39: Heat 39 stirring, heating, and sampling procedure. Comparison of experimental and model predicted results for Heat 39 using fitted slag phase mass transfer coefficients. (middle) Steel concentration profile, (bottom) slag concentration profile.

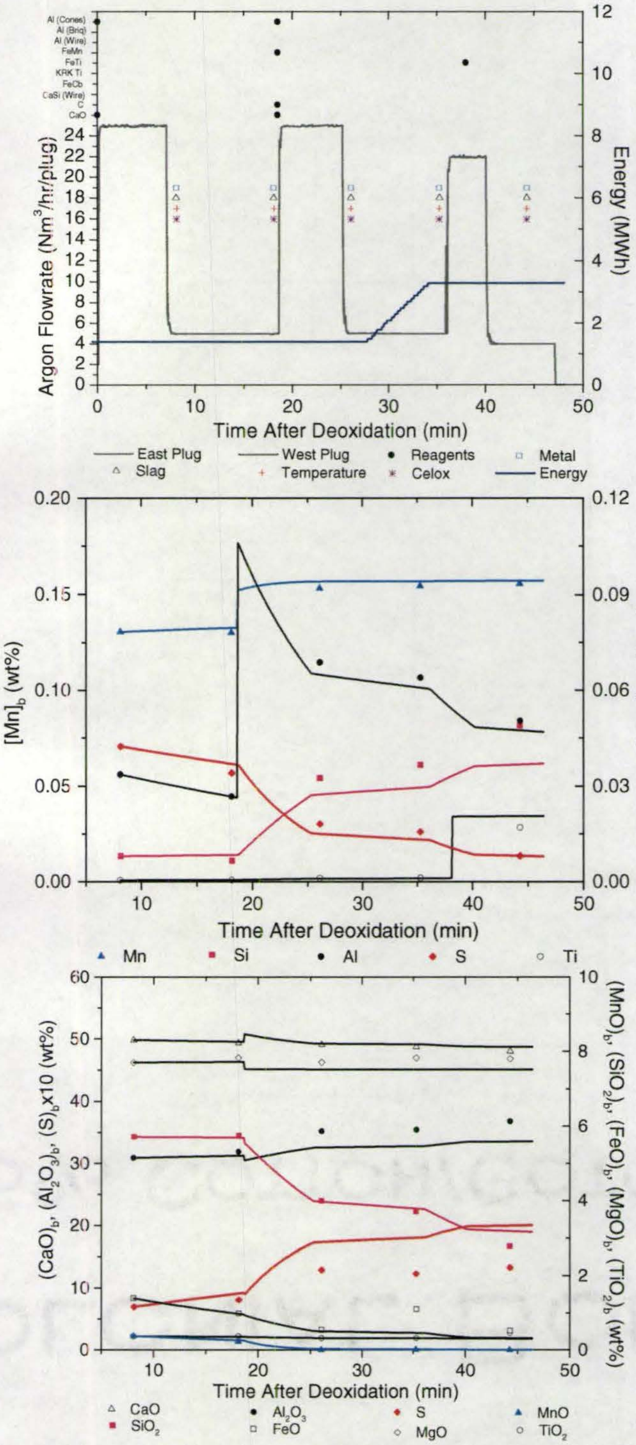

Figure F-40: Heat 40 stirring, heating, and sampling procedure. Comparison of experimental and model predicted results for Heat 40 using fitted slag phase mass transfer coefficients. (middle) Steel concentration profile, (bottom) slag concentration profile.

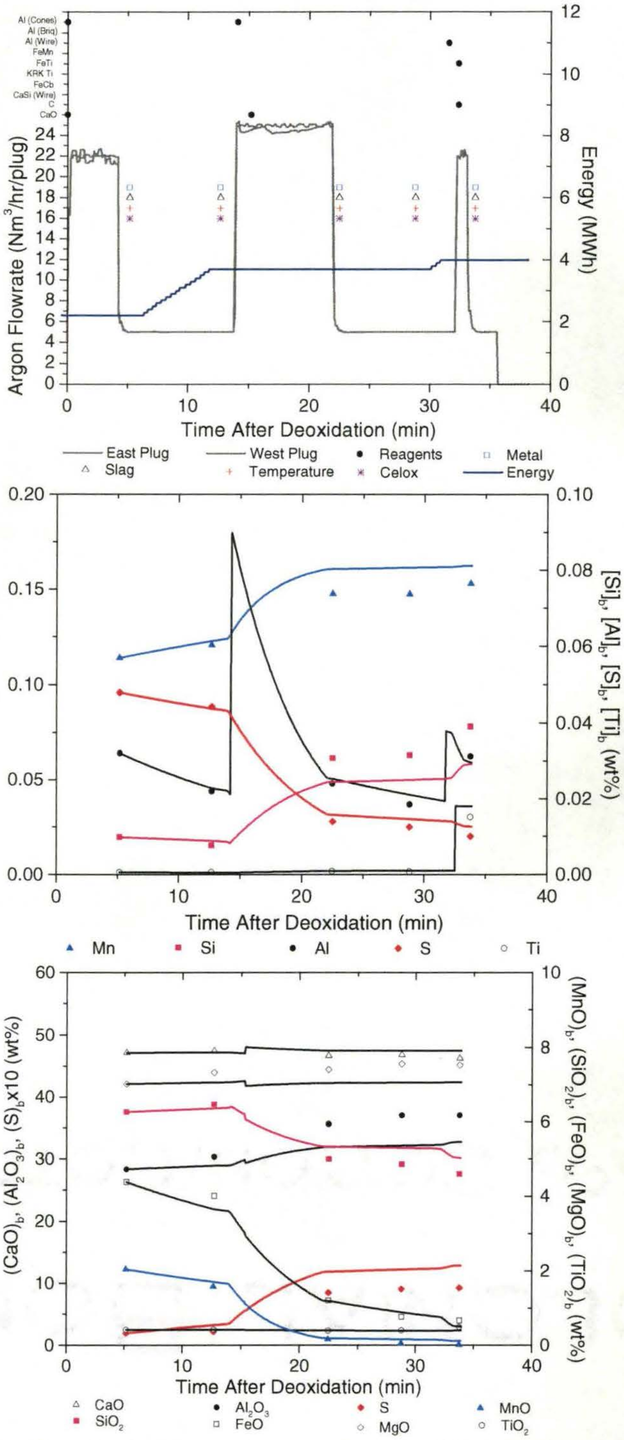

Figure F-41: Heat 41 stirring, heating, and sampling procedure. Comparison of experimental and model predicted results for Heat 41 using fitted slag phase mass transfer coefficients. (middle) Steel concentration profile, (bottom) slag concentration profile.